Oklahoma Department of Transportation
200 NE 21st Street, Oklahoma City, OK 73105-3204

FINAL REPORT ~ FHWA-OK-16-03

UNDERSTANDING THE BEHAVIOR OF PRESTRESSED GIRDERS AFTER YEARS OF SERVICE

Royce W. Floyd, Ph.D., P.E.
Jin-Song Pei, Ph.D.
Cameron D. Murray, M.S., Ph.D. Candidate
Brittany Cranor, EIT, M.S.
School of Civil Engineering and Environmental Science (CEES)

Peng F. Tang, Ph.D.
School of Electrical and Computer Engineering (ECE)

Gallogly College of Engineering
The University of Oklahoma
Norman, Oklahoma

December 2016

Oklahoma Department
of Transportation

The Oklahoma Department of Transportation (ODOT) ensures that no person or groups of persons shall, on the grounds of race, color, sex, religion, national origin, age, disability, retaliation or genetic information, be excluded from participation in, be denied the benefits of, or be otherwise subjected to discrimination under any and all programs, services, or activities administered by ODOT, its recipients, sub-recipients, and contractors. To request an accommodation please contact the ADA Coordinator at 405-521-4140 or the Oklahoma Relay Service at 1-800-722-0353. If you have any ADA or Title VI questions email ODOT-ada-titlevi@odot.org.

UNDERSTANDING THE BEHAVIOR OF PRESTRESSED GIRDERS AFTER YEARS OF SERVICE

FINAL REPORT ~ FHWA-OK-16-03

ODOT SP&R ITEM NUMBER 2256

Submitted to:
Dawn R. Sullivan, P.E.
Director of Capital Programs
Oklahoma Department of Transportation

Submitted by:
Royce W. Floyd, Ph.D., P.E.
Jin-Song Pei, Ph.D.
Cameron D. Murray, Ph.D. Candidate
Brittany Cranor, EIT, M.S. Student
School of Civil Engineering and Environmental Science (CEES)
Peng F. Tang, Ph.D.
School of Electrical and Computer Engineering (ECE)
The University of Oklahoma

December 31, 2016

TECHNICAL REPORT DOCUMENTATION PAGE

1. REPORT NO. FHWA-OK-16-03	2. GOVERNMENT ACCESSION NO.	3. RECIPIENT'S CATALOG NO.

4. TITLE AND SUBTITLE Understanding the Behavior of Prestressed Girders after Years of Service	5. REPORT DATE Dec 2016
	6. PERFORMING ORGANIZATION CODE
7. AUTHOR(S) Royce W. Floyd, Ph.D., P.E., Jin-Song Pei, Ph.D., Cameron D. Murray, Brittany Cranor, Peng F. Tang, Ph.D.	8. PERFORMING ORGANIZATION REPORT
9. PERFORMING ORGANIZATION NAME AND ADDRESS Donald G. Fears Structural Engineering Laboratory School of Civil Engineering and Environmental Science The University of Oklahoma, 303 E. Chesapeake St., Norman, OK 73019	10. WORK UNIT NO.
	11. CONTRACT OR GRANT NO. ODOT SPR Item Number 2256
12. SPONSORING AGENCY NAME AND ADDRESS Oklahoma Department of Transportation Office of Research and Implementation 200 N.E. 21st Street, Room G18 Oklahoma City, OK 73105	13. TYPE OF REPORT AND PERIOD COVERED Final Report Oct 2013 - Sep 2016
	14. SPONSORING AGENCY CODE

15. SUPPLEMENTARY NOTES

16. ABSTRACT

A comprehensive study including detailed analysis and shear testing to failure was conducted on two AASHTO Type II girders obtained from the I-244 bridge over the Arkansas River in Tulsa after approximately 47 years in service. Small-scale girders with a matching design were also tested individually and as a composite bridge section to evaluate the effects of composite behavior in resisting shear. Additionally, a number of inverse techniques and non-destructive testing methods were evaluated to determine their applicability for determining material properties and detecting damage in prestressed concrete bridges. In all shear tests of the two full-size girders, the applied loads exceeded expected loads whether determined from shear capacity calculations, flexural capacity by strain compatibility, or design demands from AASHTO LRFD. Tests of the individual and composite small-scale girders indicated a significant increase in load carrying capacity for girders within a composite bridge section. A simple yet effective 1-D model was established to predict time-dependent behaviors of pretensioned concrete and improvements were made to the backbone technique used for processing free vibration response data for nonlinear system identification and damage detection purposes through this project. The overall research provided important information on the structural and composite behavior of aged prestressed girder bridges critical to shear and on methods for identifying properties of aged members, structural health monitoring, and damage detection.

17. KEY WORDS Structural Design, Bridge Design, Maintenance, Prestressed Concrete, Shear, Backbone Technique, Failure Analysis, Composite Action	18. DISTRIBUTION STATEMENT No restrictions. This publication is available from the Office of Research and Implementation, Oklahoma DOT.

19. SECURITY CLASSIF. (OF THIS REPORT) Unclassified	20. SECURITY CLASSIF. (OF THIS PAGE) Unclassified	21. NO. OF PAGES 189	22. PRICE N/A

Form DOT F 1700.7 (08/72)

SI* (MODERN METRIC) CONVERSION FACTORS

APPROXIMATE CONVERSIONS TO SI UNITS

SYMBOL	WHEN YOU KNOW	MULTIPLY BY	TO FIND	SYMBOL
		LENGTH		
in	inches	25.4	millimeters	mm
ft	feet	0.305	meters	m
yd	yards	0.914	meters	m
mi	miles	1.61	kilometers	km
		AREA		
in^2	square inches	645.2	square millimeters	mm^2
ft^2	square feet	0.093	square meters	m^2
yd^2	square yard	0.836	square meters	m^2
ac	acres	0.405	hectares	ha
mi^2	square miles	2.59	square kilometers	km^2
		VOLUME		
fl oz	fluid ounces	29.57	milliliters	mL
gal	gallons	3.785	liters	L
ft^3	cubic feet	0.028	cubic meters	m^3
yd^3	cubic yards	0.765	cubic meters	m^3
		NOTE: volumes greater than 1000 L shall be shown in m^3		
		MASS		
oz	ounces	28.35	grams	g
lb	pounds	0.454	kilograms	kg
T	short tons (2000 lb)	0.907	megagrams (or "metric ton")	Mg (or "t")
		TEMPERATURE (exact degrees)		
^{o}F	Fahrenheit	5 (F-32)/9 or (F-32)/1.8	Celsius	^{o}C
		ILLUMINATION		
fc	foot-candles	10.76	lux	lx
fl	foot-Lamberts	3.426	candela/m^2	cd/m^2
		FORCE and PRESSURE or STRESS		
lbf	poundforce	4.45	newtons	N
lbf/in^2	poundforce per square inch	6.89	kilopascals	kPa

APPROXIMATE CONVERSIONS FROM SI UNITS

SYMBOL	WHEN YOU KNOW	MULTIPLY BY	TO FIND	SYMBOL
		LENGTH		
mm	millimeters	0.039	inches	in
m	meters	3.28	feet	ft
m	meters	1.09	yards	yd
km	kilometers	0.621	miles	mi
		AREA		
mm^2	square millimeters	0.0016	square inches	in^2
m^2	square meters	10.764	square feet	ft^2
m^2	square meters	1.195	square yards	yd^2
ha	hectares	2.47	acres	ac
km^2	square kilometers	0.386	square miles	mi^2
		VOLUME		
mL	milliliters	0.034	fluid ounces	fl oz
L	liters	0.264	gallons	gal
m^3	cubic meters	35.314	cubic feet	ft^3
m^3	cubic meters	1.307	cubic yards	yd^3
		MASS		
g	grams	0.035	ounces	oz
kg	kilograms	2.202	pounds	lb
Mg (or "t")	megagrams (or "metric ton")	1.103	short tons (2000 lb)	T
		TEMPERATURE (exact degrees)		
^{o}C	Celsius	1.8C+32	Fahrenheit	^{o}F
		ILLUMINATION		
lx	lux	0.0929	foot-candles	fc
cd/m^2	candela/m^2	0.2919	foot-Lamberts	fl
		FORCE and PRESSURE or STRESS		
N	newtons	0.225	poundforce	lbf
kPa	kilopascals	0.145	poundforce per square inch	lbf/in^2

*SI is the symbol for the International System of Units. Appropriate rounding should be made to comply with Section 4 of ASTM E380.
(Revised March 2003)

ACKNOWLEDGEMENTS

The authors appreciate Mr. Walt Peters from ODOT Bridge Division for his support and technical guidance offered to our work. Mr. Doug Martin and Voss Engineering are acknowledged for donating the elastomeric bearing pads. The ground penetrating radar testing crew from the ODOT Materials Division led by Mr. Matt Romero is appreciated.

The following students who participated in the project and made a contribution are acknowledged: Mr. Kyle A. Roeschley, former undergraduate and master's student from ECE OU; Ms. Alexandria Stumps, Mr. Connor Casey, Mr. Alieu Jobe, Mr. Stephen Tanksley, and Ms. Chandler Funderburg, undergraduate students from OU CEES; Mr. Troy M. Bowser, undergraduate and master's student from OU CEES; Mr. Soroush Mohammadzedah, former Ph.D. student from OU CEES; and Mr. Arthur Wendling and Ms. Kavitha Sadhasivam, former master's students from CEES OU.

EXECUTIVE SUMMARY

The state of Oklahoma is making a push to eliminate all structurally deficient bridges within the state by the year 2020 after consistently ranking near the bottom of the national list of structurally deficient bridges in the early 2000s. In order to address shear capacity concerns related to additional bridges not currently classified as deficient, the research described in this report was initiated by ODOT focused on a comprehensive study of two AASHTO Type II girders obtained from the I-244 bridge over the Arkansas River in Tulsa during its replacement in 2013 after about 47 years in service. The shear capacity of the prestressed girders used for this bridge and others built during the same time period is a concern because the AASHTO Standard Specifications used to design these girders employed a less conservative design methodology, often referred to as the "quarter-point rule", than what is specified in the current AASHTO LRFD Specifications. Approximately one fourth of the bridges (not including culverts) in Oklahoma are precast prestressed concrete girder and slab bridges, and of these, approximately 10% (400) were designed and put into service using the so called "quarter-point rule" in the AASHTO Standard Specifications, leaving them potentially vulnerable to concerns with shear capacity. Bridges designed earlier, in the 1960s and 1970s, are potentially more vulnerable since they used lower strength Grade 40 shear reinforcement. As the state makes a major push to replace structurally deficient bridges, it is important to have a clear understanding of the actual capacity of in-place bridges designed under the past specifications when rating using the current specifications. This understanding could potentially have a major influence on whether a particular bridge requires load posting or replacement.

The two girders examined in this project are representative of separate designs for 30 ft and 46 ft spans. Both girders were subjected to a battery of non-destructive tests to assess the effects of damage over time and to destructive shear testing at each end. The project included a detailed study of the contribution of the bridge deck and entire bridge system to shear capacity through testing the real-world girders with a section of the original deck and diaphragms intact, through construction and testing of a scaled composite bridge section, and through detailed structural analysis. This research provided important information on the structural and composite behavior of aged prestressed girder bridges critical to shear and on methods for identifying properties of aged members, structural health monitoring, and damage detection.

As has been reported in the literature, shear capacity calculations can vary dramatically and the results described in this report indicate limited agreement between different methods. The girders that were tested showed good ductility and a large amount of cracking before failure, despite being in service for more than 45 years. Corrosion at the ends did cause some issues, especially at high loads. Spalling was often initiated by the corrosion cracking at the ends, potentially leading to bond loss. Bond loss behavior due to corrosion is important since similar deterioration is common in simply supported precast concrete girder bridges in Oklahoma. The 2012 AASHTO LRFD simplified method was not a conservative method to calculate shear capacity for the bridge girders tested, and this research indicated that the Modified Compression

Field Theory methods of 2004 AASHTO LRFD is the best balance of accuracy and conservativism. In all tested cases however, the applied loads exceeded expected loads determined from shear capacity calculations or flexural capacity by strain compatibility depending on the failure type. Experimental loads also exceeded demands calculated using the current design loads and load distribution factors. Testing of the scaled bridge girders and scaled composite bridge section indicated that the composite section added significant shear capacity compared to an individual girder.

A number of methods were evaluated for determining properties of aged girders and monitoring structural health. A simple yet effective 1-D model was established by leveraging an existing initial value problem model for concrete creep and strand relaxation in post-tensioned concrete and Guyon’s instantaneous elastic shortening analysis based on a boundary value problem to predict time-dependent behaviors of pretensioned concrete. By directly utilizing draw-in time history measured from a pretensioned concrete beam and other section and material properties, many facets of bond-transfer behavior can be predicted revealing the insights into the time-dependent interaction of strand and concrete that would otherwise be obscure in current literature. Backbone analysis methods for free vibration data were substantially advanced through work on the project and have great potential for nonlinear system identification and damage detection purposes in prestressed concrete bridges. System identification of flexural rigidity based on elastic flexural testing data and using cracking moment to evaluate effective prestress force were also shown to be effective methods.

Table of Contents

List of Figures

List of Tables

1. INTRODUCTION

1.0 Nomenclature

A_v	area of shear reinforcement within spacing, s (in^2)
b'	width of web (in.)
b_v	effective web width taken as the minimum web width within d_v (in.)
b_w	width of web (in.)
d	distance from extreme compression fiber to centroid of tensile reinforcement (in.)
d_p	depth to centroid of prestress force from extreme compression fiber (in.)
d_v	effective shear depth taken as the distance between the resultant tensile and compressive forces due to flexure (in.)
f'_c	specified compressive strength of concrete (psi)
f_d	stress due to unfactored dead load at tension face (psi)
f_{pc}	compressive stress in concrete after losses at centroid of the section resisting external loads or at the junction of the web and the flange when the centroid is within the flange (psi)
f_{pe}	stress in concrete due to effective prestress force at tension face (psi)
f_{sy}	tensile capacity of shear reinforcement (psi)
f_{yt}	yield strength of transverse reinforcement (psi)
I	moment of inertia of cross-section (in^4)
j	ratio of distance between centroid of compression and centroid of tension and total depth
M_{cre}	moment causing flexural cracking at section due to external loads (in.-lb)
M_{max}	maximum factored moment due to external loads (in.-lb)
M_u	factored moment at section (in.-lb)
s	spacing of shear reinforcement at section (in.)
s_{xe}	a spacing factor given in the code
V_c	concrete contribution to shear strength (lb)
V_{ci}	nominal shear strength provided by concrete when diagonal cracking results from combined shear and moment (lb)
V_{cw}	nominal shear strength provided by concrete when diagonal cracking results from high principal tensile stress in web (lb)
V_d	shear force at section due to unfactored dead load (lb)

V_i	factored shear force at section due to externally applied loads associated with M_{max} (lb)
V_n	nominal shear capacity (lb)
V_p	vertical component of effective prestress force at section (psi)
V_s	steel contribution to shear strength (lb)
V_u	factored applied shear at section (lb)
y_t	distance from centroid of gross section to tension face (in.)
α	angle of inclination of transverse reinforcement
ε_s	net longitudinal tensile strain at the centroid of the tension reinforcement
λ	modification factor for lightweight aggregate; 1.0 for normal weight

1.1 Background and Motivation

In 2013, two bridge girders were selected from separate spans of the eastbound side of the I-244 bridge over the Arkansas River in Tulsa, OK for testing at the Fears Structural Engineering Laboratory at the University of Oklahoma (OU). The bridge was constructed in the late 1960's and its demolition in 2013 provided a rare opportunity to test girders that were in service for decades. The ends of the girders included some corrosion damage that is typical of urban bridges in Oklahoma and may have some effect on the shear capacity of the girders. The Oklahoma Department of Transportation (ODOT) is interested in the shear capacity of older bridge girders because of the deterioration of the end regions and because these girders were designed under an older version of the American Association of State Highway and Transportation Officials (AASHTO) bridge code. The bridge code at the time assumed a different critical section for shear (the quarter span point) than what is used today and also provided a different method of calculating shear capacity. The design demands from the previous code and the deterioration over time combine to potentially result in low ratings for shear using the current methods. It is possible that the older designs are not only less conservative for shear, but the presence of corrosion could reduce the bond of prestressing strands near the member ends. In addition to the specific concerns of ODOT, there have been few previous studies of bridge girders at the end of their service life, and even fewer that considered shear capacity specifically.

This report presents results from the research including a comparison of tested capacities from both ends of the two bridge girders to AASHTO codes and the American Concrete Institute (ACI) code (AASHTO 1973; AASHTO 2012; ACI 2014). No literature was found documenting shear performance of aged Type II girders, so this research adds to the body of knowledge on shear. Issues of corrosion of the girder ends were also examined as they relate to the performance of the beam up to the quarter span point. The information gained from the testing described is intended to inform rating decisions for bridges constructed with similar girder designs and deterioration. Additionally, methods for examining behavior and identifying important characteristics from in-service girders were investigated and developed, and the results of these efforts are also presented.

The end regions of concrete members are of particular importance to the designer of a prestressed concrete girder for several reasons. The ends are where the largest shear forces are present, where prestress force is transferred to the concrete, where the largest stresses due to prestress release are located if no harping or strand debonding is utilized, and where corrosion is most likely to occur. Corrosion at this location is common because joints between simply supported spans tend to leak water and deicing chemicals on the ends of the girders. Even though the stress at the extreme end is zero, the “end” of the girder in this report refers to the first quarter of the span (because this was the critical section for shear at the time these girders were designed). The strand transfer length is included in this section. While the presence of a prestress force improves the shear capacity of a section, strand bond can be lost when shear cracking occurs (Kaufman and Ramirez 1988; Nordby and Venuti 1957). If bond is lost, the capacity of the member is significantly diminished.

1.2 Problem Statement

The project described in this report consisted of a comprehensive study including both testing and analysis of two real-world AASHTO Type II girders obtained during replacement of the I-244 bridge over the Arkansas River in Tulsa after about 47 years in service. It also included detailed study of composite action in the form of testing the real-world girders and a scaled composite bridge section. This research provides critical supplemental information and improves upon previous research focused on the shear capacity of one real-world girder sponsored by ODOT at the University of Oklahoma and answers numerous questions concerning bridge girders put into service during the same time period. It includes detailed information concerning composite behavior of prestressed girder bridges critical to shear. It also provided opportunities for a significant quantity of additional research focused on identifying important properties of in-service bridges using non-destructive testing methods.

1.3 Project Objectives

1. Identify, obtain and transport representative girders from the I-244 bridge site to the laboratory.

2. Analyze girders and composite structures for shear based on
    - AASHTO Standard Specifications
    - AASHTO LRFD Specifications

3. Conduct analytical and numerical analysis of transfer bond/transfer length behavior.

4. Perform system identification to determine effectiveness of the various methods and girder parameters including: transfer length, effective prestress, and other properties of aged real-world girders.

5. Conduct shear capacity tests on each end of the girders including composite action.

6. Perform load tests on a scaled beam-slab structure to experimentally determine the composite action.

7. Conduct experimental analysis to determine actual transfer bond parameters for use in the analytical analysis of prestress transfer.

1.4 Previous Research on Shear in Aged Girders

1.4.1 Overview

Several state departments of transportation and other states entities have studied the behavior of girders after many years of service. ODOT has sponsored some research on the behaviors of girders after they have been in service, and the study described in this report extends the previous research, Pei et al. (2008). Previous studies were examined to help decide the best methods for predicting the capacities, procedures for testing, ways to place the instrumentation, and methods of analyzing the data.

There have been few studies that looked specifically at the shear capacity of older concrete girders. A number of studies have been conducted to test aged prestressed concrete girders for residual prestress or flexural strength (Shenoy and Frantz 1991; Halsey and Miller 1996; Pessiki et al. 1996; Czaderski and Motavelli 2006; Lundqvist and Riigimaki 2010), but few have focused specifically on shear capacity.

Several studies were performed at the University of Florida on large scale sections in shear. In these studies, the researchers focused on varying the shear span to depth (*a*/*d*) ratio, which alters the interaction between bending and shear stresses. These studies found that for *a*/*d* ratios of 3 or less, bond shear failures are common. When *a*/*d* is approximately equal to 4, compression or shear-compression failures occurred. Finally, at *a*/*d* of 5 or greater the failure mechanism transitioned to flexure. This work also found the ACI and Modified Compression Field Theory (MCFT) methods to be conservative for *a*/*d* of 3 or less (Hamilton et al. 2009; Ross et al. 2011).

At the University of Utah, seven 42-year-old girders were recovered for shear tests. These tests were performed at an *a*/*d* ratio of 1.5 using a single point load. Code equations were found to be conservative and Strut and Tie Modeling (STM) was more accurate given that the load was near the support (Osborn et al. 2010).

Prior work at the University of Oklahoma (OU) was conducted in 2008 when researchers tested a 40-year-old AASHTO Type II girder in the lab to compare the 1973 and 2004 AASHTO codes. This girder was tested at *a*/*d* of 1.0 and the researchers found that all codes were conservative at this location (Martin et al. 2011). The study described in this report is a continuation of this work for ODOT, testing larger *a*/*d* ratios. The girder in this older study was damaged and the deck had been completely removed, so the current study expands the work to girders in better condition with partial deck and diaphragms remaining.

1.4.2 Factors Affecting Shear Behavior in Aged Prestressed Girders

Shear behavior depends on many factors such as the span to depth ratio (*a*/*d*), concrete tensile strength, shear reinforcement, and effective prestress. When a specimen ages, other factors add to the complexity – loss of bond of the prestressing strands in the end regions and deterioration of the concrete. Nordby and Venuti (1957) found that the prestressing strands lost bond after the concrete had cracked. They found that fatigue failure did not occur when the specimens were uncracked. End slip did occur when the span to depth ratio was small, specifically when the embedment length was less than 6 feet (Nordby and Venuti 1957).

Kaufman and Ramirez (1988) ran tests on I-beams with the shear span within the development length and outside the development length. End slip occurred in the tests with the shear span within the development length but not in the spans outside the development length. Tests were done on beams with and without shear reinforcement. The shear reinforcement provided the concrete with the capability to withstand higher load which increased the shear capacity (Kaufman and Ramirez 1988).

Maruyama and Rizkalla (1988) focused on the effects of small shear span to depth ratio and shear reinforcement on the shear capacity. The beams failed before expected and end slip was recorded due to the critical section being within the development length. Cracks occurred at the location that the ACI 318 code predicted for the development length. Strain gauges on the stirrups showed yielding of stirrups before the prestressing strands slipped. The beam could not be failed in shear due to the slippage of the strands and yielding of a portion of the stirrups (Maruyama and Rizkalla 1988).

1.4.3 Shenoy and Frantz (1991)

Two post-tensioned box girders with spans of 45 feet were taken from a deteriorated bridge for replacement with new girders and tested. The box girders were 36 in. by 27 in. and 27 years old. One of the girders did not have any visual cracking or corrosion. The other exhibited cracking and spalling. The goal of this study was to determine the strength, prestress losses and amount of chloride ions within the concrete causing corrosion (Shenoy and Frantz 1991).

Calculations were made to estimate the maximum load and deflection. The deflection was calculated using the moment area method and ACI code was used to determine the maximum load. The girders were simply supported on 2 in. diameter rollers placed on piers. The girder was loaded at third points to mimic the loading of two axles. At midspan of the girder, eighteen inches of concrete that covered the prestressing strands were removed to place strain gauges on the strands. Strain gauges were also placed at the top and sides at midspan of the girder. The two rams at each load point were connected with prestressing strands to rocker plates at the web. The rams could only extend five inches so chucks were used to maintain the load while the ram was reset. Each time the ram was reset, the instrumentation was documented and cracks marked. The test was ended after the girder could not support any additional load (Shenoy and Frantz 1991).

The design plans were not available at the time of testing so the researchers had to assume the material properties of the girders. The compressive strength was initially assumed to be 6000 psi, but was determined to be higher with compressive tests. Eight cores were taken after testing to determine the modulus of elasticity and compressive strength. Samples of the prestressing strands were taken to test for strand strength and to determine the modulus of elasticity (Shenoy and Frantz 1991).

The study found that the two beams behaved similarly. The beams showed linear elasticity until flexural cracking. The estimated capacities were very close to the actual capacities of the girders. The cracks were typical flexural cracks, and very few shear cracks occurred. Concrete strains were linear until flexural cracking occurred. The measured strain of the strands was determined to be inconsistent and determined to not add any information to the results. The measured prestress losses were determined with a cracking moment test. The girder was loaded until a crack was observed and reopened to calculate the prestress losses. The measured prestress losses were much less than the predicted losses (Shenoy and Frantz 1991).

1.4.4 Shahawy et al. (1993)

The study was conducted on thirty-three AASHTO type II girders that were specifically made for the research. The goals of this study were to determine the development length and shear strength of the girders (Shahawy et al. 1993).

The study was designed to test each end of the girder to failure, first by testing one end then moving the supports, thereby eliminating the damage from the span, and testing the other end. LVDTs were placed on the end of the strand to measure any end slip of the strand to determine if bond was lost during any test (Shahawy et al. 1993).

The shear strengths were compared to predicted value from AASHTO 1989, current specifications at the time, and the revisions from 1990 and 1991 Interim Specifications for that code to evaluate the effectiveness of the changes. The results from the study would help with modifications to the future AASHTO code. The conclusion was the AASTHO 1989 specifications estimated the shear capacity better than the revised specifications (Shahawy et al. 1993).

1.4.5 Pessiki et al. (1996)

Two prestressed I-beams, 24 in. wide by 60 in. tall with a span of 89 feet, were taken from a bridge in service for 28 years to test. The beams were still in good condition upon removal. The beams were tested in three-point bending. The beams were first loaded to cracking, and then were unloaded and the crack was reopened. The beams were finally loaded to failure (Pessiki et al. 1996).

Strain was measured between the shear cracks using strain gauges. The load vs strain plots were evaluated to determine the cracking load along with the visual observation. The plots exhibited a bilinear response and the point where the slope changed was taken as the cracking load. The effective prestress force was then determined using the cracking load, section properties and elastic analysis. Cores were taken from the beam and tested for modulus of elasticity and compressive strength. Failure was due to crushing of the concrete in the compression zone before the beam could fail due to shear or flexural cracking (Pessiki et al. 1996).

1.4.6 Pei et al. (2008)

Research was previously done at the University of Oklahoma on a similar project to the one described in this report, which is an extension to the previous work. The earlier study examined the shear capacity of a single AASHTO Type II girder taken from the westbound side of the I-244 bridge over the Arkansas River in Tulsa, Oklahoma, after being in service for several decades. The research was performed to determine the shear capacity, prestress losses, and material properties of the AASHTO Type II girder. The girder was not carefully removed from the bridge and had been abandoned; it was corroded on one end which was retrofitted with fiber reinforced polymer sheets, and all of the deck had been removed.

Elastic flexural tests were done on the girder to determine the stiffness. The girder was supported four different ways to get a thorough analysis of the stiffness. The support conditions were 30 feet apart with a 5 foot cantilever on each side, 35 feet apart with a 5 foot cantilever on the retrofitted end, 35 feet apart with a 5 foot cantilever on the other end, and simply supported 40 foot span. The load point was placed at midspan and 10 feet on either side of midspan. A test was run with each support condition and load condition for a total of 12 tests. The stiffness was determined for the girder assuming it was not constant along the length of the girder. The camber of the girder was also measured.

Shear tests were performed on the girder with the load point located three feet from end of the girder to guarantee a shear failure. The damaged ends of the girder were then cut off and more shear tests were performed. The shear capacity calculated using AASHTO-Standard Specifications (1973), AASHTO-LRFD (2004) and ACI Committee 318-08 (2008) were compared to each other. The experimental shear capacity was compared to the calculated using each of the specifications. Cores were taken from the girder to test for compressive strength and modulus of elasticity (Pei et al. 2008).

The research provided a better understanding of the condition of girders in the state of Oklahoma similar to the one tested. The girder was found to exceed the current demands (Pei et al. 2008).

1.4.7 Ross et al. (2011)

This paper summarized the study conducted by Hamilton III et al. (2009). Four AASHTO Type III girders were salvaged from a bridge in Florida and tested for shear failure using three point bending. A total of six tests were conducted; two girders were tested at both ends and the other two only at one end. The location of loading varied for each test. Neoprene pads were used at the support to allow for rotation and to prevent torsion. LVDTs were placed at the load point to measure deflection, at the end of the strands to measure strand slip and at the supports to measure the compression of the neoprene pads. Strain gauges and strain rosettes were placed at discrete locations along the beam to measure the strain in the girder. The experimental results were compared to current specifications and specifications at the time the girder was cast – AASHTO (1973), AASHTO LRFD (2007) and ACI (2008) (Ross et al. 2011).

The results showed that the girders being thirty years old did not compromise their integrity. The specifications produced conservative values compared to the experimental results. However, predicted failure modes did not always match the experimentally observed failure modes (Ross et al. 2011).

1.4.8 Osborn et al. (2012)

This paper described the master's thesis from Parry Osborn (Osborn, 2010). This study examined eight AASHTO Type II girders taken from a bridge in Utah that was in service for forty-two years. Some ends where retrofitted with carbon fiber reinforced polymer while others were left in the original condition (Osborn 2010). The goals in this study were to determine a way to retrofit existing girders in service to prevent them from needing to be replaced (Osborn et al., 2012).

Several flexural tests were performed to determine the prestress force loss due to the years of service of the girders. Cracking moment tests were performed to determine the cracking load and prestress losses. To determine the prestress loss, cracking moment tests were performed, and strain gauges were used to determine what load cause the bottom fiber to have a zero stress. Shear tests were conducted to determine the shear capacity. The shear test setup included varying spans with the load point 4 feet from the end of the girder. The spans ranged because each girder was tested on both ends and the researchers did not want damage from the first test to affect the second test. The experimental capacities were compared to AASHTO (2009) and ACI (2008) specifications. The results showed that the capacities determined using the specifications were conservative compared to the experimental values (Osborn et al. 2012).

1.5 Shear Strength Calculation Methods

1.5.1 AASHTO Standard Specifications (1973)

The AASHTO shear philosophy has evolved considerably since the 1970's. At that time, the governing bridge code was the AASHTO Standard Specifications for Highway Bridges (from here on referred to as AASHTO-STD). This code used a load factor design (LFD) philosophy for concrete. One concern regarding bridge girders designed at this time is the location of the critical section for shear. The code at this time recommended investigating shear only in the middle half of the span. The reasoning was that the critical section for shear would be at a location where shear and flexural forces interact. At locations closer to the support than the "quarter-point" the shear demand was to be taken the same as at the quarter-point. It is possible that higher shear demands at the ends could lead to a lack of conservativism for these older designs.

Nominal shear strength is determined in AASHTO-STD in a similar fashion to ACI 318 (2014) (described in Section 1.4.3); by summing the contributions of the steel and the concrete. The shear resistance in AASHTO-STD in 1973 is given by Eq. (1.1) (AASHTO 1973).

$$V_n = V_c + V_s = 0.06f'_c b' jd + \frac{2A_v f_{sy} jd}{s} \tag{1.1}$$

where:

b' = width of web (in.)
j = ratio of distance between centroid of compression and centroid of tension and total depth
f_{sy} = tensile capacity of shear reinforcement (psi)
s = spacing of shear reinforcement at section (in.)

This procedure is quite similar to the ACI (2014) method, although it is more simplistic with regards to the contribution of concrete to shear strength. As for the steel contribution to shear strength, the "2" in the numerator of the second term in Eq. (1.1) would correspond to a crack angle of 26.6 degrees, as opposed to 45 degrees in the ACI code. A smaller crack angle makes sense because prestress forces are known to flatten stress trajectories in girders (Wight and MacGregor 2012), however if the actual crack angle is greater than 26.6 degrees the steel capacity will be overestimated. A minimum shear steel requirement is given by Eq. (1.2).

$$A_v \geq \frac{100b's}{f_{sy}} \tag{1.2}$$

There is no upper limit on shear reinforcement in AASHTO-STD. However, the concrete contribution to shear strength is constrained by an upper limit on compressive strength of 3000 psi. A positive result of this requirement is that most girders designed at this time required a larger amount of shear steel, despite the demand being taken further into the section. This conservativism with regards to concrete strength could improve the ductility of girders loaded in shear from this time period.

1.5.2 AASHTO LRFD Specifications

The AASHTO bridge code has changed considerably overall since the 1970's. The current code now uses a probabilistic Load and Resistance Factor Design (LRFD) design philosophy (AASHTO 2012). For the rest of this report, the LRFD code (2012 version) will be referred to as AASHTO-LRFD. AASHTO-LRFD began using a new shear design methodology in 1994 known as the "sectional design model" based on Modified Compression Field Theory (MCFT) (Collins et al. 1996; Vecchio and Collins 1986; Hawkins et al. 2005). This method was rather complex and was not preferred by designers as it required an iterative solution. This procedure was simplified in 2008 and there are now multiple options to calculate concrete shear capacity in the 2012 AASHTO-LRFD. The AASHTO-LRFD "simplified procedure" is similar to the ACI method (section 1.5.3) because it divides a member into sections controlled by flexure-shear and web-shear (Hawkins et al. 2005). Shear resistance is taken as the sum of the concrete shear strength, steel contribution to shear strength, and a term to account for the influence of prestress force on shear strength. Concrete contribution to shear strength is taken as the lesser of the resistance when cracking is caused by combined shear and moment or the resistance when cracking occurs in the web due to shear only (Eqs. 1.3-1.5).

$$V_c = lesser\ of\ V_{ci}, V_{cw} \tag{1.3}$$

$$V_{ci} = 0.02\sqrt{f'_c}b_v d_v + V_d + \frac{V_i M_{cre}}{M_{max}} \geq 0.06\sqrt{f'_c}b_v d_v \tag{1.4}$$

$$V_{cw} = \left(0.06\sqrt{f'_c} + 0.30 f_{pc}\right) b_v d_v + V_p \tag{1.5}$$

where:

b_v = effective web width taken as the minimum web width within d_v (in.)
d_v = effective shear depth taken as the distance between the resultant tensile and compressive forces due to flexure (in.)

The general method provided by AASHTO-LRFD is based on MCFT. MCFT assumes that a series of shear cracks will form in the web of a member, creating a network of diagonal concrete shear struts (in compression) and vertical steel stirrups (in tension) that work together to carry the total shear demand. Each concrete strut also carries some tension and the sum of the tension in all the struts is the concrete's contribution to the shear strength. In order to find shear resistance by MCFT, the factors β and θ must be determined. The factor β describes the ability of the concrete to transmit tension and shear and θ is the crack angle (or angle of diagonal compressive stress). In the original MCFT procedure, a series of tables were used to relate strains to β and θ. In the current AASHTO-LRFD "general method" there are two equations used to estimate these factors, the β calculation is shown in Eqs. 1.6-1.8.

If $A_v \geq$ Minimum A_v, (1.6)

$$\beta = \frac{4.8}{(1+750\varepsilon_s)} \tag{1.7}$$

else,

$$\beta = \frac{4.8}{(1+750\varepsilon_s)}\frac{51}{(39+s_{xe})} \tag{1.8}$$

where:

ε_s = net longitudinal tensile strain at the centroid of the tension reinforcement

s_{xe} = a spacing factor given in the code

The crack angle, θ, can be found by the relationship in Eq. (1.9).

$$\theta = 29 + 3500\varepsilon_s \tag{1.9}$$

This new procedure based on equations instead of tables was developed by Bentz et al. (2006) in 2006 to simplify the MCFT procedure. If the minimum amount of shear steel is not provided, the equation for β assumes no transverse reinforcement. These simplified calculations should be conservative for almost all combinations of β and θ as compared to the original tabular method. Today, the tables are maintained in AASHTO-LRFD as an appendix and are still allowed for design. The concrete contribution to shear strength is then given as a function of β by Eq. (1.10).

$$V_c = 0.0316\beta\sqrt{f'_c}b_v d_v \tag{1.10}$$

Finally, the steel contribution in AASHTO-LRFD is generally a function of the crack angle, rebar spacing, section depth, stirrup angle, area, and yield strength of the reinforcement. This relationship is given in Eq. (1.11).

$$V_s = \frac{A_v f_y d_v (cot\theta + cot\alpha) sin\alpha}{s} \tag{1.11}$$

where:

α = angle of inclination of transverse reinforcement

MCFT was introduced as a comprehensive, rational method for analyzing concrete members subjected to shear. Despite its more complicated nature, it should provide more accurate results than the ACI method and the AASHTO-STD method. It is hard to say definitively what effect older codes have on the conservativism of older designs because there are many variables involved in terms of demand and capacity. Because of the complex nature of these problems it is important to have experimental data from old girders for comparison to design codes.

1.5.3 ACI Shear Provisions

Early research at the University of Illinois found that transverse reinforcement restrains shear cracking and improves ductility after web cracks form (MacGregor et al. 1965). These findings led to equations for the shear capacity of concrete and minimum shear reinforcement (MacGregor and Hanson 1969). The shear methodology in the ACI Building Code Requirements for Structural Concrete (ACI 2014) was developed based on this early work and the equations remain largely unchanged. The ACI treatment of shear in prestressed concrete is given in Chapters 9 and 22 of the 2014 code and involves a separate calculation for the contribution of the steel and the concrete to the shear resistance (ACI 2014). The nominal shear capacity of a section is given by Eq. (1.12).

$$V_n = V_c + V_s \tag{1.12}$$

where:

V_n = nominal shear capacity (lb)
V_c = concrete contribution to shear strength (lb)
V_s = steel contribution to shear strength (lb)

For prestressed concrete members, the ACI code offers two methods to calculate shear capacity of the concrete: a simplified method and a more complex method that takes into account different cracking behavior and failure mechanisms. The complex method provides an equation for web-shear cracking and flexure-shear cracking to find the controlling type of cracking at a given section. For this research, the minimum of the capacity given by the two methods was chosen. The simplified method is given in Eq. (1.13) and Eq. (1.14).

$$V_c = (0.6\lambda\sqrt{f'_c} + 700\frac{V_u d_p}{M_u})b_w d \tag{1.13}$$

where:

$$2\lambda\sqrt{f'_c}b_w d \leq V_c \leq 5\,\lambda\sqrt{f'_c}b_w d \tag{1.14}$$

and:

λ = modification factor for lightweight aggregate; 1.0 for normal weight
f'_c = specified compressive strength of concrete (psi)
V_u = factored applied shear at section (lb)
d_p = depth to centroid of prestress force from extreme compression fiber (in.)
M_u = factored moment at section (in.-lb)
b_w = width of web (in.)
d = distance from extreme compression fiber to centroid of tensile reinforcement (in.)

For the more complex method in ACI, the concrete contribution related to flexure-shear capacity is given by Eqs. (1.15-1.18).

$$V_{ci} = 0.6\lambda\sqrt{f'_c}b_w d_p + V_d + \frac{V_i M_{cre}}{M_{max}} \tag{1.15}$$

where:

$$d_p \geq 0.8h \tag{1.16}$$

$$M_{cre} = \left(\frac{I}{y_t}\right)\left(6\lambda\sqrt{f'_c} + f_{pe} - f_d\right) \tag{1.17}$$

$$V_{ci} \geq 1.7\lambda\sqrt{f'_c}b_w d \tag{1.18}$$

and:

V_{ci} = nominal shear strength provided by concrete when diagonal cracking results from combined shear and moment (lb)
V_d = shear force at section due to unfactored dead load (lb)
V_i = factored shear force at section due to externally applied loads associated with M_{max} (lb)
M_{cre} = moment causing flexural cracking at section due to external loads (in.-lb)
M_{max} = maximum factored moment due to external loads (in.-lb)
y_t = distance from centroid of gross section to tension face (in.)
I = moment of inertia of cross-section (in^4)
f_{pe} = stress in concrete due to effective prestress force at tension face (psi)
f_d = stress due to unfactored dead load at tension face (psi)

The nominal shear force required to cause web-shear cracking is given by Eqs. (1.19) and Eq. (1.20).

$$V_{cw} = \left(3.5\lambda\sqrt{f'_c} + 0.3f_{pc}\right)b_w d_p + V_p \tag{1.19}$$

where:

$$d_p \geq 0.8h \tag{1.20}$$

and:

V_{cw} = nominal shear strength provided by concrete when diagonal cracking results from high principal tensile stress in web (lb)
f_{pc} = compressive stress in concrete after losses at centroid of the section resisting external loads or at the junction of the web and the flange when the centroid is within the flange (psi)
V_p = vertical component of effective prestress force at section (psi)

The shear strength supplied by the transverse reinforcement is given by Eq. (1.21). For vertical shear stirrups, the ACI code assumes a crack angle of 45 degrees. This approach likely overestimates the angle of shear cracking for prestressed beams but will give a conservative value for the steel contribution to shear strength.

$$V_s = \frac{A_v f_{yt} d}{s} \tag{1.21}$$

where:

A_v = area of shear reinforcement within spacing, s (in^2)
f_{yt} = yield strength of transverse reinforcement (psi)

The ACI methodology has not changed since the 1970's. ACI also allows the use of a strut-and-tie model for analysis and design in discontinuity regions of concrete beams.

1.5.4 Strut and Tie Models

Another option allowed by both ACI and AASHTO-LRFD is the strut-and-tie model (STM). At regions near discontinuities (e.g. loads, supports, cross section changes); St. Venant's Principle is no longer an accurate assumption (Nilson et al. 2005). These D-regions can be defined as sections of the beam within a distance equal to the member depth from the discontinuity. At these locations, Bernoulli beam theory does not provide accurate results for the shear capacity because the strain distribution is not linear. The STM was developed in the late 1800's to solve these types of problems (Schlaich et al. 1987). STM creates a truss analogy where diagonally cracked concrete forms compressive "struts," and the longitudinal and transverse reinforcement form tension "ties." The strength of the individual struts and ties are then compared to the force demands calculated using the truss model. The STM does not provide a unique solution like the sectional methods, but will give a lower bound shear strength. STM has been used to verify details in concrete members but can be difficult to apply (Hawkins et al. 2005).

1.5.5 Bond-Shear Models

Ross and Naji (2013) describe a method for calculating the bond-shear capacity of a prestressed concrete member. These procedures are similar to the AASHTO 5.8.3.5 provisions for longitudinal reinforcement in end regions with modifications to account for bond failure. Bond-shear failures are initiated by the formation of cracks in the end region that reduce the available development length. When the available development is reduced, the precompression in the ends is also reduced, lowering the shear capacity. This model allows the calculation of the shear force required to initiate this type of failure. The method was verified experimentally for *a*/*d* ratios of 1.0 to 4.4. The method is based on moment equilibrium about the top of a shear crack including the forces in the bottom strands, harped strands, shear steel, and reaction force at the support. The full procedure is well laid out in Ross and Naji (2013), so this report will only detail how certain values were obtained. Figure 1.1 is taken from Ross and Naji (2013) and shows the free body diagram used for this method.

1.6 Summary

Previous research reviewed from the literature focused on the prestress losses and shear capacity of prestressed girders in comparison to the values determined using the AASHTO specifications after the girders were replaced due to age. Some research, such as Osborn et al. (2012), was focused on determining ways to adequately repair girders determined to be unfit for service. The research described in this report was focused on providing information that can be used to prevent girders with adequate strength from being rated deficient or replaced only because they are aged or designed using past versions of the AASHTO specifications. Table 1.1 summarizes previous studies for comparison to the results presented in this report.

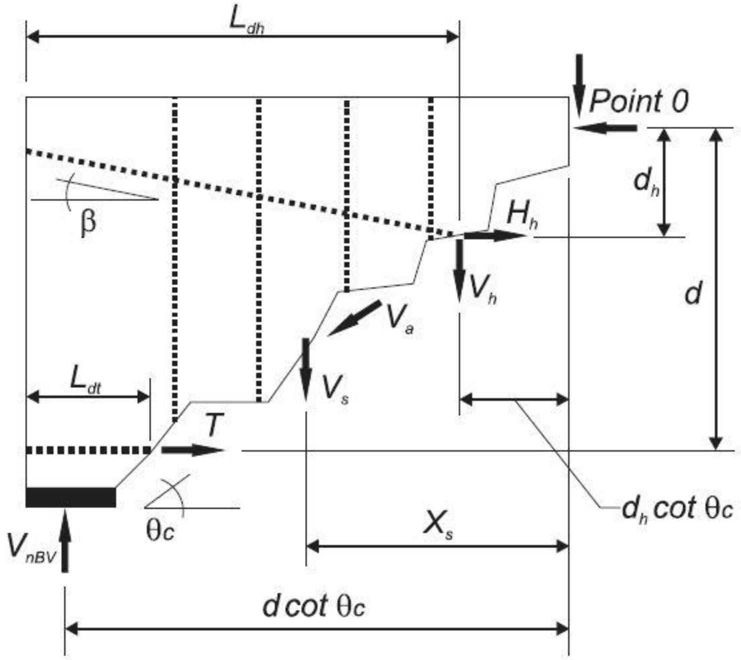

Figure 1.1: General free body diagram (taken from Ross and Naji, 2013)

The study described in this report is different from Shenoy and Frantz (1991), Pessiki et al. (1996), and Ross et al. (2011) in that it focused on the evaluation of AASHTO Type II girders. Shenoy and Frantz focused on how corrosion affected the shear and moment capacities along with prestress losses of the beams. The beams in Shenoy and Frantz were tested at midspan to cause a failure in flexural rather than shear. This study focused on shear behavior and effect of aging on material properties. Pessiki et al. (1996) studied the capacities and prestress losses of in service I-beams. The study found the failure mode to be crushing of the concrete in the top flange. The beams were loaded at midspan and had a high height to width ratio which is considered to be a slender beam. This study examined girders with a much smaller height to width ratio and loading closer to the end, both of which affect the shear capacity of the girder. Ross et al. (2011) had similar goals and test setup to the current study, and the results of those shear tests showed different failure modes from failure modes predicted by analysis.

Shahawy et al. (1993), Pei et al. (2008), and Osborn et al. (2012) examined AASHTO Type II girders similar to those from the current study. Shahawy et al. used a similar test setup as the current study. The goal of Shahawy et al. was to determine if the revisions to the AASHTO Specifications were better at predicting shear capacity. The girders tested by Shahawy et al. were designed to the AASHTO 1989 Specifications, were constructed specifically for research, and were never in service.

The work performed by Pei et al. (2008) has several differences from the research described, which was intended to expand on the previous work. The girders in the research described in this report were taken from the eastbound bridge at the same location and should be subject to similar loads and climate conditions as the girder

Table 1.1: Summary of Studies Reviewed in the Literature

Author	Summary of Research
Shenoy and Frantz (1991)	• 2 post-tensioned box girders • Removed from service • Tested for prestress losses and corrosion • Used inverse analysis to determine deflection and load • Third-point load configuration • Material properties were unknown
Shahawy et al. (1993)	• 33 Type II AASHTO girder • Cast for research • Shear tested at both ends • Compared to AASHTO specification • Provide AASHTO with recommendations for revisions
Pessiki et al. (1996)	• 2 prestressed I-beams • Removed from service • Cracking moment tests • Elastic flexural tests • Effective prestress calculated using cracking load and elastic flexural tests • Unable to fail beams in shear due to compression in the deck • Cores taken for material properties
Pei et al. (2008)	• Previous study in which current study is an extension • One type II AASHTO girder • Removed from service • Flexural tests • Shear tests and cracking moment tests • Cores taken for material properties • Capacities compared to AASHTO LRFD (2004), ACI (2008), and AASHTO (1973)
Ross et al. (2011)	• 4 type III AASHTO girders • Removed from service • shear tested: 2 on both end, 2 on only one end • Three-point tests • Supported on neoprene pads • LVDTs placed on strands to measure end slip • Compared to AASHTO (1973), AASHTO (2007), and ACI (2008)
Osborn et al. (2012)	• 8 type II AASHTO girders • Removed from service • Cracking moment and shear tests • Compared to AASHTO (2009) and ACI (2008)

examined in the previous study. The current girders were tested with the section of deck directly over the top flange in place and ends in reasonable condition. The girder was loaded within a region of the beam accurately described by beam theory as opposed to in the discontinuity region examined by Pei et al. (2008). The girders used in the current study had different numbers of prestressing strands but the same shear reinforcement as the Pei et al. (2008) girder. The research results described in this report add to the findings from the previous study.

2. Shear Tests of Aged AASHTO Girders

2.1 Introduction

Two girders taken from the I-244 bridge over the Arkansas river in Tulsa, Oklahoma, were tested as part of this program. The first, girder “A,” was a 32-ft-long AASHTO Type II girder prestressed with six straight ½ in. strands and four harped strands. This girder had been cut from the full bridge in a way that left a section of the 8.5 in. thick deck of a roughly equal width to the top flange intact. The second girder is labeled as girder “C” in this study, and it was taken from a different span of the same bridge. Girder C was a 46-ft-long AASHTO Type II girder prestressed with ten straight strands and six harped strands. It was delivered with a roughly 36 in. wide portion of deck. The deck was not cut symmetrically about the center of the girder however, so an additional 10 in. of deck was cast on the short side to regain section symmetry using a concrete mixture designed to match the strength of cores taken from the deck of Girder A. Girder C also had partial diaphragms remaining at the center and the ends. Both girders were reinforced for shear with double No. 4 Z bars spaced at 4 in. for the first 12 in. of the beam from each end, 8 in. until 30% of the length from each end, and 12 in. for the interior 40% of the beam. Figure 2.1 and Figure 2.2 show the cross sections of the girders and the sections including the deck, respectively. The deck of both girders included a 2 in. concrete wearing overlay. This overlay tended to control the ability of the deck to carry compression forces.

In order to build on the work of Martin et al. (2011), the *a*/*d* ratios for this study were continued from the starting point of 1.0. Girder A was tested once on each end, at *a*/*d* ratios of 2.5 and 2.0. Girder C was tested at *a*/*d* ratios of 3.0 and 3.83 (the “quarter-point”). The girders were supported at one end and at a location that left the opposite end overhanging such that it would not be damaged by or influence the test of the opposite end. Neoprene bearing pads were used to match field conditions. A single point load was applied through a steel plate using a hydraulic actuator.

2.2 Transport of Girders to Fears Lab

The two girders were selected from the I-244 Eastbound bridge over the Arkansas River in Tulsa during a visit to the site in the spring of 2013 before demolition began on the bridge. These two specific girders were chosen as representative of two of the four reinforcement configurations used for the AASHTO Type II girders in different spans of the bridge. The locations of the chosen girders within the bridge are shown in Figure 2.3, and the typical bridge cross-section at these locations is shown in Figure 2.4. Girder A was cut from the bridge with the deck intact out to the edges of the top flange, girder C was cut from the deck such that a 3 ft width of the deck and diaphragms transverse to the girder were removed with the beam. It was intended that this deck would be symmetric about the girder axis, but the actual cut was not. The removal of girder C from the bridge is shown in Figure 2.5.

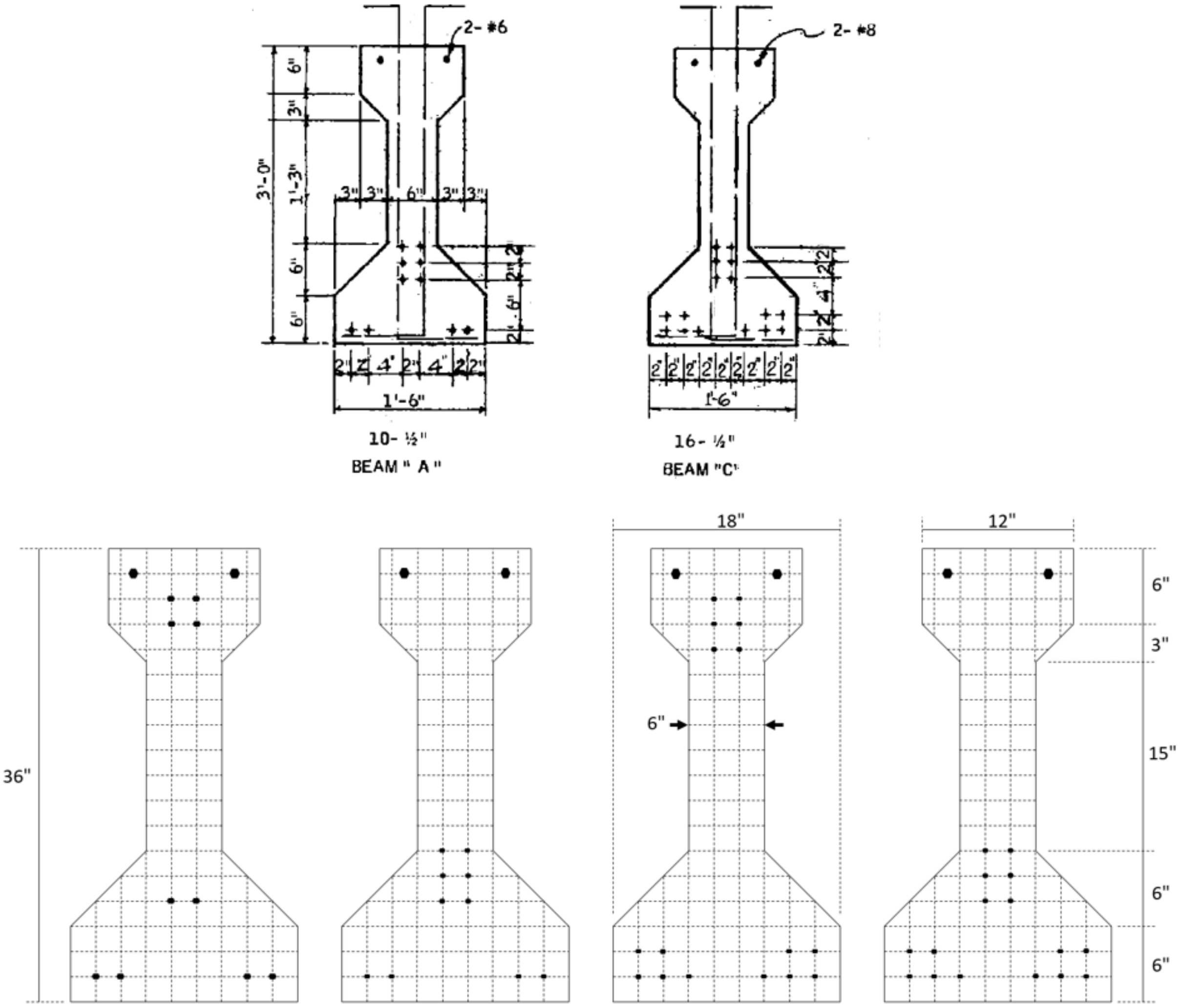

End details of girder A

Middle details of girder A

End details of girder C

Middle details of girder C

Figure 2.1: Two typical girder cross-sections, “A”, and “C”, selected from the I-244 bridge over the Arkansas River in Tulsa, OK with 10 1/2 in. strands and 16 1/2 in. strands, respectively, (top) shows original drawings provided by ODOT at midspan, (bottom) shows end and middle details of the girders (2” grid shown by dashed lines)

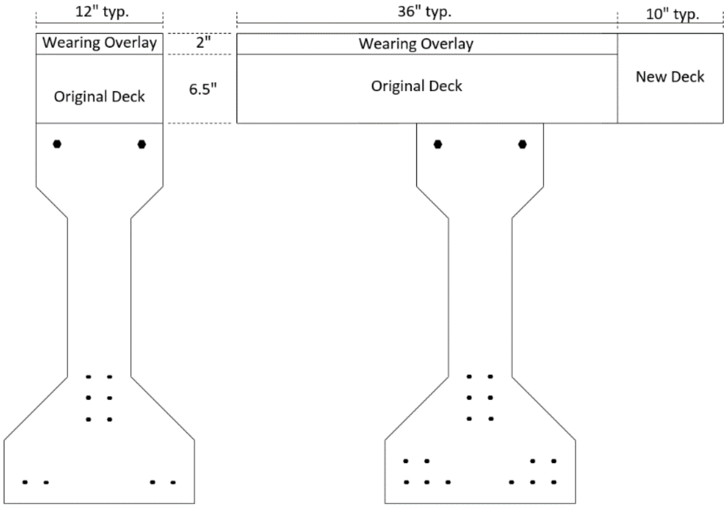

Figure 2.2: Details of remaining deck on girders A (left) and C (right)

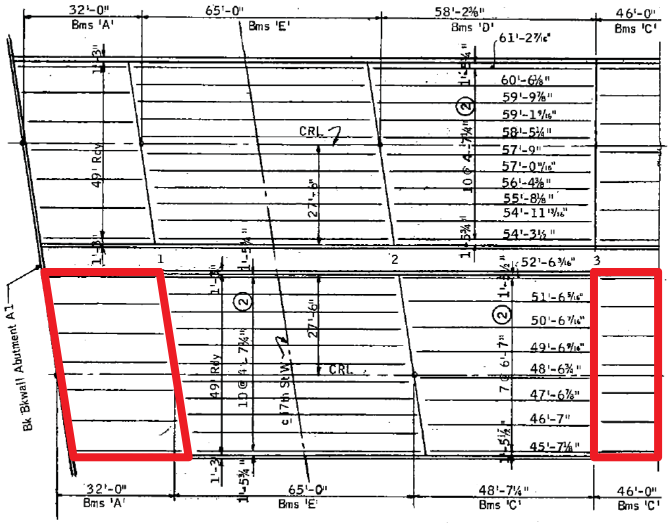

Figure 2.3: Location of beams A and C within the bridge section (extracted from the drawings provided by ODOT)

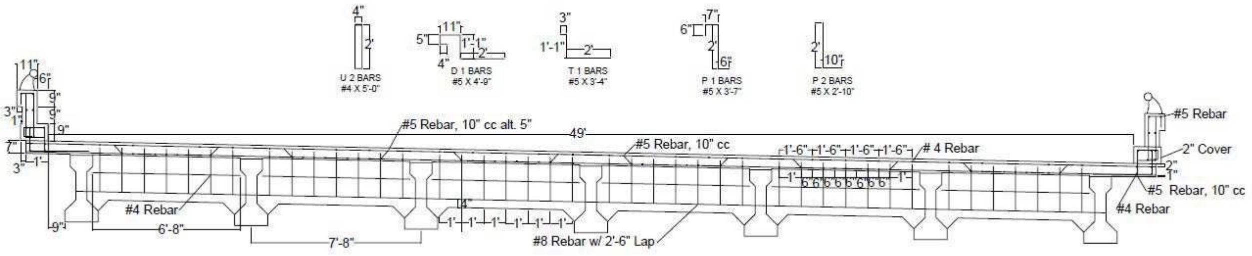

Figure 2.4: Whole section of the bridge section where girders A and C were taken

Figure 2.5: Removal of girder C from the I-244 bridge over the Arkansas river in Tulsa, OK on September 4, 2013 (photo courtesy of Gary Quinonez with Manhattan Road & Bridge)

The two girders were delivered to Fears Structural Engineering Laboratory on October 18, 2013 on flatbed trailers, as shown in Figure 2.6, and were unloaded using two 20 ton cranes rented from Allied Steel Construction, as shown in Figures 2.7 and 2.8. The beams were placed on wooden supports in the yard of Fears Lab and were stabilized with timber bracing. Several views of each girder are shown in Figures 2.9 and 2.10.

Figure 2.6: Arrival of girders at Fears Lab on flatbed trailers on October 8, 2013

The two girders were stored in the yard until space related to other projects was cleared inside Fears Lab. The girders were moved into Fears Lab on July 29, 2014 using 15 ton and 10 ton capacity forklifts rented from Allied Steel Construction. The transportation of the girders into Fears Lab can be seen in Figures 2.11 and 2.12.

Figure 2.7: Unloading of girder A using 20 ton rental cranes on October 8, 2013

Figure 2.8: Unloading of girder C using 20 ton rental cranes on October 8, 2013

Figure 2.9: Two views of girder A showing details of condition on October 8, 2013

Figure 2.10: Two views of girder C showing details of condition on October 8, 2013

Figure 2.11: Transportation of girder A into Fears Lab on July 29, 2014

Figure 2.12: (a) Placement of girder A into the load frame at Fears Lab, and (b) girder C into its storage position within the lab

2.3 Preparation for Testing

2.3.1 Girder "A"

A number of tasks were performed before testing girder A in shear was possible. These included analysis of the girder section, which is discussed in Chapter 3, preparation of a detailed instrumentation and testing plan, configuration and testing of all instruments and data acquisition equipment, preparation of the girder and test setup, and inverse testing to determine girder material properties, which is discussed in Chapter 6.

2.3.1.1 Instrumentation and testing plan

An initial review of previous large girder shear testing was conducted to develop ideas for the shear testing setup and instrumentation plan. The primary testing plan for girder A consisted of the following steps:

1. initial inverse testing of girder A involving measurement of camber and a series of elastic flexural tests used to estimate girder material and sectional properties,

2. dynamic tests of Girder "A" using a modal hammer, and

3. shear testing of both ends of the girder.

The estimated material and sectional properties were used in calculations for strength of the girder in the proposed testing configurations. The details of the inverse testing are included in Section 6.1. The shear test locations were chosen based on the location of the quarter-span point, and on the *a*/*d* ratio for the particular loading configuration. Values of 2.0 and 2.5 were selected for the *a*/*d* ratios in order to create maximum shear stresses within a section of the girder where beam behavior controls, or B-region. This is defined by St. Venant's principle as a region located more than a distance equal to the section depth away from a load or geometric discontinuity. Support conditions were chosen based on several discussions among the PI and co-PI informed by input from Mr. Walt Peters. Elastomeric bearing pads with a 1 in. thickness placed on top of reinforced concrete blocks were chosen for use as support conditions in order to recreate the real-world support conditions as indicated on the plans provided by ODOT. Instrumentation was chosen such as to collect the data required to accurately describe the behavior of the girder under load and is described in Section 2.4.

2.3.1.2 Data acquisition testing and instrumentation calibration

The data acquisition system was entirely built out of this project and consisted of a National Instruments (NI) CompactDAQ 8-slot USB chassis, an NI 9205 analog input module, and an NI 9219 universal analog input module. The central chassis and the modules were connected together through a board of universal connectors. Specific data acquisition .vi files were written in LabVIEW for each of the test setups. An additional file was written for the specific purpose of calibrating the instruments. Extensive testing was conducted on the DAQ system to eliminate electrical shorts and other issues.

Appropriate foil strain gauges could not be obtained for use in testing girder A due to issues with the manufacturer and a review of other strain gauge types was conducted to determine the best fit for capturing crack initiation. All instruments were calibrated in the configuration used for each of the tests immediately before the tests were conducted. The instruments were calibrated using a specific calibration .vi file to read voltage response from the instruments and known standards for comparison. The load cells were calibrated using the Fears Lab Baldwin Universal Testing machine that is externally calibrated once each year. All LVDTs were calibrated using a micrometer and the wire potentiometers were calibrated using a standard steel rule. A number of points were collected for each instrument and a calibration factor was calculated using a linear least squares fit to the data. Each of the .vi files was tested with the specific instruments attached.

2.3.1.3 Girder preparation

The remaining end diaphragms were removed from the ends of girder A using a sledge hammer and a variety of chisels while stored in the yard of Fears Structural Engineering Lab. Immediately after the beams were brought into Fears Lab, girder A was painted white and a 3 in. reference grid was drawn along the length of the member. The calculated beam centerline was used as the zero base point for the reference grid. Numbered vertical grid lines were placed every foot along the length of the girder to create a unified numbering system. The grid continued to approximately ±15 ft in each direction. The ends of girder A were skewed during construction to align with the skew of the girder span. Accurate information could not be obtained concerning the orientation of the transverse steel located near the girder ends, the locations of which were critical for development of the plan for inverse testing to determine EI. Mr. Matt Romero of the Oklahoma Department of Transportation brought a team from the Materials Division to Fears Lab and used a Hilti PS 1000 ground penetrating radar system to locate the transverse reinforcement and harping points for the prestressing strands, shown in Figure 2.13. These locations were marked on the girder surface in green as part of the grid system. The finished grid system is shown in Figure 2.13. Each proposed load point was prepared for load application by placing Hydro-Stone gypsum cement to remove any surface irregularities and create a smooth surface for load application.

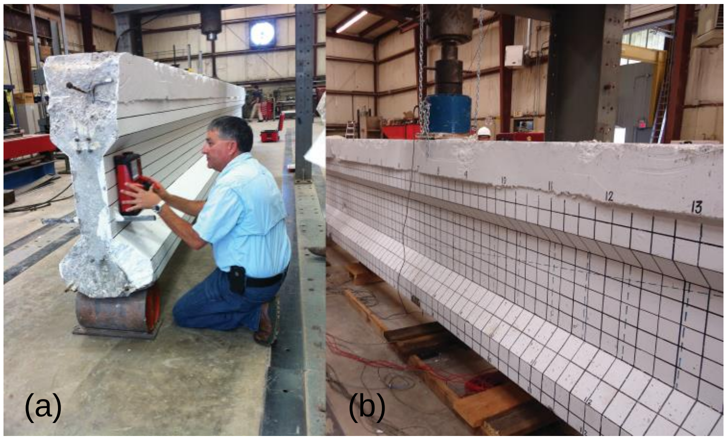

Figure 2.13: (a) Mr. Matt Romero using ground penetrating radar to locate transverse reinforcing bars in girder A, and (b) finished reference grid showing transverse steel locations for girder A

2.3.2 Girder “C”

Preparation for testing girder C was very similar to that for testing girder A. These preparations included analysis of the girder section, which is discussed in Chapter 3, preparation of a detailed instrumentation and testing plan, configuration and testing of all instruments and data acquisition equipment, and preparation of the girder and test setup.

2.3.2.1 Instrumentation and testing plan

The information obtained during testing of girder A was used to develop the shear testing setup and instrumentation plan for girder C. The primary testing plan for girder C consisted only of shear testing each end of the girder. No inverse testing was conducted on girder C.

The estimated material and sectional properties were used in calculations for strength of the girder in the proposed testing configurations. The shear test locations were chosen based on the location of the quarter-span point, and on the *a*/*d* ratio for the particular loading configuration. Values of 3.0 and 3.83 were selected for the *a*/*d* ratios in order to create maximum shear stresses within a B-region of the girder and to increase the number of data points beyond those obtained for girder A. Support conditions were the same as used for girder A. Instrumentation was chosen such as to collect the data required to accurately describe the behavior of the girder under load and is described in Section 2.4.

2.3.2.2 Data acquisition testing and instrumentation calibration

Additional strain gauge channels were added to the data acquisition system in the form of two NI 9236 strain gauge modules. Appropriate foil gauges were ordered well in advance of shear testing to accommodate the 24-26 week lead time on the instruments. Mr. Murray developed new data acquisition programs in LabView specifically for the shear tests on girder C in order to handle the added channels. All instruments were calibrated in the same way as for girder A.

2.3.2.3 Girder preparation

The girder was first painted white to facilitate observation of cracks during testing and a vertical reference grid was drawn at 1 ft intervals for use in identifying crack locations (see Figure 2.14). The grid was based and numbered using the same procedure as for girder A described in Section 2.3.1. This grid was later detailed to every six inches vertically and horizontally in the areas of the load points. The girder was moved into position in Fears Lab using Hilman^{TM} rollers placed at each end and hand winches attached the Fears Lab strong floor as shown in Figure 2.14. Lifting seats were constructed to ensure stability of the non-symmetric section.

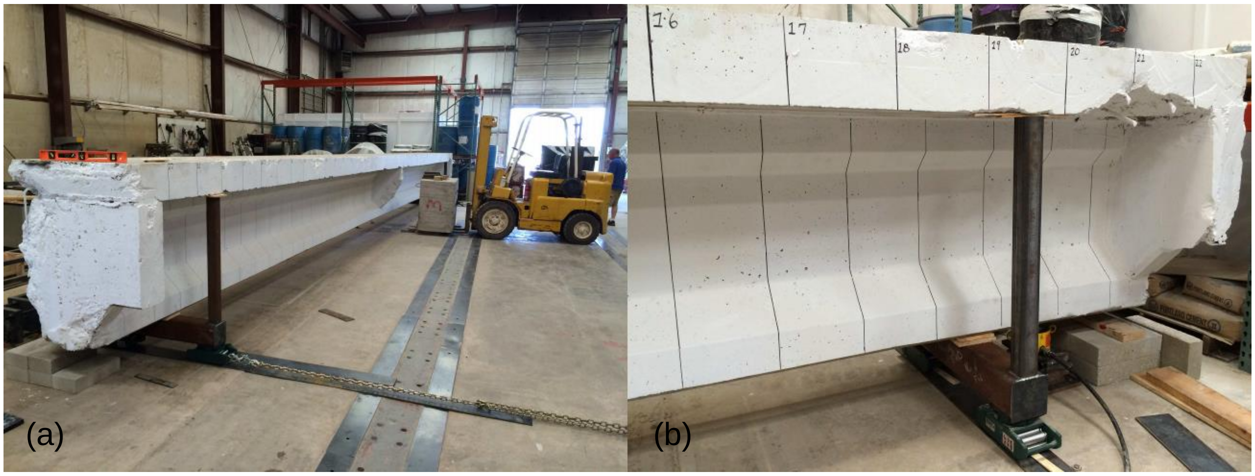

Figure 2.14: (a) Moving of girder C and (b) the gridlines on girder C

Girder C was removed from the bridge with the intention of obtaining a 36 in. wide section of the bridge deck symmetric about the girder web. The deck section as-received was not symmetric and 10 in. of concrete was added to the deck to create a symmetric section after the girder was in place in the testing frame. Reinforcing bars matching the original reinforcement configuration and sufficient to transfer the expected compression forces across the joint were doweled into the existing deck using epoxy. Preparation for casting the deck extension is shown in Figure 2.15. A concrete mixture designed to match the strength of deck cores taken from girder A was used to cast the extension. Continuity was maintained by embedding No. 4 reinforcing bars in the existing deck section using structural epoxy to the depths specified by the epoxy manufacturer. The spacing was selected based on the spacing of steel in the bridge deck and on interface shear forces using AASHTO 5.8.4 (2012). The concrete face was roughened with a jackhammer to improve the bond between the old and new deck concrete and meet the roughened surface requirements described in AASHTO 5.8.4.3 (2012).

Figure 2.15: Construction of deck extension of girder C in progress

A composite mechanism representing the effects of adjacent girders desired for testing girder C was evaluated during preparation for testing. It was determined that space limitations in Fears Lab prevented construction of a complete deck and adjacent girder arrangement, so an equivalent mechanism consisting of beam and column sections anchored to the strong floor was considered. This mechanism was designed using a STAAD.Pro model to compare single girder and composite section behavior in order to match stiffness at a given load using the beam and column arrangement in place of the full bridge section. The reliability of results from this method were heavily debated and the decision was made to test girder C without a composite mechanism and to focus more heavily on using the scaled bridge section, described in Chapter 7, to examine load transfer between girders.

2.4 Shear Test Procedures

2.4.1 Girder “A”

A total of three shear tests were conducted on girder A. For all tests the girder was supported on a two 8 in. x 18 in. x 1 in. thick neoprene bearings resting on reinforced concrete blocks. The support at the end being tested was located with the neoprene bearing flush with the end of the member and skewed to match the beam end. The far support was located at grid location +4 ft or -4 ft for the first and second test, respectively. The supports for test 3 were located at grid locations ±4 ft. The first two shear tests consisted of an approximately 19 ft span and a single point load applied at the desired test location. Test A1 was loaded at grid location +7.25 ft, providing a span to depth ratio of 2.5. Test A2 was loaded at grid location -8.75 ft, providing a span to depth ratio of 2.0. The final test (A3) had a span of 8 ft with the load positioned at grid location 0.0, providing a span to depth ratio of 1.33.

Load, deflection, displacement of the bearing pads, strain at discrete points, and strand end slip were monitored using the various instruments and the NI data acquisition system throughout each test at a sampling rate of 200 Hz. Figure 2.16 shows the testing configuration for shear tests A1 and A2 and Figure 2.17 shows the arrangement of the individual instruments. Applied load was monitored using a 400 kip capacity Interface model 1252 load cell. Deflection was monitored with two wire potentiometers at the load point to account for any torsion during the test. For test A1 one wire potentiometer was also located between the load point and each support. Tests A2 and A3 included only the two wire potentiometers at the load point, and deflection was monitored manually for these two tests using a laser level and a scale attached to the beam web as shown in Figure 2.18. Deflection caused by deformation of the bearing pads was measured using two LVDTs at each support attached to the bottom beam flange using brackets as shown in Figure 2.17.

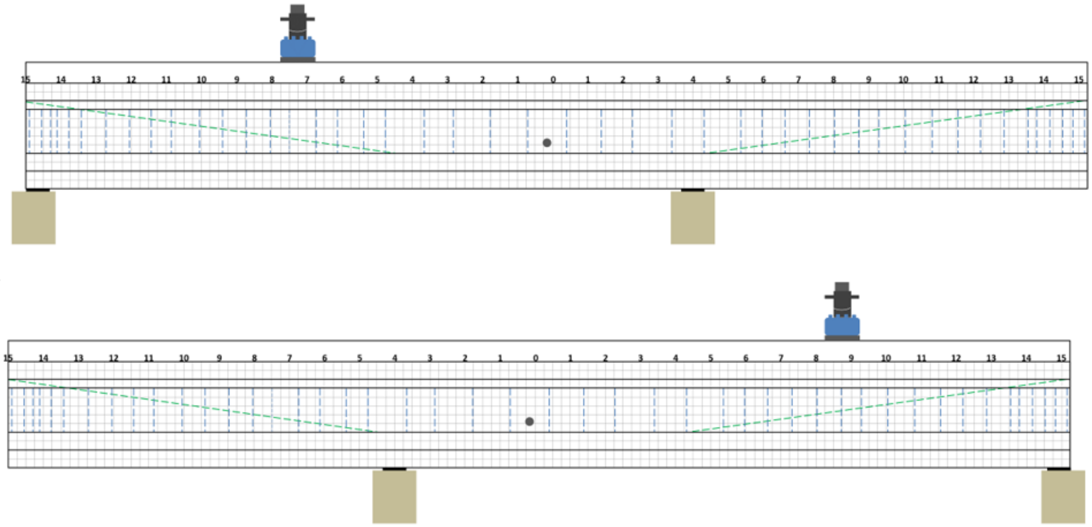

Figure 2.16: Overview of test setup for (top) shear test A1, and (bottom) shear test A2

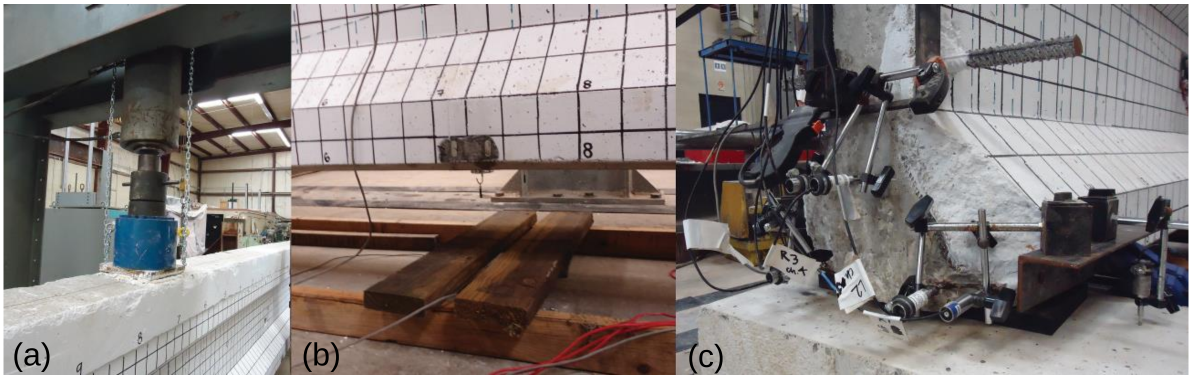

Figure 2.17: (a) Load application point and 400 kip load cell, (b) wire potentiometers used for monitoring deflection and setup used to protect them from debris, and (c) LVDTs and brackets used for monitoring strand slip and support deflection

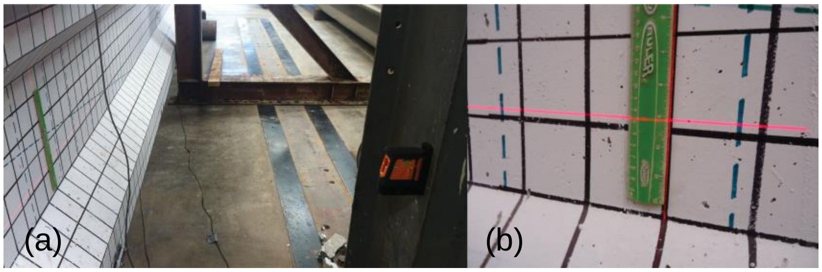

Figure 2.18: (a) Laser level used for manual deflection measurement at the load point, and scale attached the girder web used for tracking deflection

End slip was monitored for 8 strands during shear tests A1 and A2. The LVDTs were placed on brackets with the plunger of the LVDT touching the exposed strand such that any displacement of the strand was recorded by a corresponding extension of the LVDT. Placement of the LVDTs is shown in Figure 2.17 and the arrangement of LVDTs for each test is shown in Figure 2.19. Strand slip was not monitored for the third shear test due to it being located on the central section of the member where end slip was not an issue.

Strain was monitored at points of interest using Bridge Diagnostics, Inc. (BDI) ST-350 dynamic strain transducers, shown in Figure 2.20. The surface was first prepared using a grinder to remove paint and any other deleterious substances and the gauges were attached at the desired locations using steel tabs and epoxy. The locations of the strain gauges were chosen such as to provide the most useful information on cracking of the girder during the shear tests. Channel limitations for the test A1 required that only a single strain gauge rosette could be used, which was placed at +9.5 on the grid and 10 in. above the bottom flange. The reorganization of wire pots for test A2 allowed for placement of strain gauges at the base of the bottom flange of both sides of the girder at the load point (- 8.75) in addition to a rosette at grid location -11.5 and 6 in. above the bottom flange. The rosettes were intended to capture the behavior of the girder related to flexure shear and web shear cracking and the gauges at the load point were intended to capture flexure cracking information.

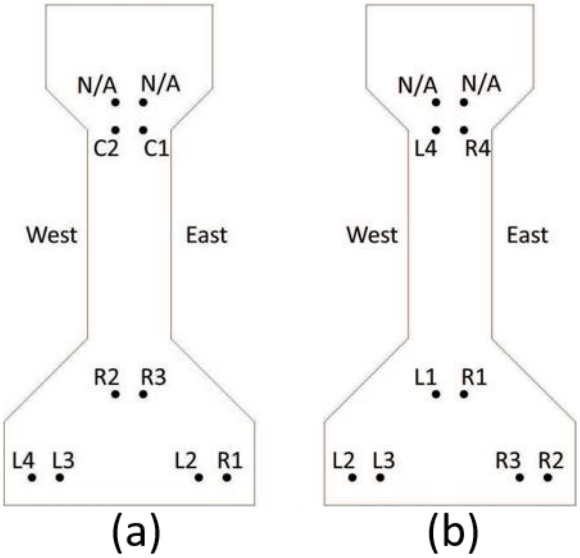

Figure 2.19: Arrangement of strand slip monitoring LVDTs for (a) test A1 and (b) test A2

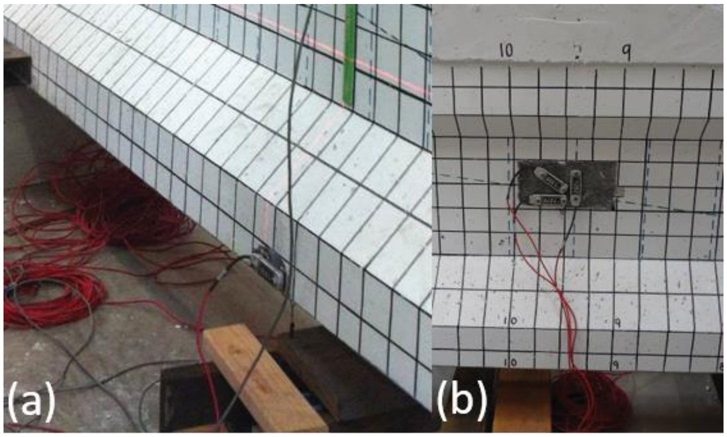

Figure 2.20: (a) BDI strain gauges at the load point for shear test 2, and (b) the strain rosette used for shear test 1

Load was applied for each test in 5 kip increments with a pause between increments to inspect the test setup and look for potential cracks. Once the first crack was observed, cracks were traced with red permanent marker and marked with the load at which they were observed, as shown in Figure 2.21. Once the beam reached the estimated failure load, or showed signs of eminent failure, cracks were no longer marked after each increment. Videos and pictures were taken to document significant moments during all shear tests, the records of which were used for detailed analysis of failure mechanism in conjunction with automatically recorded time histories of all data measurement instrumentation.

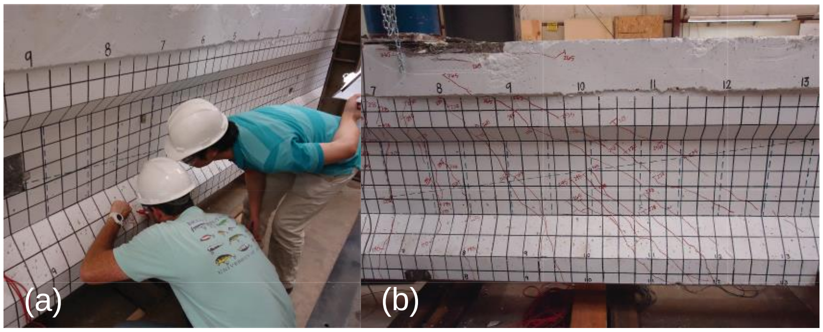

Figure 2.21: (a) Graduate research assistants marking cracks between load increments, and (b) cracking pattern for test A1 with cracks marked in red

2.4.2 Girder "C"

Girder C was tested at both ends similarly to what was done for girder A. Span to depth ratios of 3.0 and 3.83 were tested to continue the trend of moving outward from the support. An overview of the testing configurations for girder C is shown in Figure 2.22. Girder C was instrumented more heavily than girder A in order to gather more information about the shear behavior. Figure 2.23 shows the instrumentation plan for test C1. LVDTs were used to measure strand slip in eight of the ten straight strands in the girder (Figure 2.24). As in previous testing, wire potentiometers were used to measure under-load deflection and four LVDTs were used to account for deflection of the bearing pads. Five BDI strain gauges (labeled "Bridge Gauges" in Figure 2.23) were attached to the top and bottom flanges of the beam to monitor strain distribution in the section under the load. Additionally, fifteen foil type strain gauges (labeled "short" and "long" strain gauges in Figure 2.23) were attached to the concrete at strategic locations. Four of these gauges were placed on top of the deck width to observe the influence of the deck width on the load distribution. Six were arranged on the web of the girder at an angle perpendicular to expected shear cracks in order to catch shear cracks as they formed and to observe the strain in the web before the formation of these cracks. The rest were arranged in a similar fashion to the BDI gauges. Unfortunately, several of these gauges were damaged during installation. The foil gauges are very delicate, and it is not unusual for there to be attrition before data is collected.

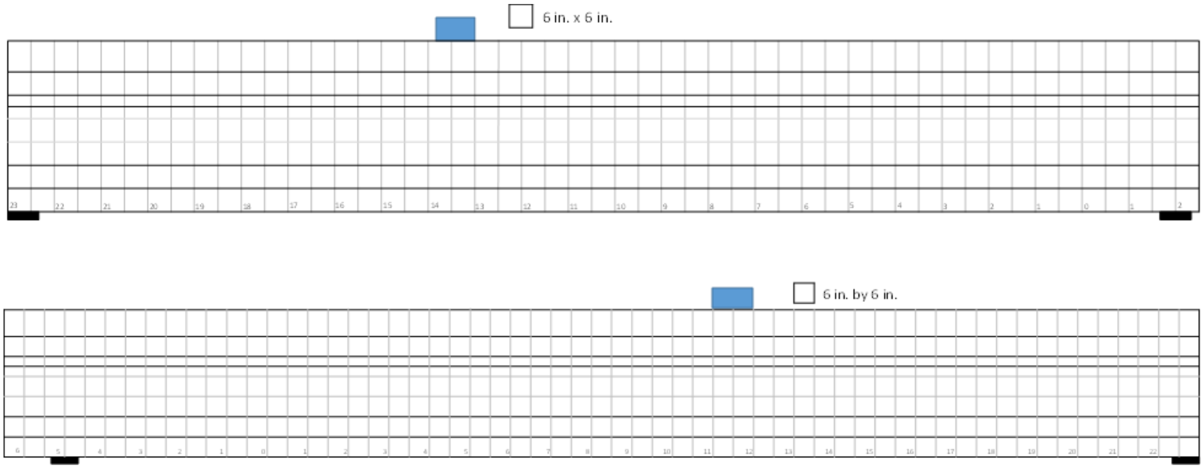

Figure 2.22: Overview of test setup for (top) shear test C1, and (bottom) shear test C2

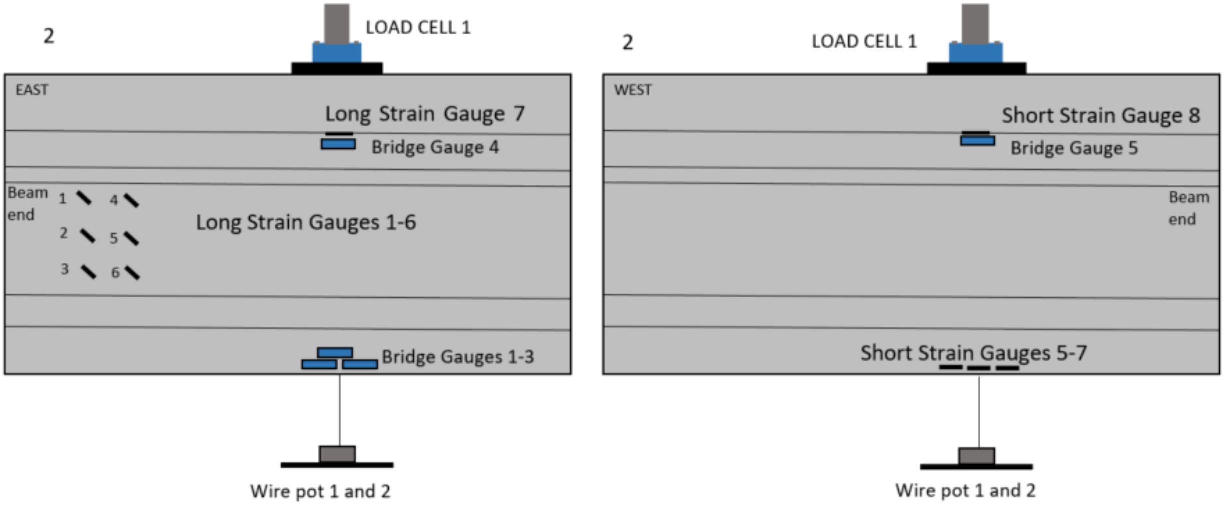

Figure 2.23: Instrumentation for both sides of girder C for test C1

Figure 2.24: Arrangement of LVDTs at the beam end

In order to achieve the required shear span to depth ratio for test C1, a 25 ft span was selected. This span was chosen in order to reduce the damage caused to the other end of the beam during the first test. The load was applied at 9 ft from the south end (grid location 14.5 ft) of the beam to obtain an *a*/*d* of 3.0 (9 ft / 3 ft = 3.0). Figure 2.25 shows an overview of the test setup. The support conditions and load application were similar to those used for the shear tests of girder A described in Section 2.4.1.

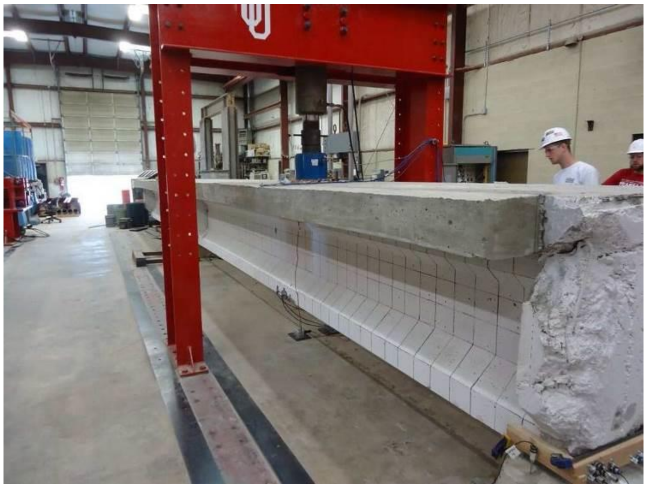

Figure 2.25: Test C1 setup

Since previous testing was performed quite close to the support, the second shear test of girder C (C2) was performed at the “quarter-point.” At the time these girders were designed, the critical section for shear was taken at one quarter of the length of the girder. For this girder that corresponds to 11.5 feet into the girder from the end (grid location 11.5 ft) for an *a*/*d* ratio of about 3.8. The span for this test was 28 feet (3 feet longer than for shear test one) in order to increase the shear demand on the tested end. At this location, the shear and moment capacities were expected to be very similar and a flexural failure was anticipated.

The setup for test C2 was very similar test C1 in terms of instrumentation. The same set up of LVDTs, wire pots, and BDI strain gauges was used. The locations of the foil strain gauges used for this test were altered slightly. Since the strain gauges on the underside of the deck did not attach properly during test one, these were moved to the web so there were eight total strain gauges arrayed on the web during test C2. Figure 2.26 shows the instrumentation plan for this test with the exception of the LVDTs and strain gauges atop the deck. The arrangement of LVDTs was the same as shown in Figure 2.24.

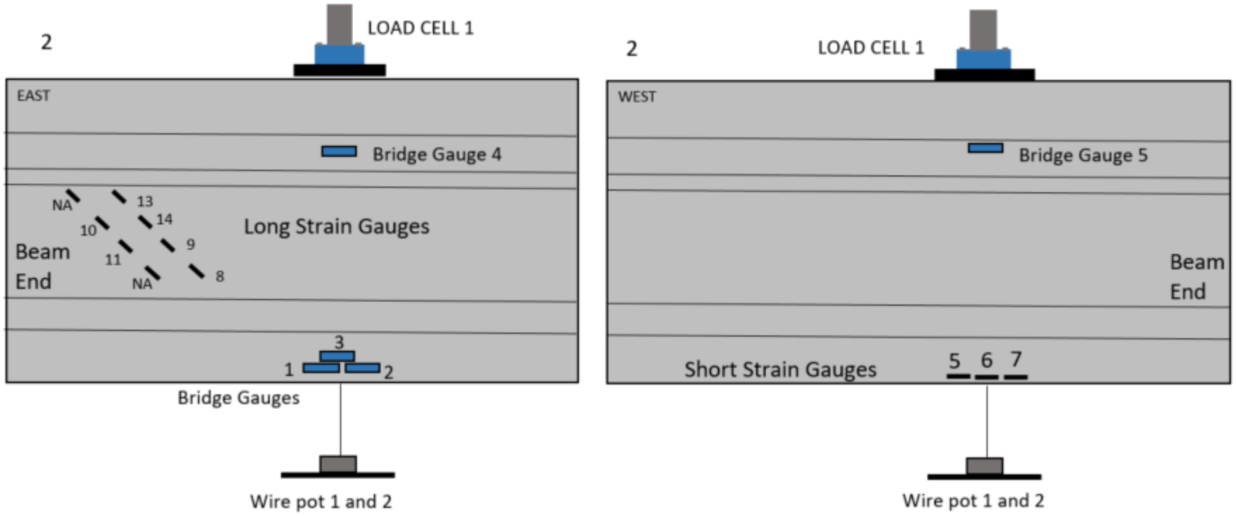

Figure 2.26: Instrumentation for girder C for test C2

2.5 Shear Testing Results

2.5.1 Testing Girder “A”: Results

2.5.1.1 Test A1

The first shear test of girder A (A1) was performed at an *a*/*d* of 2.5 and a span length of 18.75 ft. Initial cracking occurred at a load of 170 kips directly under the load point. The first shear crack was a web shear crack 4.5 ft away from the load towards the near support and occurred at a load of 225 kips. As the load was increased, several shear cracks began to enter the bottom flange. At a load of 255 kips, the bottom four strands slipped, leading to a loss of load carrying capacity. Slip was measured for six of the strands before failure, possibly influenced by corrosion (Figure 2.27) present at the girder end. According to discussions with ODOT engineers, similar corrosion is frequently observed in Oklahoma bridges. Load was increased to 260 kips, at which point the deck overlay delaminated. The maximum load resulted in an applied moment of approximately 1162 k-ft and applied shear of approximately 155 kips, including dead load. The cracking pattern for this test is shown in Figure 2.28. Initial flexure cracking occurred in the immediate vicinity of the load point. Flexure-shear and web shear cracks occurred between the load point and near support as shown in Figure 2.28. The failure mode for test A1 can be characterized as “bond-shear” because strand slip reduced the capacity of the section and ultimately led to failure. The strand slip reduced the available prestress force and contributed to the shear cracking and shear failure mechanism. A picture of the failure is given in Figure 2.29. The deflection measurements for test A1 were lost due to a malfunction of the wire potentiometers.

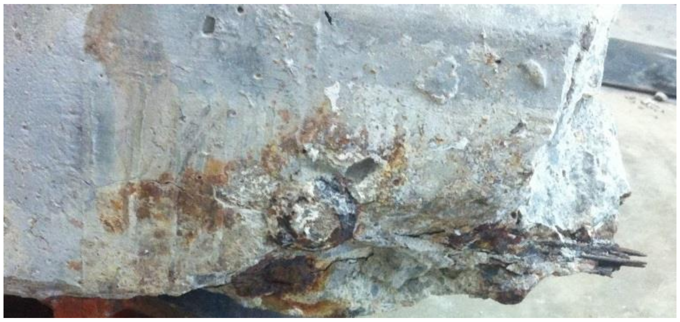

Figure 2.27: Corroded ends of strands that exhibited initial strand slip during test A1

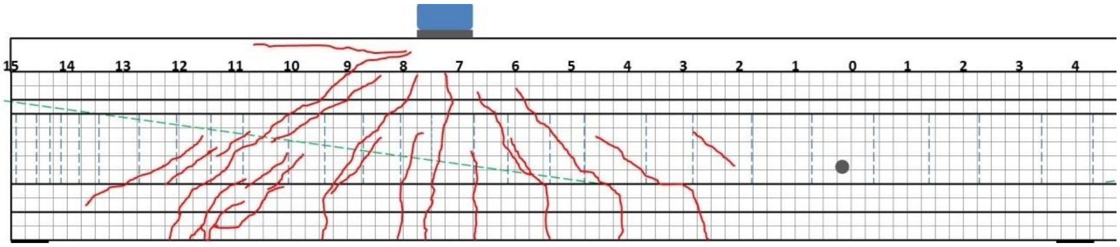

Figure 2.28: Shear test A1 cracking pattern (3 in. grid shown)

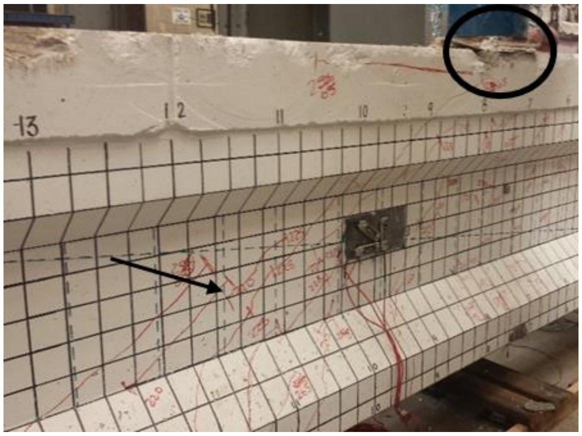

Figure 2.29: Cracking and failure patterns for shear test A1 at failure inclined shear cracks are identified using a black arrow and crushing of the deck concrete at the extreme compression fiber is highlighted with a black circle

2.5.1.2 Test A2

The second shear test of girder A (A2) was performed at an *a*/*d* of 2.0 and a span length of 19 ft. Initial cracking occurred directly under the load point at a load of 190 kips, corresponding applied moment of approximately 797 k-ft, and applied shear of approximately 128 kips. The first shear crack was observed at a load of 225 kips in the web and the bottom flange roughly 1 ft away from the support. Load was increased to an ultimate value of 289.5 kips, corresponding to an applied moment of 1197 k-ft and applied shear of 193 kips, at which point there was a sudden failure corresponding to delamination of the deck overlay and rupture of multiple prestressing strands. The strands ruptured approximately 1 ft away from the load point in the direction of the longer side of the span. The cracking pattern is shown in Figure 2.30 and failure photos are given in Figures 2.31 and 2.32.

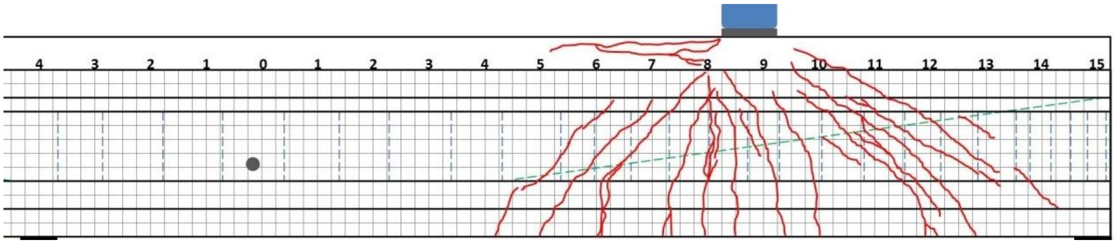

Figure 2.30: Shear test A2 cracking; strand rupture occurred at the 8 ft mark (3 in. grid shown)

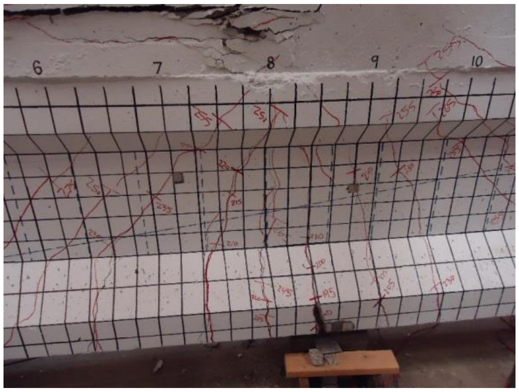

Figure 2.31: Test A2 failure, note deck crushing at the top of the image and the large flexural crack at the bottom where strand failure occurred

The average load versus deflection for the two wire potentiometers placed at the load point for test A2 are shown in Figure 2.33. The point of visually observed first cracking is shown with an open square, the point of slope change indicating cracking is shown with an open circle, and the point of first shear cracking is shown with an open diamond. This plot indicates a period of constant load and yielding at maximum load which is indicative of a flexural failure (marked with an “x”. This failure type was confirmed by crushing of the extreme compression fiber and fracture of at least two of the bottom layer prestressing strands.

The final shear test exhibited only web shear cracks, and could not be loaded to complete failure due to the limiting capacity of the load frame, which is 400 kips.

Diagonal cracking (Figure 2.34) was observed between the supports and the load point indicating a stress distribution characteristic of a section of the girder where beam behavior does not dominate, or D-region. This region is defined by St. Venant's principle as a section within a distance equal to the depth of the section from a load or geometric discontinuity.

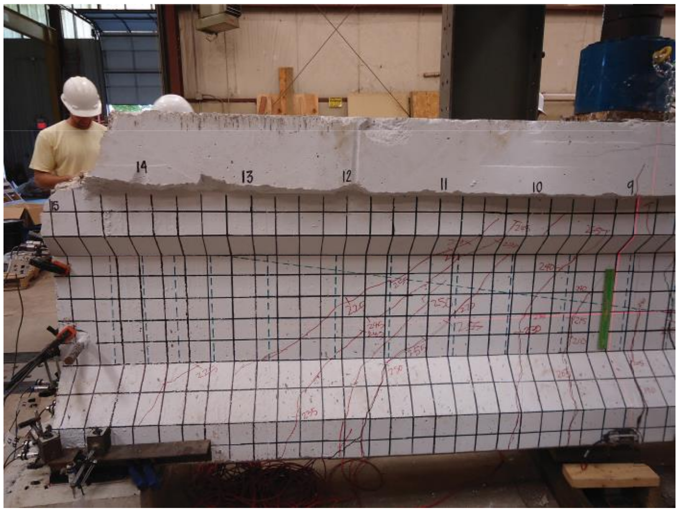

Figure 2.32: Cracking pattern for test A2 between the load point and near support

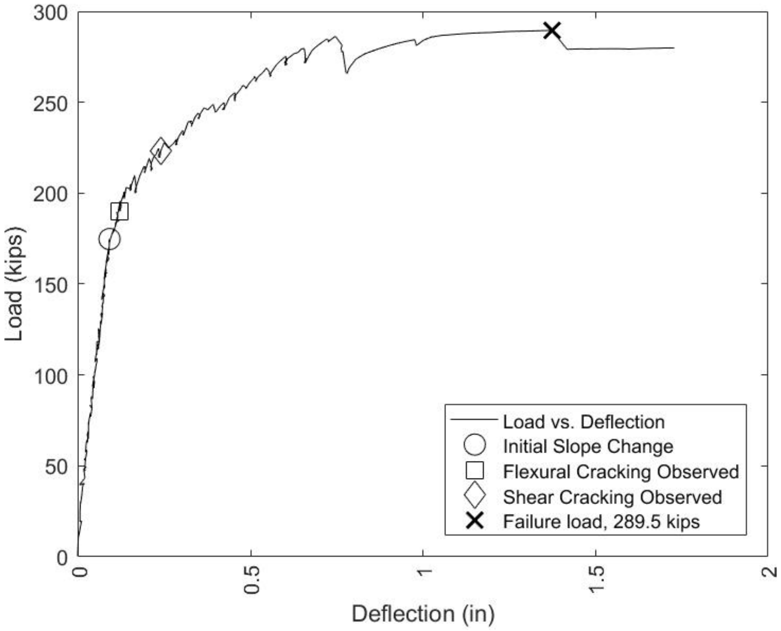

Figure 2.33: Load deflection plot for test A2 truncated at the failure point based on an average of the two wire pots

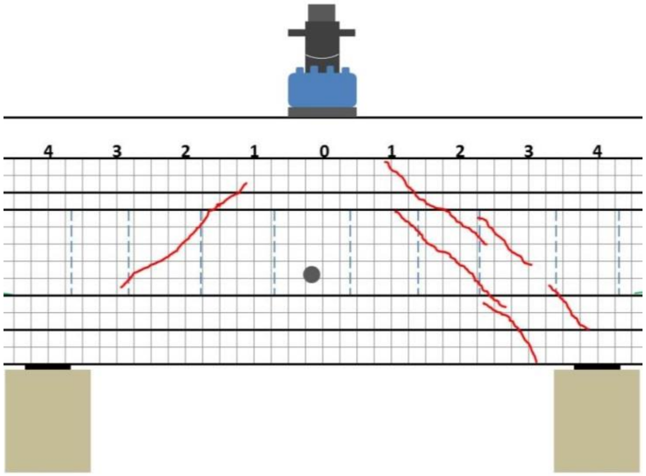

Figure 2.34: Cracking pattern for shear test A3

2.5.2 Testing Girder "C": Results

2.5.2.1 Test C1

The first shear test of girder C (C1) was performed at an *a*/*d* of 3.0 with a span length of 25 ft. The test was performed on October 16, 2015 at Fears Lab; testing began around 10:50am. Once the data acquisition software was initialized, load was applied in 10 kip increments and the researchers present for the test monitored the girder for any signs of cracking. At an applied load of 90 kips, spalling was observed at the end nearest the load point. There was corrosion of the strands at that end similar to that described for girder A, which corrosion had initiated several cracks, particularly on the outer strands. The level of corrosion on this end is typical based on site visits to girders from this time period. The bearing force caused the pre-existing cracks at this end to open and for pieces to spall off of the bottom flange (Figure 2.35). At this point the test had to be stopped so the LVDTs on the strands at that end could be repositioned. The LVDTs monitoring strand slip and bearing deflection were mounted to the sides of the bottom flange on this end of the girder, so spalling caused these instruments to move and no longer provide accurate readings. The spalling behavior ceased at a load of 110 kips, so it appears there were no bearing issues outside of the initial spalling.

When the test was resumed the load continued to be increased at 10 kip increments after the discovery of the spalling until web-shear cracks were observed at a load of 160 kips at the web-top flange interface (Figure 2.36). At this point, load increments were decreased to 5 kips. From here on, web shear cracking was observed at every load increment, and either these cracks grew or new ones appeared at every step (Figure 2.37). The initial web shear cracks extended the full height of the web at a roughly 26 degree angle, beginning 2 ft away from the support. The location of these cracks and the fact that they were recognized before any cracks under the load point formed indicate that shear was the controlling load case at this point.

Figure 2.35: Spalling under load initiated by cracking caused by corrosion

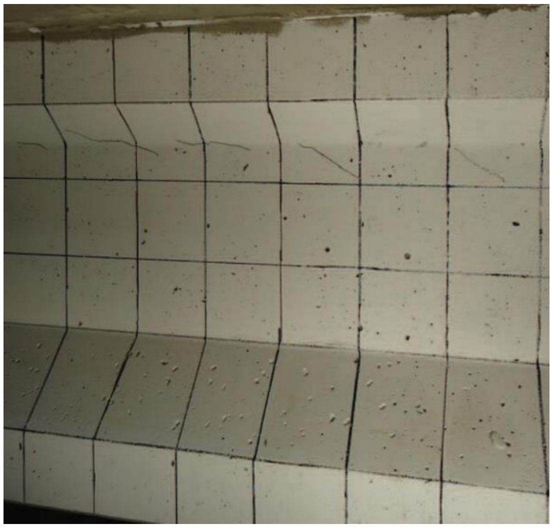

Figure 2.36: Initial shear cracking for test C1

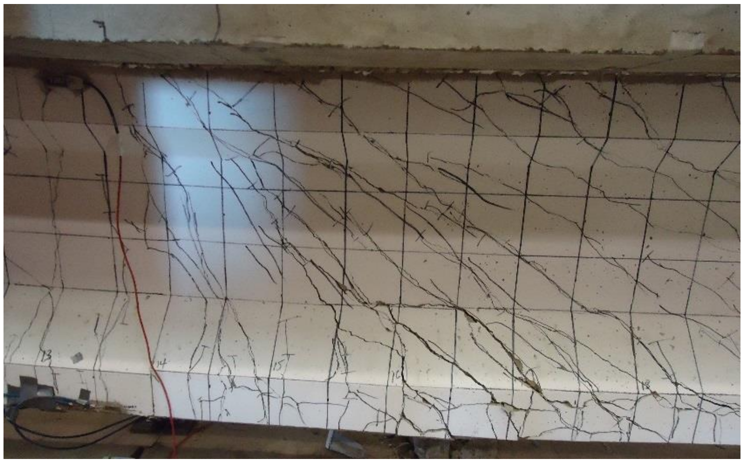

Figure 2.37: Test C1 failure, note large shear cracks and failure of the bottom flange concrete

Flexural cracking under the load was observed at 185 kips and at a load of 195 kips some shear cracks began to enter the bottom flange of the girder. A data acquisition error caused this test to be halted at 195 kips before continuing the load to failure. The load was removed, and the error fixed, at which point loading was continued. This also provided an opportunity to re-position the LVDT's that had been shifted by the spalling concrete. After fixing the data acquisition error, load was returned to 195 kips at the same increments as before. Between load steps the girder was observed to verify that no new cracks formed. As expected, until the load returned to 195 kips, the forces were redistributed internally the same way as in the first test. As load increased beyond 195 kips, several shear cracks began to align themselves with the strands in the bottom flange, indicative of a possible bond-shear issue (Figure 2.38).

Once the load was returned to 195 kips, the shear cracks turned downward into the bottom flanges across the bottom of the beam. Flexure cracks also continued to extend up towards the deck. As loading continued, shear cracks formed at an even spacing and on either side of the load point (Figure 2.39). At 265 kips, some of the shear cracks in the bottom flange extended horizontally, along the same height as the prestressing strands. This sort of cracking could indicate bond-shear issues. Once the load surpassed 300 kips, more plastic behavior was observed and the girder became unable to sustain additional load. At this point the hydraulic ram ran out of travel, and the test was delayed to insert an additional spacer before the maximum load was applied.

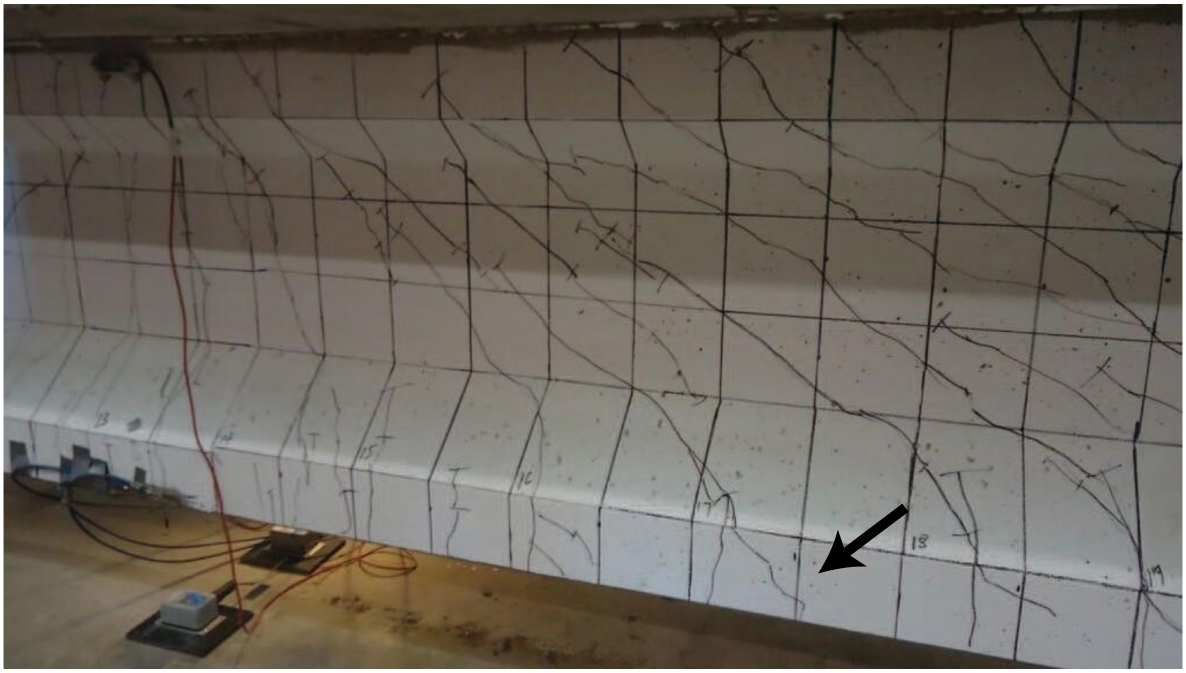

Figure 2.38: Shear cracking at 250 kips (arrow indicates cracks aligning with strands)

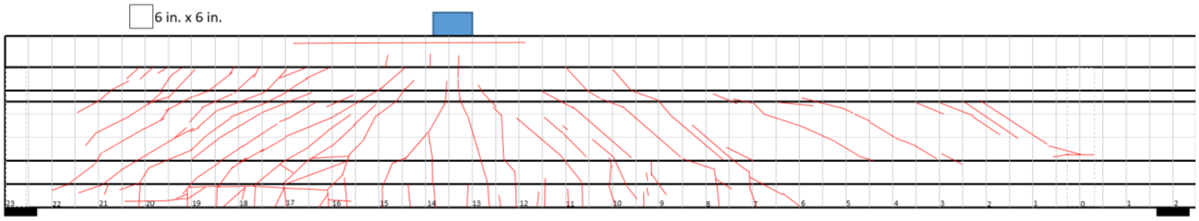

Figure 2.39: Test C1 cracking (6 in. grid shown)

After a spacer was added, the load was applied without interruption from 0 kips to the maximum load of 318 kips. The final stages of loading were characterized by increased deflection compared to load (loss of stiffness) and by growth of the shear cracks at the level of the prestressing strands. Ultimately, failure occurred when these shear cracks caused strand slip, and the deck concrete crushed. As observed in the shear tests of girder A, the weak link in the deck concrete is the overlaid wearing surface. In each case, once the neutral axis of the member reached this overlay, the ability of the deck concrete to sustain any more load was lost (Figure 2.40). The overall cracking pattern for test C1 is shown in Figure 2.39 and photos of the failure are given in Figure 2.40.

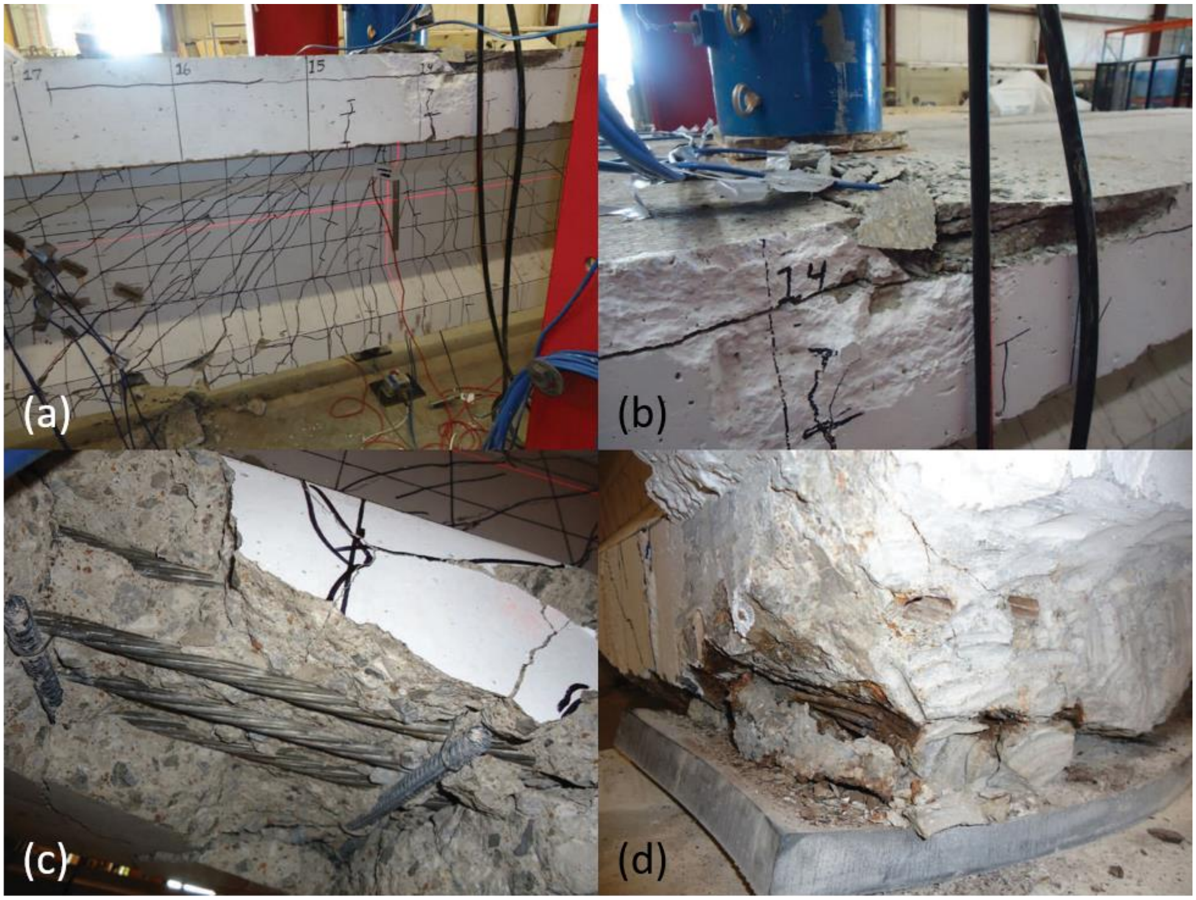

Figure 2.40: Final condition of Girder "C": (a) shows overall condition, (b) shows crushed deck concrete, (c) shows exposed strands under bottom flange, and (d) shows strand slip of about one inch and corrosion

Figure 2.41 shows a load-displacement curve for the girder from the second and third rounds of this test. This figure shows the behavior of the girder from 0 kips up to the point when no more load could be applied. There are four points highlighted on the curves, the points of initial flexure and shear cracking and the maximum loads for each iteration of the test. Plastic deformation at the end of the tests would be related to initial crack growth and moment-shear cracking from the final stages of the test, respectively. The flexural and shear capacities calculated for the girder are also shown as horizontal lines labelled with the particular method.

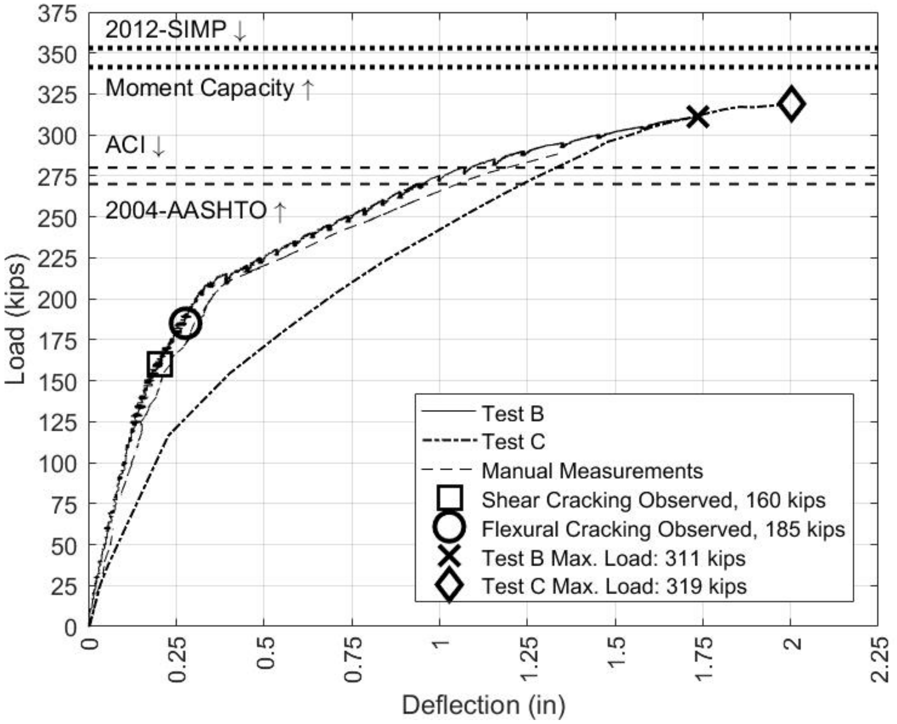

Figure 2.41: Load-displacement curve (C1b)

Figure 2.42 presents the results from strain gauges atop the deck alongside the load during the third iteration of the test. Strain gauge 2 is roughly one foot away from the center of the girder and 3 and 4 are located 20 inches from the center on either side. The purpose of these gauges was to measure the distribution of load in the slab. As one would expect, the strain is larger close to the load and smaller towards the edge of the slab. From this figure, it is clear that load was distributed into the slab extension and that the deck concrete received a large portion of compression strain even towards the edges.

Finally, Figure 2.43 shows the loss of bond in multiple strands on the bottom row. Measurements for the LVDTs on strands 5, 7, and 10 as described in Figure 2.24 are shown in Figure 2.43. These strands had the largest bond loss and are provided as representative of the overall beam behavior. LVDTs on strands 6 and 8 measured smaller slip values and strand 12 exhibited approximately zero slip. Shear cracks extended into the transfer length of these strands and when these cracks were wide enough the strands lost anchorage completely, leading to the failure. This can be seen in Figure 2.43, as the four strands lost bond near the failure load.

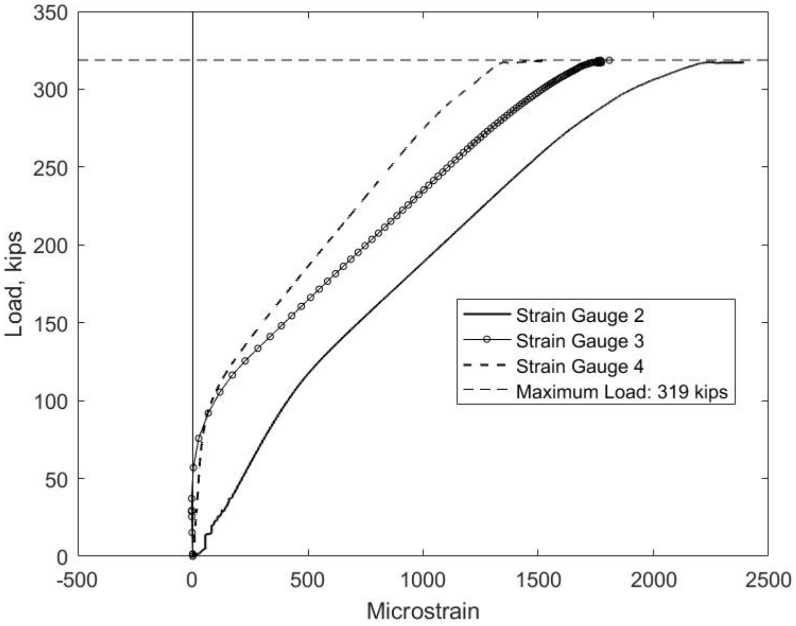

Figure 2.42: Strain gauges from deck

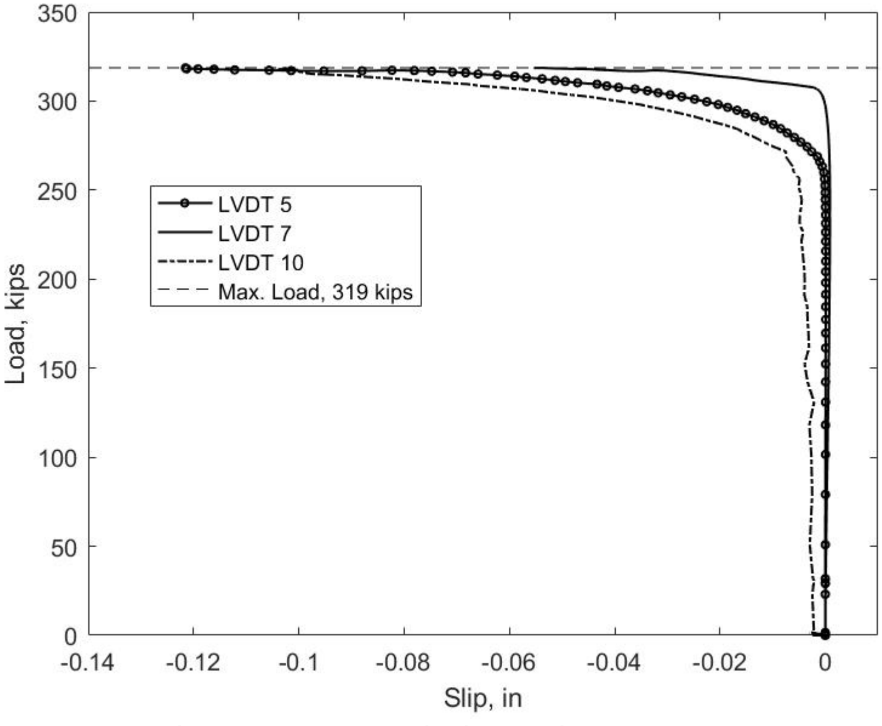

Figure 2.43: Strand slip at failure for test C1

2.5.2.2 Test C2

The test was performed on November 20, 2015 at Fears lab, beginning in the late morning. The data acquisition system was initialized and load was applied in 10 kip increments until initial cracking was observed. Between load increments the girder was inspected for cracking and any cracks were marked before applying more load. The second test of girder C (C2) was performed at an *a*/*d* of 3.83, corresponding to a quarter of the original span length. In the 1973 AASHTO-STD this point would have been taken as the critical section for shear. However, this far into the span moment is expected to control the failure. The test span was increased to 28 ft to increase the shear demand on the short side of the span.

The first observed cracks were web-shear cracks approximately 2 ft from the supports (Figure 2.44) at a load of 150 kips followed by flexural cracking at 160 kips. The first cracks were several web shear cracks near the support and near the web-top flange interface. At this point load increments were decreased to 5 kips for the rest of the testing. The shear and flexural cracking increased in size and number until the end of the test. Flexural cracks extended to the top flange at a load of around 160 kips and reached the deck at around 190 kips. At 195 kips, web shear cracks began to grow into the bottom flange becoming flexure-shear cracks. As load increased some of these cracks oriented themselves more horizontally along the height of the strands. An overview of the cracking from test C2 is shown in Figure 2.45. Load was increased up to 301 kips at which point a leak in the hydraulic actuator used to apply load caused the test to be halted. Load was removed from the girder until the hydraulic system could be topped up with fluid. After this, the load was applied until ultimate failure occurred at a load of 297 kips. As in previous tests, the girder failed when the forces in the deck overlay were too large, causing the overlay to delaminate and crush. The compressive forces during this test were so large that the top flange crushed and compression steel in the top flange and the deck buckled (Figures 2.46 and 2.47). This failure type could be described as compression-shear or a flexural failure. Compression-shear is caused by shear cracks entering the compression flange (Ross et al. 2011).

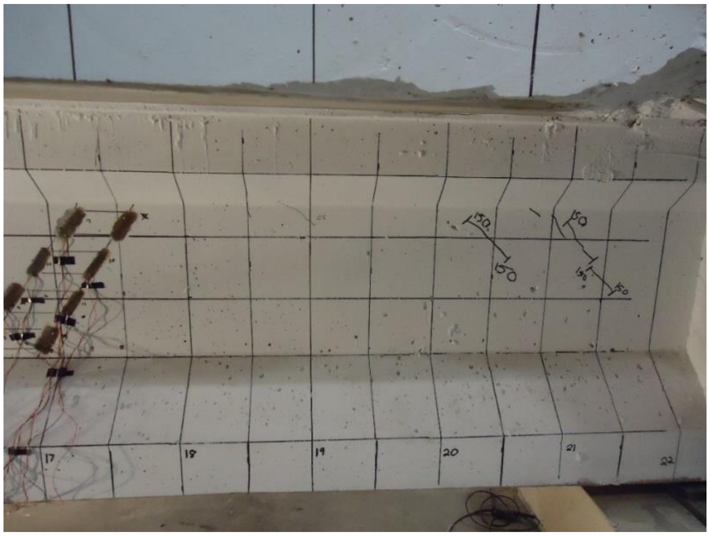

Figure 2.44: Initial cracking in test C2

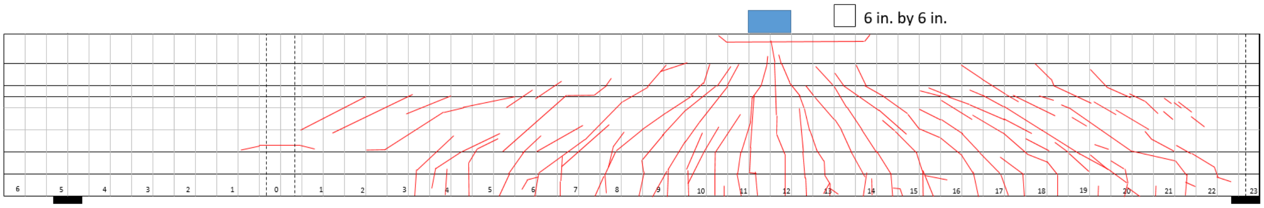

Figure 2.45: Overall cracking for test C2

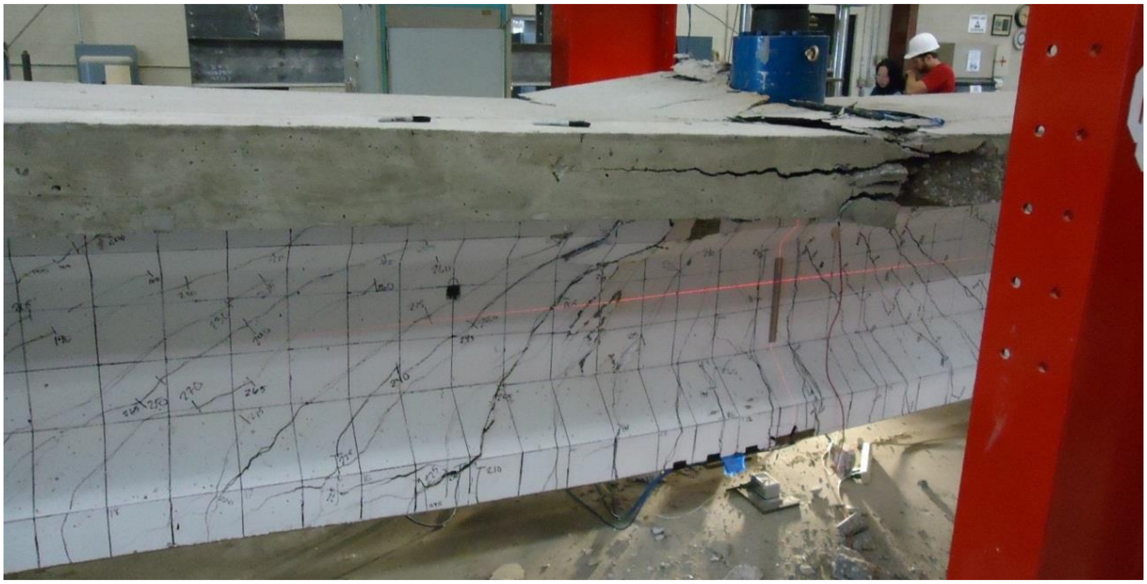

Figure 2.46: Test C2 failure, showing a large shear crack in the center of the image that entered the top flange causing catastrophic compression failure

Figure 2.47: Buckled steel and failure along plane of wearing surface

Figure 2.48: Buckled compression steel in girder

The load deflection curves for both tests are shown in Figure 2.49. There was an issue with the wire potentiometers that occurred at around 230 kips, so manual measurements are shown in lieu of the potentiometer data past this point. There was good agreement between the potentiometers and the manual deflection measurements up to this point. In Figure 2.49 there is a clear change in slope that occurs after the initial cracking corresponding to a decrease in stiffness due to the cracks. After cracks formed there was an increase in deflection of 3.75 in. and an abundance of additional cracks. This type of behavior is ductile and provides plenty of warning before failure.

Figure 2.50 shows the strand slip data from the bottom six strands of the girder. Unfortunately, the apparatus that was used to hold the strands in position shifted, causing the LVDTs to extend. Because of this, it is hard to quantitatively describe the slip in the strands during the test. It is, however, possible to determine which strands slipped and when. LVDT 10 appears to show slip at the time of initial cracking. This LVDT corresponds to the center-left strand. As the load surpassed 200 kips, all other strands on the bottom row appear to slip at some point. Again, the magnitude of slip is hard to determine, but it is at least 0.03 inches. It is unlikely this slip significantly affected the moment capacity of the section, especially given that the compression steel buckled.

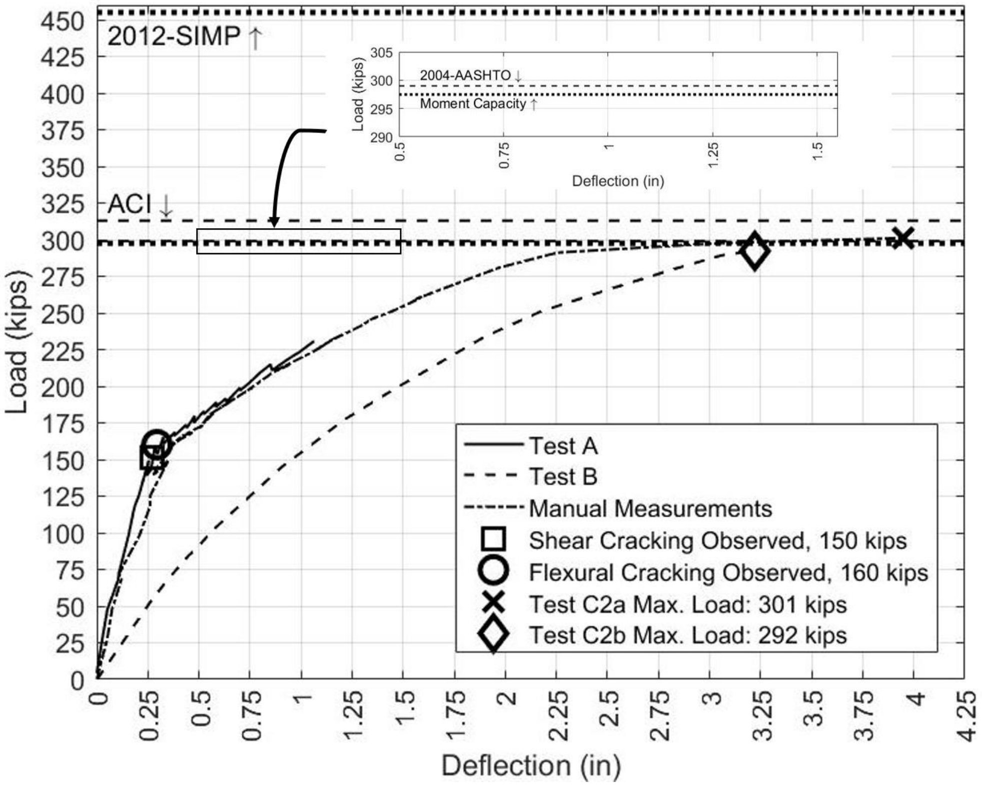

Figure 2.49: Load vs. deflection for test C2

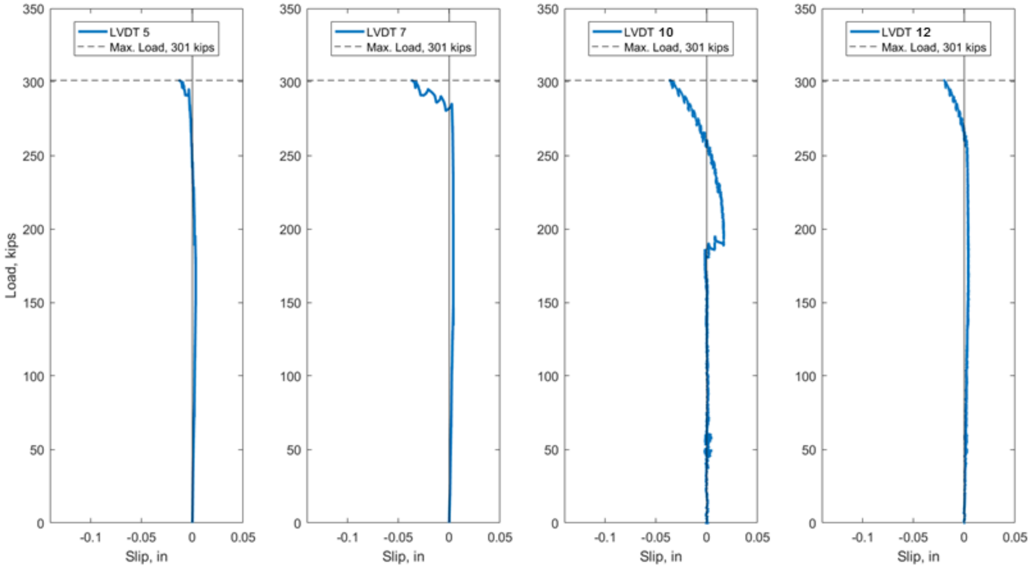

Figure 2.50: Slip for bottom row of strands

2.5.3 Summary of All Shear Tests

A summary of all shear tests is shown in Table 2.1.

Table 2.1: Summary of Shear Test Results for Girders A and C

Property/Result	A1	A2	C1	C2
a/d	2.5	2.0	3.0	3.83
Span (ft)	18.75	19.0	25.0	28.0
P_{cr} (kips)	170	190	160	150
V_{cr} (kip-ft)	101	127	102	88
M_{cr} (kip-ft)	760	790	922	1017
P_{max} (kips)	260	290	318	301
V_{max} (kips)	159	180	204	179
M_{max} (kip-ft)	1162	1197	1832	2040
Failure Mode	Bond-Shear	Flexural (strand rupture)	Bond-Shear	Compression-Shear

2.6 Material Properties

2.6.1 Overview

Cores were taken from both girder A and girder C for compression testing and modulus of elasticity testing. Twelve 3 in. cores were taken from the web of girder A resulting in 3 in. x 6 in. cores. The core locations were selected based on providing a representative sample of the concrete in the shear region of each test and a distribution of concrete compressive strength throughout the depth near the mid-section of the girder and at one end. Some core locations are shown in Figure 2.51. Two cores approximately 2 in. in diameter were taken from the deck at grid locations -3.5 and -0.5 ft. Seven 4.25 in. cores were taken from the central section of the beam for testing elastic modulus. Six 3.75 in. diameter cores were taken from the web of girder C for compressive strength and modulus of elasticity testing and three cores were taken from the deck of girder C for compression testing. Two samples each of prestressing strand and mild steel were taken from girder A for tensile strength and modulus of elasticity testing.

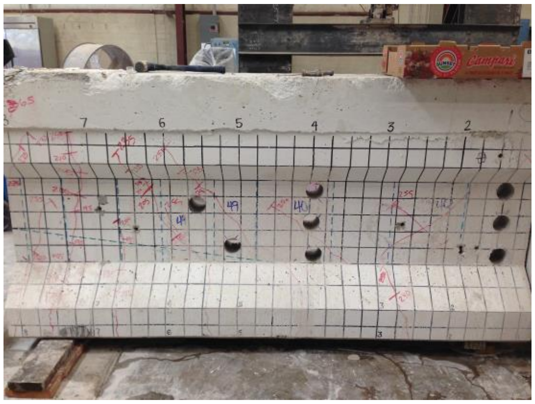

Figure 2.51: Photo showing girder A section after coring was completed

2.6.2 Concrete Properties

Six 3 in. diameter cores taken at different locations along girder A were tested for compressive strength. The specimen IDs are descriptive of the location of the core. The first letter (N or S) is whether it is north or south of the center of the girder. The number is the grid location in feet from the center line. The final letter (T, M or B) is when multiple cores were taken from the girder at the same location where the ID stands for top, middle and bottom of the web section of the girder.

The results of the compressive strength tests for the cores taken from the web of girder A are presented in Table 2.2. The average compressive strength for the cores was 6270 psi. Using the ACI 214.4 (2003) specification factor of 1.05, the equivalent compressive strength of the girder is 6570 psi. The measured compressive strength is close to the predicted compressive strength of 6000 psi. There was not a significant difference in compressive strength along the length of the girder.

Table 2.2: Compressive strength of 3 in. diameter cores from the web of girder A

Specimen ID	Load (lb)	Compressive Strength (psi)
N4.00T	45680	6460
N4.00M	46920	6630
N1.25T	40700	5760
N1.25M	47130	6660
S9.75T	42605	6020
S10.25B	43235	6110

Modulus of elasticity of the concrete was determined using seven cores approximately 4.25 in. in diameter. The modulus of elasticity for each core was based on the second and third loading cycles is provided in Table 2.3. The average modulus of elasticity of the girder concrete was 4750 ksi. The estimated modulus of elasticity was 4420 ksi based on the ACI equations using the compressive strength. The predicted modulus of elasticity is less than the measured modulus of elasticity which makes the preliminary calculations a conservative estimate. The modulus of elasticity did not show a significant difference along the length of the girder.

Two cores approximately 2 in. in diameter were taken from the deck at grid locations -3.5 and -0.5 ft. Each core was cut into three equal sections and tested for compressive strength. Table 2.4 documents the compressive strength from the cores.

Table 2.3: Modulus of elasticity of 4.25 in. cores taken from the web of girder A

Specimen ID	Modulus of Elasticity-Cycle 2 (ksi)	Modulus of Elasticity-Cycle 3 (ksi)	Modulus of Elasticity (ksi)
N0.50	4947	5042	4995
S0.50	4966	5109	5038
S3.00	4525	4542	4534
S3.75T	4420	4431	4426
S3.75B	4831	4916	4874
S4.50T	4696	4795	4746
S4.50B	4615	4623	4619

Table 2.4: Compressive strength of 2 in. diameter cores from the deck of girder A

Specimen ID	Load (lb)	Compressive Strength (psi)
S3.5a	31160	7830
S3.5b	27455	6900
S3.5c	30390	7640
S0.5a	27900	7010
S0.5b	27805	6990
S0.5c	27325	6870

The average compressive strength of the deck concrete cores at -3.5 ft was 7730 psi. Specimen b was ignored due to mild steel in the sample causing an inaccurate measurement of the core's concrete compressive strength. The average compressive strength of the concrete cores at -0.5 ft was 6960 psi. The average compressive strength of all 5 cores (excluding Specimen S3.5b) was 7270 psi. The modification by ACI 214.4 (2003) factor of 1.08 gives a compressive strength for the deck of 7840 psi. The deck concrete does not consist of only concrete from the original pour. The resurfaced concrete most likely had a different design mixture and strength. The measured compressive strength is much higher than the assumed value of 6000 psi. The compressive strength for deck and girder were originally assumed to be the same. The specifications for girder concrete are typically higher than for deck concrete, so it was unexpected for the deck to have a higher compressive strength. However, the specified compressive strength for the girders on the plans provided by ODOT was only 5000 psi compared to the typically specified 4000 psi for deck concrete. Greater compressive strengths for the deck are much less likely with modern construction, as girder concrete is often specified at compressive strengths of up to 10,000 psi. The concrete from the deck and girder were not cast at the same time and could explain the difference in the compressive strength.

The compressive strength of the cores taken from the web and deck of girder C are presented in Table 2.5. The average compressive strength of the cores taken from the girder web was 6900 psi and the average compressive strength for the cores taken from the deck was 5840 psi.

Table 2.5: Compressive strength cores from girder C

Girder Section	Specimen ID	Load (lb)	Compressive Strength (psi)
Web	W1	85850	7830
	W2	73195	6920
	W3	72780	6430
Deck	D1	71925	6340
	D2	74760	6550
	D3	52850	4640

2.6.3 Steel Properties

Two prestressing strand samples taken from girder A between grid locations -0.75 and -2.25 feet were tested for tensile strength and modulus of elasticity. Table 2.6 provides the modulus of elasticity and ultimate strength of each strand. The average modulus of elasticity of the strands was 26350 ksi. The average tensile strength of the

Table 2.6: Modulus of elasticity and ultimate strength of prestressing strands

Specimen ID	Modulus of Elasticity (ksi)	Ultimate Strength (ksi)
0.75-2.25West	26600	282.8
0.75-2.25East	26100	284.3

strands was 283 ksi, confirming that the strands were Grade 270, as specified in the plans provided by ODOT.

Two samples of mild steel used for the shear stirrups in girder A were tested for yield stress, ultimate strength and modulus of elasticity. Two samples from the steel in the diaphragm were also tested for yield stress, ultimate strength and modulus of elasticity. The results are shown in Table 2.7. The average yielding strength, modulus of elasticity, and ultimate strength for the stirrups are 54.8, 32750, and 87.9 ksi, respectively, and for the diaphragm 51.1, 27500, and 84.2 ksi. These values confirm the steel to most likely be Grade 40 which was assumed during the preliminary analysis.

Table 2.7: Yield strength, modulus of elasticity and ultimate strength of mild steel

Property	Stirrup 1	Stirrup 2	Diaphragm 1	Diaphragm 2
Yield Stress (ksi)	54.4	55.2	51.6	50.5
Modulus of Elasticity (ksi)	29,300	36,200	26,800	28,200
Ultimate Strength (ksi)	87.4	88.4	85.5	82.8

3. Analysis

3.0 Nomenclature

a	shear span length
d	structural depth of the cross-section

3.1 Overview

Detailed drawings of each girder were created using AutoCAD, the drawings provided by ODOT, and the actual measurements of the beams. A sample of these drawings is shown for girder A in Figure 3.1. A re-creation of the entire bridge cross-section was also created using typical sections provided by ODOT. These drawings were created for the purpose of quick reference in the analysis process. A detailed series of Excel spreadsheets was created to analyze a single beam section in terms of shear and moment diagrams, section properties from measured dimensions, service stresses, prestress losses using the AASHTO LRFD (2007) and ACI 318 (2011) methods, nominal moment capacity using strain compatibility and the ACI equation for prestressing steel stress, and nominal shear capacity using the AASHTO LRFD and ACI methods. These spreadsheets were used to calculate the capacities used for selecting load locations for the shear tests and for comparison to the measured values for each loading configuration. Similar spreadsheets were also created for other methods of shear analysis.

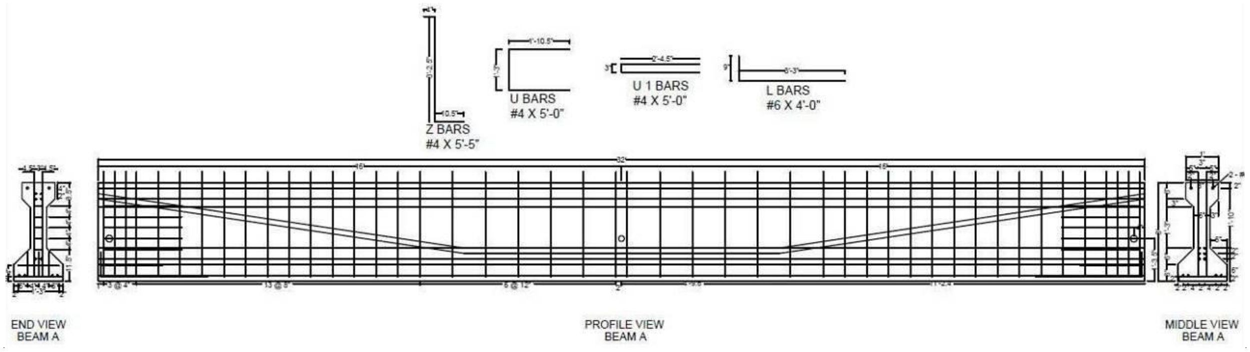

Figure 3.1: Example of drawings created for girder A for use in analyses

Models of the complete bridge cross-section were created for both girder A and girder C beam cross-sections using the program LEAP CONSPAN (now called LEAP Bridge Concrete). These models were used for determining load distribution between girders in the full bridge section based on the AASHTO specifications.

3.2 AASHTO Analyses

Both girder A and girder C were analyzed for shear using the methods of AASHTO Standard Specifications (1973); AASHTO LRFD (2007); and ACI 318 (2014) at the critical sections described by the various codes and at the sections where the girders were loaded during the shear tests. The Excel spreadsheets developed for these analyses were used to examine a variety of load cases. The AASHTO refined method was used to estimate prestress losses, which were then used to determine the effective prestress required for shear calculations. The capacities calculated for girders A and C and the values measured during the corresponding shear tests are presented in Tables 3.1 to 3.4. The “Estimated” column includes the values calculated using loads estimated from the calculated moment capacity, the “Experimental” column includes the values calculated using the loads obtained during experimental testing, and the “Applied” column includes the values measured during the shear tests. Concrete and steel properties measured from the samples taken from girder A were used for all capacity calculations.

Table 3.1: Capacities determined using the code methods for the Test A1 configuration (*a*/*d* = 2.5)

Capacity Type	Estimated	Experimental	Applied
Maximum Load, *P* (kips)	239	260	260
ACI Shear Capacity (kips)	179	179	159
AASHTO (2004) Shear Capacity (kips)	157	155	
AASHTO (2012) Shear Capacity (kips)	98.1	97.8	
Shear Angle AASHTO 2004 (degrees)	37.0	37.3	39.5
Shear Angle AASHTO 2012 (degrees)	49.9	50.0	
Strain Compatibility – Moment Capacity (kip-ft)	1056	1070.5	1162
ACI Moment Capacity (kip-ft)	836	981.1	

Table 3.2: Capacities determined using the code methods for the Test A2 configuration (*a*/*d* = 2.0)

Capacity Type	Estimated	Experimental	Applied
Maximum Load, *P* (kips)	256	289.5	289.5
ACI Shear Capacity (kips)	179	179	180
AASHTO (2004) Shear Capacity (kips)	151	152	
AASHTO (2012) Shear Capacity (kips)	95.4	95.3	
Shear Angle AASHTO 2004 (degrees)	36.8	36.1	42.8
Shear Angle AASHTO 2012 (degrees)	50.0	50.0	
Strain Compatibility – Moment Capacity (kip-ft)	1019	1019	1197
ACI Moment Capacity (kip-ft)	806	806	

Table 3.3: Capacities determined using the code methods for the Test C1 configuration (*a*/*d* = 3.0)

Capacity Type	Estimated	Experimental	Applied
Maximum Load, *P* (kips)	341	318	301
ACI Shear Capacity (kips)	135	179	204
AASHTO (2004) Shear Capacity (kips)	172	172	
AASHTO (2012) Shear Capacity (kips)	108	119	
Shear Angle AASHTO 2004 (degrees)	36.8	36.8	30.7
Shear Angle AASHTO 2012 (degrees)	49.8	46.8	
Strain Compatibility – Moment Capacity (kip-ft)	1933	1933	1832
ACI Moment Capacity (kip-ft)	1445	1445	

Table 3.4: Capacities determined using the code methods for the Test C2 configuration (*a*/*d* = 3.83)

Capacity Type	Estimated	Experimental	Applied
Maximum Load, *P* (kips)	297	301	301
ACI Shear Capacity (kips)	185	185	179
AASHTO (2004) Shear Capacity (kips)	177	177	
AASHTO (2012) Shear Capacity (kips)	117	115	
Shear Angle AASHTO 2004 (degrees)	37.3	37.3	33.2
Shear Angle AASHTO 2012 (degrees)	48.2	48.8	
Strain Compatibility – Moment Capacity (kip-ft)	1997	1997	2040
ACI Moment Capacity (kip-ft)	1502	1502	

3.3 Bond Shear Failure Analysis (Ross and Naji 2013)

This method was used in the study described in this report for completeness, even though every failure cannot be characterized as a bond transfer failure. Slip was observed in tests A1 and C1, indicating some bond issues. In test A1, compression failure of the deck overlay caused failure, so the bond shear capacity by Ross and Naji (2013) was not reached. In test C1, slip was also observed and the failure occurred due to crushing in the deck and delamination of the wearing overlay.

Selecting some of the values required for this method is somewhat subjective. For each test, a failure crack was chosen from the photos of each failure. This crack was chosen based on observations about the mode of failure. In test C1 for example, the cracking pattern is given in the top of Figure 3.2. At the bottom of figure one, the red line shows the crack chosen for the analysis. This crack extends from the bottom of the girder into the deck near the load point. It also intersects the development length of the strands closest to the support. Moments are then taken about the green line in the bottom of Figure 3.2. In Figure 3.2, the vertical dashed lines represent the shear steel. For analysis, the heavy black dashed lines were assumed as the stirrups contributing to shear resistance since the other stirrups crossed were crossed very near where they would be hooked. A summary of values calculated based on the bond-shear failure mechanism is given in Table 3.5.

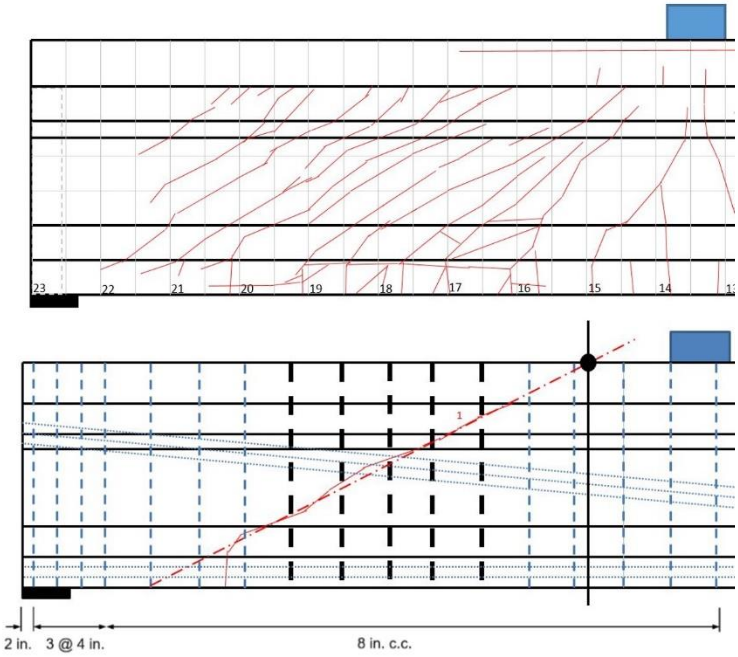

Figure 3.2: Selection of critical crack for Ross and Naji (2013) using test C1

Table 3.5: Ross and Naji (2013) bond-shear method summary

Test	Nominal Bond-Shear Capacity (kips)	Experimental Shear Capacity (kips)	Slip observed?	Error (%)
A1	197.8	159	Y	24.5
A2	190.2	180.0	N	5.6
C1	225.8	204	Y	10.7
C2	278.7	179	N	55.7

3.3.2 Girder “A”

Some slip was observed during test A1, so it is possible that the bond-shear method can be applied. The diagram including shear crack and stirrups used, is given in Figure 3.3. The Ross and Naji (2013) method predicts a nominal bond-shear capacity of 198 kips, compared to an experimental capacity of 159 kips. This represents a 24.5% error. A possible source of error is the force contributed by the shear steel. The model assumes that this steel has yielded, but it is possible some bars do not contribute this much force to the bond-shear resistance.

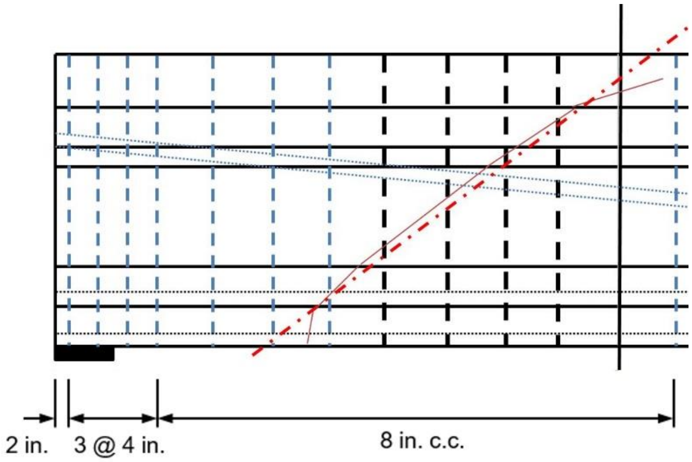

Figure 3.3: Critical crack for test A1

Slip was not measured in test A2, in fact a strand ruptured during this test, indicating the girder reached its moment capacity. Surprisingly, the nominal bond-shear capacity was only 5.6% different than the experimental capacity (190 kips and 180 kips respectively). The crack diagram for A2 is shown in Figure 3.4.

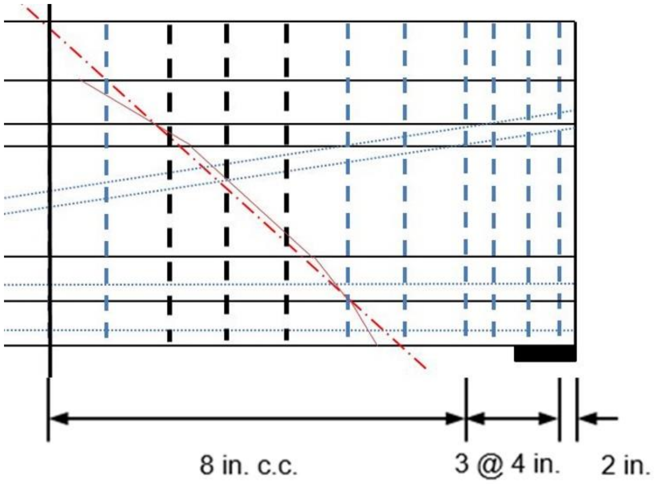

Figure 3.4: Critical crack for test A2

3.3.3 Girder "C"

Slip was observed during test C1, indicating that the bond-shear model may be applicable. The diagram for this test is given in the bottom of Figure 3.2. The nominal bond-shear capacity was calculated as 225.8 kips, compared to 204 kips from the shear test. This is an error of 10.7%. In this test the bond-shear capacity was predicted quite closely. In test C2, no slip was observed, so it is unlikely that a bond-shear method would provide an accurate representation of capacity. The critical crack used for capacity calculation is shown in Figure 3.5. The nominal bond-shear capacity was 278.7 kips and the experimental capacity was 179 kips. This is an error of 55.7%. It is worth noting that this test was performed at the quarter span point and so it was unlikely that any bond issues would occur.

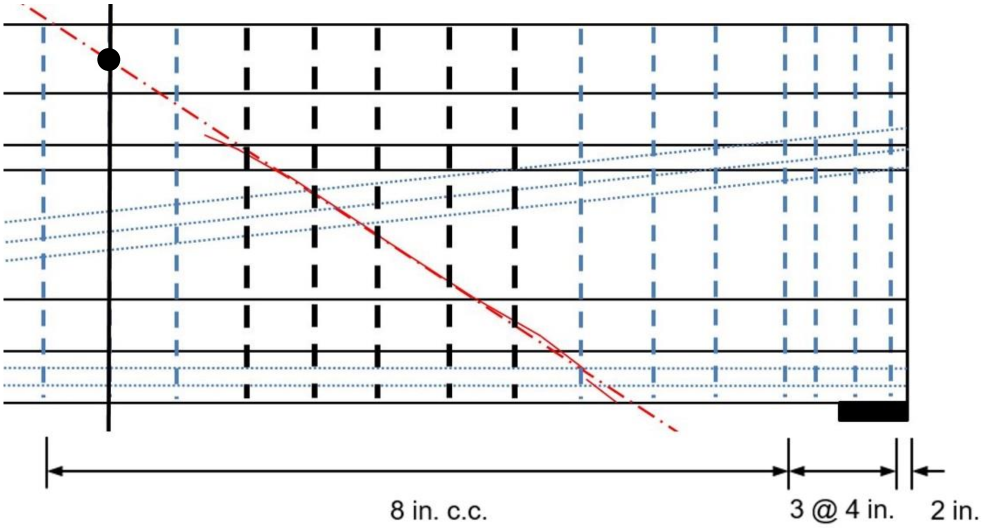

Figure 3.5: Critical crack for test C2

3.4 Strut and Tie Models

The strut and tie models used to examine the capacity of girder A were based on the requirements of ACI 318 (2011) and AASHTO LRFD (2007). The section between the applied load and the support was considered as a D-region and the truss layout was arranged using the actual crack angles measured during the corresponding shear tests. These truss layouts are shown in Figures 3.6 and 3.7 with struts indicated by solid lines and ties by dashed lines. Both were relatively complicated arrangements in order to account for the effect of the harped strands. The models for both tests predicted the failure to be controlled by the capacity of the tension tie in the straight strands at a load of 130.4 kips for test A1 and 140.0 kips for test A2. These predicted loads were substantially less than the measured values, but in both cases the failure was at least partially controlled by tension in the prestressing strands. Strand fracture was observed for test A2.

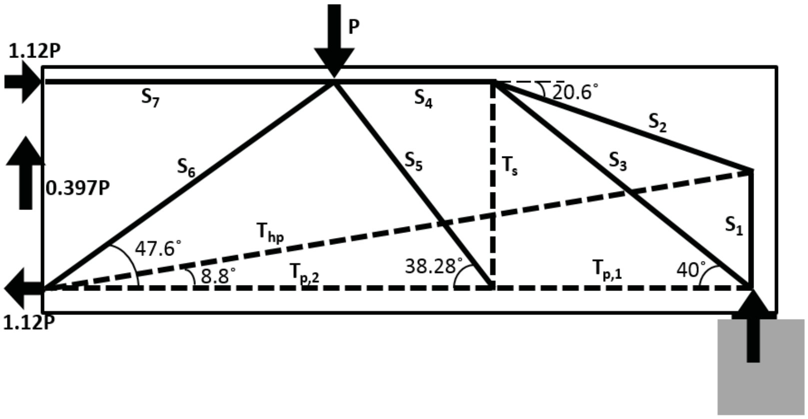

Figure 3.6: Strut and tie model for configuration of shear test A1

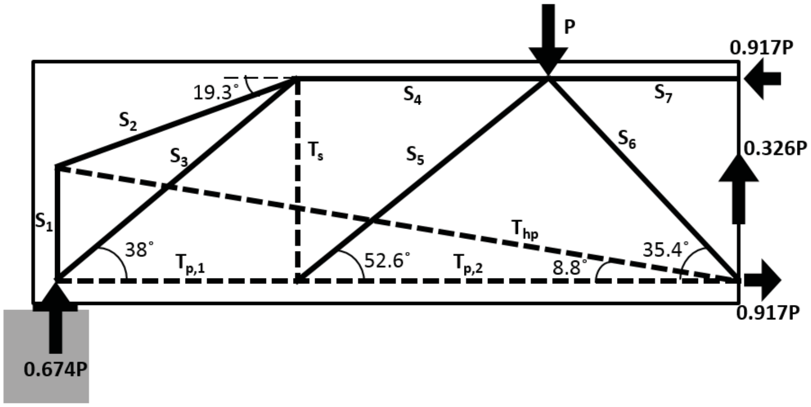

Figure 3.7: Strut and tie model for configuration of shear test A2

3.5 Comparison of Code Predictions Experimental Values

Results from the four shear tests were compared to the ACI method (ACI), the 2012 AASHTO LRFD simplified procedure (2012-SIMP), the 2012 AASHTO LRFD general method (2012-GEN), the 1973 AASHTO Standard Specifications (1973-STD) and the AASHTO LRFD MCFT tabular method (2004-AASHTO). For this work, M_{max} was determined based on the expected flexural capacity of the section using strain compatibility. M_{cre} was determined using estimated effective prestress forces and including the dead load from the remaining deck. The code versus experimental capacities for all tests are shown in Figure 3.8. All expected capacities are nominal; no strength reduction factors are included.

In Figure 3.8 there is a general trend that the 2012-GEN and 2004-AASHTO methods (both based on MCFT) give conservative estimates of strength for each location tested. In the case of the 2012-GEN method, the estimate was conservative by a factor (experimental ultimate shear/predicted ultimate shear) of 1.8 to 2.5. The 2004-AASHTO methodology is slightly less conservative, with factors between 1.10 and 1.47. The 2012-GEN was developed as a simplification of the 2004-AASHTO method and it was reported by its developers to be more conservative (Bentz et al. 2006). Both of these methods also predict a low concrete contribution to shear strength. The concrete contribution to shear strength is influenced by the factor β which differs between the 2004-AASHTO and 2012-GEN methods. In all cases, the 2012-GEN method provided a low capacity and predicted a large shear crack angle (~50 degrees), limiting the capacity contribution from the stirrups. The equation for the shear crack angle is based on the strain at the level of the tension reinforcement; in these cases, the applied moment increased the strain, resulting in a reduced capacity. The moment was relatively high because the girder had to be supported near the center to facilitate testing both ends, increasing the applied moment for a given shear demand. The 2004-AASHTO method produced a more reasonable prediction of shear crack angles than the 2012-GEN method.

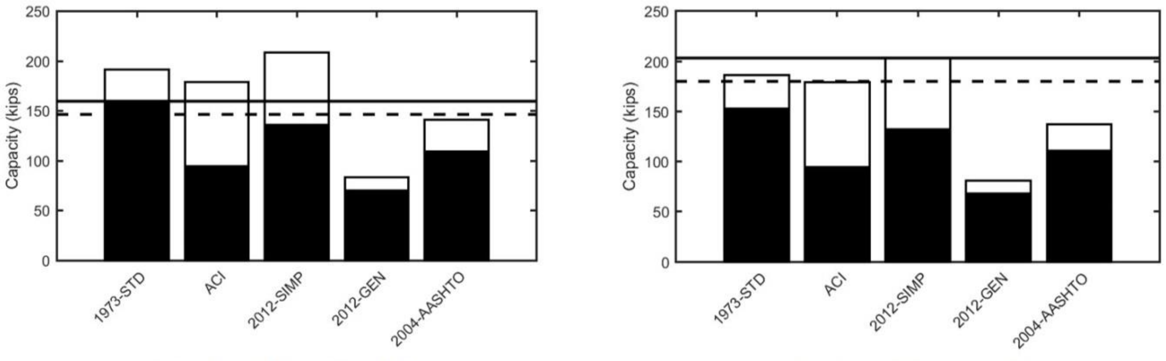

(a) Test A1: a/d = 2.5

(b) Test A2: a/d = 2.0

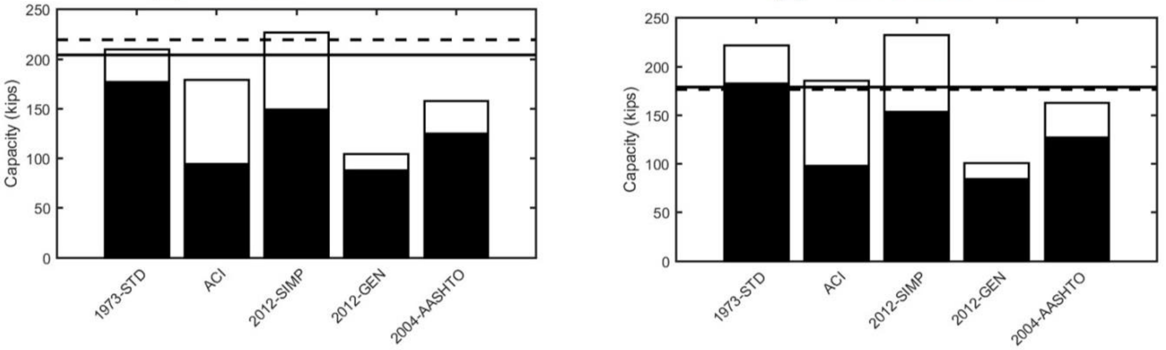

(c) Test C1: a/d = 3.0

(d) Test C2: a/d = 3.83

■ Steel Contribution
□ Concrete Contribution
— Shear Demand at Failure
- - Shear Demand at Nominal Flexural Strength

Figure 3.8: Tested capacities compared to code predictions

The other shear equations were occasionally un-conservative. For test A1, the 1973-STD, ACI, and 2012-SIMP were all un-conservative, over predicting capacity by factors of 1.20, 1.12, and 1.31 respectively. During test A1 there was a loss of bond due to shear cracking and possibly due to corrosion. This test can be characterized as a bond-shear failure. Based on strain compatibility, the flexural capacity of the section should have been reached at an applied load of 239 kips; less than the 260 kip applied load at failure. In this case, the capacity of the section was estimated conservatively by strain compatibility, even when bond was lost due to shear cracking. One could argue that the estimated force to fail the section was conservative based on moment capacity determined by strain compatibility, however the shear equations failed to predict a loss of bond due to shear cracking, which is potentially un-conservative.

During test A2, prestressing strands near the load point ruptured, indicating a flexural failure. The flexural capacity of the section based on strain compatibility was exceeded during the test. The extent of shear cracking indicates that the girder maintained adequate ductility and load carrying ability during the test. At the failure load, all shear capacity calculations were conservative.

Test C1 resulted in a bond-shear failure with shear cracks entering the zone of prestress transfer and reducing the capacity of the section. The codes were conservative with the exception of the 2012-SIMP, which indicated a capacity 11% higher than the experimental value. Test C2 on the other hand was performed at the quarter-point, the critical location for shear per the 1973 code. In this case, the applied load exceeded the flexural capacity as calculated by strain compatibility. The code equations were conservative with the exception of the 1973-STD and 2012-SIMP which produced predictions 24% and 30% higher than the experimental values, respectively.

Calculated shear capacities were normalized by the actual shear capacity to compare the accuracy of the different methods. Not considering test A2, which can be characterized as a flexural failure, the normalized capacities were averaged to determine how accurate they were in general. The results of this analysis are shown in Table 3.6, where a number greater than 1.0 indicates that the code method over-predicted capacity and a number less than 1.0 indicates a conservative prediction. The 2012-GEN method is by far the most conservative, followed by the 2004-AASHTO method. ACI and 2004-AASHTO provided the most accurate results in this study. The 1973-STD and 2012-SIMP methods were generally un-conservative for these cases. It is important to note that although this report compares observed capacities to predicted shear capacities, these failures may not be entirely due to shear, with flexure or bond-loss contributing to the failure.

Table 3.6: Normalized capacities from each method

Method	Average Normalized Capacity	Coefficient of Variation
1973-STD	1.16	9.83%
ACI	1.01	12.1%
2012-SIMP	1.24	8.93%
2012-GEN	0.533	5.01%
2004-AASHTO	0.857	8.44%

In all of the tests performed for this study, there was a relatively high applied moment in relation to the applied shear, as compared to if the full span were tested. Because the spans were typically supported near the original girder centerline, higher loads were needed to reach the shear capacities of the sections. This changes the shear behavior by altering the internal stresses in the section. MCFT accounts for this by altering the angle of cracking based on the strain in the section. If these sections were loaded in the field, there would be a larger applied shear and smaller moment for a given load near the supports. The most concerning load case was test A1 because the shear capacity was overestimated by ACI and the 2012-SIMP methods and shear cracking caused strand slip in the section.

3.6 Comparison of Demands and Experimental Values

The design load demands based on AASHTO LRFD (2012) and AASHTO Standard Specifications (1973) were determined for girders A and C using the commercial program LEAP CONSPAN (now called LEAP Bridge Concrete) produced by Bentley. Each of these bridges was modelled in a similar fashion in order to examine the effects of the full bridge on demands and capacity as outlined in the AASHTO specifications. The design trucks and load distribution factors for both sets of requirements were used to calculate the moment and shear values along the length of the span. Figure 3.9 shows the typical layout of the model for each bridge. Analysis was performed for girder 2 and girder 4 for both bridge layouts to evaluate the sections with the largest shear demands.

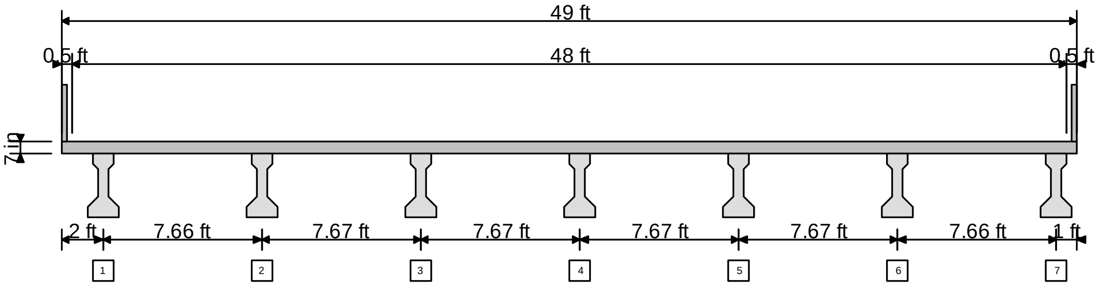

Figure 3.9: Typical LEAP Bridge Concrete model

Figure 3.10 shows the demand, nominal moment capacity, and experimental ultimate moments for the girder 2 location of the bridge model based on the configuration for tests A1 and A2. The demands shown are from the strength I and service I limit states from AASHTO LRFD and the strength limit state from 1973 AASHTO. The nominal capacity is greater than the strength level values for the 1973 AASHTO STD and the 2012 AASHTO LRFD. The experimental moments were also larger than the calculated nominal moment capacities at the locations tested. Figure 3.11 presents the same information except for the girder 4 location, the middle girder of the bridge model. Again, the capacity exceeded demand, and the tested moments exceeded the calculated nominal moments.

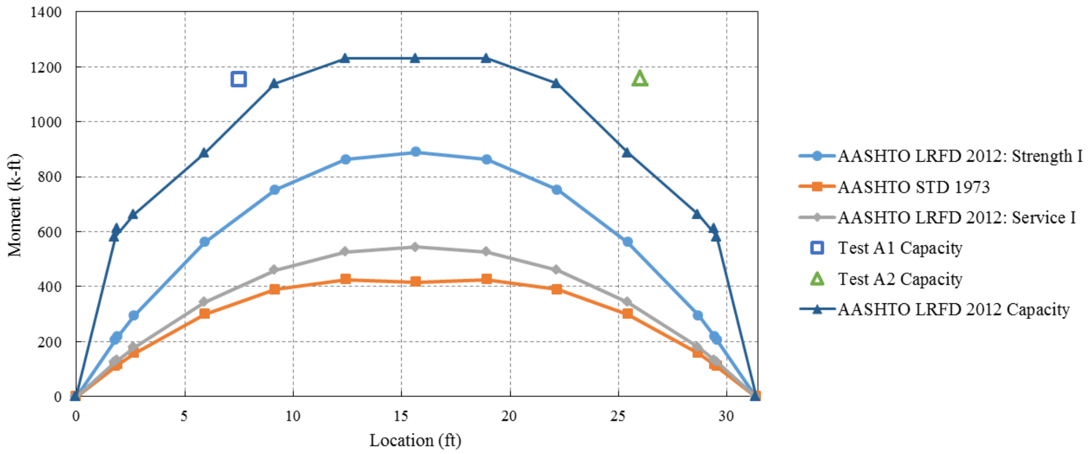

Figure 3.10: Girder A moment demand, beam location 2

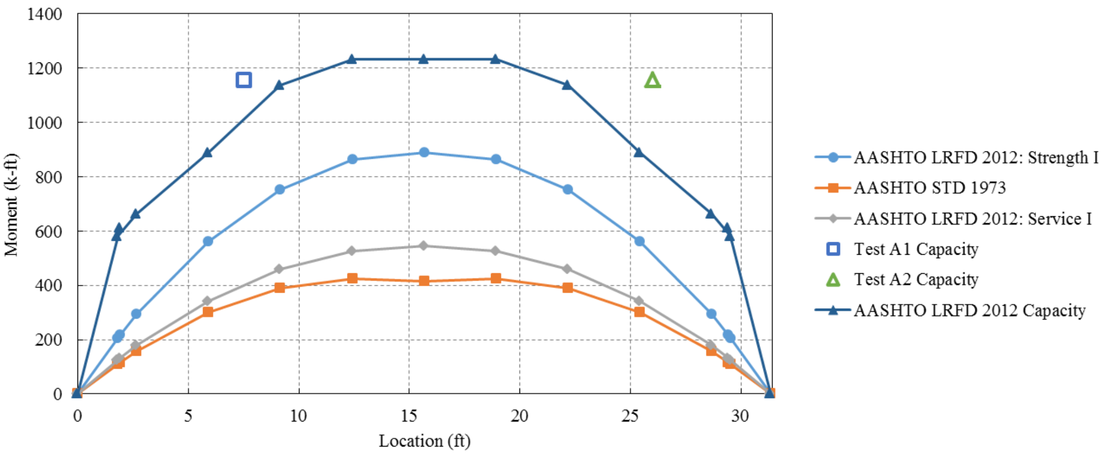

Figure 3.11: Girder A moment demand, beam location 4

Shear demand for the girder A configuration model is given in Figures 3.12 and 3.13. These figures represent the demand for beam locations 2 and 4, respectively. The shear capacities have not been added to these diagrams; LEAP Bridge Concrete does not output shear capacity in the same fashion. Again, the experimental capacities exceed the demands for every limit state. These comparisons are made in Section 3.5. Also, note that the demand placed on the girders during testing also exceeded the maximum demand for every limit state for the entire length of the girder.

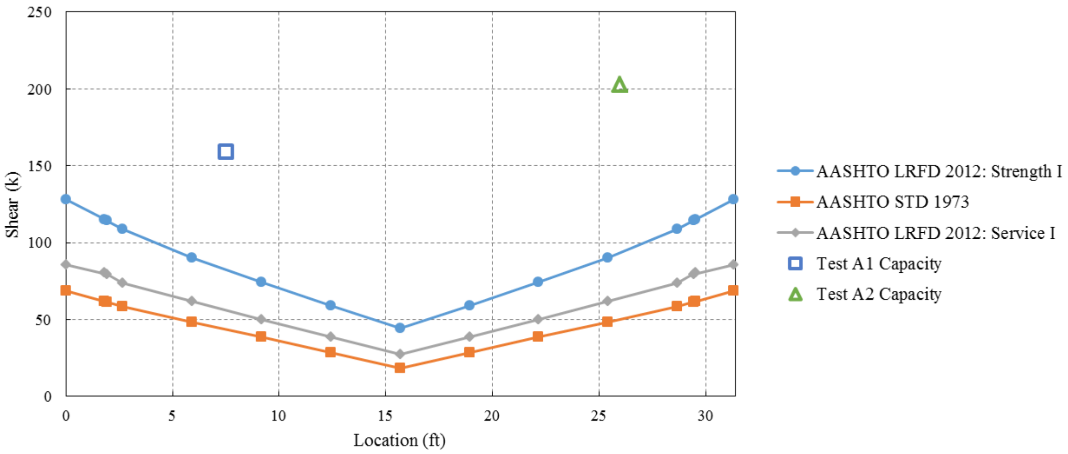

Figure 3.12: Girder A shear demand, beam location 2

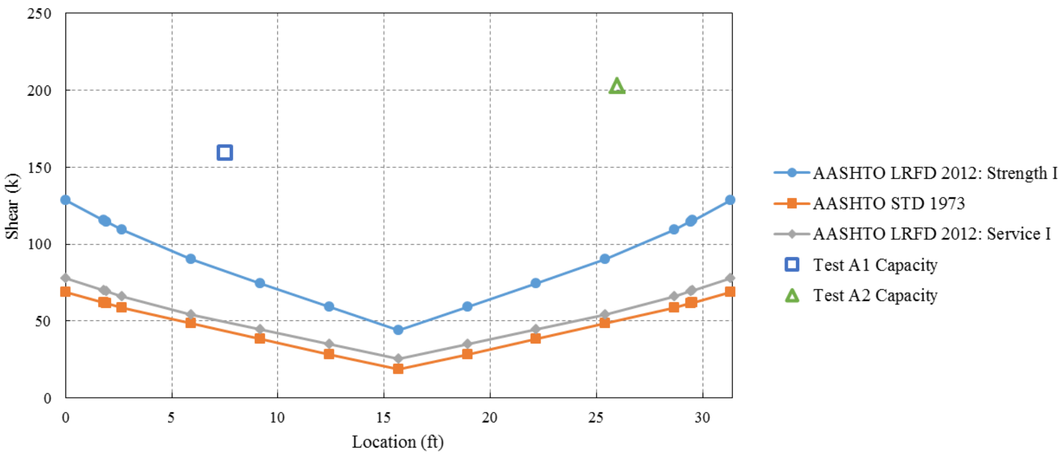

Figure 3.13: Girder A shear demand, beam location 4

The moment demands for girder C are given in Figures 3.14 and 3.15. The demand for each limit state is very similar for both beam locations. As for girder A, the experimental capacities exceeded the nominal moment capacities and the demand at the tested locations. Figures 3.16 and 3.17 show the shear demand for both beam locations for the girder C design. The shear demand was exceeded by the experimentally applied shear for the AASHTO LRFD and AASHTO STD.

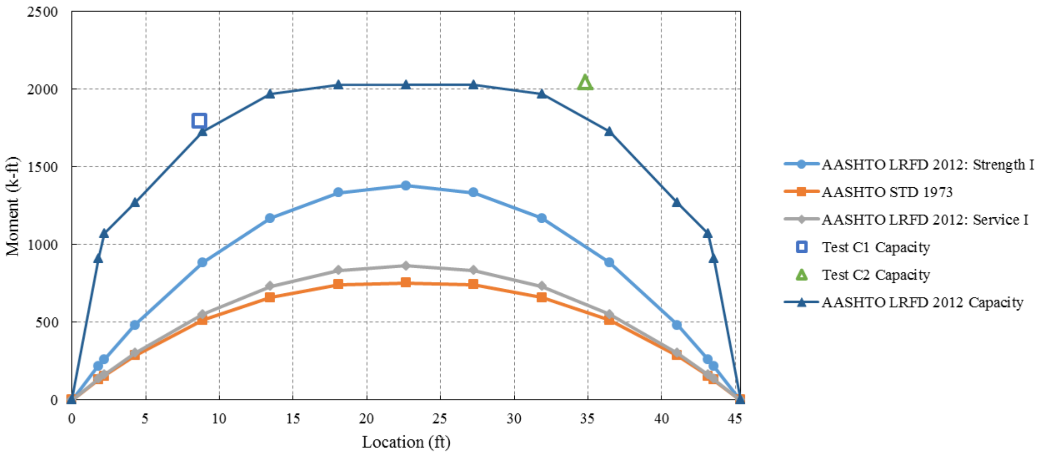

Figure 3.14: Girder C moment demand, beam location 2

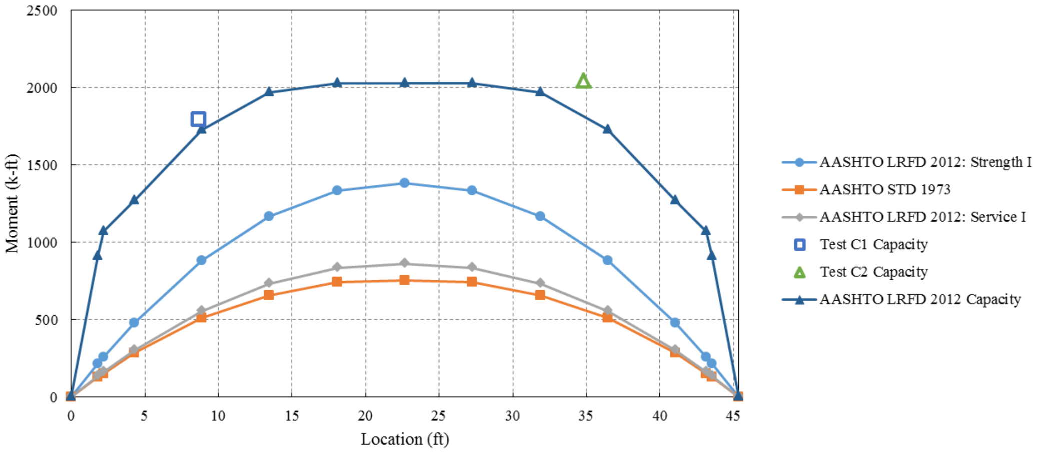

Figure 3.15: Girder C moment demand, beam location 4

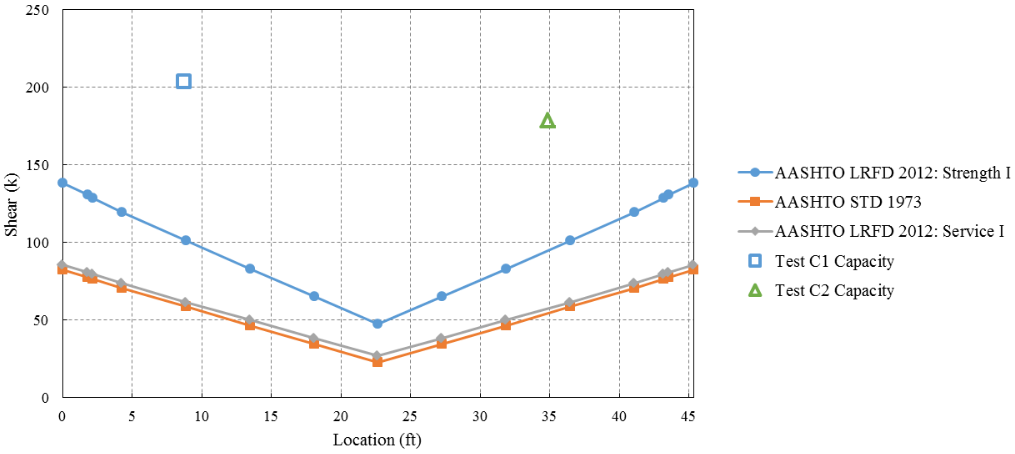

Figure 3.16: Girder C shear demand, beam location 2

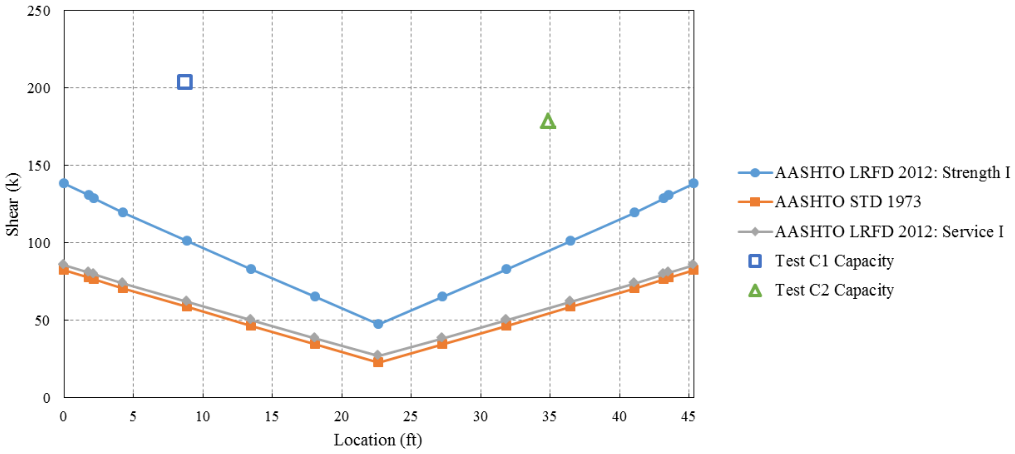

Figure 3.17: Girder C shear demand, beam location 4

4. Analysis of Bond and Transfer Length

4.0 Nomenclature

A_c	cross-sectional area of concrete
A_s	cross-section area of strand
$\frac{A_s}{A_c} \triangleq p$	area ratio
α	factor that represents the bond stress distribution shape along the transfer length (typically between 2 and 3, but values have been estimated by several experimental results and theoretical studies)
b	experimental constant for (Eq. 4.2) assumed to be 0.25 for ½ in. seven-wire strands.
d_b	strand diameter
δ	strand end slip (in.)
ε_{si}	initial strand strain (in./in.)
E_c	Young's modulus of concrete in linear elastic stage
E_{ps}	Young's modulus of strand
$\frac{E_{ps}}{E_c} \triangleq m$	Young's modulus ratio
f	stress in strand as in Guyon (1953)
f_b	bond stress
f_{si}	initial stress in strand at the moment of release as in Guyon (1953)
f_M	the maximum value of f, $f_M = \frac{f_i}{1+mp}$ from Guyon (1953)
f'_c	cylindrical compressive strength of concrete in psi
$g(z,t)$	the displacement of the strand relative to the concrete along the z-axis
$g_0(t)$	the draw-in value at the free end, i.e., $g(0,t)$
$\frac{d_g}{d_z}$	longitudinal strain in strand at $t = 0$ as in Guyon (1953)
k	as in Eq. (4.7)
l_0	the initial length of the post-tensioned prestressed concrete beam as in Eq. (4.7)
l_{0s}	the initial length of the strand in the post-tensioned prestressed concrete beam as in Eq. (4.7)
l_t	transfer length (in.)
$P(t)$	resultant force in strand/concrete
P_i	initial resultant force in strand/concrete at the moment of release, i.e., t = 0

P_M	the maximum value of P, $P_M = \frac{P_i}{1+mp}$
S	free end slip per Eq. 4.3 (in.)
w_c	unit weight of concrete in pcf
$x(t)$	transfer length
z	abscissa starting from the free end
t	time
η	concrete viscosity as in Eq. (1)
$\lambda(t)$	characteristic length for elastic anchorage

4.1 Literature Review of Strand Slip and Transfer Length

Guyon (1953) proposed an expression for determining transfer length based on the amount of strand end-slip during the release of tension in the prestressed strand.

$$l_t = \alpha \frac{\delta}{\varepsilon_{si}} \tag{4.1}$$

where:
l_t = transfer length (in.)
α = factor that represents the bond stress distribution shape along the transfer length (typically between 2 and 3, but values have been estimated by several experimental results and theoretical studies)
δ = strand end slip (in.)
ε_{si} = the initial strain in the strand (in./in.)

Balazs (1993) proposed a modification of Guyon's formula to consider the shape of the strand and its surface pattern to modify the linear bond stress distribution.

$$l_t = \frac{2}{1-b} \frac{S}{\varepsilon_{si}} \tag{4.2}$$

where:
b = experimental constant assumed to be 0.25 for ½ in. seven-wire strands.

This is essentially Eq. (4.1) with a different α coefficient, which can take into consideration the shape of the bond stress distribution by considering the tendon type (wire or strand) and its surface pattern (crimped, indented or deformed). The assumed bond stress-slip relationship: $f_b = c\sqrt{f'_{ci}}\delta^b$ can be used to determine *b*. If *b*=1/3 or *b* approaches 0, the values α = 3 and α = 2 are obtained as proposed by Guyon for linear and constant bond stress distributions over the transfer length, respectively. For ½ in. seven-wire strands, b=0.25, therefore, $\alpha = 2.67$ (Balazs 1993).

Additionally, non-linear relationships for the bond stress distribution were considered, so that the transfer length is a function of both the draw-in and initial prestress (expressed for ½ in. seven-wire strands).

$$l_t = \frac{111S^{0.625}}{{f'_{ci}}^{0.15}\varepsilon_{si}^{0.4}} \tag{4.3}$$

or

$$l_t = \frac{3.5f_{si}}{\sqrt{f'_{ci}\sqrt{S}}} \tag{4.4}$$

where:
f_{si} = the compatible initial prestress (psi)
S = the free-end slip (in.).

Compared to Eq. (4.1), Eq. (4.3) is a better indicator of draw-in variation and Eq. (4.4) estimates the variation of the initial prestress (Balazs 1993).

Marti-Vargas et al. (2007) proposed modifications to Guyon's formula. They proposed expressions using end slip and the α factor.

$$l_t = \alpha\frac{\delta}{\varepsilon_{si}} \tag{4.5}$$

where:
l_t = transfer length (in.)
δ = strand end slip at the free end of a prestressed concrete member (in.)
ε_{si} = initial strand strain (in./in.)
α = coefficient representing the shape factor of the bond stress distribution along the transfer zone.

Two hypotheses were considered: α = 2 for uniform bond stress distribution (linear variation in strand stress) and α = 3 for linear descending bond stress distribution (parabolic variation in strand stress).

Eq. (4.5) can be rewritten as:

$$l_t = \alpha\frac{\delta E_p}{f_{si}} \tag{4.6}$$

where:
E_p = modulus of elasticity of the prestressing strand
f_{si} = strand stress immediately before prestress release.

The study concluded that the optimal α value is 2.44, although considering other parameters (i.e. concrete compressive strength) could make the equation more accurate (Marti-Vargas et al. 2007).

The use of Airy stress function for modeling prestress bond described in Guyon (1953) was thoroughly reviewed using both Guyon and other references. This concept was found to not be useful in pursuit of the goals of the project described in this report, though it may be useful for 3D finite element modeling in future projects.

4.2 Bond Testing

Summaries of bond testing methods used in previous studies were prepared and used to facilitate discussion of the most effective testing methods to use for measuring the distribution of strand slip within the transfer length and the strand draw-in time history. A method similar to the ECADA test method proposed by Marti-Vargas et al. (2006) was selected based on this discussion.

A concrete mix was designed to meet the compressive strength requirements of the original girders as well as the composition and fresh properties required by the current ODOT specifications for use in construction of the bond test specimens. A series of trial batches were made to refine the mix design and achieve the required properties.

4.2.1. Background

The test method ECADA was developed by Marti-Vargas et al. (2006). This method uses a steel frame and hydraulic jack to apply the prestress; after which concrete specimens can be cast, cured, released, and pulled out. A summary of the testing setup and method is presented in Figures 4.1 and 4.2.

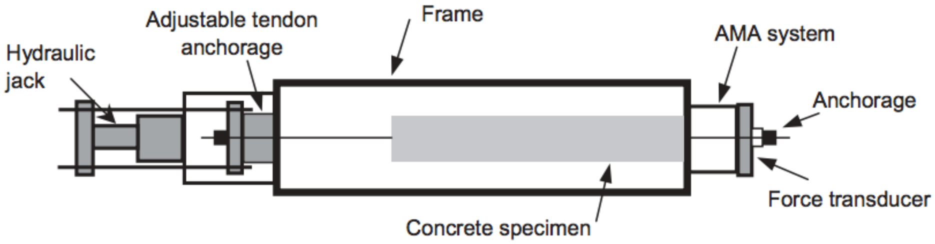

Figure 4.1: ECADA testing setup (Marti-Vargas et al. 2006 MCR)

The ECADA method measures the force in the strand after tension in the strand is released and stabilized. Then a pull-out test is performed by pulling one end of the strand until “the slippage or breakage of the reinforcement or failure of the concrete by splitting” occurs (Marti-Vargas et al. 2006). The test method proved systematic and reliable in testing several parameters to analyze the transfer and anchorage lengths of concrete specimens. It was proposed that it could be standardized and used for many different specimen lengths. In another study published by Marti-Vargas et al. (2006), the ECADA pull-out method was compared with three other methods of determining transfer and anchorage lengths, including Guyon’s formula. Several other parameters were considered, including compressive strength of the concrete, cement content, water/cement ratios, and total embedment lengths. From these studies, the ECADA method was again proposed as accurate and possible to standardize for predicting the transfer length (Marti-Vargas et al. 2006 PCI).

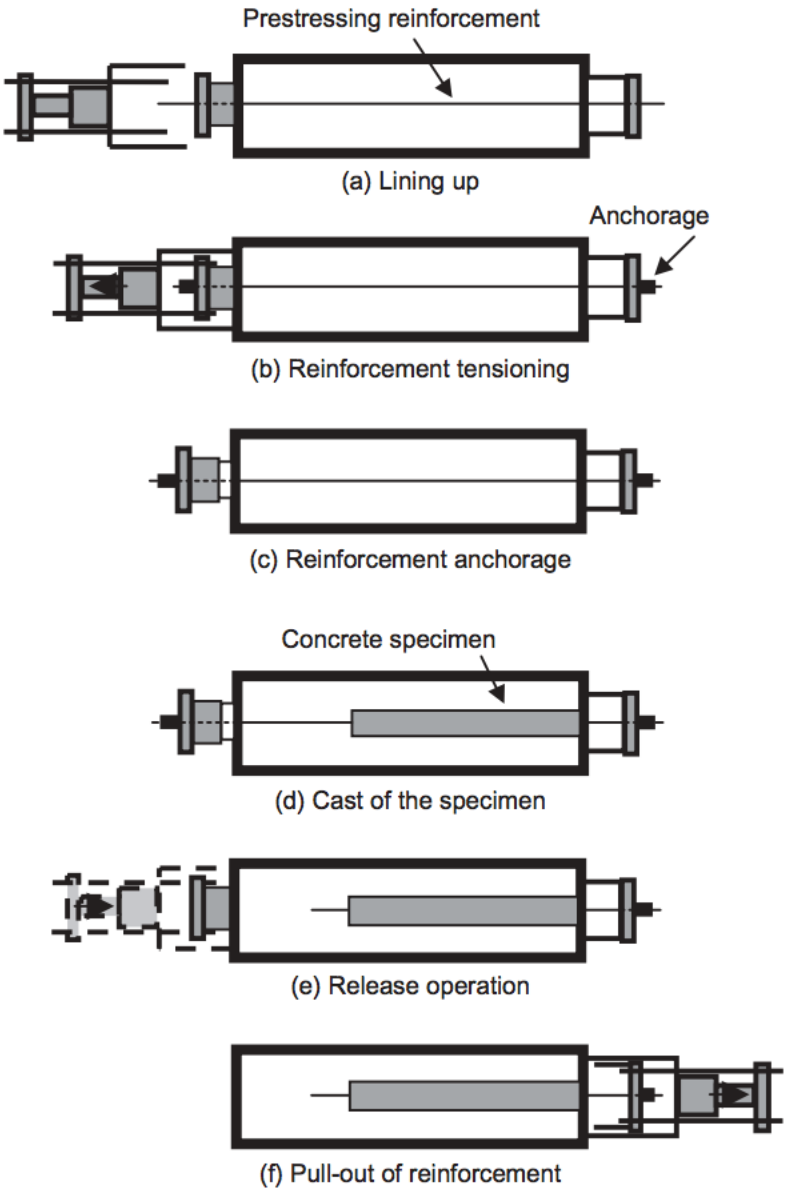

Figure 4.2: ECADA testing phases (Marti-Vargas et al. 2006 MCR)

Marti-Vargas et al. (2007) measured the strand end slip of concrete specimens in the ECADA testing setup using linear variable differential transducers (LVDTs). The “free end” of the specimen is defined as the side where pretension is released. This side of the strand is “free” to slip into the concrete after the tension is released. The “anchored end” or “embedded end” of the specimen is defined as the end that backs up to the plate in the frame. This end of the specimen mimics the embedment length that would be capable of maintaining a bond between the concrete and prestress strand in larger concrete specimens. From these tests, a factor value of $\alpha = 2.44$ was proposed. They also concluded that the variability in free end slip was not as reliable as anchored end slip in predicting the transfer length (Marti-Vargas et al. 2007).

4.2.2. Testing Procedures

4.2.2.1 Overview

A test setup similar to the ECADA test was designed and fabricated to perform comparable bond stress distribution analyses for the transfer lengths of pretensioned concrete specimens. All testing was performed at the Donald G. Fears Structural Engineering Laboratory at the University of Oklahoma in Norman, Oklahoma. Figure 4.3 shows the overall setup at Fears Lab showing three frames with concrete specimens under prestress.

Figure 4.3: Overall bond testing setup

4.2.2.2 Specimen Parameters

The concrete specimens had a cross section of 4 in. by 4 in. with a concentrically located single prestressing strand. Five lengths were considered: 26 in., 30 in., 34 in., 38 in., and 42 in. in order to bracket the calculated transfer length of 35.1 in. using the ACI (2011) equation. All specimens were cast with a single 3.65 ft^3 batch of concrete and were kept under the same curing conditions. The prestressing strands used were ½ in. special, Grade 270 7-wire strands. The strands were surface clean with small amounts of rust on them, the same condition in which they were received. Table 4.1 shows the mix design that was used, Table 4.2 the fresh concrete properties, and Table 4.3 the strand properties. All strands were tensioned to 75% of their ultimate tensile strength or 202.5 ksi to follow typical bond testing procedures. Other values of prestress may need to be tested in the future, such as the 188 ksi used for the girders tested in this research program, but results of this testing could be extrapolated to other situations.

The mix design was developed to meet the Oklahoma Department of Transportation (ODOT) standards for bridge girder design (ODOT 2009). Table 4.4 outlines the specifications for the concrete mixture.

Table 4.1: Concrete Mix Design Used for Bond Pullout Tests

Material	Quantity
Cement (lb/yd^3)	900
Limestone (lb/yd^3)	1500
Sand (lb/yd^3)	1205
Water (lb/yd^3)	297
Water/Cement Ratio	0.33
Air Entraining Agent (fl oz/cwt)	1.0
High-Range Water-Reducer (fl oz/cwt)	3.8

Table 4.2: Fresh Properties of Concrete Used for Bond Pullout Tests

Property	Quantity
Ambient Temperature (°F)	55
Slump (in.)	8.0
Mix Temperature (°F)	65
Unit Weight (lb/ft^3)	148.6
Air Content (%)	5.5

Table 4.3: Properties of Prestressing Strand Used for Bond Pullout Tests

Property	Quantity
Diameter (in.)	0.52
Area (in^2)	0.1669
Tensile Strength (ksi)	270
Elastic Modulus (ksi)	28,600

Table 4.4: Concrete Specifications

Description	Standard	Mix Used
Class of Concrete	P	P
Minimum Cement Content (lb/yd^3)	564	900
Air Content (%)	5 ± 1.5	5.5
Water/Cement Ratio (lb/lb)	0.25-0.44	0.33
Slump* (in.)	3 ± 1	8.0
Minimum Compressive Strength at testing (psi)	4000	4150

*If using a high-range water-reducing admixture, limit the slump to a maximum of 9 in.

4.2.2.3 Testing Equipment

Steel frames were designed by the research team at OU and fabricated on site. The frames mimic the ECADA testing setup by Marti-Vargas and can be seen in Figure 4.4. Two 200 kip hydraulic jacks were used to tension and de-tension the strands in the arrangement shown in Figures 4.5 and 4.6.

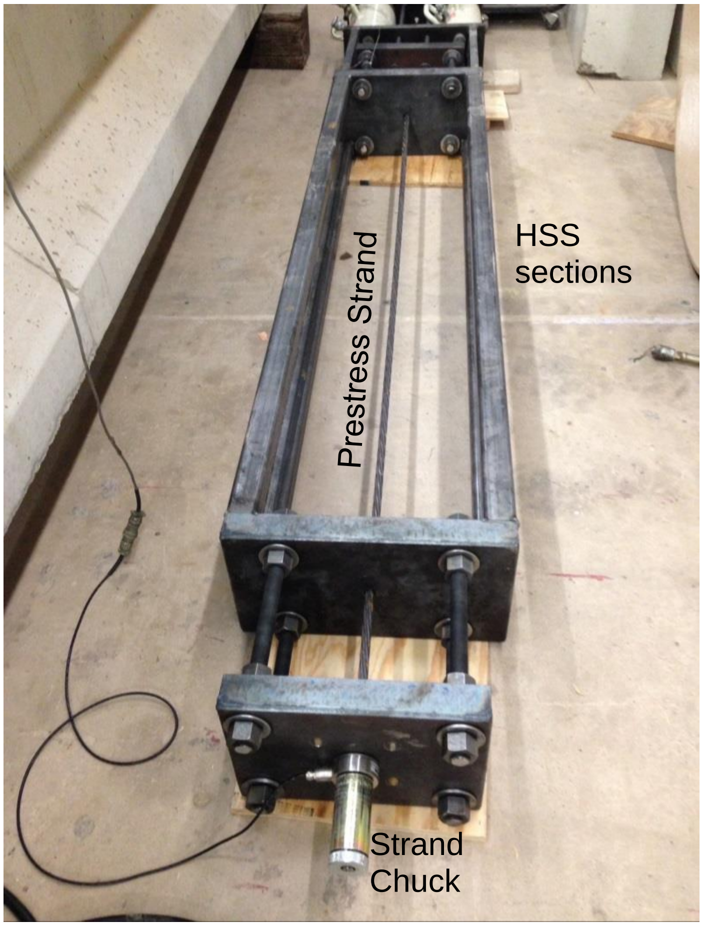

Figure 4.4: Basic bond testing frame arrangement

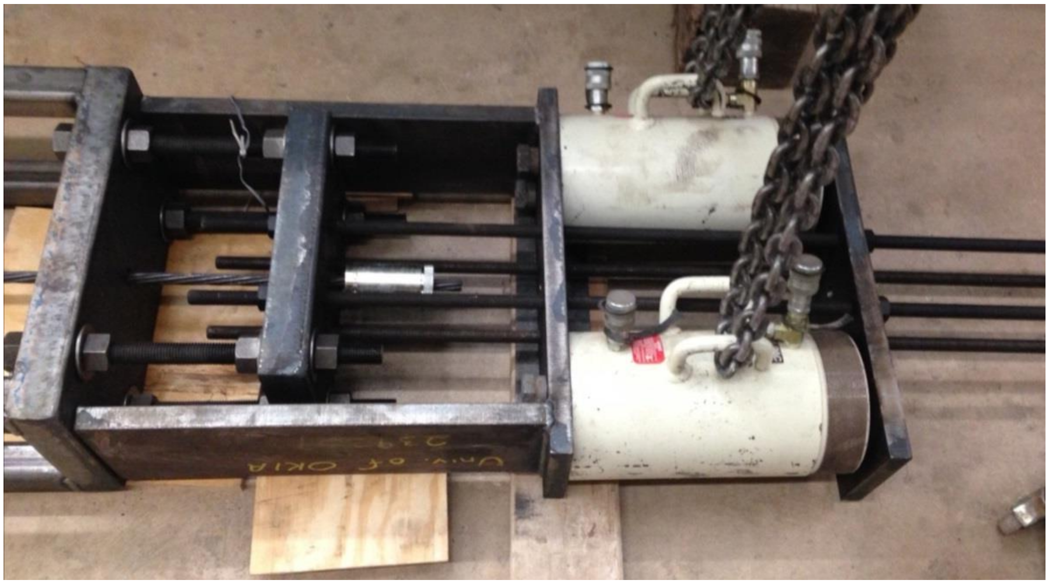

Figure 4.5: Ram assembly attachment

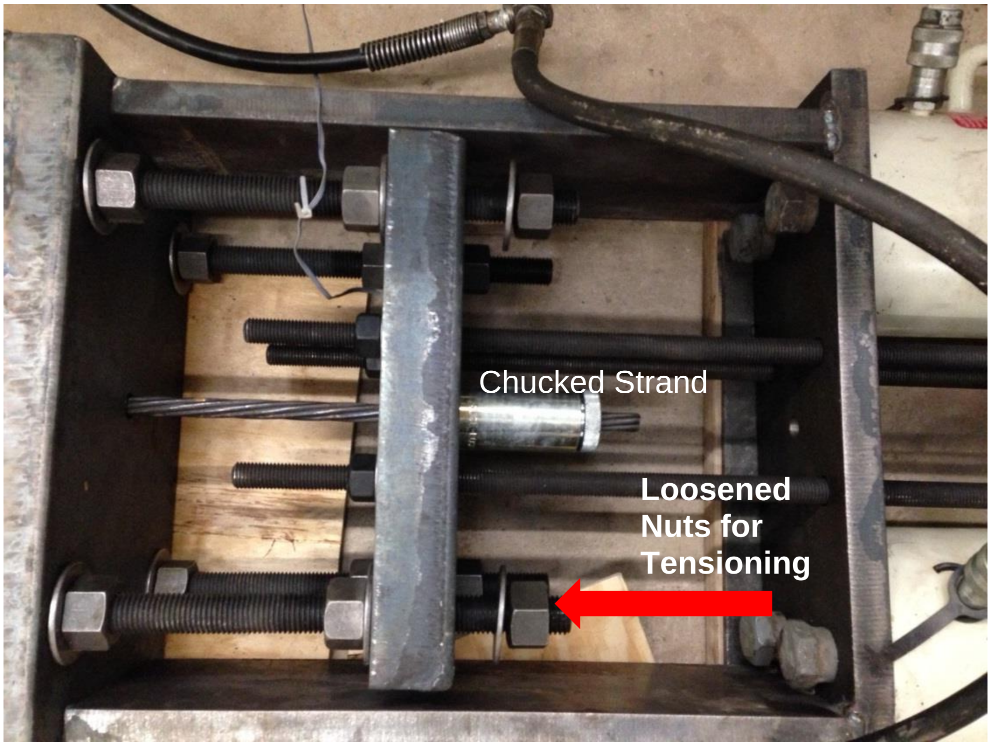

Figure 4.6: Ram assembly end strand connection

Formwork was built for the cross sectional dimensions (4 in. by 4 in.) with an end spacer to adjust for different specimen lengths. All five specimens were cast simultaneously with the same batch of concrete to reduce the variability in the testing. The arrangement of the formwork in one of the testing frames is shown in Figures 4.7 and 4.8. Once the formwork was completed, the testing procedure continued as follows:

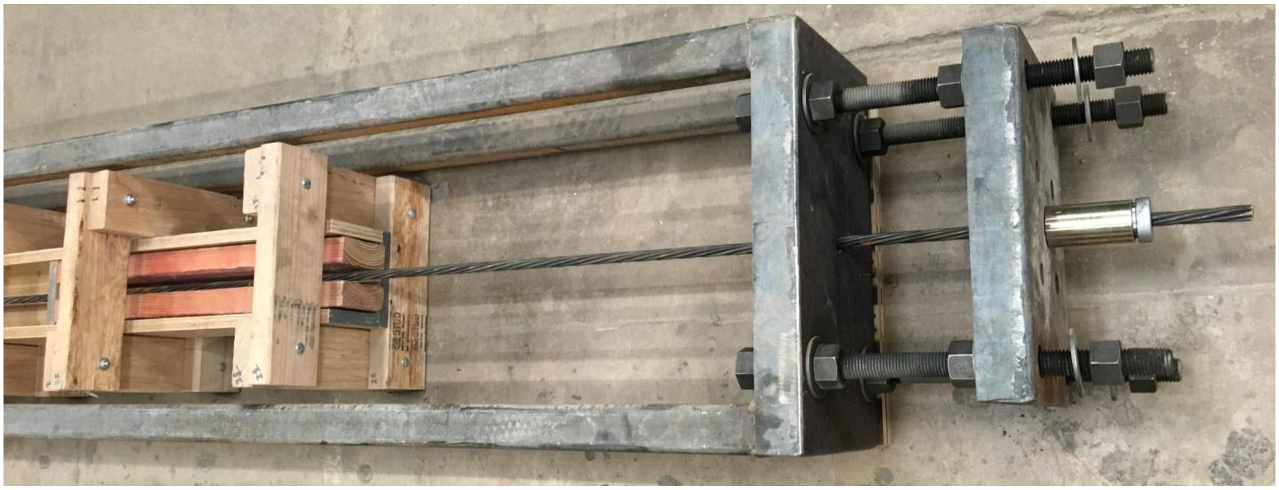

Figure 4.7: Free end of testing setup

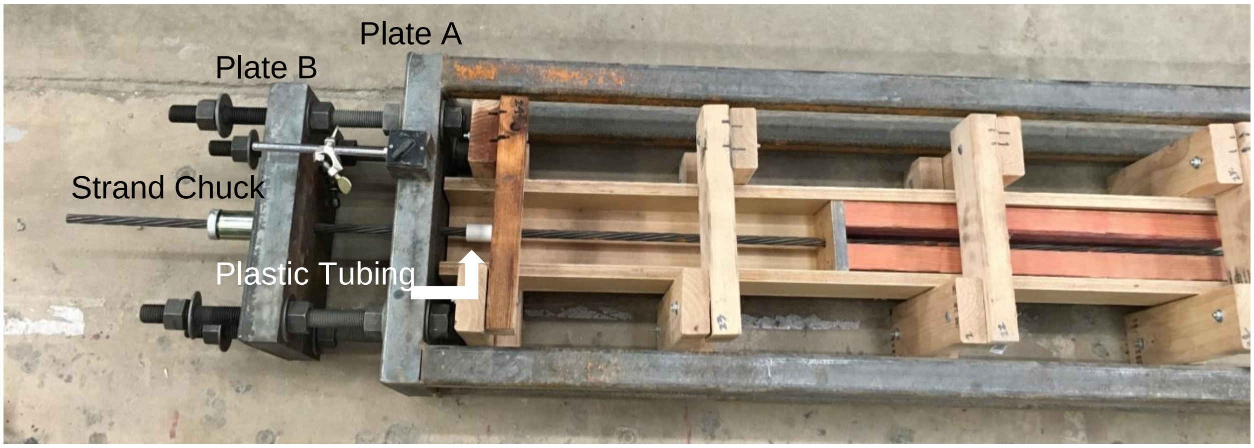

Figure 4.8: Anchored end of testing setup

1. Insert specimen formwork in frame and line up using spacers
2. Cut 0.5 in. special strand to 9 ft and insert through center of plates “A” and “B” on both ends of the frame, chucking the strand on the outside of both “B” plates
3. Include 2 in. plastic tubing around strand on anchored end of specimen as a bond breaker.
4. Place load cell on ram assembly to measure hydraulic ram loading (Figure 4.9)
5. Add protective barrier above frame for safety precaution during tensioning (Figure 4.10)

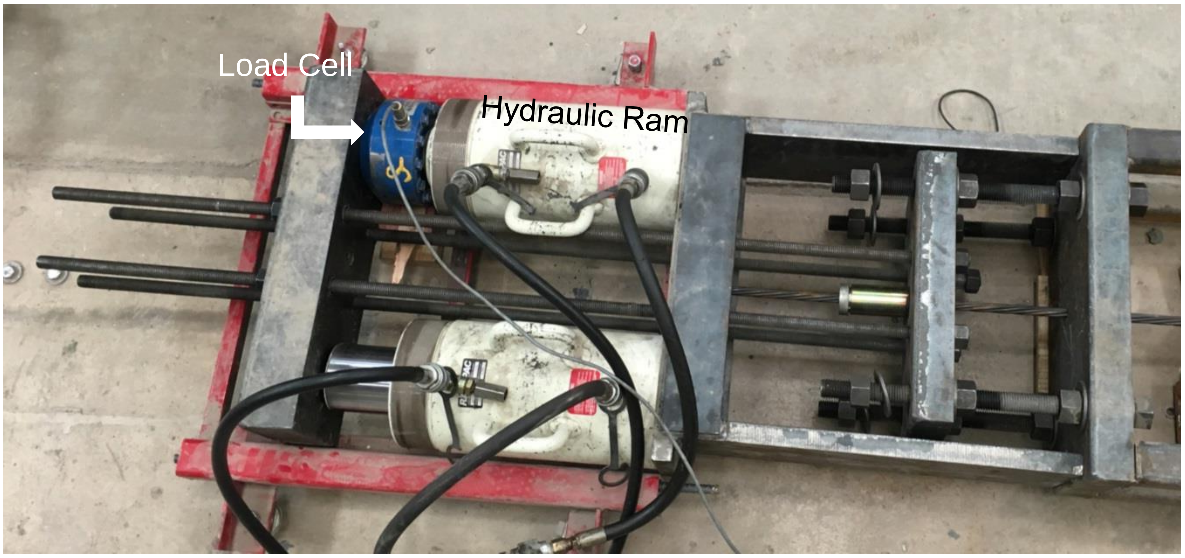

Figure 4.9: Ram assembly with load cell

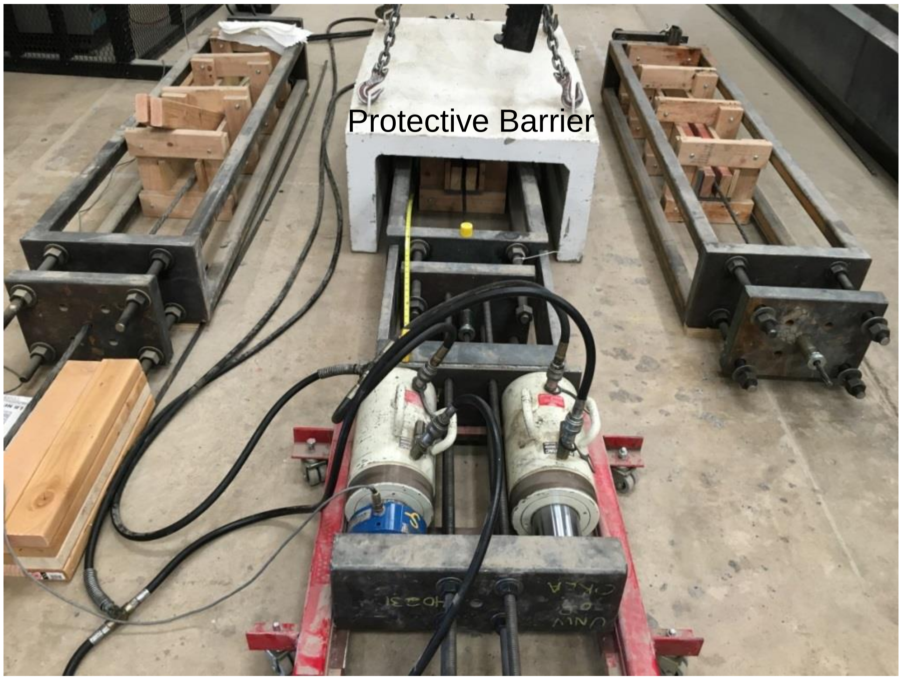

Figure 4.10: Testing setup with protective barrier ready for tensioning

6. Tension strand to 210 kips and hand tighten bolts on the inside of tensioning plate “B,” so to hold the tensioned strand in place. This way, when the bolts are tightened, the strand will return to roughly 202.5 ksi.
7. Cast specimens
    a. Perform slump and air content tests according to ASTM C143 and C231 respectively
    b. Cast cylinders according to ASTM C31 to determine compressive strength
    c. Use vibrator to consolidate concrete
    d. Trowel top of specimens
    e. Cover all specimens with tarp and store in dry, warehouse conditions (ambient temperature 55 °F, fresh concrete temperature 65 °F)

A completed specimen is shown in Figure 4.11.

Figure 4.11: Completed casting of bond specimen

4.2.2.4 Instrumentation and Data Collection

A load cell was used to verify the force applied by one of the hydraulic jacks. Two linear variable differential transducers (LVDTs) were used for each specimen to measure the strand end slip at both the anchored and free ends of the specimens for a total of ten. No internal measuring devices were used in order to leave bond between the concrete and the steel strand undisturbed. All instruments were monitored by a single data acquisition system throughout testing

The LVDTs were set up using either a wood framework or a magnetic stand attached to the load frame so that the LVDT would be just touching a Plexiglas plate attached to a steel block clamp placed on the strand at both the free (Figure 4.12) and anchored ends (Figure 4.13). All LVDTs were arranged so that they would extend as the strand slipped into the specimens, therefore they began at a retracted position within their range.

Figure 4.12: LVDT setup on free end of specimen

Figure 4.13: LVDT setup on anchored end of specimen

The procedure for de-tensioning and data collection was as follows:

1. The LVDTs were set at a sampling rate of 5 Hz during the de-tensioning process
2. The bolts that held were loosened behind plate “B,” so when the hydraulic rams were retracted the plate would move to release the tension in the strand
3. Once the de-tensioning was completed for all 5 frames, the sampling rate of the LVDTs was set at 1 Hz for 24 hours after de-tensioning
4. Measurements were then taken once a day for the next three days, therefore obtaining data for 4 days after de-tensioning

4.2.3. Bond Testing Results

No visible cracks were seen on the specimens throughout the testing process. The parameters considered when plotting the data for the LVDTs were primarily end slip versus stress during de-tensioning, end slip versus time, and end slip versus specimen length. The “free end” of the specimen is defined as the end where the prestress was released. This end of the strand is “free” to slip into the concrete after the tension is released. The “anchored end” or “embedded end” of the specimen is defined as the side that backs up to the plate in the frame. This end of the specimen mimics the embedment length that would be capable of maintaining a bond between the concrete and prestressing strand in larger concrete specimens. When using data from the LVDTs, both the free end and anchored end slips were considered separately and also summed together to see the total slip through the specimen. All data was plotted for each frame. The frames correspond to the different specimen lengths given in Table 4.3.

Plots of free end and embedded end slip versus the stress in the strand were completed for each frame and can be seen in Figure 4.14. The positive and negative values can be seen as absolute values for the amount of slip into the concrete.

From these plots, a general trend of increased slip as the strand stress decreased can be seen. The small jumps in slip, particularly for the free end, could be due to the coarseness of the sand and rock in the concrete catching the strand at an irregular way or small cracks around the strand opening up to enable the strand to slip through. The trend shows a non-smooth relationship between the reduction of stress in a strand and its ability to slip into the concrete. The embedded end shows significantly less slip, which is due to the bonding between the strand and the concrete throughout the specimen length. Table 4.4 shows the highest values for slip during de-tensioning for each of the specimens in inches.

Table 4.5: Specimen Lengths for each Frame

Frame Number	Specimen Length (in.)
1	42
2	38
3	34
4	30
5	26

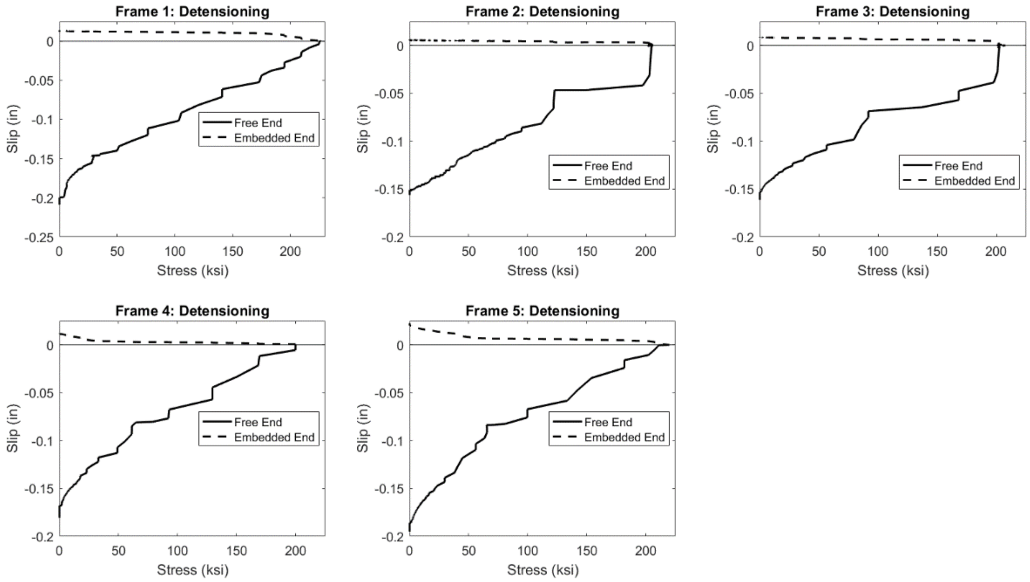

Figure 4.14: End slip versus stress for each bond pullout specimens

Table 4.6: Maximum Strand End Slip During De-Tensioning

Specimen	Anchored (in.)	Free (in.)	Total (in.)
Frame 1 (42 in.)	0.0029	0.1997	0.2026
Frame 2 (38 in.)	0.0042	0.1434	0.1476
Frame 3 (34 in.)	0.0013	0.1391	0.1404
Frame 4 (30 in.)	0.0631	0.1831	0.2462
Frame 5 (26 in.)	0.0182	0.1829	0.2011

Additionally, Figure 4.15 shows a comparison of the end slip (free, anchored and both ends) versus the different specimen lengths during the de-tensioning.

These comparisons show that there was a much higher slip on the free end of the specimens compared to the embedded end. The 30 in. specimen showed a higher slip than the 26-in. specimen, which could be a discrepancy due to variation in the slip measurements for either one or both of these specimen lengths. The general trends of the slip measurements, however, can still be observed. For the embedded end, there was a significant amount of slip for the shortest two specimens of 26 and 30 in., but nearly no slip for the longer three specimens. Therefore, the longer three specimens likely were longer than the embedment length required to sufficiently create a bond between the prestress strand and the concrete. Additionally, it is likely that the actual transfer length for these specimens was between 30 and 34 in. Because only five data points were taken for comparison, more specimen lengths would need to be tested to create a complete depiction of the embedment length and how it corresponds to slip. For the free ends of the specimens, there is an overall similar amount of slip, which seems reasonable, for these ends of the specimens are all presumably equally capable of slipping into the specimens during release. The smaller specimen lengths, however, should have slipped all the way through the specimen because of the lack of complete

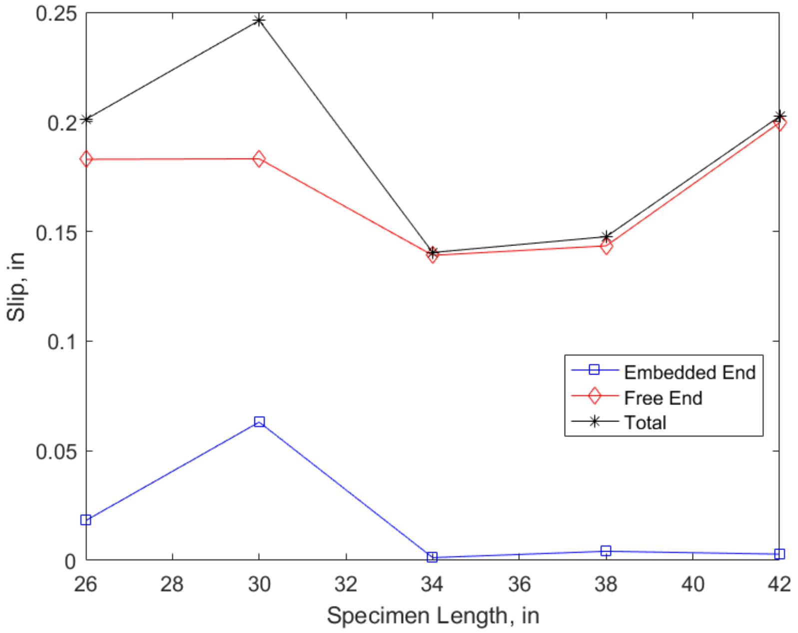

Figure 4.15: De-tensioning slip versus specimen length

transfer length (and subsequent bonding between the concrete and prestressing strand), therefore increasing the free end slip. This trend was not seen as clearly in the data.

After the strands were de-tensioned, the rate of measurements was changed to 1 Hz. These measurements continued for 24 hours and plots of this data for each frame can be seen in Figure 4.16 as slip in in. versus time.

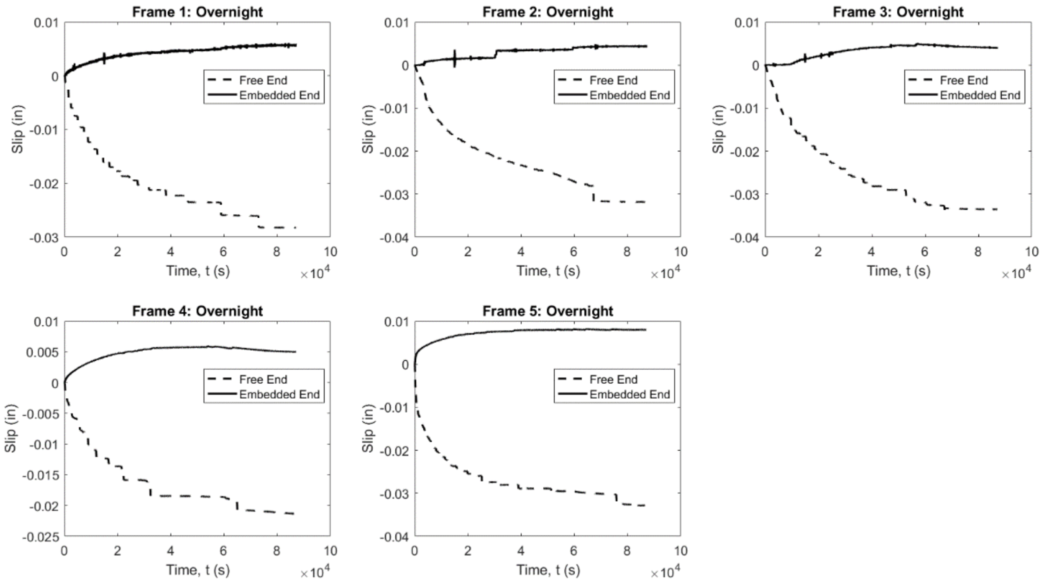

Figure 4.16: Slip versus time overnight after de-tensioning

These plots show that a significant amount of slipping occurs during the first 24 hours after de-tensioning. The maximum measurement for end slip was taken 24 hours after de-tensioning (the maximum value after 1 day), as well as 2 days and 4 days after de-tensioning. Table 4.5 shows these end slip values in in. for the free end, anchored end, and overall slip for each of the specimen lengths. The maximum end slip (free, anchored and both ends) in in. versus the different specimen lengths after 1 day and 4 days can be seen in Figures 4.17 and 4.18.

In both the 1-day and 4-day plots for the different specimen lengths, a similar trend can be seen. Like during the de-tensioning, the embedded end of the specimens 34 in. and longer have nearly no end slip, reiterating the assumption that the transfer length is most likely between 30 and 34 in. Also, like in the de-tensioning data, the free end of the specimens show significantly more end slip than the embedded ends, but without much of a trend between the different specimen lengths. The free end slip is very similar between all of the specimens.

Table 4.7: Maximum end slip measurements for time intervals

Specimen	Time Increment	Anchored (in.)	Free (in.)	Total (in.)
Frame 1 (42 in.)	De-tensioning	0.0029	0.1997	0.2026
	1-day	0.0089	0.2279	0.2368
	2-day	0.0091	0.2307	0.2398
	4-day	0.0092	0.2307	0.2399
Frame 2 (38 in.)	De-tensioning	0.0042	0.1434	0.1476
	1-day	0.0086	0.1753	0.1839
	2-day	0.0094	0.1768	0.1862
	4-day	0.0091	0.1767	0.1858
Frame 3 (34 in.)	De-tensioning	0.0013	0.1391	0.1404
	1-day	0.0052	0.1726	0.1778
	2-day	0.0075	0.178	0.1855
	4-day	0.0074	0.1847	0.1921
Frame 4 (30 in.)	De-tensioning	0.0631	0.1831	0.2462
	1-day	0.058	0.2045	0.2625
	2-day	0.0572	0.208	0.2652
	4-day	0.0567	0.2114	0.2681
Frame 5 (26 in.)	De-tensioning	0.0182	0.1829	0.2011
	1-day	0.0263	0.2159	0.2422
	2-day	0.027	0.2184	0.2454
	4-day	0.0274	0.2195	0.2469

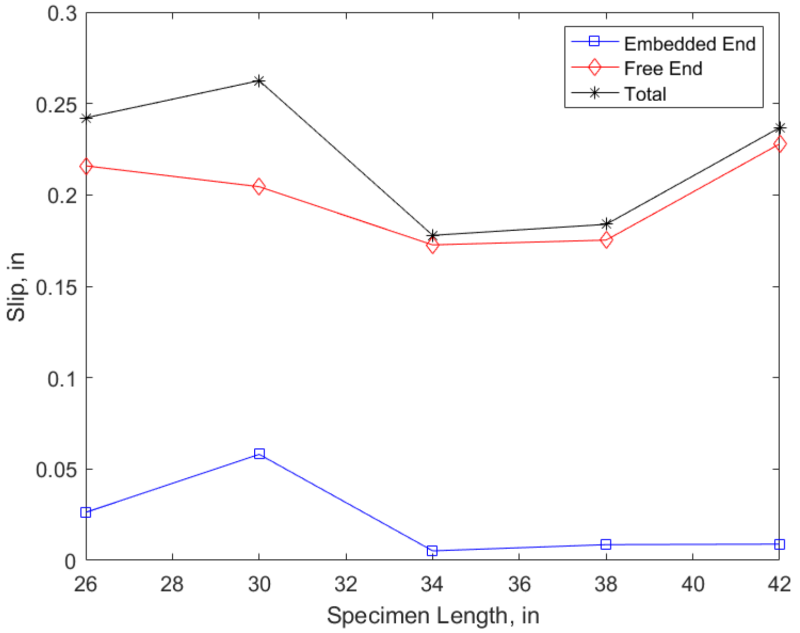

Figure 4.17: Maximum end slip versus specimen length after 1 day

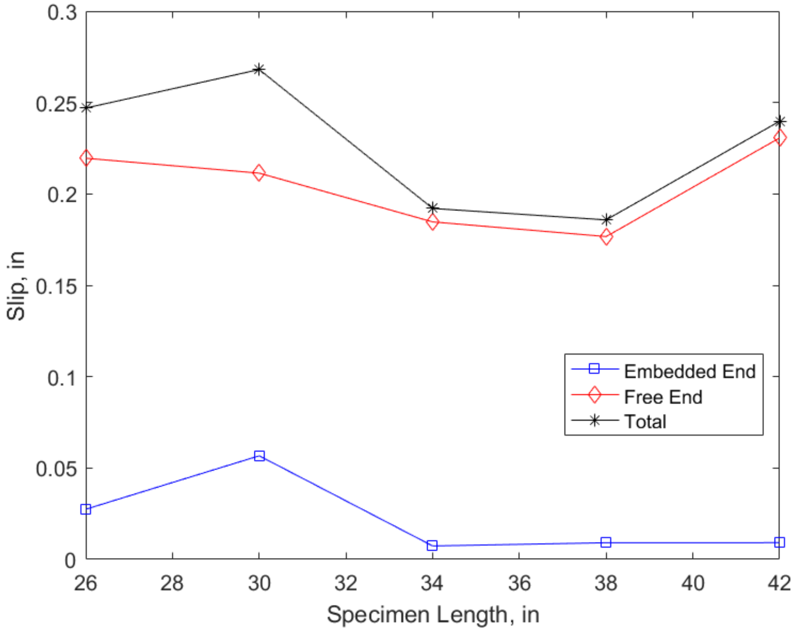

Figure 4.18: Maximum end slip versus specimen length after 4 days

Overall, a trend can be seen when comparing the embedded end slip versus specimen lengths that generally assumes that the transfer length of these specimens is between 30 and 34 in. The previously calculated transfer length from the ACI equation of 35.1 in. compares closely with the results of this study, which supports the methodology used in this project. While the estimated transfer length is between 30 and 34 in., inaccuracies in measuring the actual effective stress in the strand could have caused the calculated transfer length to be slightly higher. A calculated transfer length of 35.1 inches, however, is not far out of the range of 30-34 in. and an increased number of specimen lengths would aid in creating a more accurate depiction of the transfer length determined from this study.

The free end slip was not as useful in assessing the transfer length in this study, showing no obvious trend between the different specimen lengths. Determining the length in which the anchored end slip was insignificant when comparing end slip versus specimen lengths was the most valuable comparison in estimating transfer length. Including data for the 24 hours after de-tensioning showed an increase in end slip over time overall, but not a significant change in end slip for the embedded end.

The testing methods used in this project showed results that are capable of providing consistent, useful data. The setup, instrumentation, and testing methods can be streamlined as a consistent way to continue testing bond stress in pretensioned concrete specimens by using end slip as a function of estimating the transfer length. Further tests on different concrete and strand parameters, as well as for different specimen lengths is recommended to make further conclusions on a proposed model for the bond stress distribution within the transfer length of prestressed concrete specimens.

4.5 Prediction of Time-Dependent Bond Transfer in Pretensioned Concrete Using Draw-In Data

4.5.1 Overview

Time evolution of prestress loss and bond transfer length holds vital information concerning long-term performance of pretensioned pretressed concrete. To extract this time-varying information, we propose to utilize long-term measurements of strand draw-in, which could be more effectively obtained than concrete or strand surface strain measurements. Theoretical investigations combined with numerical studies of experimental data are carried out for this purpose. This study builds on a boundary value problem (BVP) model which quantifies draw-in for instantaneous elastic response. A one-dimensional linear viscoelastic standard solid model is employed to model the creep of concrete, which is a simple but effective model of the time-dependent response of pretensioned concrete. Guyon's BVP model is generalized to include time dependence and then combined with an existing initial value problem (IVP) model for post-tensioned concrete leading to a new mixed model for time-dependent prestress loss and bond transfer in pretensioned concrete.

Analysis was undertaken in this study to (i) quantify long-term prestress loss and bond-transfer behaviors by applying the proposed model and directly utilizing measured draw-in time history data, (ii) validate the proposed quantitative analysis by using scaled pretensioned concrete beams with different types of aggregates and strengths of concrete - among others factors, and (iii) offer discussion of future work. For example, introducing concrete drying shrinkage into the proposed model seems promising and is necessary to provide an improved representation of the time-dependent behavior of prestressed concrete.

4.5.2 Motivations and technical challenges

Long-term performance of pretensioned concrete has been an active area as large numbers of pretensioned concrete bridge girders were used in construction in the fifties and sixties of the last century and have been reported to experience some aging-related issues. On one hand, prestress loss with time directly concerns the remaining load carrying capacity of pretensioned concrete - just as in post-tensioned concrete. On the other hand, bond transfer behavior is different for pretensioned concrete, when the prestressing force is not fully established within the so-called bond transfer zone, a region from a free end up to transfer length of a pretensioned concrete beam where the effective prestress increases from zero at the free end to the full effective prestress at the end of the transfer length. There are two transfer zones for each strand in a beam, one at each end. For example, the section shear capacity contribution provided by the effective prestress force within transfer zone is location-dependent, increasing from zero at the free end to the full amount at the immediate transfer length. Assessing actual shear capacity of pretensioned concrete girders designed according to the quarter-point rule specified by previous versions of the AASHTO Bridge Design Specifications AASHTO Standard Specifications (1973) and after decades in service motivates us (Pei et al. 2008; Martin et al. 2011) to examine whether and how transfer length would change with time and consequently, whether and how the section properties would vary with time for a more robust long-term performance evaluation of an entire girder. Bond transfer, which is vital to pretensioned concrete, needs to be thoroughly and carefully considered in both design and analysis because bond transfer directly affects service stresses and all section capacities directly associated with prestressing force.

The goal of the study described in this section was to understand and exploit time history of draw-in as a means to infer prestress loss and transfer length as functions of time. To do so, we need various properties of the concrete and strand, such as (perhaps) concrete surface strain time histories. As strand draw-in is a quantity that can be more conveniently measured than other quantities (i.e., strand strain, concrete surface strain). We contemplate the following questions:

1. Is draw-in a function of time?
2. Why is draw-in a function of time?
3. How does draw-in vary in time?
4. Is transfer length a function of time?
5. Why is transfer length a function of time?
6. How does transfer length vary in time?
7. How does strand force vary in time?

Studying time-dependent behavior of bond-transfer is considered rational according to pp. 191 in Guyon (1953) Chapter VII, which reads: “When the wires are released from their temporary anchorages the force to be anchored is equal to the total tension in the wires at that moment less a certain component due to the instantaneous shortening of the concrete. Later the stress in the wires in the body of the beam (i.e., outside the anchorage zones) decreases owing to the delayed strains of concrete; the magnitude of the force anchored by bond adhesion therefore decreases.”

4.5.3 Intended contributions

In addition to Guyon (1953), a report by Fédération International de la Précontrainte (FIP) (1982) is another source for mathematical modeling of bond transfer in pretensioned concrete. Other relevant publications include Balázs (1993); Baxi (2005); Oh et al. (2006); Ayoub and Filippou (2010); Beńıtz and Gálvez (2011); Geßner and Henne (2016).

The first time derivative is necessary to capture the well-established phenomenon of concrete creep and to utilize time-dependent draw-in data. Indentations on the strand and their period have a large effect on the bond (Benítz and Gálvez 2011), which is known to affect λ (the characteristic length of elastic anchorage) and, hence, draw-in. In this sense, we implicitly treat surface roughness of the strand.

We also intend to demonstrate the power of even a simple linear time-dependent model in the process of understanding time-dependent behavior of prestressed concrete. Nonetheless, more complicated and advanced creep models can be considered in future work.

4.5.4 Structure of this Section

After introducing the motivation of this study in Section 4.5.1, we specify our intended technical contributions in Section 4.5.2. Under literature review in Section 4.5.5, we first present the IVP method for modeling post-tensioned concrete before highlighting important concepts and formulas from Guyon (1953) based on Guyon's BVP formulation. Section 4.5.6 shares a physical insight into the proposed model. Key assumptions, problem formulas and governing equations are presented systematically in 4.5.6.2 by leveraging and integrating the two methods reviewed in Section 4.5.5. Section 4.5.6.3 outlines the data-based strategy, mostly because of the unmodeled error – concrete shrinkage – that is not insignificant, and for insights into the solution. Section 4.5.7 details all aspects involved in our numerical investigation of applying the proposed method to the data obtained from an experimental investigation that is used to validate the proposed model and data-based solution. Discussions for future work are given there as well. Conclusions are drawn in Section 4.5.8.

4.5.5 Literature Review

Prestress loss in post-tensioned concrete can be modelled by the following ordinary differential equation (ODE) Testa (1998):

$$\dot{P}(t) + \frac{1}{\eta}k_1 = \frac{k}{\eta}P_0\text{, where } k_1 = \frac{\frac{1}{A_CE_C}+\frac{l_{0S}}{l_0}\frac{k}{A_SE_{ps}}}{\frac{1}{A_CE_C}+\frac{l_{0S}}{l_0}\frac{k}{A_SE_{ps}}} \qquad (4.7)$$

The two parameters in the concrete standard solid model can be further understood as follows:

- How much of the prestressing force is going to be left depends on k
- How fast the prestressing force decays depends on η

To solve this ODE, we need IC, which is $P(0) = P_0$. The solution to the ODE is:

$$P(t) = P_0\left[\left(1 - \frac{k}{k_1}\right)e^{-k_1\frac{t}{\eta}} + \frac{k}{k_1}\right] \tag{4.8}$$

Using Guyon's Figure 13 (now in Figure 4.19), the displacements at each end of an infinitesimal element are defined before "the total strain" is obtained. In this figure dashed lines indicate the original shape and dotted lines the deflected shape.

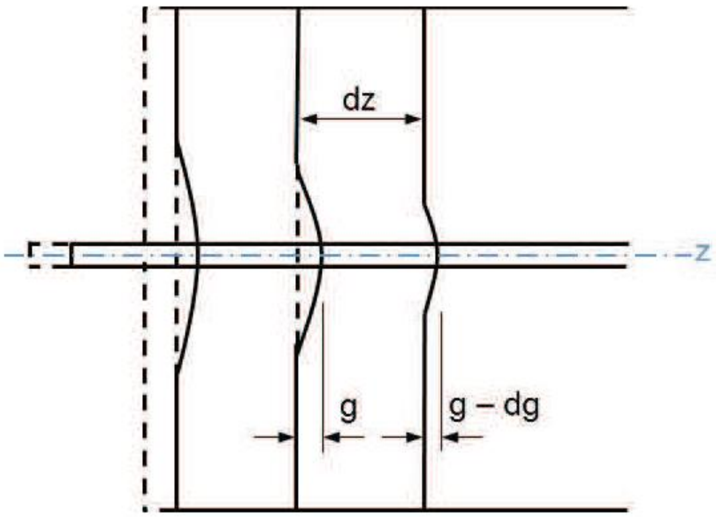

Figure 4.19: Following Figs. 11 and 13 in Chapter VII of Guyon (1953) but with a minor correction on both the concrete and strand ends.

Then, Hooke's law is applied to connect the total strain to the stress, from which an ODE is finally obtained to solve the wire stress *f* in §5 of Guyon (1953):

$$\frac{\frac{A_s f}{E_c A_c}dz + dg}{dz} = \frac{f_{si} - f}{E_{ps}} \tag{4.9}$$

$$f = \frac{f_{si}}{1+mp} - \frac{E_{ps}}{1+mp}\cdot\frac{dg}{dz} \tag{4.10}$$

where $\frac{E_{ps}}{E_c} \triangleq m$ and $\frac{A_s}{A_c} \triangleq p$. Eq. (4.10) captures the stress-strain behavior of the strand as a function of z (a coordinate along the strand), which is an important equation used again in §5 of Guyon (1953).

There are four types of bond: elastic, elastic-plastic, plastic, and friction bonds. For elastic bond, we have:

$$f = f_M\left(1 - e^{-\frac{z}{\lambda}}\right) \tag{4.11}$$

where $f_M = \frac{f_i}{1+mp}$. The bond is entirely elastic and the tension in the wire therefore varies according to an exponential law throughout. In addition,

$$\lambda = \frac{E_{ps}}{f_{si}} g_0 \qquad (4.12)$$

where λ, f_{si}, and g_0 are the characteristic length (about one-third of the transfer length according to pp.196 of Guyon (1953)), initial stress, and draw-in. The stress in the wire at any point within the anchorage is given by: $f = 0.95 f_M$ by substituting $z = 3\lambda$ into Eq. 4.11, which means that "the anchorage is effectively complete" over a total of length of 3λ.

4.5.6 1D Modeling with IVP and BVP

4.5.6.1 Conceptual overview

We extend Eq. (4.9), the key deformation compatibility equation in Guyon (1953) from $t = 0$ to $t > 0$. To do so, we have the following composition for the draw-in as a function of time:

draw-in variation in time = a contribution from strand relaxation
− a reduction from concrete creep accumulated over transfer zone

where the creep of concrete will be evaluated using the standard solid model mentioned above.

We will also extend Eq. (4.12) on p. 195 in Guyon (1953) to the time beyond $t = 0$. The measured draw-in time history can be scaled up and used as an approximated $\lambda(t)$, the characteristic length time history.

4.5.6.2 Problem formulation

Key assumptions made in this study are as follows:

i. 1-D analysis only: We look into a zone characterized by z, which goes along a strand and the concrete bonded in its vicinity.

ii. No drying shrinkage of concrete considered: This introduces an inherently unmodeled error.

iii. A perfectly bonded core in the mid-section of a beam: This core is equivalent to a post-tensioned concrete beam.

iv. No plastic/friction bond considered: An exponential stress distribution for elastic bond is considered for both strand and concrete at any time instance.

We would like to highlight Item (iii). Eq. (4.7) on post-tensioned concrete is entirely applicable to the core (where the bond stress is zero) of the same prestressed concrete but made of pretensioning. Quick reasoning can be drawn from the St.

Venant's principle: For a self-equilibrating system, the stress status would be the same except for the ends.

For this 1-D problem involving both IVP and BVP, key aspects are examined as follows:

a) Force equilibrium: This holds when there is no inertial effect.

b) Compatibility equation via strand strain: See the following equations.

c) Constitutive relations: While the strand is linear elastic, the concrete is linear viscoelastic. Specifically, a standard solid model is adopted as mentioned previously. Stress-strain behavior of each material is assumed to be uniaxial, considering normal stresses only.

d) Initial condition: At $t = 0$, strand and concrete stress, and $g(z, 0)$ are as derived in Chapter VII of Guyon (1953).

e) Boundary conditions: At $z = 0$ is a free end of the strand where $g(0, t)$ is measured draw-in. This would be the focus of our study due to the motivation of utilizing and exploiting draw-in measurements. For $z \geq x(t)$, $g(x, t) = 0$ due to perfect bonded. This should be automatically satisfied from the adoption of the post-tensioned concrete model for the perfectly bond core.

To proceed, we may start with the deformation compatibility equation, Eq. (4.9), from Guyon (1953) (after correcting the sign of the first term according to pp. 189):

$$-\frac{dg}{dz} + \frac{A_s f}{A_c E_c} = \frac{f_{si} - f}{E_{ps}} \tag{4.13}$$

which can be extended to consider time due to concrete creep:

$$-\frac{\partial g(z,t)}{\partial z} + \varepsilon_c(z, t) = \frac{P_i - P(z,t)}{A_s E_{ps}} \tag{4.14}$$

Integrating this differential equation from a free end to transfer length leads to the following equation:

$$-\int_0^{x(t)} \frac{\partial g(z,t)}{\partial z} dz + \int_0^{x(t)} \varepsilon_c(z, t) dz = \int_0^{x(t)} \left[\frac{P_i - P(z,t)}{A_s E_{ps}}\right] dz \tag{4.15}$$

where $x(t)$ represents transfer length. We have:

$$-\int_0^{x(t)} \frac{\partial g(z,t)}{\partial z} dz = \underbrace{g(0, t)}_{draw-in} - \underbrace{g(x, t)}_{no\ relative\ motion\ between\ strand\ and\ concrete} \tag{4.16}$$

Quantitatively, the draw-in $g(0, t)$ is as follows bearing in mind that $x(t)$ is targeted:

$$\underbrace{g(0,t)}_{draw-in} = \underbrace{\int_0^{x(t)} \left[\frac{P_i - P(z,t)}{A_s E_s}\right] dz}_{from\ strand\ relaxation} - \underbrace{\int_0^{x(t)} \varepsilon_c(z,t) dz}_{from\ concrete\ creep} \tag{4.17}$$

It is assumed that $P(z,t)$ is expressed as follows based on the post-tensioned case and the formula for $t = 0$:

$$P(z,t) = \underbrace{P_0\left[\left(1 - \frac{k}{k_1}\right)e^{-\frac{k_1}{\eta}t} + \frac{k}{k_1}\right]}_{mimicking\ f_M\ in\ Guyon\ (1953)} \ \ {}_{see\ pp.} \underbrace{\left(1 - e^{-\frac{z}{\lambda}}\right)}_{185\ in\ Guyon\ (1953)} \tag{4.18}$$

where we have

$$P_0 = \frac{P_i}{1+mp}, \text{ following Guyon (1953) p. 185: } f_M = \frac{f_{si}}{1+mp}, \text{ for } t = 0 \tag{4.19}$$

which indicates the inefficiency of pretensioned concrete).

The elastic deformation of concrete at $t = 0$ is given as:

$$\varepsilon_c(z,0) = \frac{A_s}{A_c}\frac{P(z,0)}{A_s E_c} = \frac{p}{A_s E_c} P(z,0) \tag{4.20}$$

while hereditary integral can be used to express the inelastic deformation of concrete at t ≥ 0 as follows:

$$\varepsilon_c(z,t) = \frac{p}{A_s}\left(\phi(t)P(z,0) + \int_0^t \phi(t-\xi)\frac{\partial P(z,\xi)}{\partial \xi} d\xi\right) \tag{4.21}$$

where the creep compliance for the standard solid model is given as follows:

$$\phi(t) = \frac{1}{kE_c}\left[1 + (k-1)e^{-\frac{k}{\eta}t}\right], k < 1 \tag{4.22}$$

$$\phi(t-\xi) = \frac{1}{kE_c}\left[1 + (k-1)e^{-\frac{k}{\eta}(t-\xi)}\right] \tag{4.23}$$

Also, we have:

$$P(z,\xi) = P_0\left[\left(1 - \frac{k}{k_1}\right)e^{-\frac{k_1}{\eta}\xi} + \frac{k}{k_1}\right]\left(1 - e^{-\frac{z}{\lambda(\xi)}}\right) \tag{4.24}$$

To reduce computational effort, an alternative form of Eq. (4.21) may be used after applying integration by parts:

$$\varepsilon_c(z,t) = \frac{p}{A_s}\left(\underbrace{\phi(0)}_{\frac{1}{E_c}} P(z,t) - \int_0^t \frac{\phi(t-\xi)}{\partial\xi} P(z,\xi)\, d\xi \right) \tag{4.25}$$

where

$$\frac{\phi(t-\xi)}{\partial\xi} = \frac{k-1}{\eta E_c} e^{-\frac{k}{\eta}(t-\xi)} \tag{4.26}$$

It can be seen that Eq. (4.20) is a special case of both Eq. (4.21) and (4.25) by taking $t = 0$.

4.5.6.3 Data-Based Solution Strategy

Our *data-based strategy* is to take Eq. (4.12) for granted. That is, we use the measured draw-in time history to estimate a λ time history. These λ values would be substituted into Eq. (4.18) until draw-in time history together with the movement time histories of both strand and concrete are estimated as in Eq. (4.27):

$$\underbrace{g(0,t)}_{draw-in} = \underbrace{\int_0^{\frac{L}{2}} \left[\frac{P_i - P(z,t)}{A_s E_{ps}}\right] dz}_{from\ strand\ relaxation} - \underbrace{\int_0^{\frac{L}{2}} \varepsilon_c(z,t) dz}_{from\ concrete\ creep} \tag{4.27}$$

which is equivalent to Eq. (4.17) with the advantage of bypassing the unknown $x(t)$. The estimated draw-in would be compared with measured draw-in; a normalized root-mean-squared (NRMS) error could be calculated as a measure to evaluate the performance of the model.

This data-based strategy is adopted for the rest of the paper because the unmodeled error would be first reflected in the NRMS error; pursuing the best fit of data without considering unmodeled error is not the goal. Computationally, the data-based strategy is more straightforward leading to a unique solution every time with simple coding.

4.5.7 Numerical Results

A brief description of test setup and procedure for the data required can be referred to Dang et al. (2016). Both unit weight (w_c) and concrete cylindrical compressive strength (f'_c) were obtained for each specimen in most cases. Range values are given in Table 4.8 for efficiency in presentation, while the individual values will be used in the analysis to be given herein.

Table 4.8: Ranges of w_c and f'_c values for the data used in this study.

Property	LWSCC 1-4	LWSCC 5	LWSCC 6-9	LWSCC 10-13	LWSCC 14-17	NWSCC 1-4	NWSCC 5-8
Nature	Clay	Shale	Shale	Clay	Shale	Limestone	Limestone
w_c (pcf)	114.0 - 119.9	118.0 – 120.3	116.4 – 122.3	117.9 – 122.4	116.3 – 123.0	144.2 – 146.8	147.0 – 148.3
f'_c	4900 –	4800 –	5800 –	6600 –	5800 –	6700 –	8800 –

Property	LWSCC 1-4	LWSCC 5	LWSCC 6-9	LWSCC 10-13	LWSCC 14-17	NWSCC 1-4	NWSCC 5-8
	7200	5200	7100	7900	8000	8000	9700

4.5.7.1 Section and materials properties

1. $A = 80.6\,in^2$, $A_s = 0.434\,in^2$. Thus we have: $A_c = A - A_s$.

2. It has been known that $E_{ps} = 28500\,ksi$, and $f_{si} = 202.5\,ksi$.
3. The ACI formula is used to estimate E_c, which can be replaced with actually measured values in the future:

$$E_c = 33 w_c^{1.5} \sqrt{f'_c} \tag{4.28}$$

where w_c is in the unit of pcf, and E_c and f'_c are in the unit of psi.

4. l_0 was recorded as 18 ft, however l_{0s} was not available. Nonetheless, we can obtain $\frac{l_{0s}}{l_0}$ from the standard solid model for concrete.

5. Regarding *k*: It comes from the standard solid model for concrete. Given its corresponding creep compliance function in Eq. (4.22), it can be seen that 1 k is equal to the ultimate creep coefficient defined as “the ratio of the creep strain to the initial strain” according to ACI 209.2R-08 pp. 5 out of 44. On p. 19 out of 44, “for the standard conditions, in the absence of specific creep data for local aggregates and conditions, the average value proposed for the ultimate creep coefficient ϕ_u is” 2.35, which was used in the first trial. Also, it points out on pp. 11 out of 44 that creep coefficient can vary from 1.2 to 9.2, which will be tested.

6. k_1 is calculated from Eq. (4.7) and affected by the value of k.

7. The values of η, strictly speaking, should come out of the creep time histories of all concrete used. By applying Eq. (4.22), it can be seen that the initial slope of a creep strain time history would be:

$$\frac{d\varepsilon}{dt}\Big|_{t=0} = \sigma_0 \frac{1-k}{\eta E_c} = \varepsilon_0 (1-k) \frac{1}{\eta} \tag{4.29}$$

from which the value of η could be estimated. However, the only available data is concrete surface strain data for LWSCC. Assuming the concrete at $z = 142.5\,cm$ is subject to a creep-like load (i.e., neglecting prestress loss) and $k = \frac{1}{2.35}$ for all, the values of η are estimated and summarized in Tables 4.9 and 4.10, which are rough values:

Table 4.9: Values of η (in the unit of day) for LWSCC 1-9 estimated by using the measured concrete

LWSCC-1	LWSCC-2	LWSCC-3	LWSCC-4	LWSCC-5	LWSCC-6	LWSCC-7	LWSCC-8	LWSCC-9
5.745	3.240	4.778	5.181	2.193	2.482	3.020	3.233	3.199

Table 4.10: Values of η (in the unit of day) for LWSCC 10-17 estimated by using the measured concrete

LWSCC-10	LWSCC-11	LWSCC-12	LWSCC-13	LWSCC-14	LWSCC-15	LWSCC-16	LWSCC-17
8.021	8.195	7.114	5.219	5.451	5.347	9.873	10.247

Since there are no concrete surface strain measurements for NWSCC, 5.267 days, the average value of η for LWSCC, will be adopted for all NWSCCs.

8. The “release” reading was taken immediately after the strand cutting process was complete. The “release” reading was the first strand slip reading. So, the time is reset to make this time instance $t = 0$ throughout.

4.5.7.2 Data-Based Estimation

To provide a convincing example for the proposed analysis, the prestress loss needs to be “predicted” first of all. See Figure 4.20.

Figures 4.21, 4.22, and 4.23 indicate that, even though the measured draw-in time histories come in different forms, the proposed method can (i) reproduce a draw-in time history that seems to be fairly similar to the measured one, and (ii) reproduce both strand and concrete movement time histories at the end that cannot be measured, but seem rational because their difference is reasonable compared to our measured values of end slip which would be a measure of the relative motion. Since the measured draw-in time histories are incomplete for LWSCC-3 and 4 by missing Day 3 data, their predictions are not available.

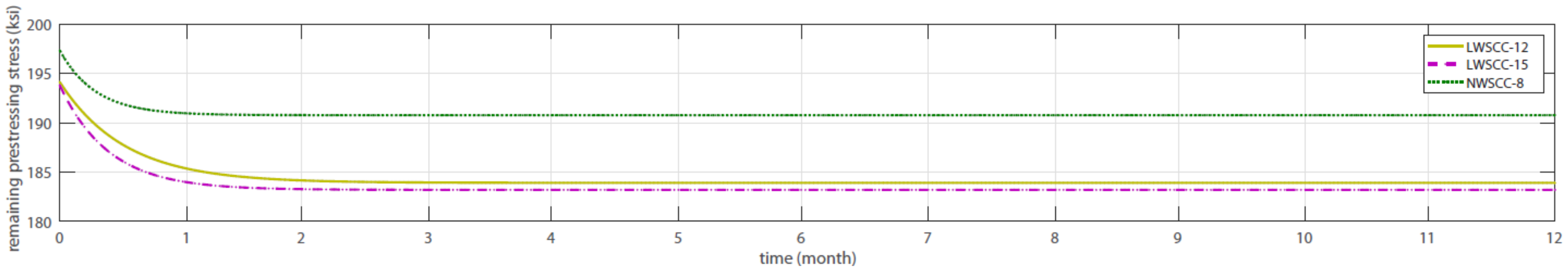

Figure 4.20: One-year prestressing loss of selected specimens by assuming the ultimate creep coefficient to be 2.35 and using the values for n in Table 2.

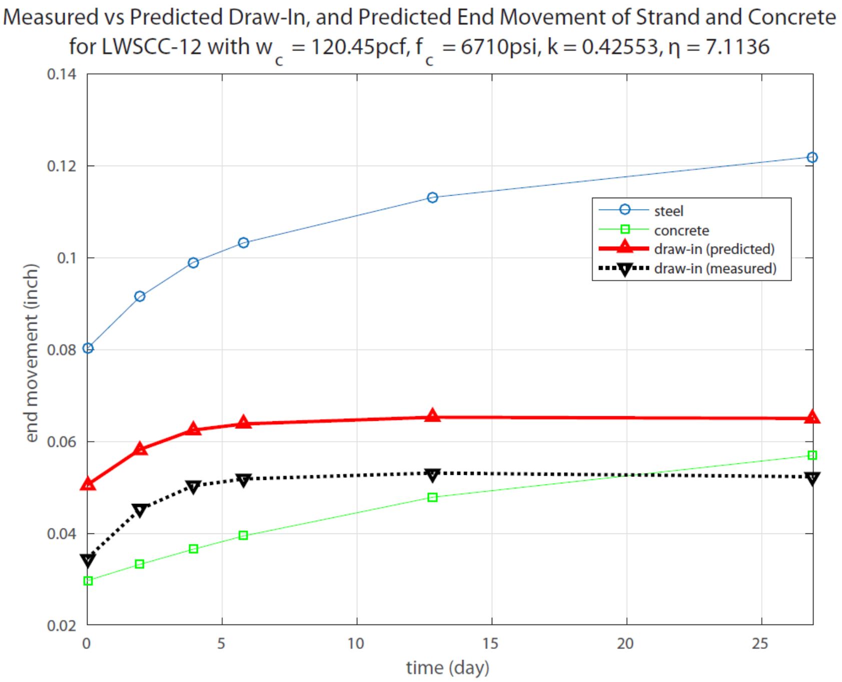

Figure 4.21: Measured vs. predicted draw-in, and predicted end movement of strand and concrete for LWSCC-12

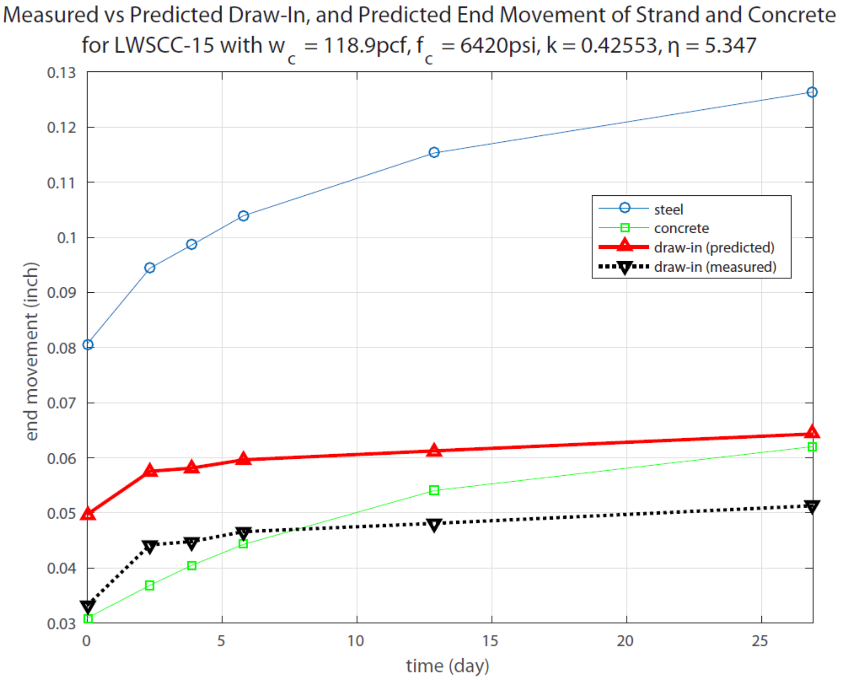

Figure 4.22: Measured vs. predicted draw-in, and predicted end movement of strand and concrete for LWSCC-15

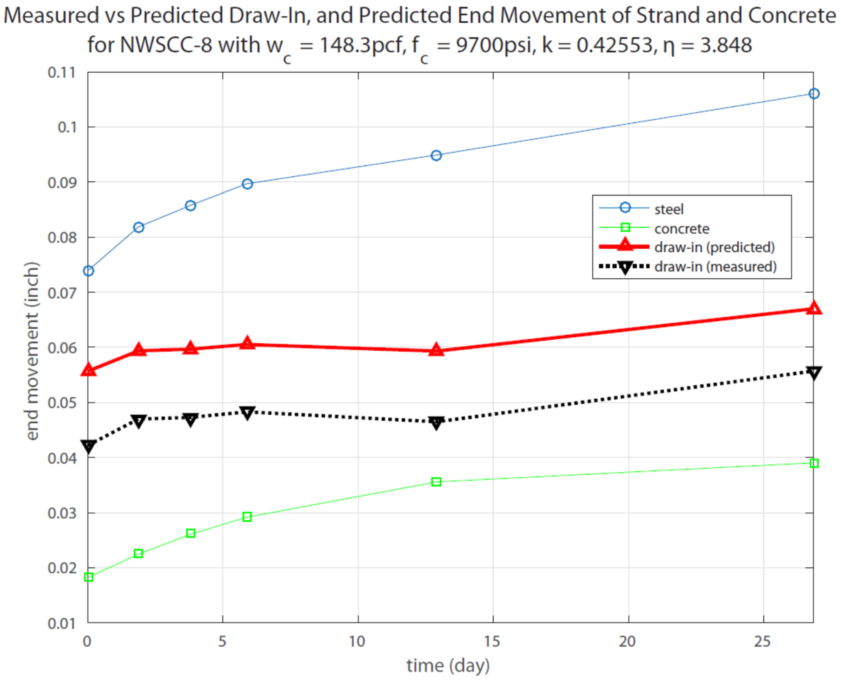

Figure 4.23: Measured vs. predicted draw-in, and predicted end movement of strand and concrete for NWSCC-8.

The estimated draw-in time histories are always over-predicting; the normalized root-mean-squared errors are summarized in Tables 4.11, 4.12, and 4.13 for LWSCC and NWSCC, respectively. These error values are nontrivial, however they are not abnormal for the well-known challenging problem of predicting time-dependent behaviors of concrete.

Table 4.11: Normalized root-mean-squared error in percentage for all LWSCC's with an average of 15.9%, where $k = \frac{1}{2.35}$ for all and η values follows Table 4.9.

ID	LWSCC-1	LWSCC-2	LWSCC-3	LWSCC-4	LWSCC-5	LWSCC-6	LWSCC-7	LWSCC-8	LWSCC-9
NRMS	27.3	15.0	NA	NA	11.2	10.7	10.1	9.9	11.0

Table 4.12: Normalized root-mean-squared error in percentage for LWSCC 10-17 with an average of 15.9%, where $k = \frac{1}{2.35}$ for all and η values follows Table 4.9.

ID	LWSCC-10	LWSCC-11	LWSCC-12	LWSCC-13	LWSCC-14	LWSCC-15	LWSCC-16	LWSCC-17
NRMS	18.3	22.4	14.5	16.7	18.9	15.8	15.6	20.5

Table 4.13: Normalized root-mean-squared error in percentage for all NWSCC's with an average of 12.1%, where $k = \frac{1}{2.35}$ and $\eta = 5.267$ for all.

ID	NWSCC-1	NWSCC-2	NWSCC-3	NWSCC-4	NWSCC-5	NWSCC-6	NWSCC-7	NWSCC-8
NRMS	14.0	18.0	11.2	2.1	12.4	9.0	15.6	13.8

The proposed method validates the suitability of applying Eq. (4.12) to arbitrary time (i.e., for inelastic deformation of concrete). Figure 4.24 typifies how this can be done: At t, an arbitrary time instance when we recorded draw-in, the value of z(t) can be conveniently obtained if we trace 95% of the maximum stress on the predicted stress distribution. This $z(t)$ can be considered as $x(t)$, the transfer length at t. Since we are concerned with limiting behavior, the maximum value of all x(t)'s is compared with three times of the maximum value of $x(t)$'s calculated from measured draw-in using Eq. (4.12). We use their ratio to quantify their difference.

This ratio is examined for all specimens whose predictions are available. This ratio turns out to be consistently small with a mean value of 1.0856 and 1.0247 for LWSCC and NWSCC, respectively. Even though the NRMS error for predicted draw-in is not insignificant, this ratio can be considered much less significant. We suspect that these approximate numbers could be applied in conjunction with Eq. (4.12) for a rough but quick estimate of the transfer length at a certain time instance in the field - whenever the draw-in measurement at the same time instance is available:

$$x(t) \approx 1.0856 \times 3 \times \frac{E_{ps}}{f_{si}} \times g(0,t), \text{ for NWSCC} \tag{4.30}$$

$$x(t) \approx 1.0247 \times 3 \times \frac{E_{ps}}{f_{si}} \times g(0,t), \text{ for LWSCC} \tag{4.31}$$

where the small ratios of 1.0856 and 1.0247 would be further validated for accuracy, and would be replaced with other properly obtained ratios for other types of concrete. The accuracy of this empirical approach for estimating transfer time would improve together with the analysis on drying shrinkage of concrete, the unmodeled error in this study.

The value of f_{si} = *202.5 ksi* is adopted in the above numerical results based on the actual initial stress in the strand. The Oklahoma Department of Transportation (ODOT) practice may prefer the value of f_{si} = *189 ksi* instead. The same numerical routine would be adopted to process the new data measurements to be collected in the future as a further validation of the proposed prediction method.

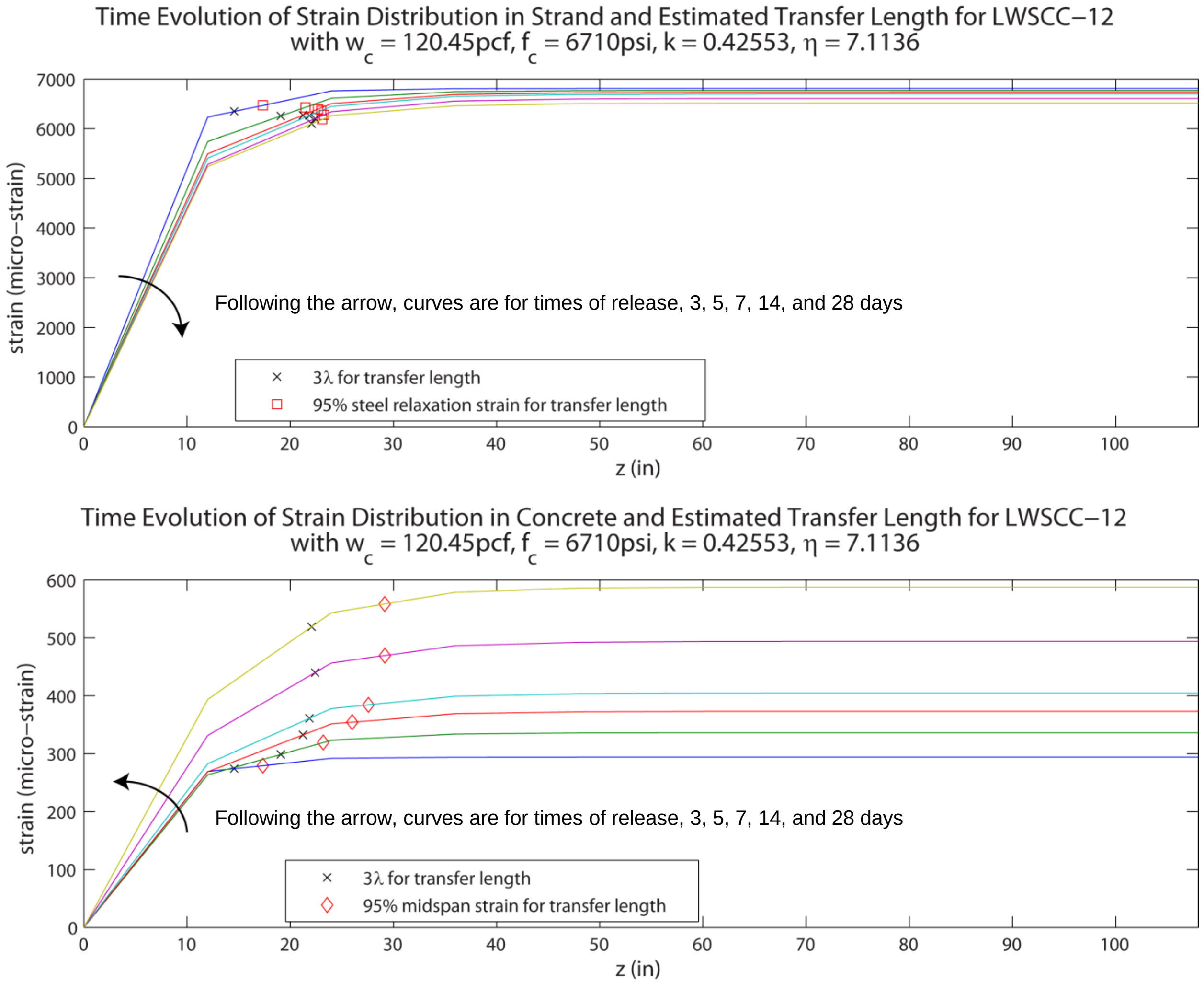

Figure 4.24: Time evolution of strain distribution for both stand and concrete and estimated transfer length in comparison with 3λ for LWSCC-12 with $w_c = 120.45\,pcf$, $f'_c = 6700\,psi$, $k = \frac{1}{2.35}$ and $\eta = 7.114\,day$. Only the left half is presented due to symmetry.

4.5.8 Summary

To predict time-dependent behaviors of pretensioned concrete, a simple yet effective 1-D model has been established by leveraging an existing IVP model for concrete creep and strand relaxation in post-tensioned concrete and Guyon's instantaneous elastic shortening analysis based on BVP. By directly utilizing draw-in time history measured from a pretensioned concrete beam and other section and material properties, many facets of bond-transfer behavior can be predicted revealing the insights into the time-dependent interaction of strand and concrete that would otherwise be obscure in current literature. Even though challenging, the proposed method has been validated to the best extent by utilizing a total of 17 lightweight and 8 normal weight scaled pretensioned concrete beams that were not designed to validate the proposed method per se. Drying shrinkage of concrete causes the most significant unmodeled error; the effect of which is discussed for future work. The principle and procedure of injecting draw-in time history measurement to time-dependent modeling of pretensioned concrete - as a critical piece of information - have been established in this study; the work enables feasible field implementation and practical application of this data-based method to clarify and explain actual bond transfer behavior critical to long-term performance of pretensioned concrete.

5. Backbone Analysis of Free Vibration Data

5.0 Nomenclature

$a(t)$	instantaneous amplitude of $x(t)$
j	imaginary unit
K	sampling rate (integer number of points per damped cycle)
N	number of points in test signal
$x(t)$	real signal
$\tilde{x}(t)$	Hilbert transform of $x(t)$
$z(t) = x(t) + j\tilde{x}(t)$	analytic signal associated with $x(t)$
$\omega(t)$	instantaneous frequency of $x(t)$
$\phi(t)$	instantaneous phase of $x(t)$
ζ	damping ratio ($\zeta = 1$ is critically damped)

5.1 Overview

This chapter summarizes why we study backbone theory, some advances we have made in backbone analysis of free vibration data, and how this kind of analysis would help in the engineering practice of the Oklahoma Department of Transportation (ODOT). Details of the ideas provided here are available in the recent OU PhD thesis (Tang (2015)).

5.1.1 Motivations

Structural Health Monitoring (SHM) and damage detection have been popular and important research areas for decades, for example Doebling et al. (1996); Housner et al. (1997); Sohn et al. (2002); Chang et al. (2003); Lynch and Loh (2006); Kerschen et al. (2006); Farrar and Worden (2007); Goyal and Pabla (2015). Monitoring civil infrastructure to collect data should not be an end goal; extracting useful information out of the data and interpreting the results to reveal meaningful implications about the civil infrastructure being monitored have always been the ultimate goal. Daunting challenges inherently reside in the process of data processing and result interpretation because this process is often where theory and reality collide with measurement noise, un-modelled complexities, and assumption inaccuracies. This calls for a great deal of extensive and in-depth research to best realize the potential of monitoring efforts by providing meaningful, accurate and timely end results to decision makers.

As an important component of SHM, advancement in system identification, especially nonlinear system identification, is in demand. We must pay attention to nonlinear material behaviors, geometric and mechanical nonlinearities. Many construction materials (e.g., concrete, asphalt, and timber) will respond in highly nonlinear ways under large or cyclic loads (e.g., loading rate-dependent viscosity or hysteresis). Unfortunately, modal analysis-based (or eigen-problem-based) linear approaches have been dominating structural health monitoring causing large un-modelled errors. Studying, understanding, and applying truly nonlinear methods to nonlinear problems in practice are in great need.

Vibration signals have been heavily studied for the purpose of many engineering disciplines including aerospace engineering, bio-medical engineering, civil engineering, electrical engineering, mechanical engineering, and more. Computerized methods of dynamical systems identification generally involve the extraction of backbone approximations from digitized signals. In addition to the Hilbert transform approach presented by Feldman (2011a), various backbone techniques are discussed in the literature; see for example Renson et al. (2016); Londoño et al. (2015); Kerschen et al.(2006); Adams and Allemang (1998). In the framework of analytic signal theory, let $x(t)$ be a real signal and $\tilde{x}(t)$ be its Hilbert transform

$$\tilde{x}(t) = \frac{1}{\pi} P \int_{-\infty}^{+\infty} \frac{x(\tau)}{t-\tau} d\tau \tag{5.1}$$

where P indicates the Cauchy principal value. The analytic signal associated with $x(t)$ is the complex signal $z(t) = x(t) + j\tilde{x}(t)$. In polar notation,

$$z(t) = a(t)e^{j\phi(t)} \tag{5.2}$$

where $a(t) = \sqrt{x^2(t) + \tilde{x}^2(t)} \geq 0$ is the instantaneous amplitude, $\phi(t) = tan^{-1}\left(\frac{\tilde{x}(t)}{x(t)}\right)$ is the instantaneous phase, and $\omega(t) = \frac{d\phi}{dt}$ is the instantaneous frequency. The phrase “analytic-signal backbone” refers to the parametric curve $a(t)$ versus $\omega(t)$.

5.1.2 Feldman’s backbone technique

Figure 5.1(a) shows a vibration signal as the free response of a single-degree-of-freedom (SDOF) system which can be used to represent a subsystem of interest in the aforementioned disciplines, and Figure 5.1(b) is the corresponding backbone curve. The vibration signal is normally a transient signal with a decaying profile in amplitude – among many other subtle details. The backbone curves of such signals are our primary focus. Many vibration signal analysis methods are dedicated to identifying the properties of the system underlying the signal, such as modal frequencies and damping ratio. Here, the goal would be to extract system properties concerning the *existence and types* of nonlinearities. This is the big picture concerning nonlinear system identification and damage detection, where signal processing and data analysis play a critical role.

(a) Time history

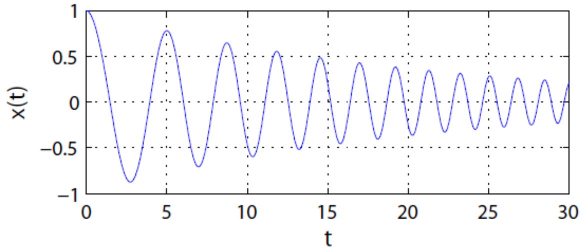

(b) Backbone

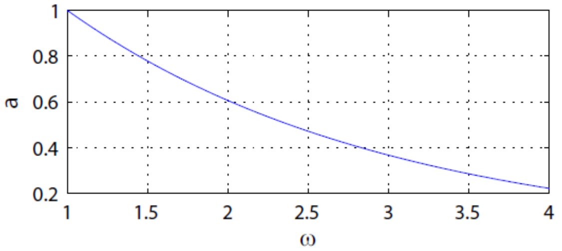

Figure 5.1: An idealized illustration of (a) a vibration signal, and (b) its backbone curve.

The heart of this research is to represent a transient signal as illustrated above using a two-dimensional curve with a distinct feature called “backbone” – see Figure 5.1(b) – defined by the signal’s instantaneous amplitude and instantaneous frequency. The concept of the “backbone” originates from Feldman’s work, e.g., Feldman (1994a, 2011a,b). It is said to be “a very helpful and traditional instrument in vibration analysis” Feldman (2011b). Figure 5.2 showcases the capability of the backbone technique for identifying many types of nonlinearity of SDOF models including but not limited to – according to Feldman (1994a) – nonlinear spring models (such as hardening, softening, backlash, pre-compressed strings, bilinear, or impact), and nonlinear damping models (frequency-dependent or frequency-independent).

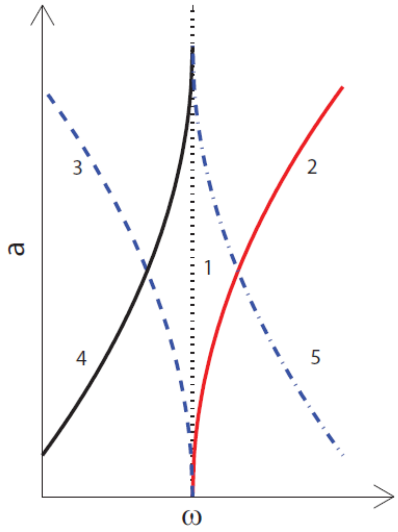

Figure 5.2: Idealized backbones of typical models: (1) linear; (2) hardening; (3) softening; (4) backlash; (5) preload. This figure is reproduced by following Feldman (2011b).

Hilbert transform is the focus of the studies due to its well-known aspect of being suitable for nonlinear and nonstationary signal processing (Cohen 1995; Hahn 1996; King 2009a,b; Feldman 2011a, just to name a few key classical references studied by us and used as the main tools. Backbone – as a system identification method introduced by Dr. Feldman based on Hilbert transform – has also been around for 20 years. Dr. Feldman's series of publications related to Hilbert transform and backbone technique starting from 1990's is summarized in Table 5.1.

Table 5.1: Overview of selected publications by Dr. Feldman starting from 1990's.

Year	**Reference**	**Topic**	**Summary**
1994	Feldman (1994a,b)	FREEVIB and FORCEVIB	Detecting nonlinearity and viscous damping ratio of a SDOF model based on backbones from free or forced response
1995	Feldman and Braun (1995)	Identification of system parameters	Estimating system parameters by using a lowpass filter on backbone
1997	Braun and Feldman (1997)	Time-frequency characteristics	Characterizing nonlinear systems from time-frequency variations of response signals
1997	Feldman (1997)	FREEVIB	Approximating free vibration backbone by using averaging instantaneous amplitude and frequency
2005	Feldman (2005)	Identification of system parameters	Estimating system parameters including natural frequency and damping using Hilbert transform
2006	Feldman (2006)	Signal decomposition technique	Proposing a signal decomposition method named after Hilbert Vibration Decomposition (HVD)
2011	Feldman (2011a,b)	Applications of Hilbert transformation	Presenting comprehensive reviews of topics related to Hilbert transform applications

5.1.3 Research needs: a motivating example

We consider the backbone technique a nonlinear system identification technique based upon instantaneous amplitude and frequency. The correspondence between the backbone feature and type of nonlinearity given in Figure 5.2 could be used as a pattern classifier because different types of nonlinearities in the system would cause the backbone to bend in different directions (with more details), whilst the backbone will not bend at all for a pure linear system. The pattern classifier idea illustrated in Figure 5.2 seems straightforward, however a significant amount of technical details demands correct and efficient solutions to bring the idea to fruition given the team's experience (Jones and Pei 2009).

As a test signal, consider

$$x(t) = e^{-\zeta t}\left[cos\left(\sqrt{1-\zeta^2}t\right) + \frac{\zeta}{\sqrt{1-\zeta^2}} sin\left(\sqrt{1-\zeta^2}t\right)\right] \tag{5.3}$$

which is the solution of the damped harmonic oscillator equation

$$\ddot{x}(t) + 2\zeta\dot{x}(t) + x(t) = 0, \text{ subject to } x(0) = 1, \dot{x}(0) = 0 \tag{5.4}$$

where t is a dimensionless time, scaled so that the undamped oscillator frequency is one. See (for example) Eq. (5.2.3) in Kovacic and Brennan (2011).

Unless filtering is utilized, analytic-signal backbones of lightly damped harmonic oscillators are oscillatory, with the magnitude of their oscillations increasing as the damping ratio ζ increases. The Hilbert transform (HT) of the test signal exists if $\zeta = 0$ (viz., the HT of $cos(t)$ is $sin(t)$). However, the HT of the test signal does not exist if $\zeta > 0$ because the integrand becomes infinite as t goes to $-\infty$; similarly it does not exist if $\zeta < 0$ because $x(t)$ is unbounded as t goes to $+\infty$. Alternatively, if the test signal $x(t)$ is assumed to be zero for $t < 0$ (an initial value problem), then the HT of $u(t)x(t)$, where $u(t)$ denotes the unit step function, does not exist because $\tilde{x}(t)$ has a logarithmic singularity at $t = 0$, caused by the jump discontinuity at that time. The undamped case, $u(t)\ cos(t)$, was discussed in detail by Loughlin (1998), but even if $\zeta > 0$, the jump discontinuity at $t = 0$ still causes the HT of the test signal to have a logarithmic singularity at that time.

It is worth noting that a 1998 survey by Adams and Allemang (1998) stated that the Hilbert transform approach to backbone extraction requires “extravagant” and “heroic” filtering efforts. The Hilbert “transformer” adopted by Feldman is a digital filtering concept aimed at correcting unfiltered Hilbert transform computations. An implementation of the Hilbert transformer concept, based on the Remez exchange algorithm, is discussed in Section 3.3 of Feldman (2011a) with online software available as part of Hilbert Vibration Decomposition (HVD). We used relevant parts of this software without modification. A significant limitation of the HVD software is that the signal length must be 691 points or more. Consequently for the results presented next, the number of cycles was increased to 20, and the sampling frequency was increased to 40 (i.e., equivalent to $K = 41$ points per damped cycle), producing a test signal with $N = 801$ points. The damping ratio was set to $\zeta = 0.02$. Figure 5.3 shows HVD results for this 801-point test signal.

Such considerations (i.e., challenges) have provoked various approximations that (eventually) produced physically sensible results for harmonic oscillators with light damping, defined here as $0 \leq \zeta \leq 0.1$ (critical damping is $\zeta = 1$). One such approximation was to introduce a “mirror” at $t = 0$, thereby reflecting the test signal from the positive time region into the negative time region; see Huang et al. (2003). Placing a mirror at $t = 0$, thereby eliminating the jump discontinuity there, is closely related to an idea discussed in Meissner (2012) where time t in the exponent of $e^{-\zeta t}$ is replaced by its absolute value $e^{-\zeta |t|}$. Computations were done in MATLAB using hilbert.m which is an implementation of Marple’s Discrete-Time ‘Analytic’ Signal method Marple Jr. (1999). To reduce discretization errors (attributable to aliasing, leakage, etc.), the test signals were carefully sampled at an integer number K points per damped cycle, where one period of a damped cycle is $\frac{2\pi}{\sqrt{1-\zeta^2}}$, verifiable from

$$\dot{x}(t) = -\frac{e^{-\zeta t}}{\sqrt{1-\zeta^2}} sin\left(\sqrt{1-\zeta^2}t\right) \tag{5.5}$$

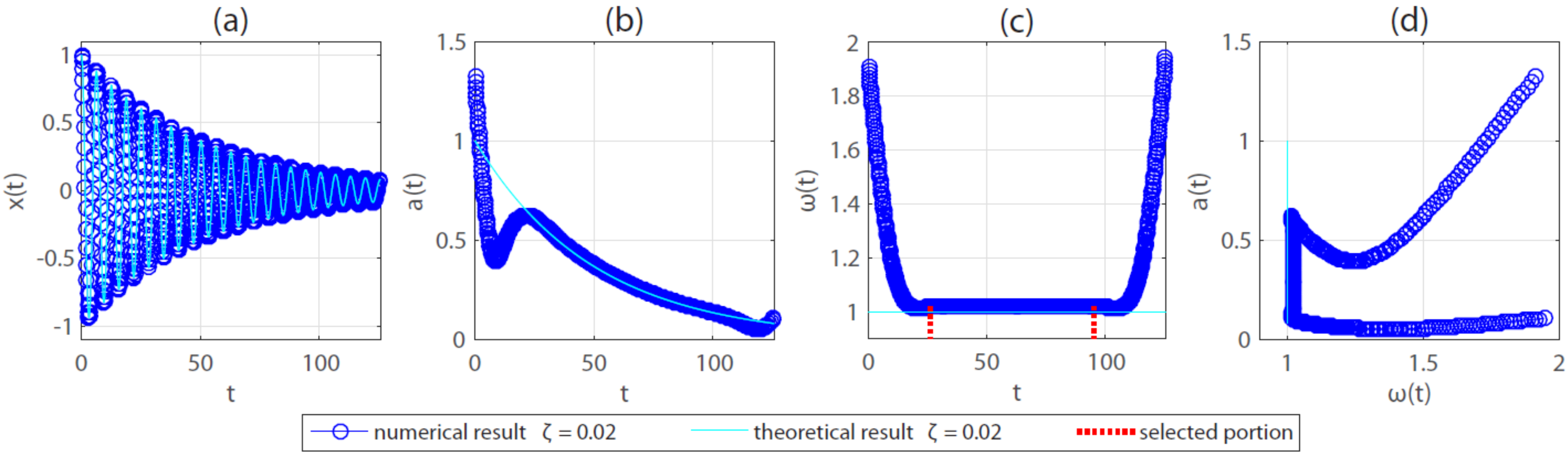

Figure 5.3: (a) Test signal $x(t)$ with $N = 801$ points, $\zeta = 0.02$, (b) instantaneous amplitude a(t), (c) instantaneous frequency ω(t), and (d) backbone $a(t)$ vs. $\omega(t)$ obtained by using online HVD software with $n = 1$, $f_p = 0.01$.

For comparison, Figure 5.4 shows unfiltered results using the mirroring technique.

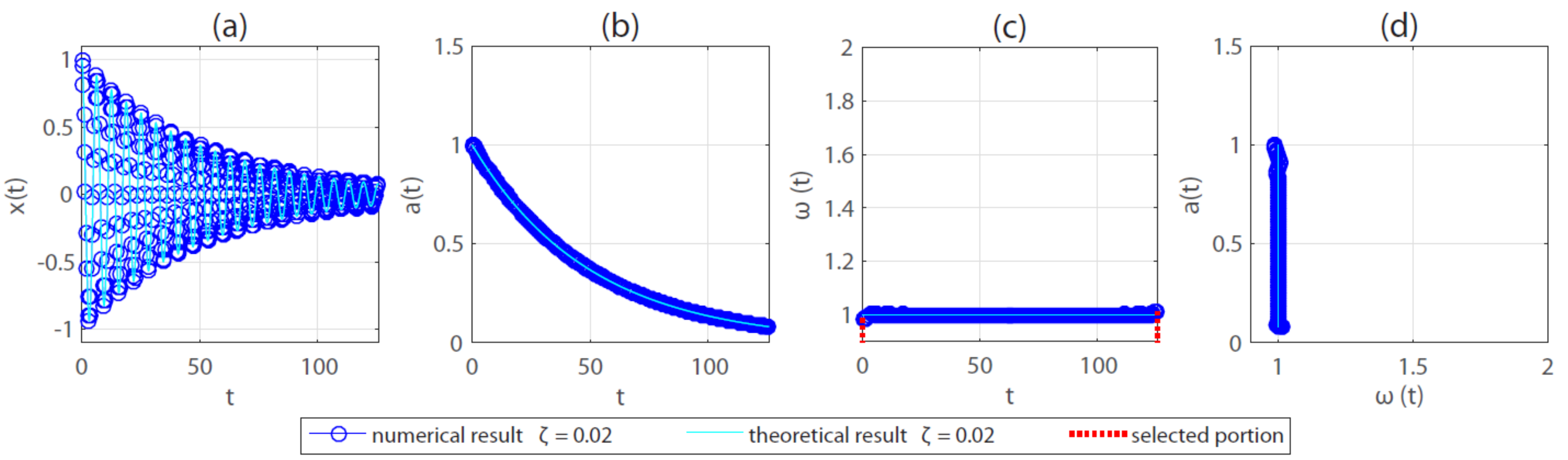

Figure 5.4: (a) Mirrored test signal x(t) with $N = 1601$ points, $\zeta = 0.02$, (b) instantaneous amplitude a(t), (c) instantaneous frequency $\omega(t)$, and (d) backbone $a(t)$ vs. $\omega(t)$ obtained by using Marple's discrete-time analytic signal method (hilbert.m).

The root-mean-square (RMS) error of the instantaneous frequency was calculated, producing 0.2267 for HVD (Figure 5.3), and 0.0027 for the unfiltered case (Figure 5.4). Because of the end effects in Figures 5.3 and 5.4, the RMS errors were re-calculated using only selected portions of the instantaneous frequency for the time between the two red marks in each figure, resulting in (respectively): 0.0199, and 0.0027.

To summarize the research needs, first, it requires an in-depth understanding of the approximation nature of applying the concepts of analytic signal and Hilbert transform to the transient signals in the specified application. When filtering is not utilized, the actual backbones would be oscillatory, as shown in Figure 5.5 for linear, hardening and softening Duffing oscillators. When filtering is utilized, a good compromise needs to be made. Second, performing the Hilbert transform on finite-length discrete signals, the so called *discrete Hilbert transform* (DHT), requires properly handling frequency leakage. Next, signal decomposition is necessary when a signal is not monocomponent in nature as almost always happens with real-world (i.e., measured) data. Also, the applicable range of the backbone technique requires a significant expansion so that the technique could be useful when the recorded response is not long enough.

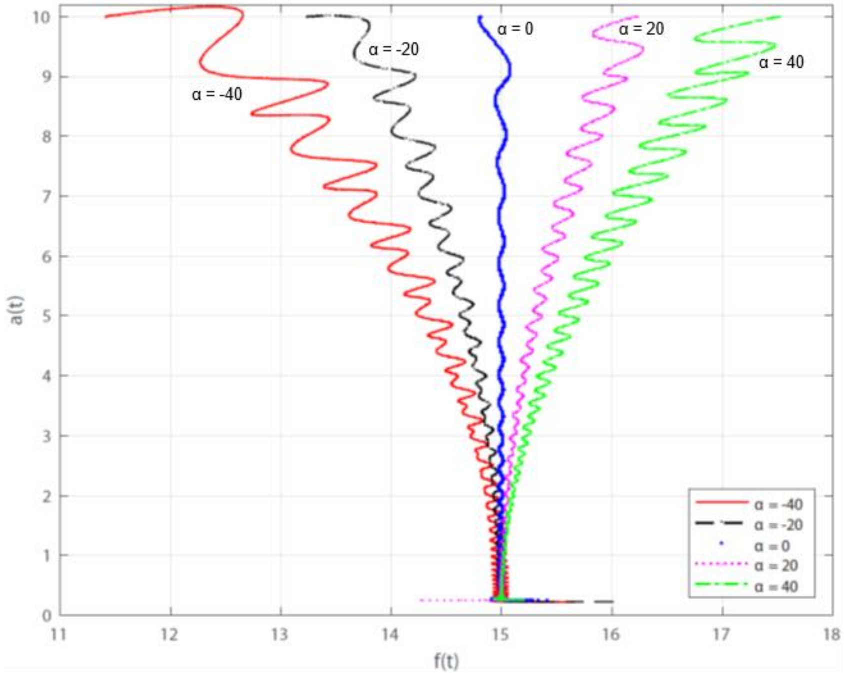

Figure 5.5: Raw backbones under various cubic stiffness α values in the Duffing oscillator of $\ddot{x}(t) + 2 \times 2\% \times (2\pi\ 15)\dot{x}\ (t) + (2\pi \times 15)^2 x(t) + \alpha x^3(t) = 0$ with initial condition $x(0) = 10$ and $\dot{x}\ (0) = 0$.

5.2 Contributions of this Work and Organization of this Chapter

To respond to the research needs, Section 5.3 puts forth two simple techniques that can effectively mitigate the end effects in the DHT; details are omitted from this chapter but are available in Tang (2015). Section 5.4 introduces a new signal decomposition method that is based on a concept called “time index” proposed by us. Section 5.5 presents sample real-world results to showcase the efficiency of our improved backbone technique. We omit our novel piecewise DHT technique for analyzing free vibration data when damping effects are large; details are available in OU PhD thesis (Tang 2015).

5.3 Simple Techniques to Ameliorate End Effects in the DHT

To minimize frequency leakage, it is essential to reduce the discrepancy caused by periodic extension. One way to achieve this goal is to reverse the original signal and concatenate this with the original signal. Figure 5.6 illustrates this idea when the reversal and concatenation take place at the right end of the original signal. The reversal and concatenation can take place at the left end of the original signal as well, however we will not illustrate and discuss this situation hereafter. This is referred to as “even extension” by following the same terminology for Fourier series and in discrete cosine transform (DCT).

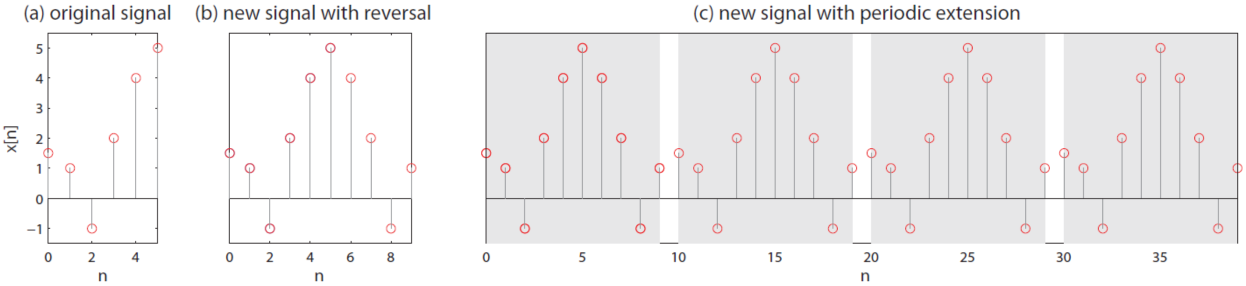

Figure 5.6: Illustration of flipping (b) and periodic extension (c). The original signal in (a) has a length of $N = 6$ and is defined for $n = 0, 1, 2, 3, 4, 5$. The new signal in (b) has a length of $2N - 2 = 10$ and is defined for $n = 0, 1, \cdots, 8, 9$.

Intuitively, this add-on procedure eliminates a sudden “jump”, i.e., a high-frequency leakage that could otherwise happen during a periodic extension. For DFT, this would help cure Gibb’s phenomenon. Nonetheless, this add-on procedure may still cause another unwanted side effect. Referring to Figure 5.6(c), the two ends of the original signal become local extrema (i.e., minima or maxima) after the proposed even extension, which may or may not be consistent with the original signal as illustrated in Figure 5.7.

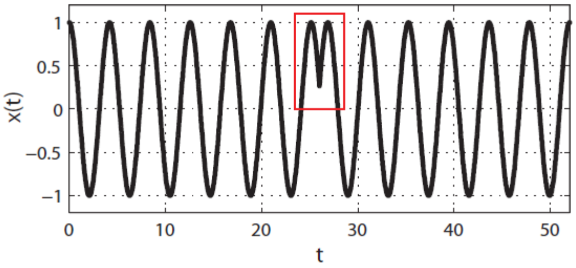

Figure 5.7: An illustration of “phase distortion”, the limitation with the proposed even extension. The red box highlights the undesired local extrema introduced by even extension.

For a typical vibration signal, there would be more than one cycle of oscillations. One such example is given in Figure 5.8. We propose two add-on procedures that could complement Marple's DHT algorithm to significantly reduce the end effects. Huang et al. (2003) contains similar but *empirical* approaches to the empirical mode decomposition.

Our work, in contrast, is not for this purpose. We first examine in-depth three major DHT algorithms, namely Cizek in Cizek (1970), Kak in Kak (1977), and Marple in Marple Jr. (1999), and conclude their mathematical equivalence. This fact about their mathematical equivalence alone could help better understand and expedite the development of DHT theories and practice. The two add-on procedures follow naturally by first quantifying the limitation of even extension adopted from Fourier series. To address this limitation, local extrema trimming is proposed with a tradeoff. Proofs concerning the two properties in Marple Jr. (1999) are provided in our work but not in this chapter.

5.4 Time Indices Based Signal Decomposition Method

To start, two mono-component signals, $x_1(t)$, $x_2(t)$, and their sum (a double-component signal), $x(t)$, can be denoted as follows:

$$\begin{aligned} &z_1(t) = x_1(t) + j\tilde{x}_1(t), z_2(t) = x_2(t) + j\tilde{x}_2(t), \\ &\underbrace{z_1(t) + z_2(t)}_{z(t)} = \underbrace{x_1(t) + x_2(t)}_{x(t)} + j\left[\underbrace{\tilde{x}_1(t) + \tilde{x}_2(t)}_{\tilde{x}(t)}\right] \end{aligned} \tag{5.6}$$

where $z_1(t)$, $z_2(t)$ and $z(t)$ are the analytic signal of $x_1(t)$, $x_2(t)$ and $x(t)$, respectively, while $\tilde{x}_1(t)$, $\tilde{x}_2(t)$ and $\tilde{x}(t)$, are the corresponding Hilbert transforms.

In this study, the following assumptions are made:

Assumption #1. $a_1(t) > a_2(t)$ and $\omega_1(t) < \omega_2(t)$, $\forall t$. This assumption is adopted from Feldman (2006, 2011b) and Feldman (2011a) (pp. 62) and applied throughout this chapter.

Assumption #2. $a_i(t)$ and $\omega_i(t)$'s are all slow varying for $i = 1, 2$, adopted from Feldman (2011b) (pp. 746). This assumption is applied whenever specified in this section. This assumption is interpreted as $a_i(t)$ and $\omega_i(t)$'s first and second time derivatives being negligible.

In a Cartesian coordinate system for analytic signal, $z_1(t)$, $z_2(t)$ and $z(t)$ can be depicted in Figure 5.9 by vectors $\overrightarrow{OA}$, $\overrightarrow{OB}$, and $\overrightarrow{OC}$, respectively. In this representation, the angle with respect to the real axis and the length of a vector are wrapped phase and instantaneous amplitude of an analytic signal, respectively. Unwrapped phase would be the corresponding wrapped phase plus a multiple of 2π's depending on how many full cycles the vector has rotated at time t.

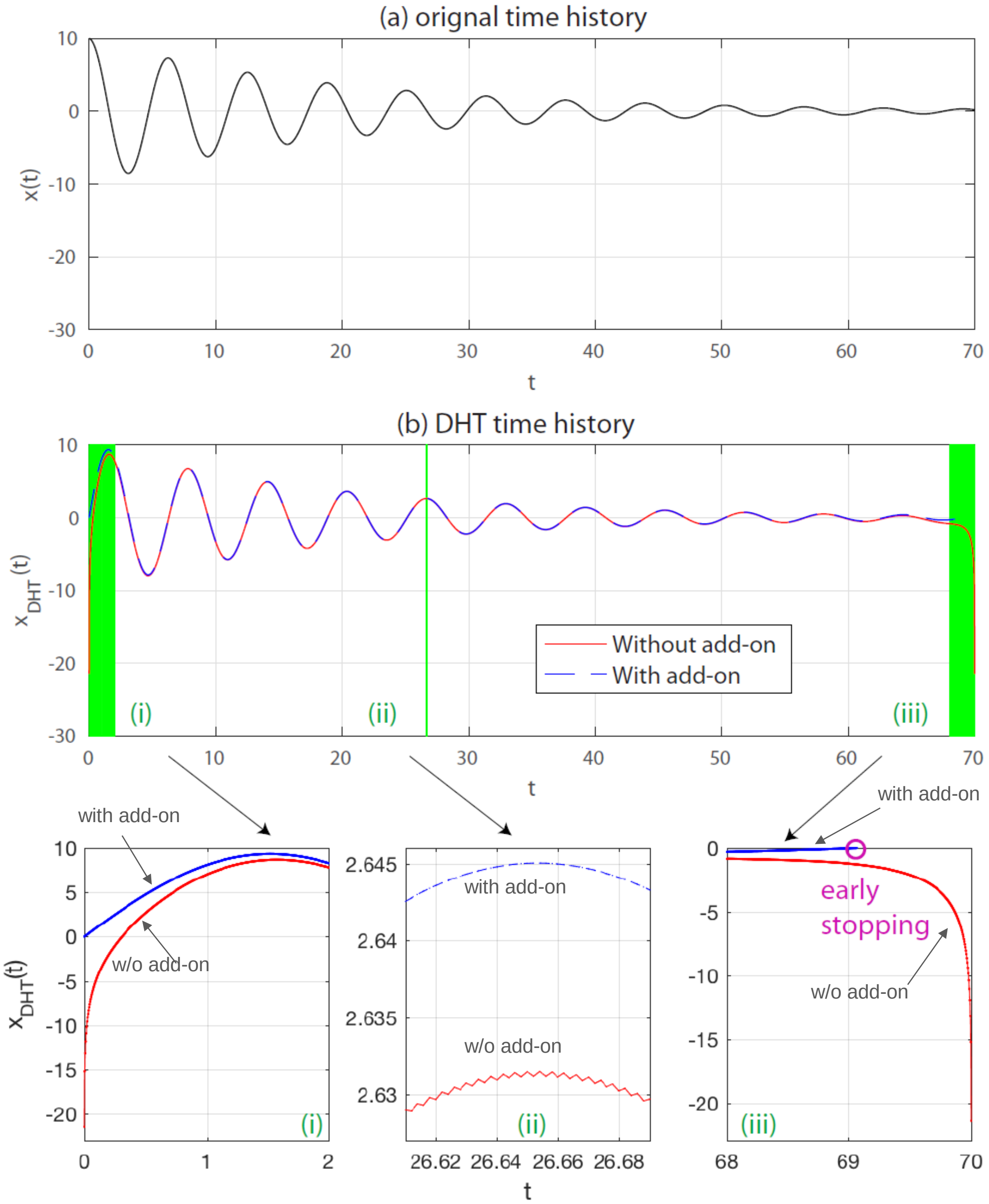

Figure 5.8: Comparison of results obtained with and without our proposed add-on procedures when Marple's DHT algorithm is used. The signal is a simple free vibration signal and has a form of $x[n] = e^{-0.05n/F_s} cos(n/F_s)$ with $F_s = 500$ and $n = 0, 1, \cdots, 35000$. $t = n/F_s$, $x(t) = e^{-0.05t} cos\, t$. (a) shows the original signal and (b) shows the DHT results with both procedures. The comparison clearly indicates that the add-on procedures not only reduce the end effects to a large extent (see Panels (i) and (ii)) but also eliminate erroneous ripples towards the mid-section (see Panel (ii)).

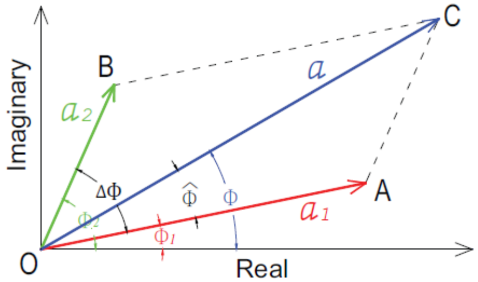

Figure 5.9: Analytic signals in complex coordinate plane for an arbitrary time instance t, where $\overrightarrow{OA}$, $\overrightarrow{OB}$, and $\overrightarrow{OC}$ depict the analytic signals $z_1(t)$, $z_2(t)$ and $z(t)$, respectively.

Applying the assumptions above, Figure 5.10 illustrates a typical rotation cycle involving $z_1(t)$, $z_2(t)$ and $z(t)$ with an additional assumption that $z_1(t)$ and $z_2(t)$ start off with no difference in wrapped phase and they both happen to be on the real axis - as shown in Panel (a). Time instances corresponding to Panels (a), (c) and (e) are of particular interest, when $z_1(t)$ and $z_2(t)$ are in phase, antiphase, and in phase again. To capture these special moments, a mapping will be introduced shortly.

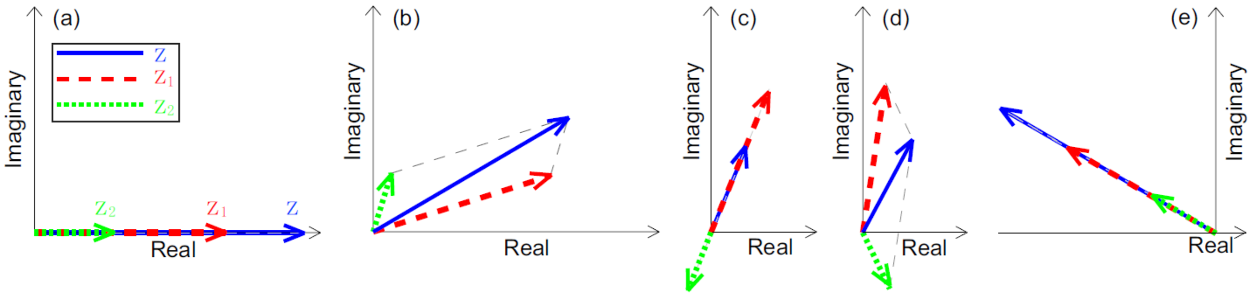

Figure 5.10: Evolution of $z_1(t)$, $z_2(t)$ and $z(t)$ with time. Time increases gradually from panels (a) to (e). As will be shown hereafter, (a) $t = t_0 = 0$, (c): $t = t_1$, and (e): $t = t_2$.

A mapping

$$f: n \longmapsto t_n, \text{ with } n \in \mathbb{N}^0 \tag{5.7}$$

is defined such that

$$\Delta\phi(t_{n+1}) - \Delta\phi(t_n) = \pi \tag{5.8}$$

where time instance t_n has a clear physical interpretation: From t_n to t_{n+1}, $\Delta\phi(t)$, the phase difference between $\overrightarrow{z_2}(t)$ and $\overrightarrow{z_1}(t)$, is increased by π. In Figure 5.10, t_n's with $n = 0$, 1, and 2 correspond to the time instances when the three vectors $\overrightarrow{z_1}(t)$, $\overrightarrow{z_2}(t)$ and $\vec{z}(t)$ line up, i.e., in Panels (a), (c) or (e) at $t = t_0$, $t = t_1$, and $t = t_2$, respectively. $\overrightarrow{z_2}(t)$ rotates π more than $\overrightarrow{z_1}(t)$ from t_n to t_{n+1}.

The innovation in this study depends heavily on the introduction of both t_n and $\Delta\phi(t_n)$. Figure 5.11(a) illustrates an important property, for $n \in \mathbb{N}^0$, $\vec{z}(t)$ and $\overrightarrow{z_1}(t)$ have the same phase value:

$$\phi(t_n) = \phi_1(t), \forall n \in \mathbb{N}^0 \quad (5.9)$$

This can be justified by applying Assumption #1 and the idea of mathematical induction starting with $\phi(t_0) = \phi_1(t_0)$. Since $\phi(t) \in C$ and $\phi_1(t) \in C$, $\hat{\phi}(t) \triangleq \phi(t) - \phi_1(t) \in C$. Given the continuity of $\hat{\phi}(t)$, $\phi(t) - \phi_1(t)$ has the same sign between t_n and t_{n+1}. Eq. (5.9) lays the foundation for the proposed signal separation method.

The procedure of the proposed signal decomposition method is given as follows:

1. Perform DHT of a given double-component signal $x(t)$ that satisfies Assumptions #1 and #2 to obtain $a(t)$, $\phi(t)$, and $\omega(t)$.

2. Option A: Locate all local maxima and minima of $a(t)$; Option B: Locate all local maxima and minima of $\omega(t)$. With either option, all corresponding time instances form the set of t_n with $n \in \mathbb{N}^0$.

3. Find all $\phi(t_n)$ values corresponding to all t_n. Given Eq. (5.9), these $\phi(t_n)$ will be considered as $\phi_1(t_n)$

4. If Option A is adopted in Step #2: Curve fit all local maxima and minima of $a(t_n)$, respectively. If Option B is adopted in Step #2: Locate all local extrema of $a(t_n)$ by picking the individual values of $a(t_n)$ with t_n obtained in Step 3. Afterwards, curve fit all maxima and minima of $a(t_n)$, respectively. Average the two approximated curves for approximated $a_1(t)$

5. Curve fit all $\phi_1(t_n)$ identified above to approximate $\phi_1(t)$. Note that the instantaneous frequency $\omega_1(t)$ can be obtained by numerically differentiating $\phi_1(t)$.

6. Construct $x_1(t)$ by $x_1(t) = a_1(t) \cos \phi_1(t)$.

7. Obtain $x_2(t)$ by using $x_2(t) = x(t) - x_1(t)$.

This signal decomposition method is named after "index method" as it relies first on identifying all time instances corresponding to t_n with $n \in \mathbb{N}^0$ through identifying peaks and valleys in $a(t)$ or $\omega(t)$. Unfortunately, Step #2 involves approximations thus introducing errors with both options. Another prominent feature of the index method is to rely on the property revealed in Eq. (5.9) to unlock the first component from the sum time history. Eq. (5.9) only involves Assumption #1; however, the execution of Eq. (5.9) under Step #3 receives errors from Step #2.

(a) Instantaneous phase

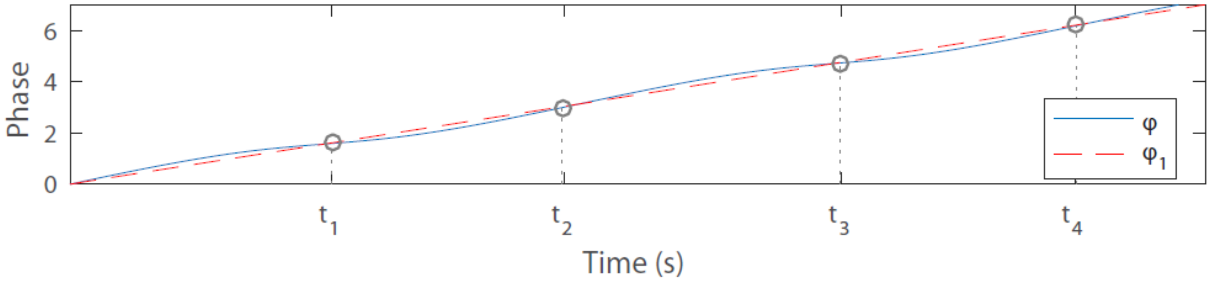

(b) Instantaneous amplitude

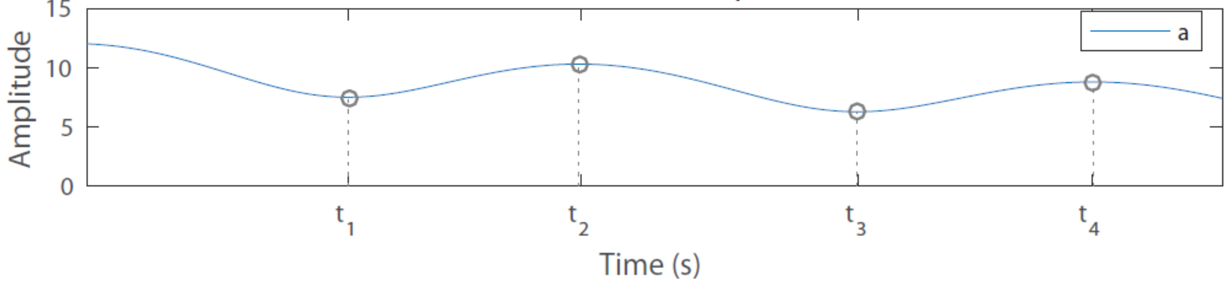

(c) Instantaneous frequency

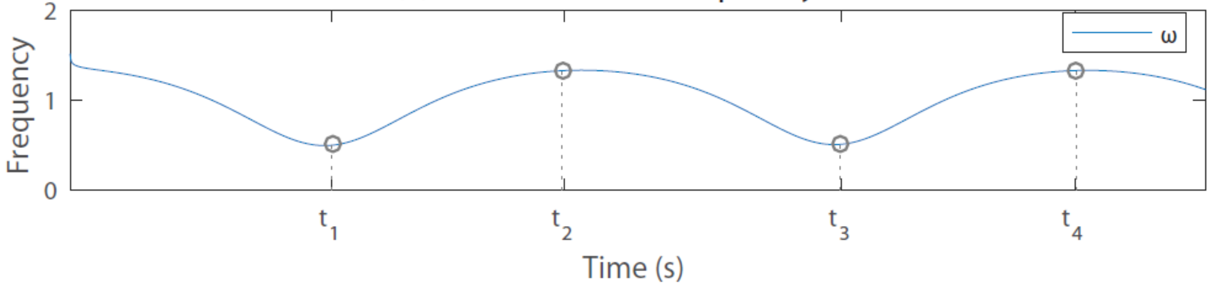

Figure 5.11: A zoom-in view of a case where the two mono-component signals are both exponentially decaying sinusoids. Panel (a) illustrates the relationship between $\phi(t)$ and ϕ_1(t). Panels (b) and (c) indicate simultaneous local maxima and minima for $a(t)$ and $\omega(t)$ in an approximate sense.

As a comparison and using four Duffing oscillators, Figure 5.12 shows the backbones of the first decomposed components and those obtained using HVD decomposition technique introduced in Feldman (2006). It is important to highlight that these results were obtained by tuning the cutoff frequency of the filter under the HVD decomposition for as good performance as possible. For the two ends of a backbone, the HVD decomposition seems to lead to a stronger end effect, making the task of valid pattern classification much more difficult, especially when automated system identification is the goal. In contrast, the proposed method leads to a backbone within a “box” where the curves plot nearly on top of one another. This contained manner indicates a more predictable data range to facilitate pattern classification. However in the middle portion of a backbone, the results from the HVD decomposition seem to oscillate less.

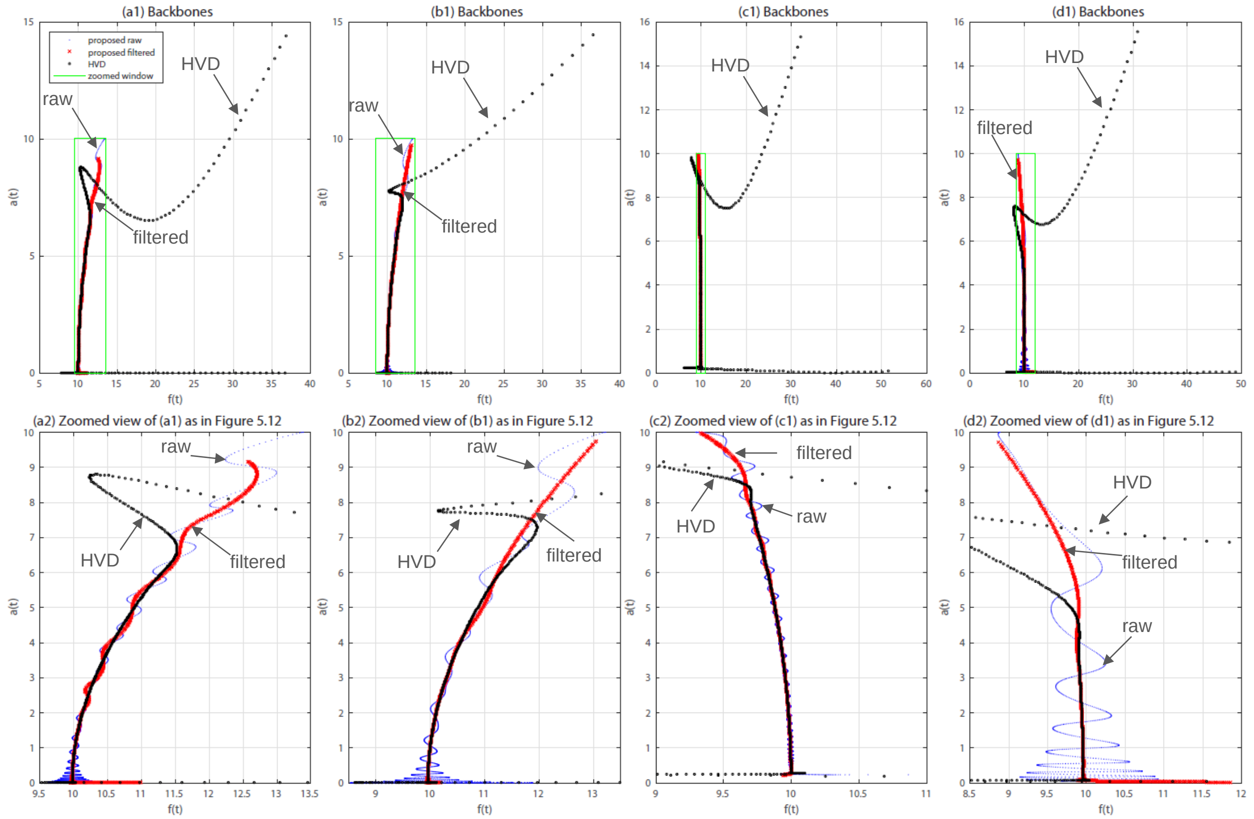

Figure 5.12: Comparison of the backbones obtained from using the proposed and HVD methods, where “proposed raw” denotes the raw backbone of $x(t)$; “proposed filtered” denotes the proposed backbone of $x_1(t)$, and “HVD” denotes the backbone obtained by using with HVD method (Feldman (2006)). Panels (a1) to (d1) are for the four Duffing oscillators. Panels (a2) to (d2) are the zoomed views of Panels (a1) to (d1) and displayed as a green box in each of Panels (a1) to (d1), respectively. When using the HVD method, the following parameter values are adopted: f_p, the cutoff frequency for the filter, is 0.04 for (b1), (b2) and (b3), and 0.02 for the rest, while the number of components is chosen to be 2 for all.

5.5 Applications of Backbone to SDOF Structural Dynamics

5.5.1 Parametric study

The following mass-normalized equation of motion for a Duffing oscillator has been utilized by Feldman (e.g., Feldman (1994a, 2006, 2011b,a)). It will serve as a benchmark equation for this study, where linear viscous damping is assumed:

$$\ddot{x}(t) + 2\,\zeta\,(2\pi f_n)\dot{x}\,(t) + (2\pi f_n)^2 x(t) + \alpha x^3(t) = 0$$
$$\text{with initial condition } x(0) > 0 \text{ and } \dot{x}(0) = 0 \qquad (5.10)$$

The parameters f_n, ζ, α, x(0) and $\dot{x}(0)$ are the natural frequency, damping ratio, nonlinear stiffness, initial displacement and initial velocity, respectively. Without losing generality, we fix $\dot{x}(0) = 0$ throughout this study to restrict the parametric study on the initial condition (IC).

To consider meaningful values for f_n and ζ, references in earthquake engineering such as Chopra (2001); Paz (1994) are consulted. Typical values for fn range from 0.3 to 22 Hz, damping ratios are summarized in Table 5.2 following Paz (1994), while values as high as 25% are considered in other literature Liang et al. (2012):

Table 5.2: Maximum values for damping ratio of real-world structures adopted from Table A17.5 in Paz (1994)

Property	Steel (Welded)	Steel (Bolted)	Concrete (Reinforced)	Concrete (Prestressed)	Masonry (Reinforced)	Wood Trusses	Wood Frames
ζ (%)	2.0	4.0	5.0	3.0	6.0	9.0	7.0

All backbone curves in Section 5.5.1 are raw backbones, i.e., unfiltered. As explained in Feldman (1994a), a backbone curve of Eq. (5.10) intersects the f-axis at the natural frequency of the linear portion of the SDOF system. With 6%, a mid-range ζ value, Figure 5.13 indicates how the backbone curves are affected by varying f_n values. The oscillations shown in the curves are a product of the method and should not be ignored in plotting the results. Figure 5.14 confirms that ζ affects only the "density" of a backbone curve, but not its bending behavior at all. An intuitive explanation is that the damping ratio affects only the rate of decrease of the response, resulting in a difference in the density of the backbone curves. IC affects only the "length" (i.e., starting point) of the backbone, but neither the bending behavior nor the "density". See Figure 5.15.

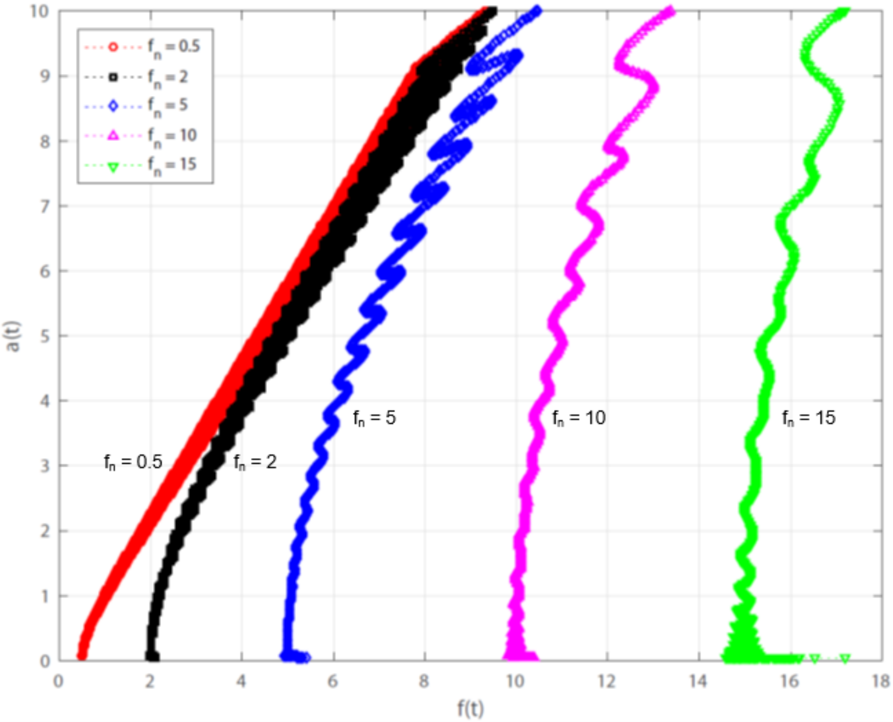

Figure 5.13: Raw backbones with various natural frequency f_n values in the Duffing oscillator of $\ddot{x}(t) + 2 \times 6\% \, (2\pi f_n)\dot{x}(t) + (2\pi f_n)^2 x(t) + 40x^3(t) = 0$ with initial condition $x(0) = 10$ and $\dot{x}(0) = 0$.

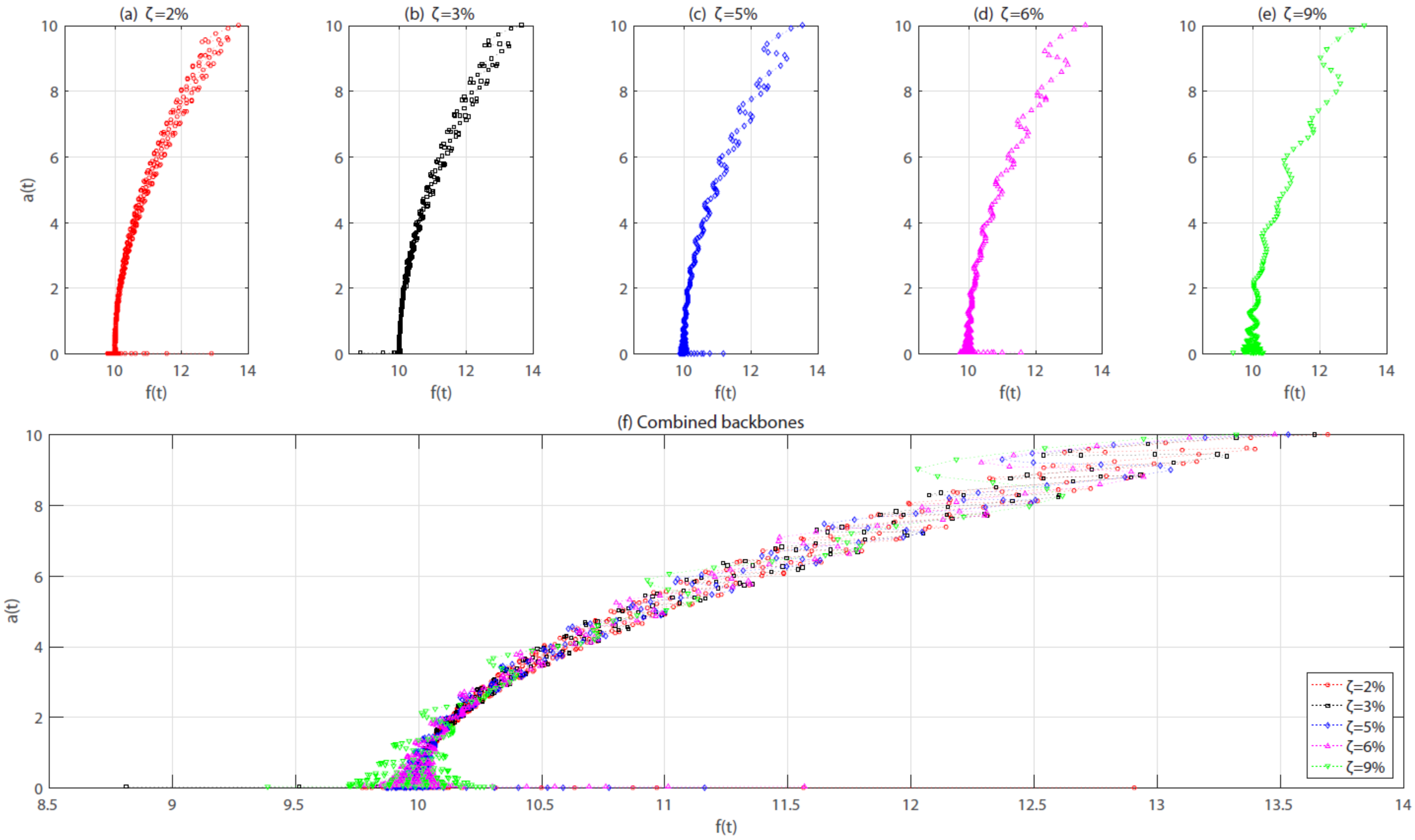

Figure 5.14: Raw backbones with various damping ratio ζ values in the Duffing oscillator of $\ddot{x}(t) + 2 \times \zeta \times (2\pi\, 10)\dot{x}(t) + (2\pi \times 10)^2 x(t) + 40x^3(t) = 0$ with initial condition $x(0) = 10$ and $\dot{x}(0) = 0$. Panels (a) to (e) are individual backbones with ζ values as labelled while all backbones are plotted together in panel (f)

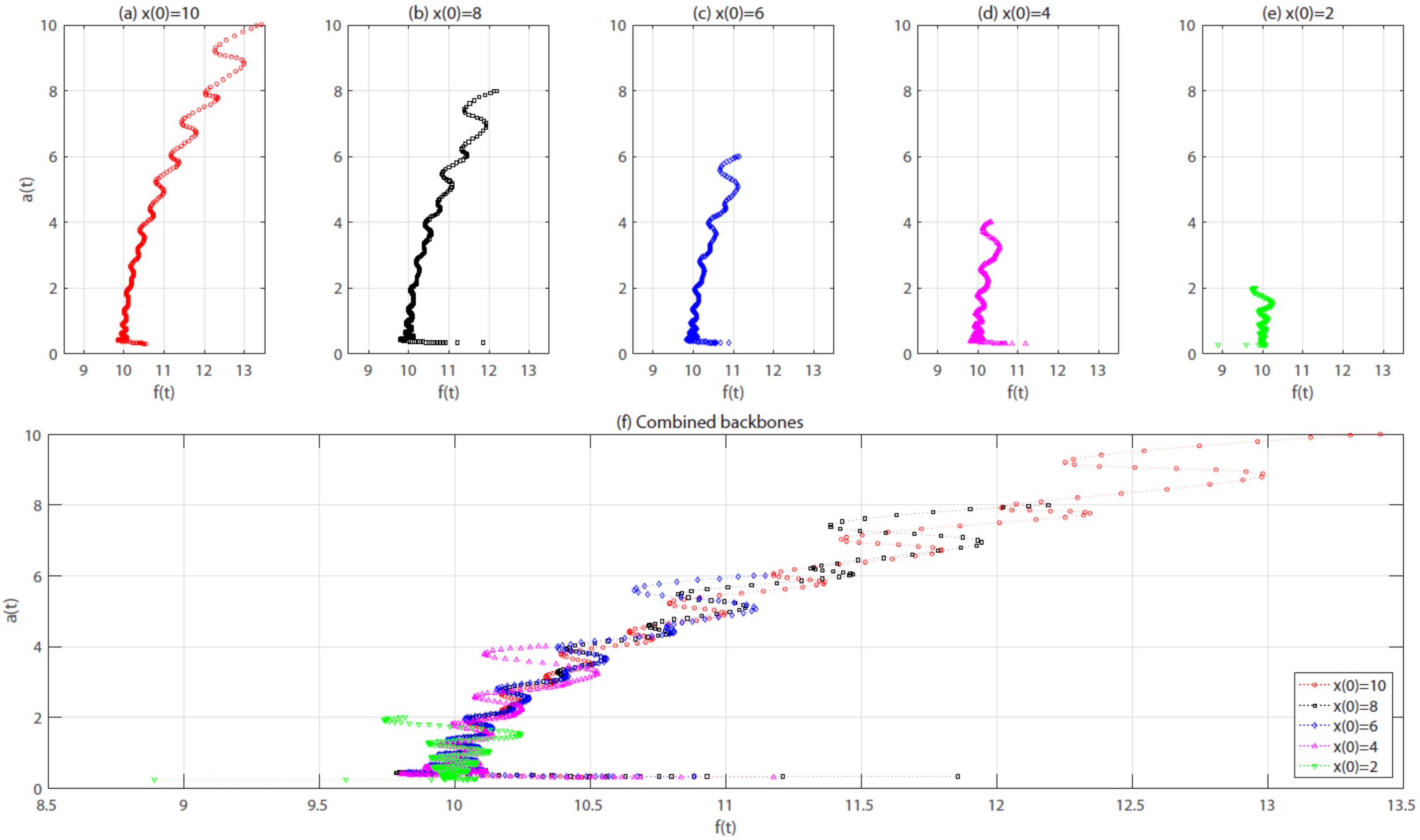

Figure 5.15: Raw backbones with various initial displacements x_0 values in the Duffing oscillator of $\ddot{x}(t) + 2 \times 6\% \, (2\pi \times 10)\dot{x}\,(t) + (2\pi \times 10)^2 x(t) + 40x^3(t) = 0$ with initial condition $x(0) = x_0$ and $\dot{x}(0) = 0$.

5.5.2 Sample result of processing real-world data

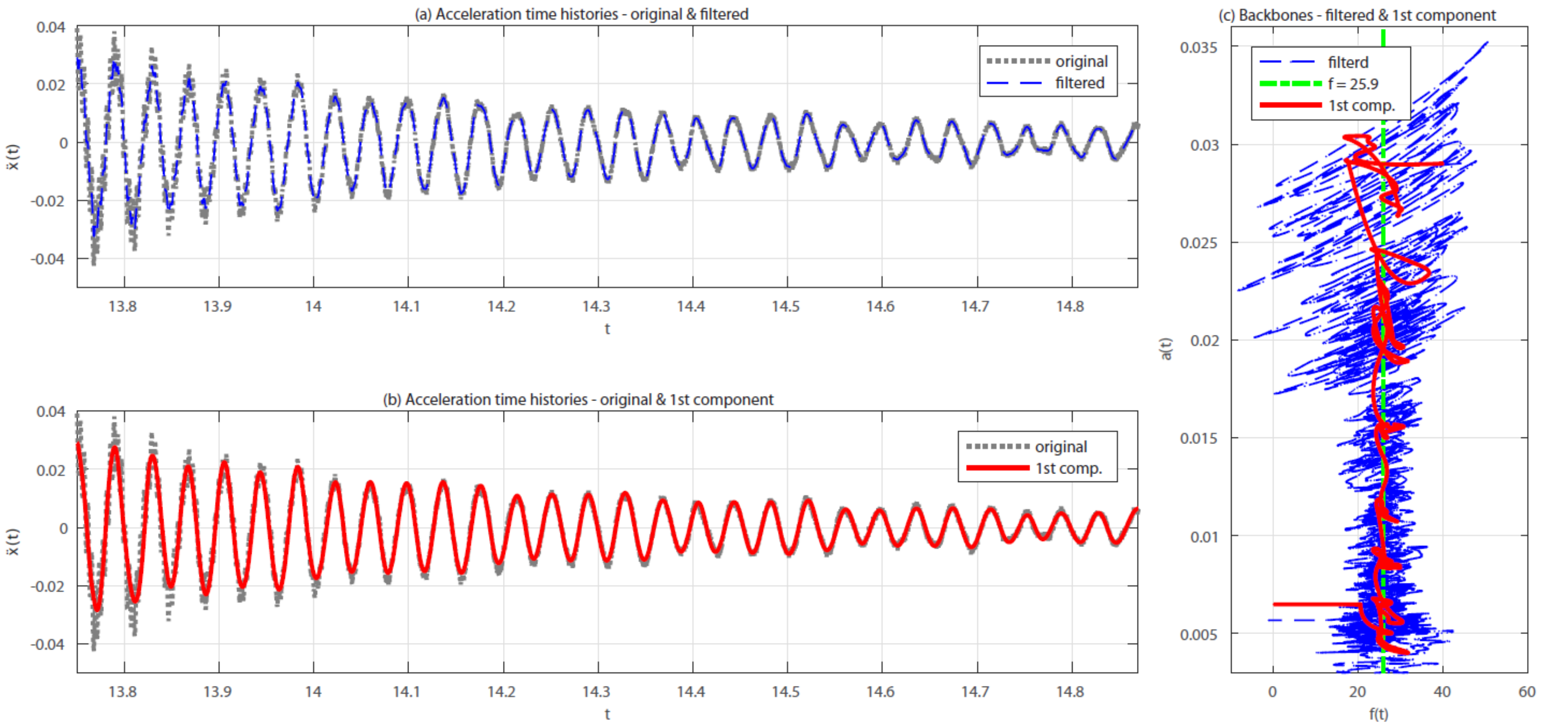

Figure 5.16: Processed results for the old girder where (a) is the original and filtered acceleration time histories of the processed data; (b) is the original and decomposed first component acceleration time histories of the processed data, and (c) is the backbones of the filtered acceleration time history and the decomposed first component. The green vertical dash-dot line in (c) is the mean value of the instantaneous frequency of the first component. The filtered and first component curves oscillate about the mean with the filtered values having greater magnitude of oscillations

5.6 Concluding Remarks

This chapter has provided a technical overview of the motivations, details and significance of the improvements made to the backbone technique used for processing free vibration response data for nonlinear system identification and damage detection purposes.

6. Inverse Methods

6.0 Nomenclature

a	horizontal length of the harped prestressing strands (in.)
A	cross-sectional area of concrete (in^2)
A_{ps}	cross-sectional area of the prestressing strands (in^2)
A_g	gross cross-sectional area (in^2)
b	width of the concrete cross-section
d_p	depth to centroid of the prestressing steel
E	modulus of elasticity of the concrete (ksi)
e	eccentricity from centroid of straight prestressing strands to centroid of concrete (in.)
e'	change in height of harped prestressing strands from end to straightening point (in.)
e_o	eccentricity from centroid of harped prestressing strands at ends to centroid of concrete (in.)
e_1'	change in height of harped prestressing strands from cut end to straightening (in.)
e_2'	change in height of harped prestressing strands from the other cut end to straightening ($e_1' > e_2'$) (in.)
f_{se}	effective prestress (ksi)
h	height of the beam (in.)
I	moment of inertia (in^4)
I_{cr}	moment of inertia of a cracked section (in^4) calculated using Eq. (6.17)
I_g	gross moment of inertia of the section (in^4)
L	length of the beam (in.)
L_{cut}	length of beam after cut (in.)
M_{cr}	measured cracking moment from the flexural test (kip-in)
n	ratio of prestressing steel modulus of elasticity to concrete modulus of elasticity

P_o	effective prestress force (kips)
w_d	dead load at the section under consideration (kips/in or kips/in^3)
x	location under consideration (in.)
y_{bot}	distance from the bottom of the girder to the centroid of the girder cross-section (in.)
Δ	measured camber (in.)
ρ_p	ratio of area of prestressing steel effective area of concrete ($\frac{A_{ps}}{bd_p}$)

6.1 Identification of Flexural Rigidity in Piecewise Manner

6.1.1 Overview

This section summarizes why we study the identification of flexural rigidify in a piecewise manner, some advances we have made, and how this kind of analysis would help the engineering practice of the Oklahoma Department of Transportation (ODOT).

A detailed plan for elastic flexural testing at varying points along the length of the "old" girder and girder A was developed for use in estimating the flexural stiffness (EI) along the length of the girder. The testing configurations were based on different stiffness zones of the girders identified by variation in reinforcement, and were selected to be compatible with previous testing performed on the "old" girder and with the proposed shear test configurations. The theoretical foundation for the method of estimating EI was carefully examined during the planning stage, including the challenge of presenting the method as a proper network. A large number of flexural tests were conducted on both the old girder and girder A using a number of load points and support conditions generating a large amount of useful data for regression analysis. Data pre-processing was conducted immediately after each test to check for any problems in the data. A number of tests required repeated loading due to torsion measured at the load point during the test, problems with the LVDTs, or other issues.

6.1.1.1 Motivations

The following problem formulation was adopted in Pei et al. (2008):

$$\Delta = \int_0^L \frac{M(x)m(x)}{EI} dx \tag{6.1}$$

$$\Delta^{piecewise\ EI} = \frac{\int_0^{\frac{L}{5}} M(x)m(x)dx}{EI_1} + \frac{\int_{\frac{L}{5}}^{\frac{2L}{5}} M(x)m(x)dx}{EI_2} + \frac{\int_{\frac{2L}{5}}^{\frac{3L}{5}} M(x)m(x)dx}{EI_3} + \frac{\int_{\frac{3L}{5}}^{\frac{4L}{5}} M(x)m(x)dx}{EI_4} + \frac{\int_{\frac{4L}{5}}^{L} M(x)m(x)dx}{EI_5} \tag{6.2}$$

$$\Delta^{piecewise\ EI} = \sum_{i=1}^{5} \frac{\int_i M(x)m(x)dx}{EI_i} \tag{6.3}$$

$$\frac{\Delta}{P} = \frac{\int_0^{\frac{L}{5}} \bar{M}(x)m(x)dx}{EI_1} + \frac{\int_{\frac{L}{5}}^{\frac{2L}{5}} \bar{M}(x)m(x)dx}{EI_2} + \frac{\int_{\frac{2L}{5}}^{\frac{3L}{5}} \bar{M}(x)m(x)dx}{EI_3} + \frac{\int_{\frac{3L}{5}}^{\frac{4L}{5}} \bar{M}(x)m(x)dx}{EI_4} + \frac{\int_{\frac{4L}{5}}^{L} \bar{M}(x)m(x)dx}{EI_5} \tag{6.4}$$

$$\frac{\Delta}{P} = \frac{h_1}{EI_1} + \frac{h_2}{EI_2} + \frac{h_3}{EI_3} + \frac{h_4}{EI_4} + \frac{h_5}{EI_5} \tag{6.5}$$

The above formulation seems to be straightforward and rational, however the involvement of "double regression" makes it questionable theoretically. Specifically, if Eq. (6.6) is equivalent to

$$y_i = x_{i1}\theta_1 + x_{i2}\theta_2 + x_{i3}\theta_3 + x_{i4}\theta_4 + x_{i5}\theta_5 \tag{6.6}$$

and then

$$Y = X^T\Theta \tag{6.7}$$

Then, the concerns are as follows:

- What exactly should be the input and output to the system being modelled, respectively?
- If y_i were indeed an output, why would it depend on both the input P and Δ? If x's were truly inputs, why would these be fixed anyway, i.e., not being measurement-dependent?
- The double regression indeed reveals some contradiction for this formulation: In the first round of regression to obtain $\frac{P}{\Delta}$, the error can be assumed Gaussian. How should this error be considered into the implementation of Eq. (6.5)? Or, what kind of error distribution is anticipated for Eq. (6.5)?

6.1.1.2 Literature review

The following writing is a summary of what Dr. Pei learned and understood from her work in function approximation using multilayer feedforward neural networks from 2010 to 2012, which directly inspires this research.

On pp. 384 of Watanabe (2007) under the left column: "If a learning machine is a regression model using a parametric function $f(x, w)$

$$p(y|x, w) \propto exp\left(-\frac{1}{2}(y - f(x, w))^2\right) \tag{6.8}$$

Then the Fisher information matrix is equal to

$$I_{ij}(w) = \int \partial_i f(x, w)\partial_j f(x, w)p(y|x, w)q(x)dx \tag{6.9}$$

where $\partial i = (\partial/\partial wi)$. The Fisher information matrix is positive definite if and only if $\{\partial if(x, w)\}$ is linearly independent.

Table 6.1: Nomenclature used in Amari et al. (2006)

Parameter	Symbol
Input vector	$\vec{x}$
Output vector	y
Input-output pair	$(\vec{x}, y)$
Parameter vector	$\vec{\theta}$
Parameter space	$M = \{\vec{\theta}\}$
Expectation of y give x	$\mathcal{E}[y]$
Average output function	$f(\vec{x}, \vec{\theta})$
PDF of input-output pair	$p(\mathrm{y}, \vec{x}, \vec{\theta}) = \frac{1}{\sqrt{2\pi}} q(\vec{x}) exp\left\{-\frac{1}{2}\left(y - f(\vec{x}, \vec{\theta})\right)^2\right\}$
Log likelihood function	$l(\mathrm{y}, \vec{x}, \vec{\theta}) = logp(\mathrm{y}, \vec{x}, \vec{\theta}) = -\frac{1}{2}\left(y - f(\vec{x}, \vec{\theta})\right)^2 + logq(\vec{x})$
Fisher information matrix	$G(\vec{\theta}) = \mathcal{E}\left[\frac{\partial l(\mathrm{y}, \vec{x}, \vec{\theta})}{\partial \vec{\theta}} \frac{\partial l(\mathrm{y}, \vec{x}, \vec{\theta})}{\partial \vec{\theta}}^T\right]$

A learning machine is called regular if $I(w)$ is positive definite for an arbitrary w. If otherwise, then the learning machine is called singular. In a singular learning machine, there exists a parameter w such that $det\ I(w) = 0$. Such a parameter is called a singularity of the Fisher information matrix. At a singularity of the Fisher information matrix, the likelihood function cannot be approximated by any quadratic form of the parameter."

Also, on pp. 384 of Watanabe (2007) under the right column: "The normal distribution ... is regular, whereas its mixture ... is singular. In general, if a learning machine has a layered structure or a hidden variable, then it is singular, in general."

6.1.1.3 New idea

The first option may be described as follows: If introducing two new index variables I_x and I_y for the effect of the location of P and Δ on $\bar{M}$ and m, respectively, we have:

$$\underbrace{\Delta}_{y}\left(\underbrace{P, I_x, I_y}_{\vec{x}}, \underbrace{\frac{1}{EI_i}}_{\vec{\theta}}\right) \overset{piecewise\ EI}{=} \underbrace{P}_{x_1} \sum_{i=1}^{5} \int_i \bar{M}\left(l, \underbrace{I_x}_{x_2}\right) m\left(l, \underbrace{I_y}_{x_3}\right) dl \underbrace{\frac{1}{EI_i}}_{\vec{\theta}} = f(\vec{x}) \cdot \vec{\theta} \quad (6.10)$$

which seems like:

$$y(\vec{x}, \vec{\theta}) = f(\vec{x}) \cdot \vec{\theta} \quad (6.11)$$

This seems like having a regular Fisher information matrix. HOWEVER, another way of thinking hints the possibility of having either a hidden layer or a mixture of Gaussian as follows:

Let us cast the "double regression" into a proper mathematical description. This is the first stab at this problem:

First regression: For a specified pair of I_x and I_y: $\underbrace{all\ P's}_{\vec{x}}, \underbrace{\frac{P}{\Delta}}_{\vec{\theta}}, \underbrace{all\ \Delta's}_{y}$ (6.12)

Second regression: $\underbrace{all\ I_x's\ \text{and}\ I_y's}_{\vec{x}}, \underbrace{five\ EI's}_{\vec{\theta}}, \underbrace{all\ \frac{P}{\Delta}'s}_{y}$ (6.13)

The aforementioned two ways of thinking consistently point to a strong possibility for this problem to have a singular Fisher information matrix:

i. Can we draw a network using the above analysis of the *first and second regressions*?
   - I cannot yet. Very likely, however, we will need a hidden layer-kind of structure

ii. If the error of $\frac{P}{\Delta}$, in each pair of I_x and I_y of *the first regression* is Gaussian, then, would be all $\frac{P}{\Delta}$'s in *the second regression* a joint Gaussian - the weights can actually be considered a parameter to be identified?

Major research questions/tasks may be given as follows:

1. How can we better understand and formulate this problem - with a sound mathematical analysis as our foundation? We do not need to be mathematicians, but at least we should learn and understand what has been done on this topic so that we are guided and our time will be not spent in vain.

2. Based on Item 1 above, how can we better design and conduct (nondestructive) static flexural tests?

3. Based on Item 2 above, how can we better process the data and program so as to justify the mathematical insights, and possibly, Dr. Jin-Song Pei's initialization vs. commonly used random initialization - This would enable us to do a better job in result interpretation.

6.1.2 "Old" Girder

6.1.2.1 Testing plan

The overall guiding principles are given as follows:

1. Improve the same tests done before. In particular, pay attention to identifying the EI values of the two ends, where there are known damages due to the shear tests done in the past. This will be achieved by not only maximizing the flexibility but also moving the supports to intentionally introduce some zeros in the coefficient matrix.

2. Combine this series of tests with the series of cracking tests for productivity in data processing (for “before, during and after” a change in the system). This explains how the five positions for the loading point were decided: They were selected by Dr. Floyd on June 15, 2014 after examining the profile the harped strands on the girder. This also explains having LVDTs located at $x = 0', \pm 4.5', \pm 8.5'$.

3. Prioritize all possible testing configurations for efficiency and minimization of hummer error. All testing configurations can be sorted according to the location of the loading point as follows:

Primary tests: when the loading point is located at $x = 0'$. See Figure 6.1

Secondary tests: when the loading point is located at $x = \pm 8.5'$. See Figure 6.2

Tertiary tests: when the loading point is located at $x = \pm 4.5'$

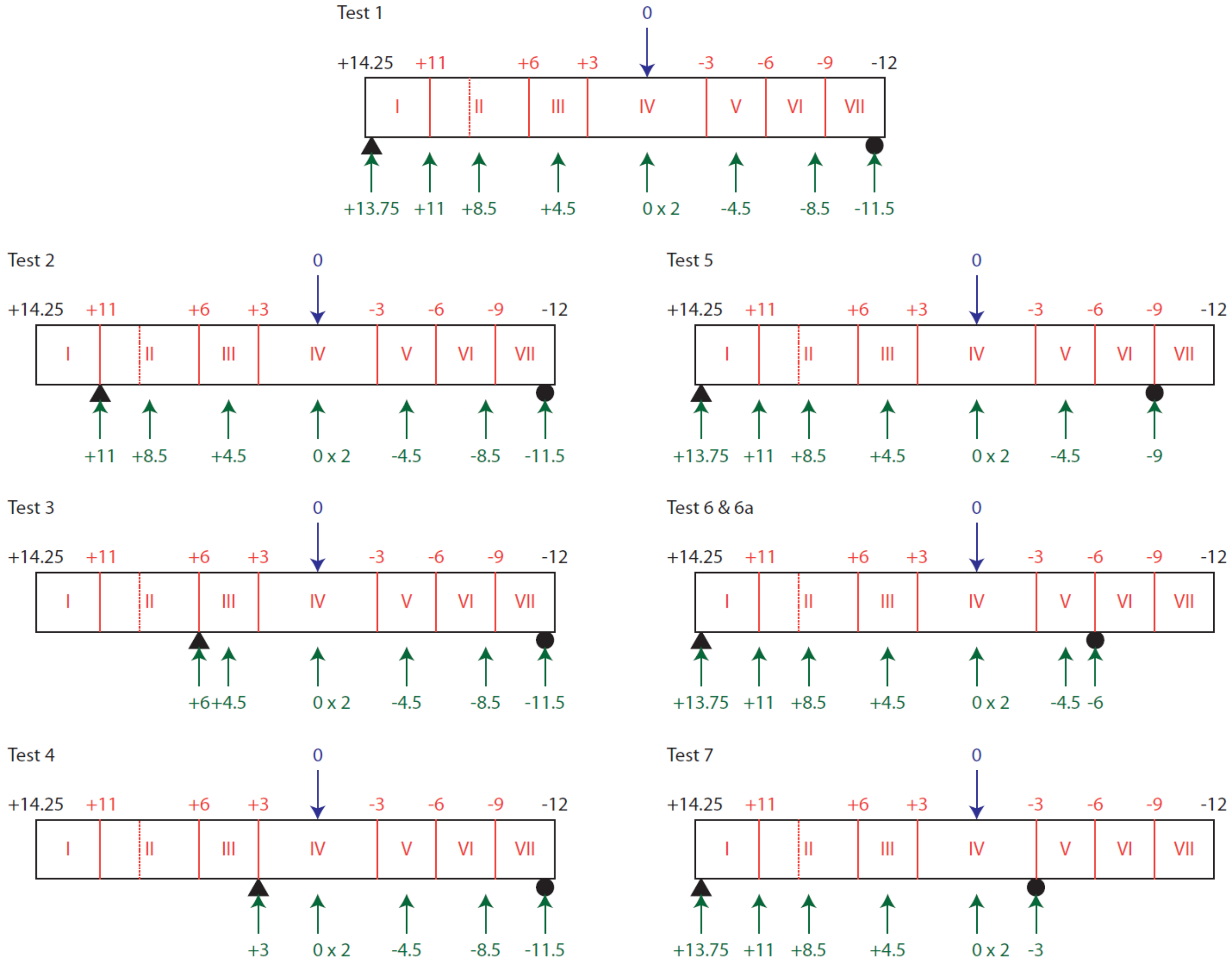

Figure 6.1: Test setup when the loading point is located at $x = 0'$.

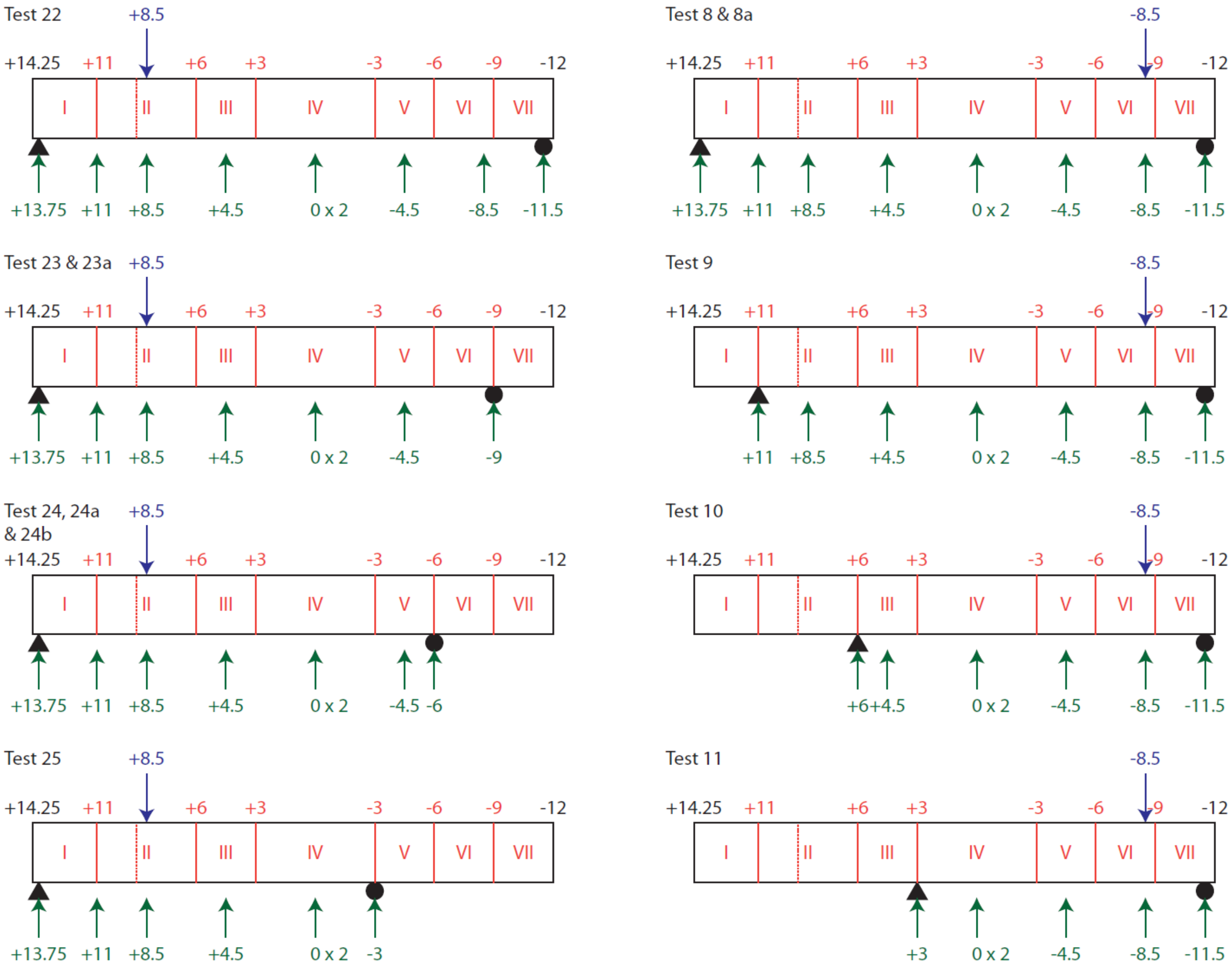

Figure 6.2: Test setup when the loading point is located at $x = \pm 8.5'$, where running through all tests under the same column was efficient.

6.1.2.2 Written notes from testing

The “old” girder was tested for the stiffness of the girder. The tests were carried out by measuring the deflection at several points along the beam with different load points and support locations. The girder was placed on steel rollers for the support locations for all tests except test 26. For test 26, the girder was placed on concrete blocks with 8 in. by 18 in. by 1 in. thick neoprene pads in between the girder and concrete block. The beam was loaded to approximately 15,000 pounds, then unloaded for each test. BDI model ST-350 strain gauges were placed on the outside of the flange near the bottom of the beam on each side under the load point to measure the strain. Each test had the strain gauge 1276 at the back side of the beam, and strain gauge 1282 at the front of the beam.

The ends of the beam had been previously cut leaving it unsymmetrical about the original center line. As placed in the load frame, the beam extended 14.25 ft to the left (North) and 12 ft to the right (South). A grid drawn on the face of the beam was marked at the center line and every 3 in. increment. To the left of the centerline was marked as positive distance, and to the right of the centerline was marked as negative distance.

LVDTs were placed under the beam along the center of the bottom of the beam to measure deflection at specified points. LVDTs C1 and C2 were placed 10.625 inches apart and split the center line with roughly 3 inches on each side to the edge of the beam. C1 and C2 were placed off of the center line to account for any torsion of the beam during loading. Each test was carried out the same way unless otherwise mentioned below.

When test 8 was completed, the LVDT R3 at the right support was stuck and did not compress or extend. Therefore, the LVDT was lubricated and checked. Test 8a was performed to get deflection measurements at the right support.

6.1.2.3 Preprocessing results

A sample preprocessing result is given in Figure 6.3.

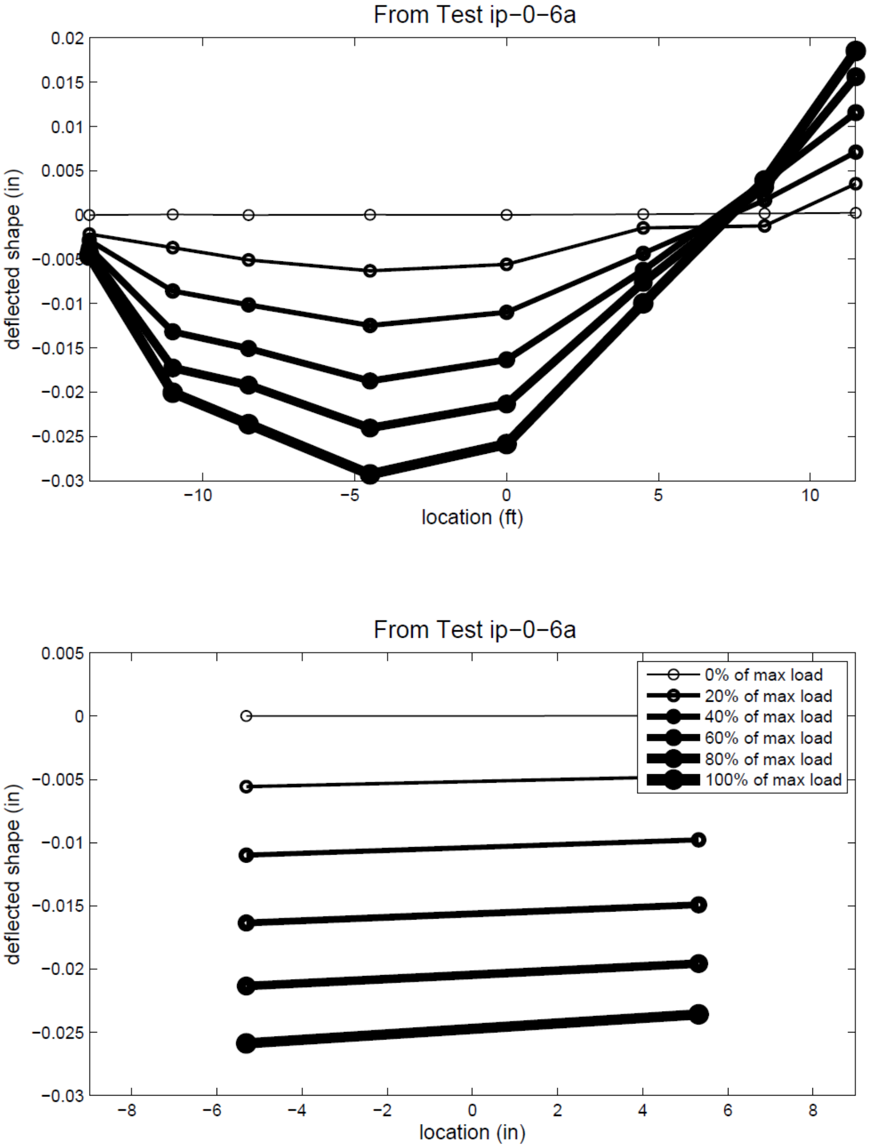

Figure 6.3: A sample preprocessed result when the loading point is located at $x = 0'$.

6.1.3 Girder A

The rationale for decision making is given as follows:

1. We follow the principle for testing the old girder for inverse problem in July of 2014 by moving the supports progressively to intentionally introduce some zeros in the coefficient matrix and by measuring both deflection and lifting along the length of the girder.

2. Given the massiveness and the ultimate importance for shear capacity of Girder A, the number of these tests has to cut down.

3. The division of the EI “zones” is not based on possible damage status as for the old girder. Rather, it is based on the location of the harping points, and reinforcement distribution. In particular, Dr. Floyd wrote on August 6, 2014 that “The U1 bars in the web ... extend only 2’ 4”. The U bars in the bottom flange extend 1’ 10.5” and the L bars nearest the girder soffit extend 3’ 3” with all beginning 2” from the beam end. This would mean the last of the end zone reinforcement would be about 3.5 ft from the end of the beam.” The harping points were measured to be 4.5’ north and south, however it would be nice to stay consistent with how the shear tests would be supported. In addition, the division of the EI zones is merely an approximation of a continuous EI variation along the length of the girder.

4. Since there would be no “cracking tests” to match results with and more importantly, for efficiency of moving the massive Girder A, two out of the three loading points “coincide” with the loading points with those for the future shear tests.

6.1.4 Concluding Remarks

This section has provided a technical overview of the motivations, details, and significance of the improvements made to the identification of flexural rigidity in a piecewise manner for system identification and damage detection purpose.

6.2 Other Inverse Problems: “Cracking Moment Tests”

6.2.1 Overview

Beyond the scope of the proposal, this idea was initiated as a possible method for determining effective prestress for the aged bridge girders. It was determined that measurement of effective prestress and concrete tensile strength was possible using cracking moment tests at two different locations, one within the harped strand portion of the girder and one within the central portion of the girder where all strands were at an equal eccentricity. The different eccentricities of the strands at these two locations would produce different stress distributions within the girders and would, in theory, result in different cracking moments. A set of two equations was developed based on this idea and the stress distributions at each of the two locations. Plans were originally made to perform cracking moment tests on girder A, girder C, and the “old” girder already at Fears Lab to use in determining effective prestress. The plans for all girders were modified due to concerns that cracks would cause problems for both the elastic flexural tests and subsequent shear tests. The cracking moment tests for girder A and girder C were instead incorporated with the measurements taken during shear testing. The cracking moment test for the “old” girder was also conducted, but results were inconclusive due to existing shear cracks near the ends of the beam.

6.2.2 Small-Scale Beams

In order to test the feasibility of the overall idea, two small-scale prestressed beam specimens were tested multiple times to cracking in the upright and inverted orientation to create different stress distributions within the girder and simulate different stress conditions within the girder. These beams were available from a previous project and were labeled SS1 and SS2. The experimental cracking moment along with section properties of the beam can be entered into Eq. (6.14) for the upright beam tests and Eq. (6.15) for the inverted beam tests. The two equations can then be solved using the tensile strength of the bottom fiber, f_r (ksi), to calculate the effective prestress, f_{se} (ksi). The effective prestress for the beams could then be compared to the calculate prestress in Wendling (2014). The beams tested for the small scale testing correlates to beams 23 and 24 of Wending (2014). Eq. (6.14) and Eq. (6.15) could also be used to calculate the effective prestress of the “old” girder and girder A if the equations accurately calculated the effective prestress of a known specimen.

$$f_r = -\frac{f_{se}A_{ps}}{A_g} - \frac{f_{se}A_{ps}e y_{bot}}{I_g} + \frac{\frac{w_d x}{2}(L-x)y_{bot}}{I_g} + \frac{M_{cr}y_{bot}}{I_g} \tag{6.14}$$

$$f_r = -\frac{f_{se}A_{ps}}{A_g} + \frac{f_{se}A_{ps}e(h-y_{bot})}{I_g} + \frac{\frac{w_d x}{2}(L-x)(h-y_{bot})}{I_g} + \frac{M_{cr}(h-y_{bot})}{I_g} \tag{6.15}$$

Where:
A_{ps} = cross-sectional area of the prestressing strands (in^2)
A_g = gross cross-sectional area (in^2)
e = distance between the centroid of the prestressing strands and the centroid of the girder (in.)
y_{bot} = distance from the bottom of the girder to the centroid of the girder cross-section (in.)
I_g = gross moment of inertia of the section (in^4)
w_d = dead load per linear inch at the section under consideration (kips/in)
x = location under consideration (in.)
L = length of the beam (in.)
M_{cr} = measured cracking moment from the flexural test (kip-in)
h = height of the beam (in.)

Each beam had the same 6 in. by 14 in. by 8 ft dimensions and one 0.6 in. prestressing strand 2 in. from the bottom of the beam. Both beams were observed to have longitudinal cracks at the as-cast bottom of the beam.

Each beam was tested in the upright position (with the strand at the bottom of the beam), labeled ‘u’, and the inverted position (with the strand at the top of the beam), labeled ‘i’. Each beam was loaded to cracking, unloaded, and then reloaded to reopen the crack. The tests where the beam was first cracked were labeled with an ‘a’. The tests where the crack was reopened were labeled with a ‘b’ and in one case, where the crack was reopened a second time, labeled ‘c’. A BDI Model ST-350 strain gauge mounted on each side of the beam near the bottom at midspan was used to measure the strain at a crack location. Six wire potentiometers (wire pots) were used to measure the deflection of the beam. Two wire pots were placed at midspan and two were placed at each third point of the span. A Trans-Tek Model 353 LVDT was clamped to the strand and used to measure end slip at each end of the beam. A single load cell was placed between the hydraulic ram and the spreader beam in order to measure the load. All instruments were connected to and read by a single data acquisition system as the test was also intended to test the data acquisition equipment.

Each beam was loaded with 2.5-kip increments, and the cracks observed were marked and labeled with the corresponding load between increments. The load for the first beam was applied using third-point loading as shown in Figure 6.4(a). The third point loading was a difficult configuration to predict where the first crack would initiate. Therefore, the load configuration was changed to a single point load at midspan for the second beam to force a crack through the center. The loading configuration for the second beam is shown in Figure 6.4(b). For this configuration both rollers were used at the single location in order to provide a stable load transfer between the spreader beam and the bearing plate.

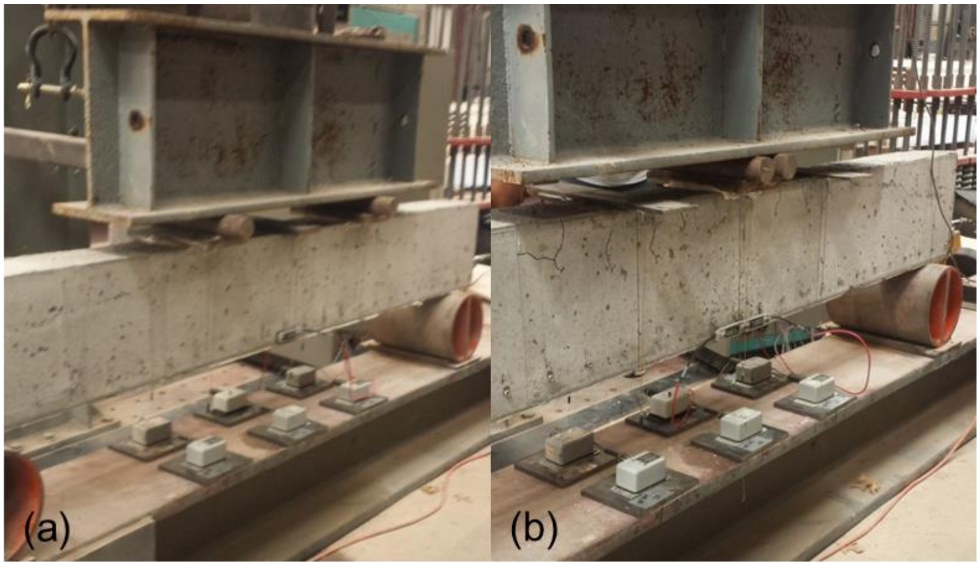

Figure 6.4: Loading configuration of each beam – (a) third point and (b) single point at midspan

The first beam was tested first with the prestressing strand at the bottom (SS1-ua and SS1-ub). For test SS1-ua, the first crack was observed between the load increments of 15 and 17.5 kips. The strain gauges were not covering a crack so they were moved to cover a visible crack between tests SS1-ua and SS1-ub. The crack crossed by the strain gauges was located outside the south third point. Test SS1-ub was performed in the same manner as SS1-ua to reopen the cracks covered by strain gauges. Beam SS2 was first tested with the prestressing strand at the bottom (SS2-ua and SS2-ub). Since it was difficult to predict the location where the crack would propagate, the strain gauges were both placed on the front side at midspan end to end for SS2-ua, as pictured in Figure 6.5. No cracks occurred through the two strain gauges during test SS2-ua, so the strain gauges were placed on each side over the same crack for test SS2-ub. The strain gauges were not placed properly on the beam for Test SS2-ub. One strain gauge, labeled 1282, was not bolted onto the mounting tabs tightly enough and the mounting tabs for the other strain gauge, labeled 1399, did not stay bonded to the beam. Therefore, test SS2-uc the bolts for strain gauge 1282 were tightened and the test was run without strain gauge 1399. The tests of the inverted beams did not provide useful information due to pre-existing cracks at the top of the beams related to the initial prestress. Therefore, the upright beam test results were used along with the estimated tensile strength of the concrete to evaluate effective prestress.

Figure 6.5: Strain gauge placement for SS2-ua

Plots of load versus deflection and load versus slip were utilized to determine the load at cracking. The two equations developed for the different stress states were then used with the measured load and estimated concrete tensile strength to estimate the effective prestress. The measured cracking moments were 21.3 kip-ft and 27.1 kip-ft for tests SS1-ua and SS2-ua, respectively. These cracking moments corresponded to and effective prestress of 87.0 ksi and 131.3 ksi for beams SS1 and SS2, respectively. While these values were significantly less than the prestress measured by Wendling (2014), they indicated potential for the method. The tests of the small-scale beams also allowed for testing and refinement of the data acquisition system.

6.2.3 "Old" Girder

The cracking load and moment for the "old" girder was 119 kips and 684 kip-ft, respectively. The load versus deflection is shown in Figure 6.6. When the neoprene pads were used, the deflection was determined by normalizing each wire pot with the LVDTs from each support and then averaging the two. The thin gray line in Figure 6.6 is the data recorded by the data acquisition system, and the thick black line is the deflection observed visually using a ruler and laser level during testing.

The cracking moment for "old" girder was higher than expected. The cracks from previous shear tests (Pei et al., 2008) at the ends of the girder re-opened before flexural cracks were observed at the midspan of the girder, resulting in a higher applied load to cause flexural cracking. The expected cracking moment for the girder was 500 kip-ft determined analyzing stresses based on estimated effective prestress and concrete tensile strength. The effective prestress estimated using the higher cracking moment was significantly larger than larger than the 270 ksi tensile strength of the strand indicating that this value was not correct, while the value of effective prestress used to calculate the estimated cracking moment was 162 ksi.

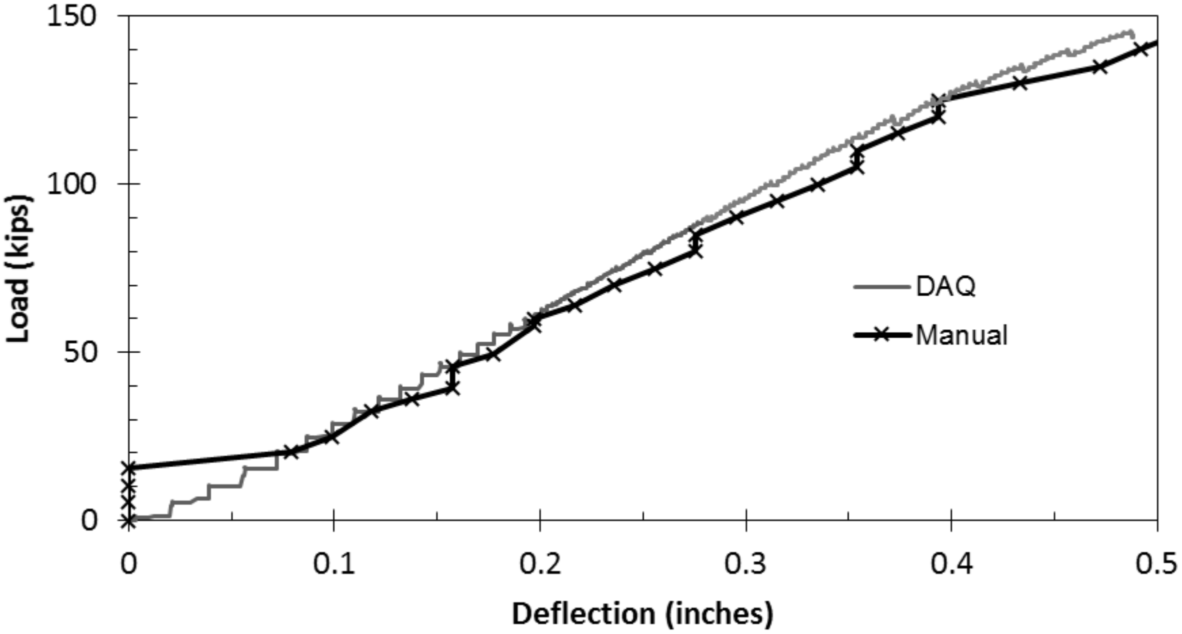

Figure 6.6: Load versus deflection at midspan for the cracking moment of the "old" girder

6.2.4 Girder "A"

For test A1, the instrumentation intended to measure the deflection under the load point malfunctioned and did not provide useful data. Therefore, the cracking load could not be determined from data recorded by the data acquisition system and only the observed value was available. The cracking load was observed at approximately 170 kips which correlates with a cracking moment of 760 kip-ft.

The load versus deflection plot for test A2, shown in Figure 2.33, was used to identify the cracking moment from test A2. The cracking load determined from the point where the slope changes on the plot was 190 kips. The value for cracking load determined from the load-deflection results was the same as the observed cracking load. The corresponding cracking moment was 790 kip-ft.

The initial prestress for girder A calculated from the 28.8 kips required strand tension given on the plans obtained from ODOT was 188 ksi. The values obtained from the measured cracking moments from tests A1 and A2 and estimated concrete tensile strength based on the relationship with the compressive strength of cores taken from the girder were 183 ksi and 197 ksi, respectively. This can be partially explained by a larger concrete tensile strength in the actual girder than that estimated using the concrete compressive strength measured using cores taken from the girder. While the actual values obtained were inconclusive, they showed merit for using the method.

6.2.5 Girder “C”

The cracking moments for tests C1 and C2 were determined from the load versus deflection relationships and confirmed using visual measurements as described for girder A. The cracking loads for these two tests were 160 kips and 150 kips, and the corresponding cracking moments were 922 kip-ft and 1017 kip-ft. These cracking moments result in an estimated effective prestress of 129.5 ksi and 144.5 ksi based on a concrete tensile strength estimated using the compressive strength of the cores. The initial prestress for girder C listed on the plans provided by ODOT was the same 188 ksi as for girder A. The values determined using the measured cracking moments were in the same range as the 150 ksi determined using the AASHTO LRFD method. Differences between the two values are related to the fact that tensile strength may not be constant across the entire girder, may differ from the estimated value, and that the first observed cracks were due to shear and not flexure.

6.3 Other Inverse Problems: “Camber Measurements”

6.3.1 Overview

Camber was measured for both girder A and the “old” girder for use in estimating the effective prestress. Before the camber of each girder was measured, the girder was marked where the camber measurements would be taken. Several methods for measuring camber were evaluated. The methods chosen for this purpose included using a taut string and using surveying equipment. The string was passed under the girder and anchored at the supports to provide a baseline at the elevation of the beam supports. Measurements between the girder soffit and the string were then taken to be the camber at each location. A steel ruler with gradations of one sixteenth of an inch was used to measure the camber. The ruler was held with the zero end flush to the bottom of the girder, and the measurement was taken from the top of the string. The camber was also measured using a surveying level and a survey rod consisting of a scale attached to a carpenter’s square. A short bubble level was attached to the square to align the rod in one axis vertically while the square was used to align the rod in the other direction by placing the horizontal leg flush with the soffit of the girder at the desired measurement location.

The survey level was placed as closely to equidistant from each location as possible. The tripod was leveled using several bubble levels on the instrument. Once the instrument was leveled, the survey rod was placed in the first location. The survey rod was placed with the square flush to the bottom of the girder and the level was used to straighten the square and ensure that it was vertical. The surveyor looked through the lens at the crosshairs and placed them on the survey rod. The horizontal line corresponded to a number on the scale, which was recorded for each location. The end values were then used to create a zero line between the two supports and normalize the measurements.

Significant difficulties were encountered using the survey method for the “old” girder due to limited space and sight distances within the lab. The string method was therefore used for the remaining measurements. Difficulties were encountered for both methods for girder A due to the fact that the soffit of the girder was very uneven. The described method was adjusted to correct this problem by moving the measurement reference to the point where the top flange intersected the beam web.

The prestressing strand configurations were used to develop relationships between the prestress force and camber of each girder. The asymmetrical strand profile of the “old” girder and creep effects caused substantial difficulty in obtaining a reasonable estimate prestress force from the camber measurements.

6.3.2 Small-Scale Beams

The camber for each small-scale beam was measured using the string method. The camber measurements were then used along with PCI (2010) equations for camber including creep coefficients (Eq. 6.16) to determine the effective prestress.

$$\Delta = 2.45\left(\frac{f_{se}A_{ps}eL^2}{8EI_{cr}}\right) - 2.7\left(\frac{5w_dAL^4}{384EI_{cr}}\right) \tag{6.16}$$

where:
Δ = measured camber (in.)
f_{se} = effective prestress (ksi)
A_{ps} = cross-sectional area of the prestressing strands (in^2)
e = eccentricity from centroid of prestressing strands to centroid of concrete (in.)
L = length of beam (in.)
E = modulus of elasticity of the concrete (ksi)
I_{cr} = moment of inertia of a cracked section (in^4) calculated using Eq. (6.17)
w_d = dead load per cubic inch at the section under consideration (k/in^3)
A = cross-sectional area of concrete (in^2)

$$I_{cr} = n\rho_p(1 - 1.6\sqrt{n\rho_p})(bd_p{}^3) \qquad (6.17)$$

where:

n = ratio of prestressing steel modulus of elasticity to concrete modulus of elasticity

ρ_p = ratio of area of prestressing steel effective area of concrete $(\frac{A_{ps}}{bd_p})$

b = width of the concrete cross-section

d_p = depth to centroid of the prestressing steel

The camber measurements taken from specimen SS2, and representative of both beams, are shown in Table 6.2. An effective prestress of 117.4 ksi was determined using the camber measurements and Eq. (6.16). This value is significantly less than the effective prestress of 154 ksi measured in Wendling (2014). Using the camber equation and 154 ksi for the effective prestress, the deflection calculated is 0.381 in. which is more than double the measured camber. This result may be partially due to differences in creep coefficient.

Table 6.2: Camber Measurements for the Small-Scale beam, SS2 at Various Locations Along the Beam Length

Person	North Support (in.)	North Third (in.)	Midspan (in.)	South Third (in.)	South Support (in.)
Person 1	0	0.125	0.156	0.125	0
Person 2	0	0.156	0.188	0.156	0
Average	0	0.141	0.172	0.141	0

6.3.3 “Old” Girder

Measurements were taken at six locations for the “old” girder, shown in Figure 6.7, in order to measure the camber along the length of the girder. The six locations were chosen to be the two supports, the location where the harping of the strands ended, the center of the girder, and the center of the section between the harping points.

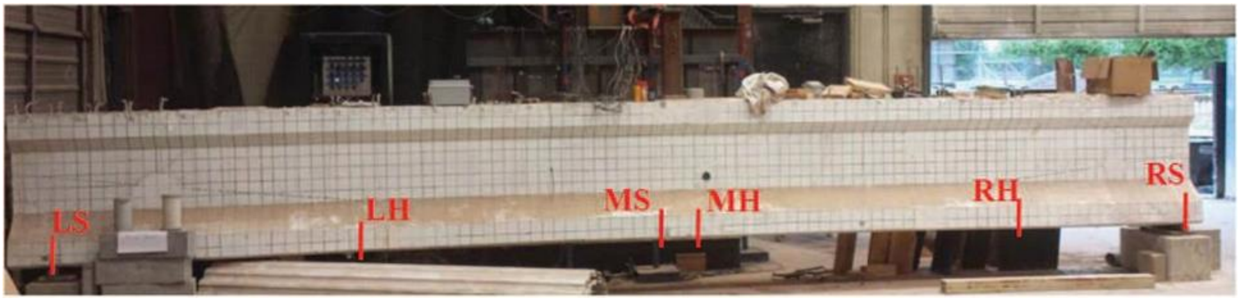

Figure 6.7: Locations for camber measurements

The equation used for calculating the effective prestress using the camber measurements, Eq. (6.18), was derived from the PCI Handbook (PCI, 2010). The multipliers are creep coefficients to take into account the change of camber over time.

The cut portion of the equation was modified to take into account the girder being cut unsymmetrically after years of service. The camber measurements are shown in Table 6.3 for the string method and the level method with the normalized values in Table 6.4. For precision and to eliminate bias by the individual taking the measurements, two individuals took measurements of the camber of the girder.

$$\begin{aligned}
\Delta &= \Delta_{with\ deck} + \Delta_{without\ deck\ and\ ends\ cut} \\
&= \left[2.2\left(\frac{P_o}{8EI}\right)\left(eL^2 + e_oL^2 + e'(L^2 - 1.33a^2)\right) - \left(2.4A_{girder} + 2.3A_{deck}\right)\left(\frac{5w_dL^4}{384EI}\right)\right]_{w/\ deck} \qquad (6.18) \\
&\quad + \left[\left(\frac{P_o}{8EI}\right)\left(eL^2 + e_oL^2 + e'(L^2 - 1.33a^2)\right) - \left(A_{girder} + A_{deck}\right)\left(\frac{5w_dL^4}{384EI}\right)\right. \\
&\quad - \left(\frac{P_o}{12EI}\right)\left(\frac{e_1'(L_{cut} - a_1)\left[0.75{L_{cut}}^2 - (L_{cut} - a_1)^2\right]}{a_1}\right. \\
&\quad \left. - \frac{e_2'(L_{cut} - a_2)\left[0.75{L_{cut}}^2 - (L_{cut} - a_2)^2\right]}{a_2}\right) - \left(\frac{P_oe_{o,1}{L_{cut}}^2}{8EI}\right) - \left(\frac{P_oe{L_{cut}}^2}{8EI}\right) \\
&\quad \left. + \left(\frac{5w_dA_{girder}{L_{cut}}^4}{384EI}\right)\right]_{cut}
\end{aligned}$$

Where:

Δ = measured camber (in.)

P_o = effective prestress force (kips)

E = modulus of elasticity of the concrete (ksi)

I = moment of inertia (in^4)

e = eccentricity from centroid of straight prestressing strands to centroid of concrete (in.)

e_o = eccentricity from centroid of harped prestressing strands at ends to centroid of concrete (in.)

e' = change in height of harped prestressing strands from end to straightening point (in.)

L = length of beam (in.)

a = horizontal length of the harped prestressing strands (in.)

w_d = dead load per cubic inch at the section under consideration (k/in^3)

A = cross-sectional area of concrete (in^2)

e_1' = change in height of harped prestressing strands from cut end to straightening (in.)

e_2' = change in height of harped prestressing strands from the other cut end to straightening ($e_1' > e_2'$) (in.)

L_{cut} = length of beam after cut (in.)

Table 6.3: Camber Measurements for the “old” Girder Using the String Method at Locations Corresponding to Figure 6.7

Person	LS (in.)	LH (in.)	MS (in.)	MH (in.)	RH (in.)	RS (in.)
1	0	0.813	1.125	1.125	0.500	0
2	0	0.813	1.125	1.125	0.563	0
Average	0	0.813	1.125	1.125	0.532	0

Table 6.4: Camber Measurements for the “old” Girder Using the Level Method at Locations Corresponding to Figure 6.7

Person	LS (in.)	LH (in.)	MS (in.)	MH (in.)	RH (in.)	RS (in.)
1	0	0.735	1.032	1.029	0.637	0
2	0	0.610	0.844	0.842	0.449	0
Average	0	0.673	0.938	0.936	0.543	0

Unlike the string method, the two sets of measurements for the level method differ by about one to two tenths of an inch. Comparing the normalized camber measurements to the string measurements, Person 1 had better consistency for the camber measurements. The effective prestress determined using the camber measurements was 301 ksi for the string method and 259 ksi for the level method. The tensile strength for the strands is 270 ksi and is not possible for the effective prestress to be greater than ultimate strength. If an estimated prestress of 162 ksi was determined using prestress loss prediction methods, the expected camber was 0.504 in. This deflection is approximately half of the measured values and indicates that the modifications for creep may not effectively account for behavior over time. The damage and modifications made to this girder likely also contributed to the large discrepancy.

6.3.4 Girder “A”

Camber measurements for girder A were taken at a number of grid points along the length of the beam in addition to midspan. The camber could not be accurately measured from the bottom of the girder because the bottom surface was determined to be uneven. The camber was determined using a chalk line placed on the girder. At each end of the girder, the string was held at the top of the web above the support and plucked to leave a chalk line on the girder. The camber was measured from the chalk line to the girded line. Eq. (6.19), from PCI (2010) along with corresponding creep coefficient multipliers, was used along with the midspan camber measurements to estimate the effective prestress.

$$\begin{aligned}\Delta &= 2.2\left(\frac{P_o}{8EI}\right)\left(eL^2 + e_oL^2 + e'(L^2 - 1.33a^2)\right)\\ &-\left(2.4A_{girder} + (2.3-1)A_{deck} + A_{deck,remaining}\right)\left(\frac{5w_dL^4}{384EI}\right) \qquad (6.19)\end{aligned}$$

where:

Δ = measured camber (in.)

P_o = effective prestress force (kips)

E = modulus of elasticity of the concrete (ksi)

I = moment of inertia (in^4)

e = eccentricity from centroid of straight prestressing strands to centroid of concrete (in.)
e_o = eccentricity from centroid of harped prestressing strands at ends to centroid of concrete (in.)

Table 6.5 displays the camber measurements taken before testing. For precision and to eliminate bias by the individual taking the measurements, two people took camber measurements on the girder. The calculated effective prestress for the girder was found to be greater than the tensile strength of the prestressing strands. If the effective prestress of 167 ksi determined using the AASHTO methods for prestress loss is used, the deflection should be 0.138 in. which is seven times less than the measured deflection. The large difference in predicted and measured camber and effective prestress are due to inaccuracy in creep coefficients and errors in the methods used. The method used to measure the camber was difficult to keep consistent due to difficulty in monitoring the tension of the string.

Table 6.5: Camber Measurements for Girder A at Various Grid Point Locations (all values in in.)

Person	N11.5	N7.5	N4.5	N4	MS	S4	S4.5	S7.5	S11.5
1	0.281	0.625	0.813	0.844	0.938	0.750	0.719	0.531	0.438
2	0.344	0.625	0.781	0.750	0.875	0.750	0.688	0.531	0.281
Average	0.313	0.625	0.797	0.797	0.907	0.750	0.704	0.531	0.359

7. Small-Scale Section Testing

7.1 Overview

Eight approximately half-scale prestressed beams designed to mimic the configurations of girder A and girder C were cast to provide additional information on the behavior of the composite bridge section compared to the individual girders. Shear tests were conducted on individual beam specimens with a composite deck section matching girder A and girder C and a scaled bridge section consisting of 4 beam lines with a composite deck cast between all beams was constructed and tested. All beams were simply supported on neoprene bearing pads with a single point load applied directly over the girder web for final shear testing similarly to the tests of girder A and girder C. The composite bridge section was tested using a specially built load frame on the Fears Lab strong floor as it was too wide for the typical load frames. Elastic tests were conducted first with the single point load applied at various locations to examine deflection and load transfer across the composite section. The elastic tests were followed by a test to failure with the single point load placed directly over the first interior girder. The individual small-scale beam tests will be used to connect the behavior of girder A and girder C to the behavior of the small-scale bridge section in order to gain insight into the behavior of a full-scale bridge.

7.2 Beam Design and Construction

7.2.1 Beam Specimens

A comparative analysis of reinforcement configurations was conducted using an approximately half-scale (22.5 in. deep) AASHTO Type II girder cross-section. Multiple reinforcement configurations were considered in order to identify a prestressing strand arrangement which would reasonably replicate the stress state in each of the two girder designs examined in the project (girders A and C). A difference in in-service stresses between the actual girders and the test specimens of less than 20% was targeted in the comparative analysis. Two designs resulted, one corresponding to each original reinforcement configuration. While using small-diameter prestressing strands would have been ideal, the configuration of the prestressing bed hole pattern limited the prestressing reinforcement to only 0.5 in. or 0.6 in. diameter prestressing strands. The compressive stress in service was deemed to be the most important parameter for the design and priority was placed on matching this value to the original girders. The stress state of girder A could be best replicated using two 0.5 in. special prestressing strands tensioned to 186 ksi and the girder C section using two 0.6 in. prestressing strands tensioned to 202.5 ksi. In both cases the strands were located 4 in. from the bottom of the specimen. These configurations resulted in a difference in calculated compression stresses between the full-scale and small-scale designs of 0.8% and 3.1% for the girder A and girder C designs, respectively. The differences in calculated tensile stress were considerably higher, 53% and 77%.

The small scale specimens were analyzed for strength using the same methods described in Section 3.2. The shear reinforcement configuration for the test specimens was scaled to represent that of the original girders based on the percentage contribution of concrete and steel to shear strength. For the original girder A and girder C configurations concrete contributed 30% of the shear strength and steel 70%. The shear reinforcement configuration of the scaled beams was then analyzed and adjusted to provide similar shear capacity and ratio of concrete contribution to steel contribution based on the chosen prestressing strand configurations. Shear reinforcement consisted of No. 3 Z-bars spaced as shown in Figure 7.1, which resulted in a concrete contribution to total shear strength of 26% and steel contribution of 74% for the girder A design and 19% concrete contribution and 81% steel contribution for the girder C design. Both designs were examined at the quarter span point and *d*/2 when calculating these ratios. Uncoated reinforcing steel was chosen to match the original girders.

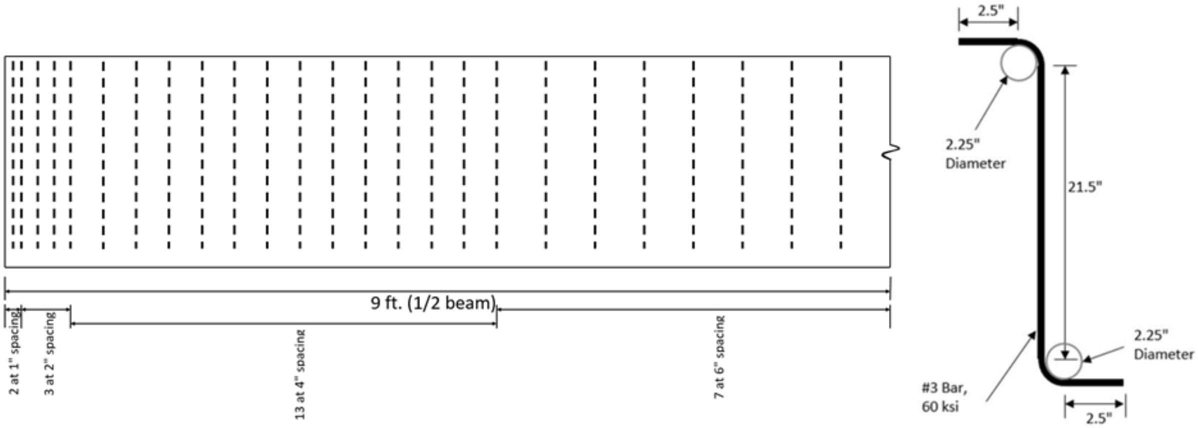

Figure 7.1: Shear reinforcement spacing and details for small-scale beam designs

A similar concrete mixture to the one developed for the small-scale bond testing was identified for use in beam construction, and is shown in Table 7.1. It had a targeted compressive strength of 4000 psi at one day of age and 6000 psi at 28 days. Wooden platforms and steel formwork sides were constructed for casting the beam specimens. The two steel prestressing abutments attached to the strong floor at Fears Lab (Figure 7.2) were used for tensioning the prestressing steel and the length of the prestressing bed allowed for casting two beams at one time. In the days preceding each beam casting, one side of the formwork was put in place and all reinforcing steel was tied in place, as shown in Figure 7.3. The prestressing strands were then tensioned on the day of beam casting. Each set of two beams was cast using a single batch of concrete mixed using equipment and materials at Fears Lab. Slump, temperature, air content and unit weight were measured at the time of casting and 4 in. by 8 in. cylinders were made for compressive strength testing at 1, 7, and 28 days of age. An example of completed beam specimens is shown in Figure 7.4. The specimens were designated by an identifier matching the large scale girder (A or C) that they represented, and a number. Six specimens corresponding to girder A were cast and two specimens corresponding to girder C. The fresh concrete properties and concrete compressive strengths measured for each beam at one and 28 days are shown in Table 7.2.

Table 7.1. Mix Design Used for Scaled Beam Sections

Material	Quantity
Cement (lb/yd^3)	851
Sand (lb/yd^3)	1459
Rock (lb/yd^3)	1372
Water (lb/yd^3)	315
w/c	0.37

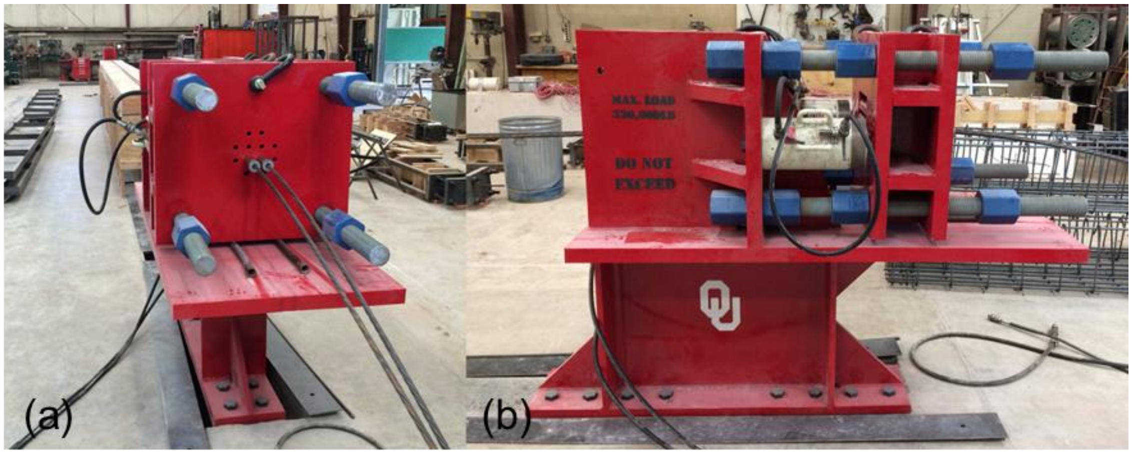

Figure 7.2: (a) View along prestressing bed, and (b) live end prestressing abutment

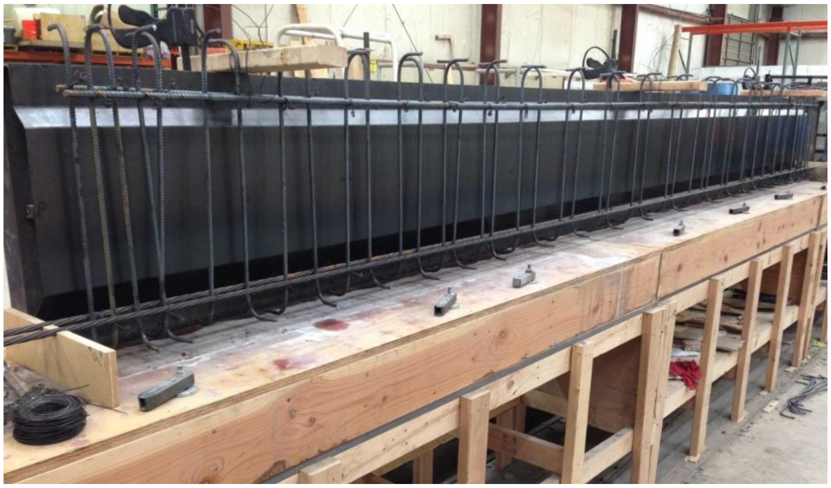

Figure 7.3. Reinforcing steel and formwork in place before beam casting

Figure 7.4: Example of completed beam specimen (A1)

Table 7.2. Concrete Properties for the Scaled Beam Sections

Specimen ID	Slump (in.)	Temp. (°F)	Air (%)	Unit Weight (lb/ft^3)	f'_{ci} (psi)	f'_c (psi)
A1	9.5	65	2.6	148.6	4190	6700
A2	9.5	69	2.7	147.7	4360	6720
A3	9.75	72	2.3	148.4	4200	6250
A4	9.0	76	2.7	147.1	4440	6520
A5	9.5	80	2.3	147.3	4250	5930
A6	9.0	82	2.4	147.5	4300	6100
C1	9.25	79	2.8	148.0	4390	5820
C2	9.75	80	2.4	148.8	4170	5700

7.2.2 Individual Beam Tests

After the scaled girders reached 28 days of age, a composite deck section matching the configuration of either girder A or girder C was cast on top of two of the beams with the corresponding design. The girder A design included a 4.25 in. thick deck section as wide as the top flange and the girder C design included a 4.25 in. thick by 18 in. wide deck section with both end and intermediate diaphragm sections as wide as the deck section. The interface shear reinforcement was carefully checked to ensure adequate load transfer and composite action. The concrete mix design used for the deck sections and the subsequent scale bridge deck was a standard ODOT class AA mix design obtained from Dolese Bros. It achieved a compressive strength of 2630 psi at one day and 4450 psi at 28 days. Overhanging formwork, shown in Figure 7.5 was constructed for each beam and the concrete was placed using a bucket and the Fears Lab overhead crane. A completed beam section is shown in Figure 7.6.

Figure 7.5: (a) Formwork and reinforcing steel for individual girder C sections and (b) formwork and cast concrete for individual scale girder A sections

Figure 7.6: Completed scale girder C section showing end and midspan diaphragm sections

Each individual beam section was tested in shear with a single point load at locations intended to provide similar configurations to girders A and C and to limit the effects of bond loss on the shear tests due to the large diameter of the prestressing strands compared to the section size. The load testing arrangement used for each beam is shown in Figure 7.7. Applied load was measured using a 100 kip capacity load cell placed beneath the load point, deflection was measured using two wire potentiometers placed beneath the load point, LVDTs were placed on the strands at both ends to monitor any strand slip during the tests, and a single BDI strain gauge was placed on the bottom flange at the load point. Load was applied in 5 kip increments until cracking occurred, after this load was applied at 2 kip increments. Cracks were marked on the west side of the girder after each load increment. The beams were simply supported on steel rollers and load was applied through a steel plate placed on a bed of sand to limit the effect of imperfections on the beam surface. In all tests, the supports were placed 4 in. from each end for a total span length of 17 ft 4 in.

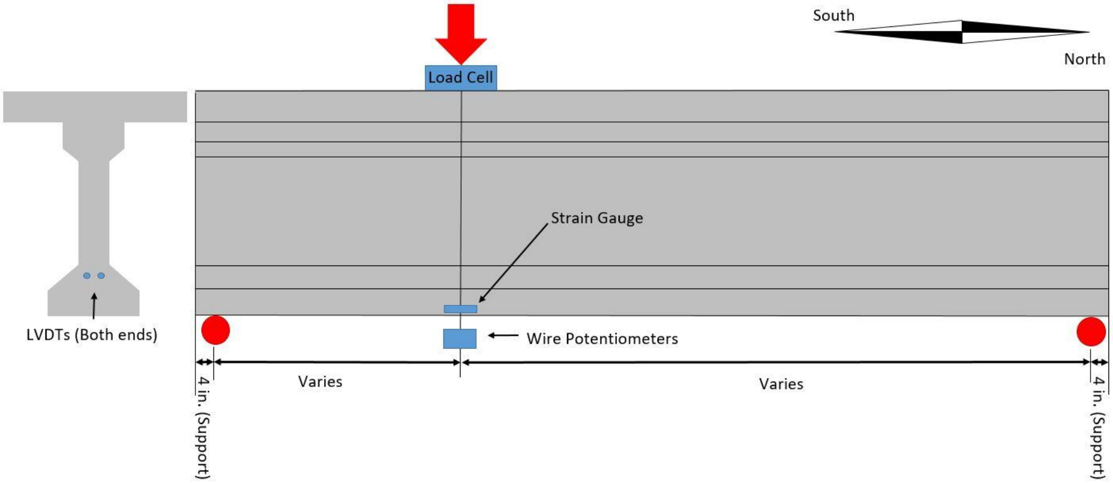

Figure 7.7: Testing setup for scaled individual beam sections

7.2.3 Scale Bridge

An approximately half-scale composite bridge section was designed to mimic the full bridge section on the plans provided by ODOT. It consisted of four girder A design beam lines and a 4.25 in. thick deck. The bridge had a total length of 18 ft and a beam spacing of 3 ft – 10 in. resulting in a total width of 13.5 ft including a 1 ft overhang. The reinforcing steel in the deck was designed to mimic the original bridge configuration and transfer the expected loads between girders. End and midspan diaphragms were included and the beams were tied together through the diaphragms using threaded rods. The diaphragm reinforcement is shown in Figure 7.8.

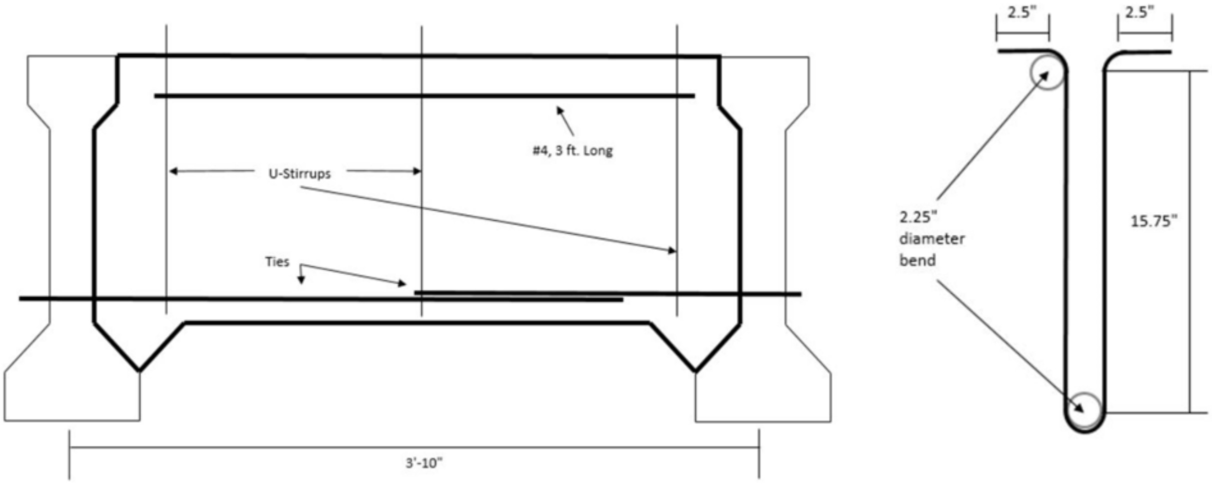

Figure 7.8: Diaphragm reinforcement for scaled bridge section and U-stirrup detail

The scale bridge beams were supported on neoprene bearing pads placed on concrete block supports. Formwork was built between the beams using plywood to mimic expected construction methods at the time the actual bridge was built (see Figures 7.9 and 7.10). The reinforcing steel was placed and held in place using plastic rebar chairs (Figures 7.10 and 7.11). The same class AA concrete provided by Dolese Bros. was used for casting the deck on the bridge section. Concrete was cast using a concrete bucket, vibrated, screeded and given a broom finish. Construction of the deck is shown in Figure 7.12 and the completed section is shown in Figure 7.13. The bridge deck was cured under wet burlap and plastic for seven days, as shown in Figure 7.14. The compressive strength of the deck concrete was 2030 psi at one day of age and 4190 psi at 28 days.

Figure 7.9: Initial framing for scaled bridge deck formwork

Figure 7.10: Completed scaled bridge deck formwork and rebar placement


Figure 7.11: Close-up of scaled bridge deck rebar placement


Figure 7.12: Scaled bridge deck construction

Figure 7.13: Scaled bridge deck section after concrete finishing

Figure 7.14: Plastic and burlap used for curing concrete deck on scaled bridge section

A specially designed steel frame was built over the scale bridge section as the frames already available at Fears Lab were too narrow. The frame and completed bridge is shown in Figure 7.15. This frame was selected over the initial idea of using single anchors to the strong floor and a spreader beam as it allowed more flexibility in elastically loading the bridge specimen. The bridge and frame were arranged so that the load could be applied at the quarter span point.

Figure 7.15: Load testing frame over the scaled bridge section

7.3 Results of Individual Beam Tests

7.3.1 Test C1s

Test C1s was performed at an *a*/*d* ratio of 3.0, corresponding to the *a*/*d* ratio of full scale girder test C1. This *a*/*d* ratio resulted in a load point located at a distance of 71.5 in. from the end of the girder. Load was increased in 5 kip increments until cracking occurred. Initially the girder was quite stiff, with only 0.13 in. of deflection when flexural cracking occurred at a load of 41.5 kips (Figure 7.16). This point is marked on the load-deflection plot given in Figure 7.17, and a change in slope can be noticed. This point is also corroborated by a rapid reduction in strain measured by the strain gauge north of the crack. When cracking occurred, the strain in the bottom flange was approximately 330 microstrain.

After this initial flexural crack, load was increased at 2 kip increments. At a load of 46 kips, shear cracks formed near the supports (highlighted in red in Figure 7.18). The formation of these shear cracks led to strand slip of 0.02 in. for one strand on the south end of the beam. Slip increased from this point to the end of the test, resulting in a maximum slip of 0.52 in. and 0.72 in. for the strands on the loaded end. The test was continued to a maximum applied force of 62.3 kips, at which point the strand slip prevented any increase in load.

The flexural capacity based on strain compatibility at this section was 204.8 k-ft for a point load of 54 kips. The shear capacity using the ACI method at this section was 50.7 kips, which corresponds to a point load of 74 kips. The predicted capacity was exceeded for flexure despite the large amount of recorded slip. The center diaphragm appeared to arrest cracking near midspan, but it is difficult to make definite conclusions since the tests of scaled girders without diaphragms were for a slightly different design. Differences in diaphragm construction over the years may reduce the applicability of any conclusions drawn from these tests as well.

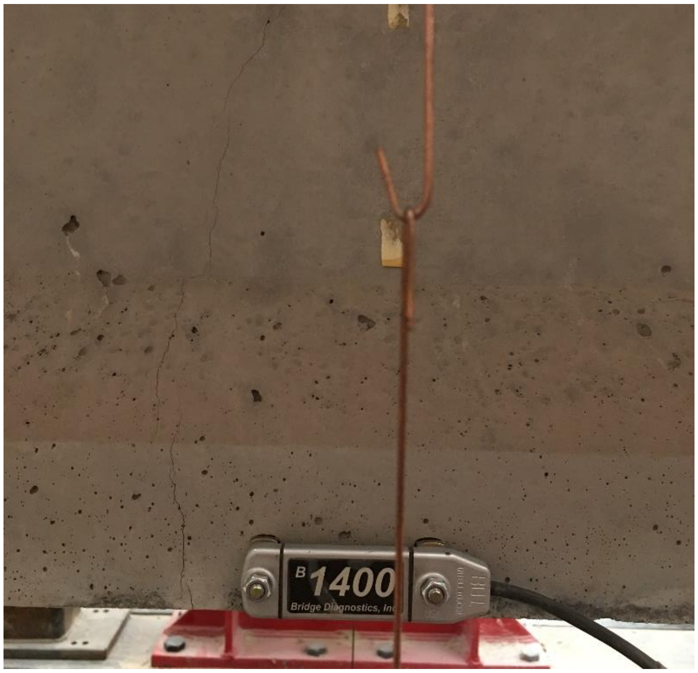

Figure 7.16: Initial flexural crack at 41.5 kips. (Note that the load point is at the center of the strain gauge attached to the bottom flange)

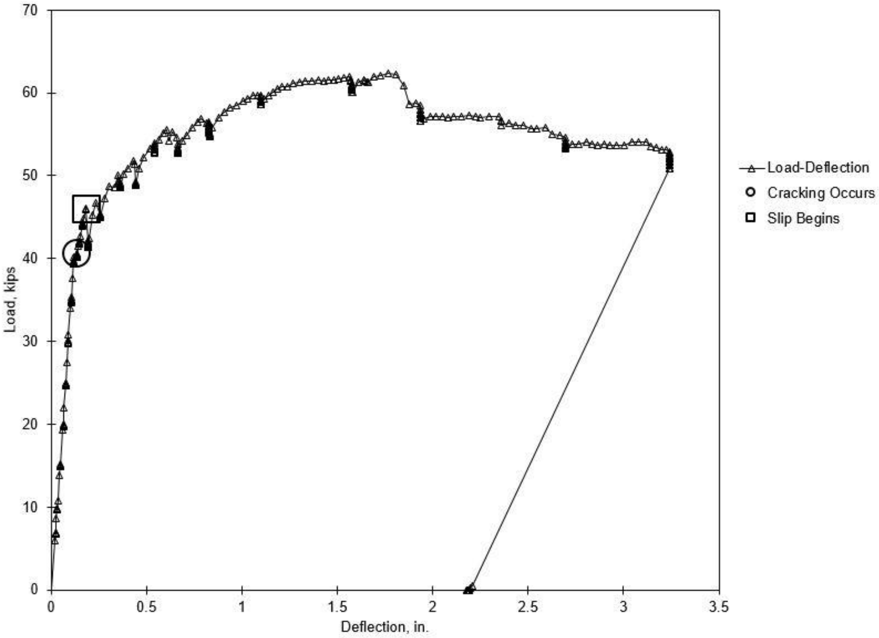

Figure 7.17: Load versus deflection plot for test C1s

Figure 7.18: Final cracking in test C1s (initial shear cracks highlighted with red and black dashed lines)

7.3.2 Test C2s

Test C2s was performed at an *a*/*d* ratio of 2.4, corresponding to the quarter-point of the girder. This location was chosen since this is the location where the scale bridge would be tested. The load point was located at a distance of 54 in. from the end of the girder. As with test C1s, little deflection was measured before cracking. A large shear crack formed at the support at a load of 40.5 kips and 0.09 in. of deflection. This point is marked on the load-deflection plot given in Figure 7.19, and a drop in load occurred due to strand slip. When this shear crack formed, slip of 0.031 and 0.037 in. was observed for the strands on the loaded end. The strain before cracking was 239 microstrain at the load point. The measured strain reduced slightly after each new crack formed.

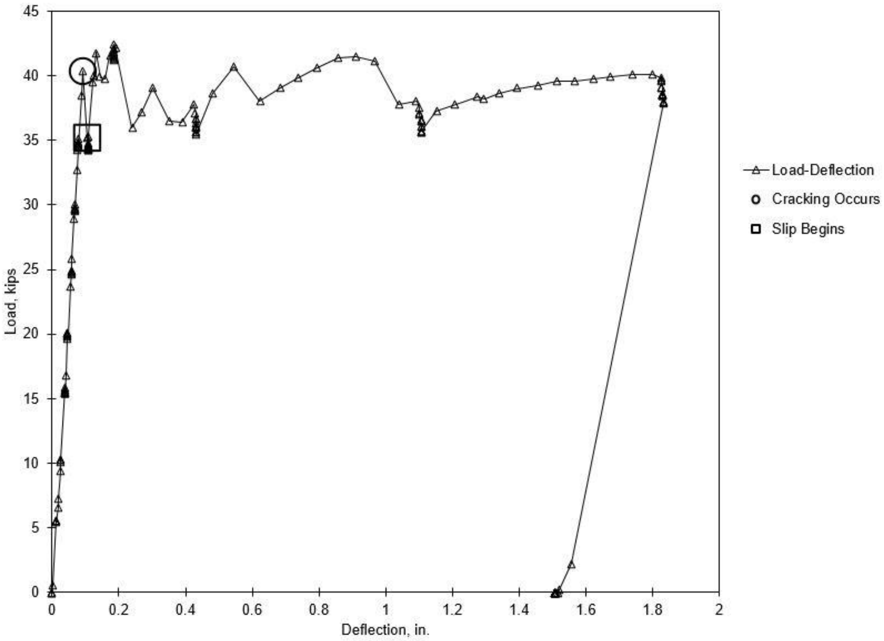

Figure 7.19: Load versus deflection for test C2s

Because of the proximity of the initial shear cracks to the support, slip increased with every load increment and prevented the addition of load. The maximum load reached in this test was 42.4 kips. The test was stopped when some crushing was observed in the deck. The maximum deflection reached was 1.83 in. The cracking pattern from this test is shown in Figure 7.20, with the initial cracks highlighted in red. Bond issues prevented the girder from reaching its estimated capacity. The girder's nominal moment capacity was 204.8 k-ft based on moment capacity (corresponding to a point load of 64.7 kips). The shear capacity by the ACI method was 63.2 kips corresponding to a point load of 82 kips. Because slip began with the initial shear cracking, the capacity of the girder was reduced. Unfortunately, this slip is a limitation of the dimensions of the test. Since the development length is roughly 92 in., the short embedment length required for this test influenced the bond behavior. Additionally, it is possible the stiffness of the end diaphragm may have influenced the test. The initial cracking occurred in shear at a very low deflection. It is possible the diaphragm contributed to the stiffness of the end region. Tests of girders A1s and A2s helped to determine the influence of the diaphragms on beam behavior, but again were for a slightly different beam design which reduces the applicability of the comparison. Another possibility is that the increased stiffness due to the available deck influenced the shear behavior. Both of these possibilities will be explored further.

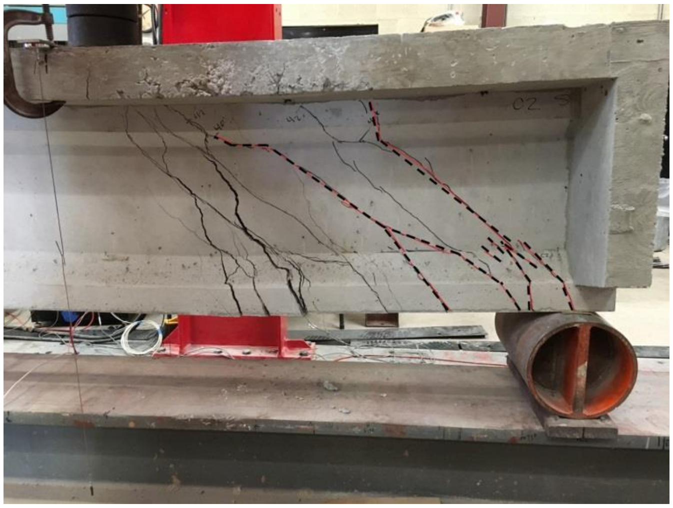

Figure 7.20: Girder C2s cracking (initial shear cracks highlighted)

7.3.3 Test A1s

Test A1s was performed at an *a/d* ratio of 2.4, corresponding to the quarter-point of the girder similarly to test C2s. This location was chosen since this is the location where the scale bridge would be tested, and because test C2s was performed at the same location. The load point was located at a distance of 54 in. from the end of the girder. Initial flexural cracking under the load point occurred at a load of 34.3 kips and 0.14 in. of deflection. This point is marked on the load-deflection plot given in Figure 7.21, and a drop in load occurred shortly after due to strand slip. Initial slip of roughly 0.025 in. was observed in both strands on the loaded end after cracking occurred. The strain before cracking was 251 microstrain at the load point immediately prior to cracking. The measured strain reduced slightly after each new crack formed.

The final behavior of the beam is shown in Figure 7.22. Extensive shear and flexural cracking was observed, and there was some ductility remaining after initial cracking and slip. Crushing in the deck occurred at the final load increments. By the end of the test, a maximum slip of 0.64 and 0.66 in. was measured in the strands at the loaded end. The maximum point load for flexure at this location was 65 kips based on strain compatibility compared to a maximum load in the test of 44.8 kips. This is a difference of 31 percent. This difference can be attributed to slip related to the embedment length and presence of shear cracks in the transfer zone. The estimated shear capacity corresponded to a point load of 83.5 kips by the ACI method.

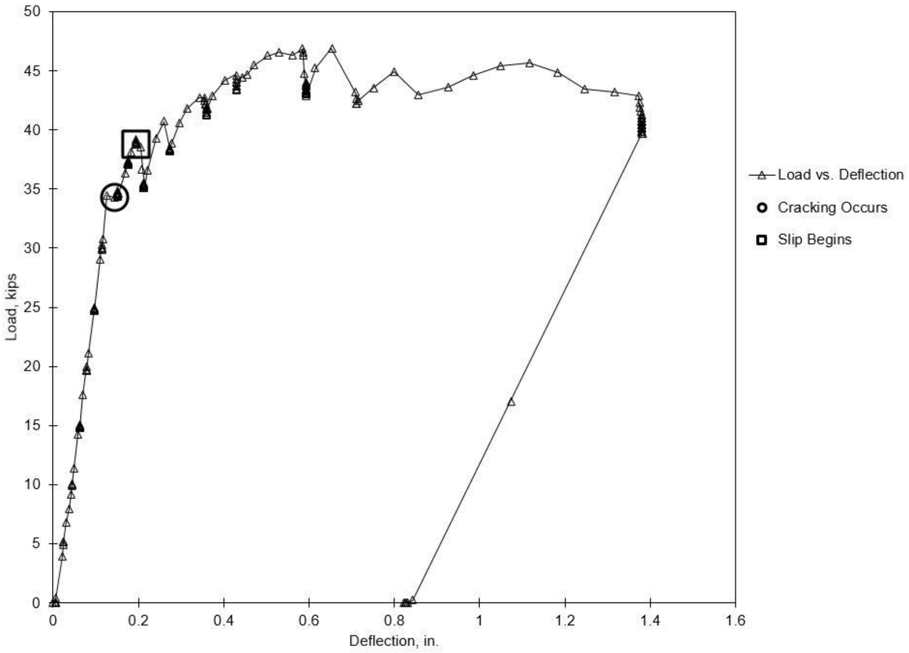

Figure 7.21: Load versus deflection for test A1s

Figure 7.22: Girder A1s cracking patterns, initial cracking shown by red and black dashed line

7.3.2 Test A2s

Test A2s was performed at an *a*/*d* ratio of 3.0, the same as test C1s. The load point was located at a distance of 71.5 in. from the end of the girder. Initial flexural cracking under the load point occurred at a load of 26.7 kips and 0.15 in. of deflection. This point is marked on the load-deflection plot given in Figure 7.23, and led to a change in slope of the load-deflection plot. Initial slip of only 0.004 in. was observed in both strands on the loaded end after cracking occurred. The strain before cracking was 241 microstrain at the load point immediately prior to cracking. The measured strain reduced slightly after each new crack formed. Slip increased to 0.165 and 0.175 in. at the loaded end at a load of 44.8 kips, this location is noticeable on the graph when the load drops off sharply. After this increase in slip, no more load could be applied. At this load, large shear cracks formed near the end of the beam (Figure 7.24).

The final behavior of the beam is shown in Figure 7.24. Extensive shear and flexural cracking was observed, and there was some ductility remaining after initial cracking. The slip and shear cracking at 44.8 kips reduced the load carrying ability of the girder. Crushing in the deck was not observed but some shear cracks oriented themselves horizontally along the top of the deck. By the end of the test, a maximum slip of 0.59 and 0.61 in. was measured for the strands at the loaded end. The maximum point load for flexure at this location was 55.3 kips based on strain compatibility compared to a maximum load in the test of 44.8 kips. This is a difference of 18.6 percent. This difference can be attributed to slip related to the embedment length and shear cracking in the transfer zone. The estimated shear capacity corresponded to a point load of 74 kips by the ACI method.

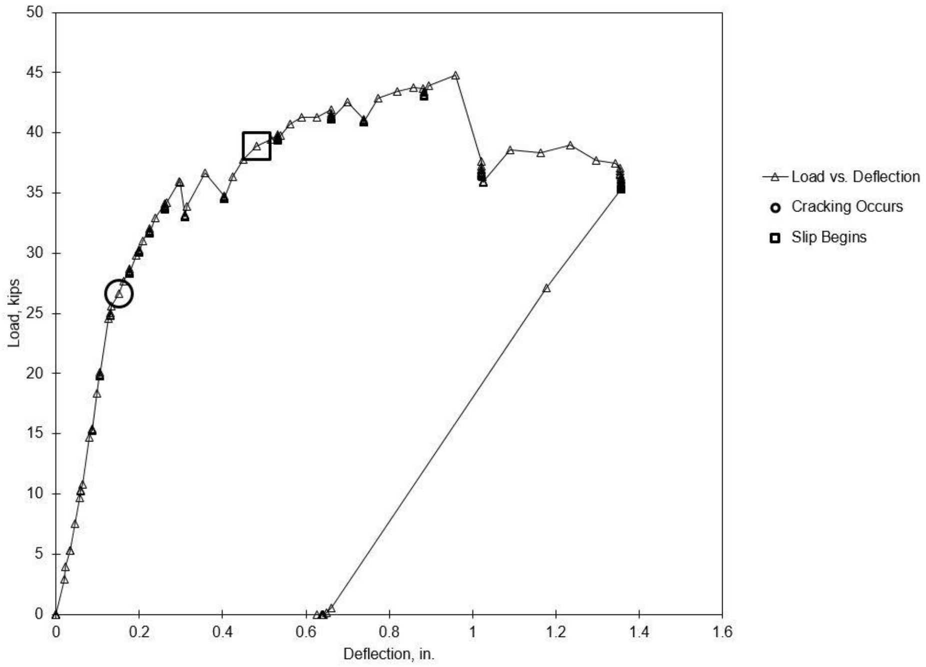

Figure 7.23: Load-deflection for test A2s

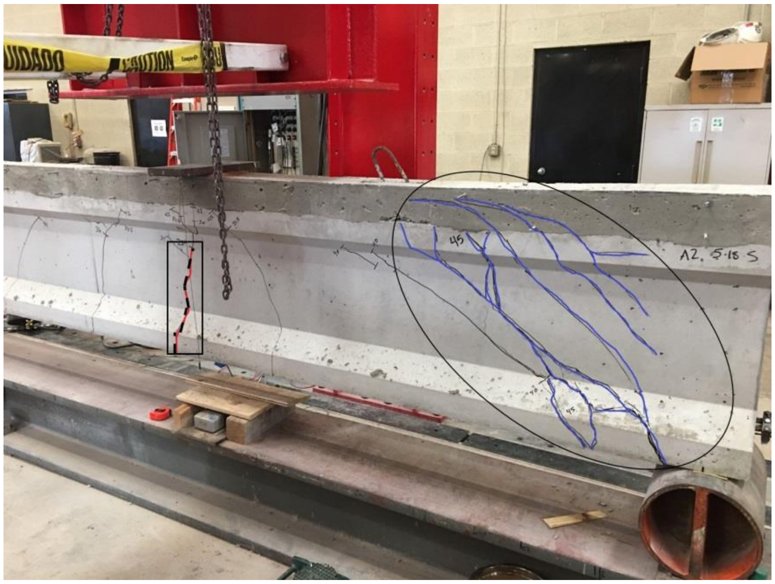

Figure 7.24: Final cracking for specimen A2s, initial flexural crack shown by a red and black dashed line and highlighted by a square, shear cracking at 44.8 kips shown with blue solid lines and highlighted with a circle

7.4 Results of Scale Bridge Test

The destructive test of the scale bridge in Fears Lab was performed on Thursday, December 8, 2016 at 11:00 AM. LVDTs and wire potentiometers were used to measure deflection at the load point under each girder. LVDTs were used to capture small movements and the wire pots were used to measure deflections greater than the stroke of the LVDTs. LVDTs were used to monitor bearing pad deflection at each support location. A surface strain gauge was attached to two end diaphragms and one middle diaphragm. Analog dial gauges were used to monitor slip at the strands. These dials were accurate to 0.0001 in. and had a range of 0.05 in. An overview of the sensor layout it shown in Figure 7.25. Similarly to the individual scale sections, load was applied in 10 kip increments until initial cracking then load increments were reduced to 2 kips.

The connection between the end diaphragms and girders was slightly cracked at the beginning of the test. The diaphragms were tied together with a number 4 bar and lapped to threaded rods that attached with nuts to the outside girders. The concrete at these interfaces was not roughened, so there were small cracks along this interface before testing began. At early load increments, these cracks expanded, indicating some bending in the diaphragms (Figure 7.26). Initial web shear cracking in the girder was observed by members of the research group at a load of 55 kips. Figure 7.27 shows the load versus deflection plot for the initial 60 kips of load. The initial observed crack is marked on this figure and the location where slope changed is also marked. It is likely the first crack occurred at a load closer to 43 kips. The initial web shear crack is shown in Figure 7.28. Slip at the loaded girder is shown in Figure 7.29.

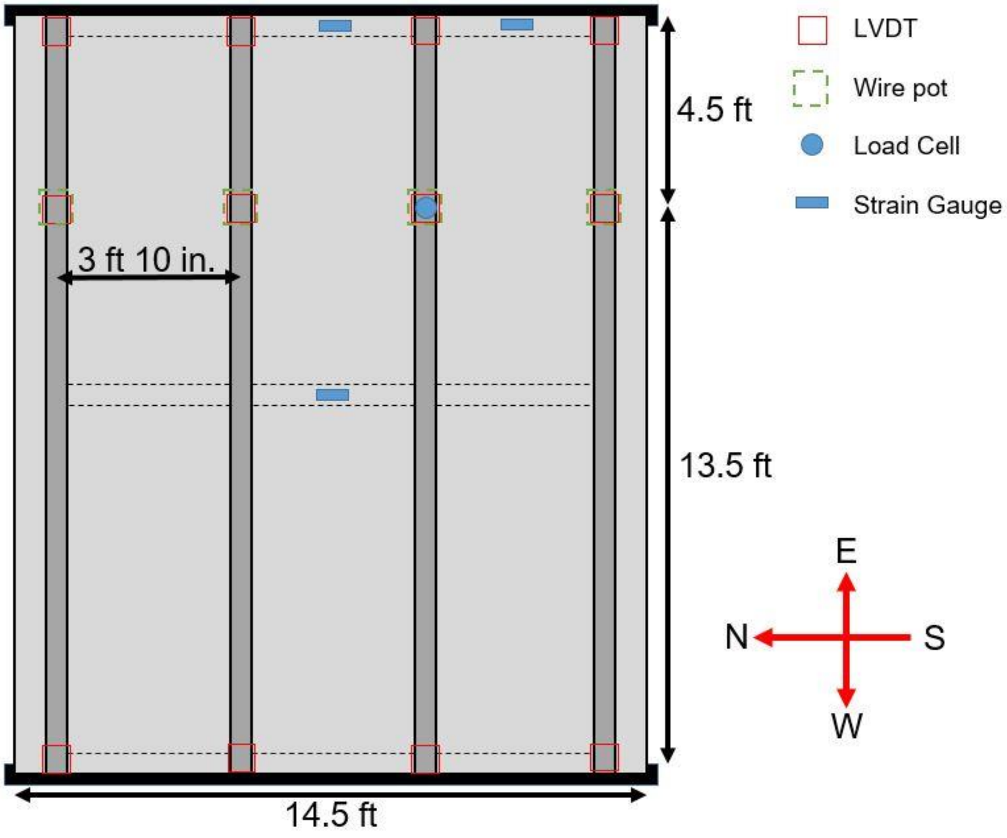

Figure 7.25: Sensor layout for scale bridge test to failure

Figure 7.26: Cracking at diaphragm-girder interface

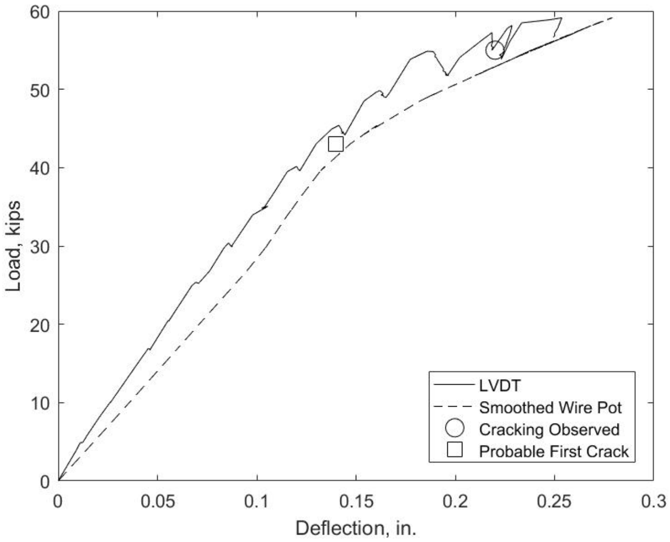

Figure 7.27: Initial load versus deflection for the scaled bridge destructive test at the load point

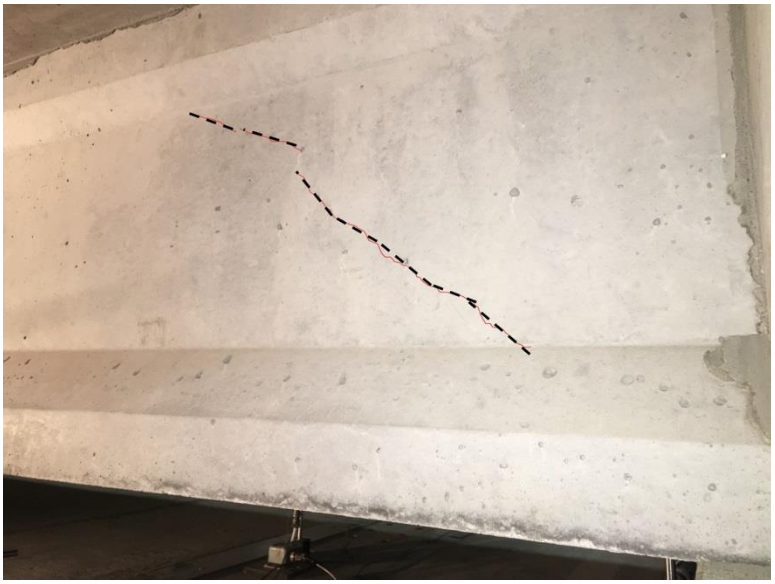

Figure 7.28: Initial web shear crack in the loaded girder (highlighted with a red and black dashed line)

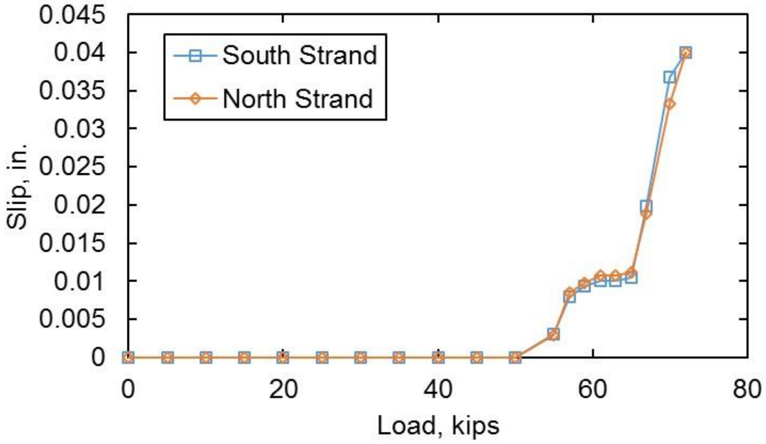

Figure 7.29: Strand slip in loaded girder (dial gauge measurements)

After initial cracking, load was increased at 2 kip increments. Shear cracks extended into the bottom flange at a load of 57 kips. At a load of 63 kips a flexural crack was observed. It is very likely that this crack appeared before this load, but direct observation was difficult because of the crack's interior location. This crack is shown in Figure 7.30. At this load, there was approximately 0.02 in. of slip in the strands of the loaded girder. It is possible that these apparent slip measurements were affected by shifting concrete at the end while the diaphragms cracked and separated from the girders. At a load of 67 kips, another shear crack appeared roughly 2 ft into the span from the previous crack (Figure 7.31). Between 67 and 75 kips of load, a bond shear type crack appeared on the loaded girder and a diagonal crack indicative of two-way slab bending behavior appeared in the deck (Figure 7.32). The slab crack extended from the southeast corner of the bridge where the diaphragm and slab meet to the load point.

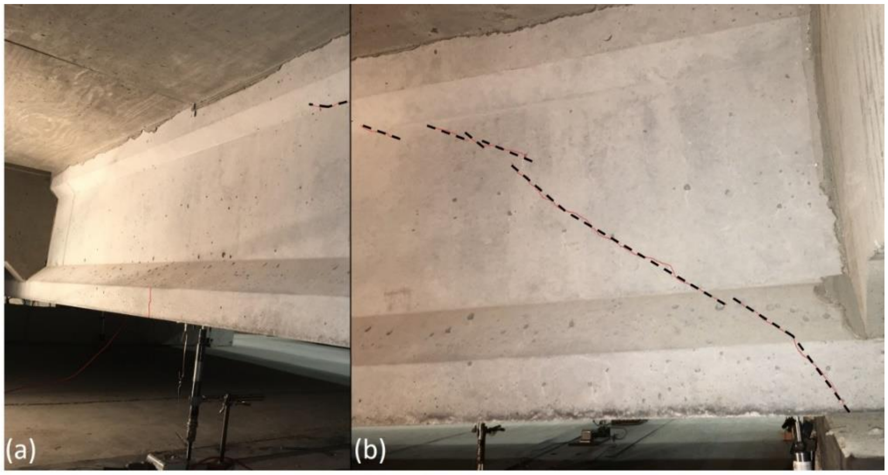
Figure 7.30: Cracking at 63 kips of load (a) flexural crack near midspan, (b) shear crack near the support for the loaded girder

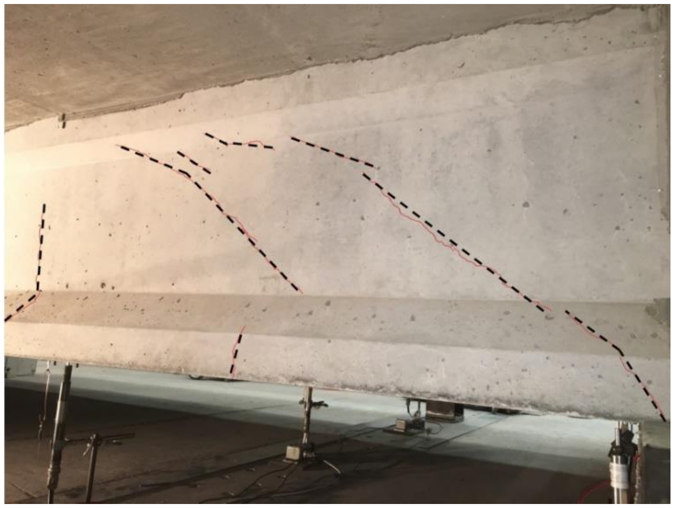
Figure 7.31: Cracking at 67 kips of load for the loaded girder

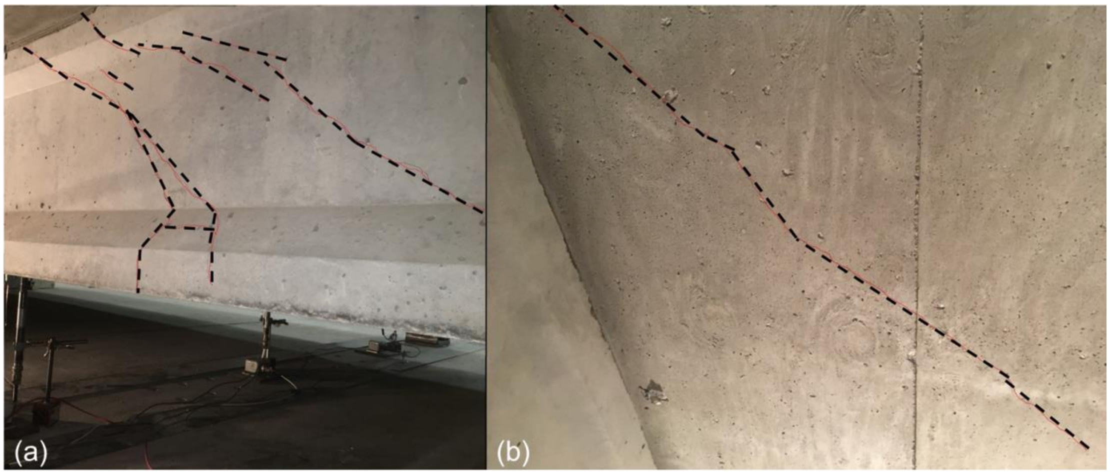
Figure 7.32: Bond shear crack in the loaded girder (left) and diagonal crack in slab (right)

At a load of 78 kips, cracking in the end girder (southernmost) occurred at the bolted connection to the diaphragm. More adequate cover to the connection should have been provided, but the bolt hole spacer shifted during concrete placement (Figure 7.33). The horizontal crack at the web to flange interface on the girder indicates torsion in the end girder. Load was applied up to a maximum of 96.4 kips, at which point there was extensive cracking to the loaded girder, including a horizontal crack where the deck connected to the girder. The load point also punched through the slab at the maximum load. Figure 7.34 shows the load versus deflection plot for the test. The northernmost girder (A3) raised off of its supports by the end of the test (Figure 7.35).

The loaded girder experienced a failure that was very similar to the individual scale section C2s. Cracking and slip was observed at a higher load for the bridge section than for the individual section. The ultimate capacity was also greatly increased, from 42.4 kips in the individual section, to 96.4 kips in the bridge deck. This is an increase of 127%. The girder had much larger post cracking and post slip stiffness due to the transfer of load through the diaphragm and the slab. After the loaded girder cracks, the diaphragms and their connections to the girders are of concern. These locations, as well as the slab are the focus of much of the damage apart from the loaded girder. The outer girder has potential to be damaged by torsion when large forced are applied to the first interior girder based on this test.

Figure 7.33: Cracking at the diaphragm to girder connection for the exterior girder nearest the load point

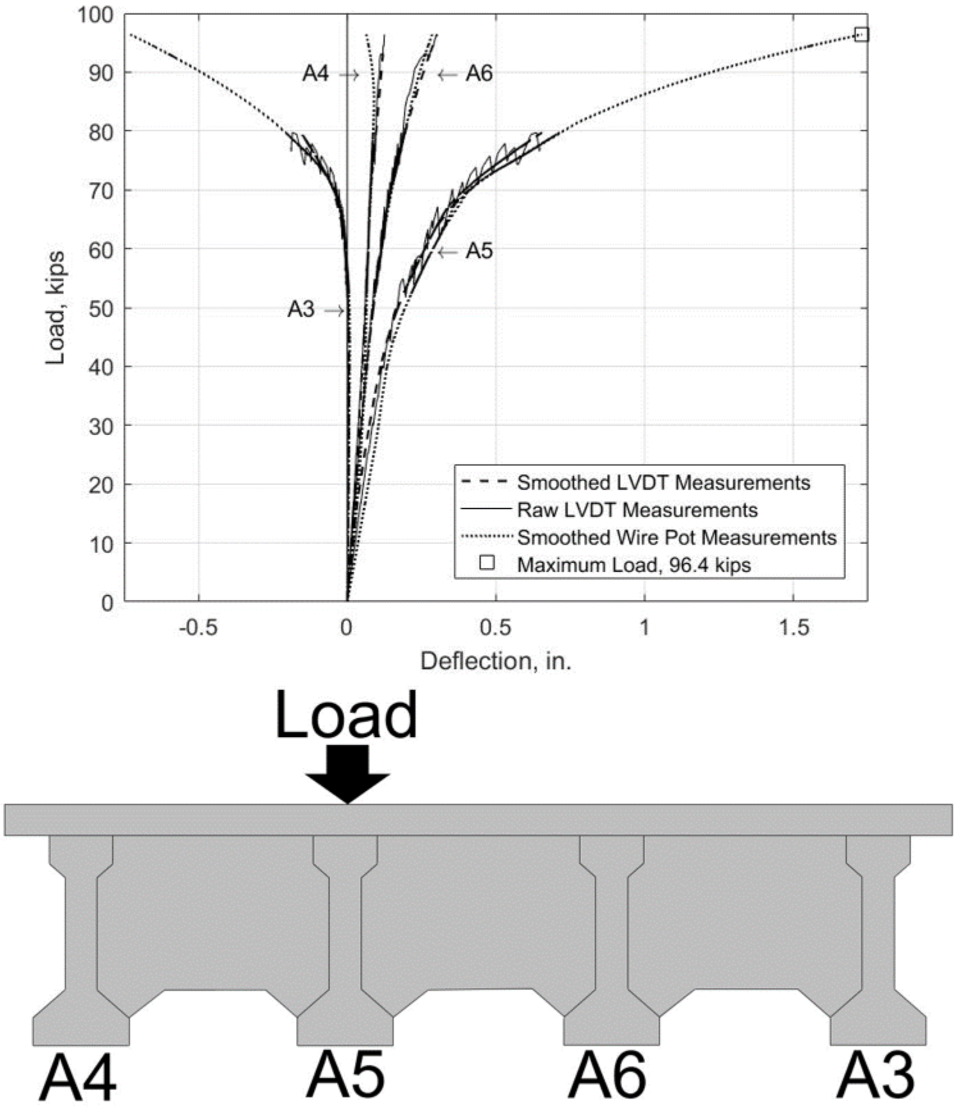

Figure 7.34: Load versus deflection plot for the destructive test of the scaled bridge section showing curves for each girder

More pictures are included of the final state of the bridge showing final cracking and deterioration. Despite the limitations of the manner in which this bridge section was scaled down, this test provided useful information about the ultimate strength behavior of bridge sections. It would be expected that if a single girder were tested and the strength was limited by its shear capacity or by strand slip, the full-scale section would distribute the force, increasing the post-cracking stiffness. It is unclear based on this test how the behavior would be affected by multiple load points across the bridge, such as two trucks located side-by-side. Figures 7.36-7.40 show additional views of the damage to the bridge section.

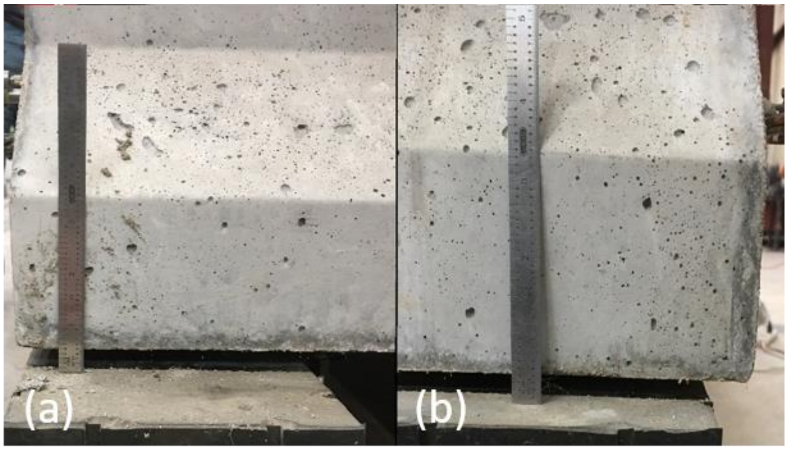

Figure 7.35: Girder A3 raised off of supports at (a) the east support and (b) the west support

Figure 7.36: Shear cracking of loaded girder at failure

Figure 7.37: Diaphragm to girder connection at girder A4 at failure

Figure 7.38: Punching shear in scaled bridge section deck at failure

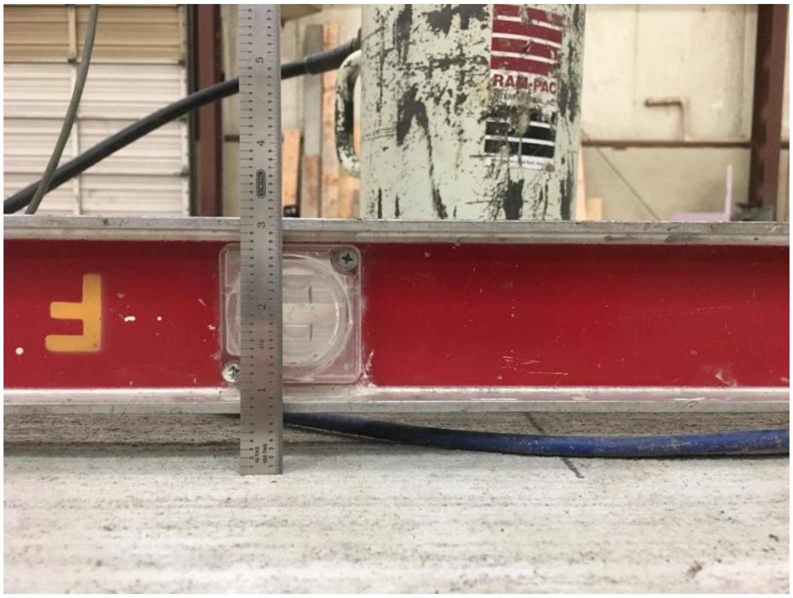

Figure 7.39: Deflection of scaled bridge section deck near the load point

Figure 7.40: Cracking in scaled bridge section slab at failure

7.5 Connection to Analysis

The capacities of the small-scale beam specimens were calculated during design using the same methods used to analyze girders A and C. Similar loading configuration and *a*/*d* ratios used for testing girders A and C were used in testing the small-scale individual beam specimens. The results of the small-scale tests will be compared to the large-scale results and calculated capacities. The results of the composite bridge section elastic tests at varying load points and to failure will be compared to the individual small-scale and large-scale beam tests and to analysis models in order to extract the effects of load transfer between beams on shear capacity of the composite system. The initial analysis model created for the scale bridge using LEAP Bridge Concrete is shown in Figure 7.41 and will be used to analyze the effects of varying loadings and load configurations once calibrated using the scale bridge test data. These results will then be extrapolated to the full bridge model using the same program.

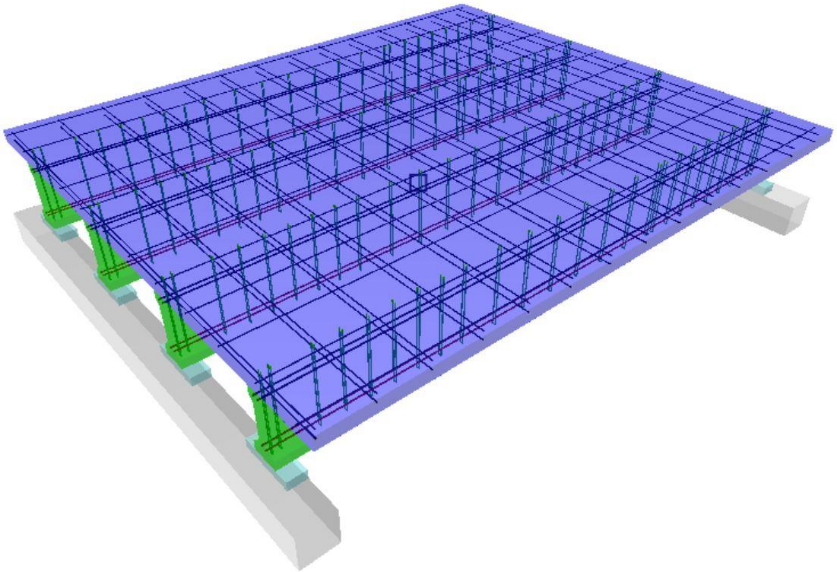

Figure 7.41: Model of scaled bridge section made using LEAP Bridge Concrete

8. Summary and Conclusions

The project described in this report primarily consisted of evaluation of the behavior of two prestressed concrete bridge girders representative of separate designs for 30 ft and 46 ft spans and removed from service after more than 45 years. Both girders were subjected to a battery of non-destructive tests to assess the effects of damage over time and to destructive shear testing at each end. The project included an examination of the contribution of the bridge deck and entire bridge system to shear capacity through testing the real-world girders with a section of the original deck and diaphragms intact, through construction and testing of a scaled composite bridge section, and through detailed structural analysis. This research provided important information on the structural and composite behavior of aged prestressed girder bridges critical to shear and on methods for identifying properties of aged members, structural health monitoring, and damage detection. As has been reported in the literature, shear capacity calculations can vary dramatically. For the tests described in this paper there was little agreement between different methods. However, the full-size girders that were tested had strengths in excess of predicted values for the failure type experienced and showed good ductility before failure despite having been in service for more than 45 years.

Specific conclusions drawn from this work are:

- In all shear test cases examined the applied loads exceeded expected loads whether determined from shear capacity calculations, flexural capacity by strain compatibility, or design demands from AASHTO LRFD. The 2012 AASHTO Simplified method was not a conservative method for calculating shear capacity for the bridge girders tested, and this research would indicate that the 2004-AASHTO method is the best balance of accuracy and conservativism.

- Corrosion at the girder ends caused some issues in behavior, especially at high loads. Spalling was often initiated by the corrosion cracking at the ends, potentially leading to bond loss. This mode of deterioration is common in simply supported precast concrete girder bridges in Oklahoma and should be taken into consideration when evaluating the shear strength of older girders near the supports.

- Using cracking moment to identify effective prestress was found to be an effective method if cracking could be forced to occur primarily due to flexure. However, using camber measurements to identify effective prestress was less effective due to difficulty in accounting for the effects of creep.

- The small-scale individual AASHTO girders failed earlier than expected due to bond issues with the relatively large prestressing strands used compared to the section size. The small-scale composite bridge section resisted significantly larger loads (approximately 125% larger) compared to the individual girders indicating a significant effect on section capacity.

- End and interior diaphragms contributed to load transfer between girders in the test of the scaled bridge section. Differences in diaphragm construction used over the years in Oklahoma may reduce the general application of this conclusion.

- To predict time-dependent behaviors of pretensioned concrete, a simple yet effective 1-D model was established by leveraging an existing initial value problem model for concrete creep and strand relaxation in post-tensioned concrete and Guyon’s instantaneous elastic shortening analysis based on a boundary value problem. By directly utilizing simple measurements (draw-in time history measured from a pretensioned concrete beam) and other section and material properties, many facets of bond-transfer behavior can be predicted. The proposed method was validated to the best extent possible with available data. Drying shrinkage of concrete causes the most significant unmodeled error; the effect of which is discussed for future work. The principle and procedure of injecting draw-in time history measurement to time-dependent modeling of pretensioned concrete - as a critical piece of information - have been established in this study. The work enables feasible field implementation and practical application of this data-based method to clarify and explain actual bond transfer behavior critical to long-term performance of pretensioned concrete.

- Improvements were made to the backbone technique used for processing free vibration response data for nonlinear system identification and damage detection purposes through this project. This technique provides an additional step in extracting useful information regarding the state of infrastructure elements from collected data.

In this study, we have extensively and intensively studied experimental data collected from the precious full-scale real-world specimens by focusing on identifying the underlying governing properties, whose values would otherwise be assumed with a great deal of uncertainties and inaccuracies involved. The purpose of this important aspect of our investigation is to facilitate the collection and analysis of field data from the aging highway bridges in Oklahoma (and other states in the U.S.) in the future so that the structural integrity of these bridges in question could be evaluated correctly and effectively by the most reliable source of information. The field data could be long-term monitoring and/or short-term field testing data, the choice of which should stem from in-house studies like the ones in this project. Here in this project, we have either developed new theoretical approach (see Section 4.5) and robust numerical algorithms (see Section 5) or collected a large amount of reliable data measurements (see Section 6.1) – in addition to other initial attempts (see Sections 6.2 and 6.3). Future studies could synthesize these efforts by taking an integrative approach. The road to success would not be easy, however the utilization of field data, the most reliable source of information, to assess the integrity of aging highway bridges in question, should remain as our strongest motivation.

REFERENCES

Adams, D. and Allemang, A. (1998). “Survey of nonlinear detection and identification techniques for experimental vibrations.” *Proceedings of the International Conference on Noise and Vibration Engineering*, 269–281.

Amari, S.-I., Park, H., and Ozeki, T. (2006). “Singularities affect dynamics of learning in neuromanifolds.” Neural Computation, 18, 1007–1065.

American Association of State Highway and Transportation Officials (AASHTO) (1973). *Standard Specifications for Highway Bridges, Customary U.S. Units*. AASHTO, 11 edition.

American Association of State Highway and Transportation Officials (AASHTO) Executive Committee, (1989) *Standard Specifications for Highway Bridges*, *Customary U.S. Units, Fourteenth Ed.,* Washington, D.C.

American Association of State Highway and Transportation Officials (AASHTO) Executive Committee (1990) *Standard Specifications for Highway Bridges*, *Customary U.S. Units, Fourteenth Ed., Interim,* Washington, D.C.

American Association of State Highway and Transportation Officials (AASHTO) Executive Committee, (1991) *Standard Specifications for Highway Bridges*, *Customary U.S. Units, Fourteenth Ed., Interim,* Washington, D.C.

American Association of State Highway and Transportation Officials (AASHTO) (2007). *AASHTO LRFD Bridge Design Specifications, Customary U.S. Units*. AASHTO, 4th Edition.

American Association of State Highway and Officials (AASHTO), (2009) *AASHTO LRFD Bridge Design Specifications, Customary U.S. Units, Fourth Ed., Interim*, Washington D.C.

American Association of State Highway and Transportation Officials (AASHTO) (2012). *AASHTO LRFD Bridge Design Specifications, Customary U.S. Units*. AASHTO, 6 edition.

American Concrete Institute (ACI) Committee 214, (2003) *Guide for Obtaining Cores and Interpreting Compressive Strength Results (ACI 214.4R-03),* Farmington Hills, MI: American Concrete Institute.

American Concrete Institute (ACI) Committee 318, (2008) *Building Code Requirements for Structural Concrete and Commentary (ACI 318-08)*, Farmington Hills, MI: American Concrete Institute.

American Concrete Institute 318 (2011). *Building Code Requirements for Structural Concrete and Commentary (ACI 318-11)*. Farmington Hills, MI.

ACI Committee 318 (2014), Building Code Requirements for Structural Concrete (ACI 318-14) and Commentary, American Concrete Institute.

ASTM Standard A370, (2014) “Standard Test Methods and Definitions for Mechanical Testing of Steel Products,” ASTM International, West Conshohocken, PA.

ASTM Standard A1061, (2009) “Standard Test Methods for Testing Multi-Wire Steel Strand,” ASTM International, West Conshohocken, PA.

ASTM Standard C39, (2012) “Standard Test Method for Compressive Strength of Cylindrical Concrete Specimens,” ASTM International, West Conshohocken, PA.

ASTM Standard C143, (2015) “Standard Test Method for Slump of Hydraulic-Cement Concrete,” ASTM International, West Conshohocken, PA.

ASTM Standard C231, (2014) “Standard Test Method for Air Content of Freshly Mixed Concrete by the Pressure Method,” ASTM International, West Conshohocken, PA.

ASTM Standard C469, (2010) “Standard Test Method for Static Modulus of Elasticity and Poisson's Ratio of Concrete in Compression,” ASTM International, West Conshohocken, PA.

Ayoub, A. and Filippou, F. C. (2010). “Finite-element model for pretensioned prestressed concrete girders.” ASCE Journal of Structural Engineering, 136(4), 401–409.

Balázs, G. L. (1993). “Transfer length of prestressing strand as a function of draw-in and initial prestress.” PCI Journal, 38(2), 86–93.

Baxi, A. N. (2005). “Analytical modeling of fully bonded and debonded pre-tensioned prestressed concrete members.” Ph.D. thesis, The University of Texas at Austin,

Benítz, J. M. and Gálvez, J. C. (2011). “Bond modelling of prestressed concrete during the prestressing force release.” Materials and Structures, 44, 263–278.

Bentz, E.C., Vecchio, F.J., and Collins, M.P. (2006) "Simplified Modified Compression Field Theory for Calculating Shear Strength of Reinforced Concrete Elements," *ACI Structural Journal,* 103(4), 614-624,.

Braun, S. and Feldman, M. (1997). “Time-frequency characteristics of non-linear systems.” *Mechanical systems and signal processing*, 11(4), 611–620.

Chang, P. C., Flatau, A., and Liu, S. C. (2003). “Review paper: Health monitoring of civil infrastructure.” *Structural Health Monitoring (SHM)*, 2(3), 257–267.

Chopra, A. (2001). *Dynamics of Structures: Theory and Applications to Earthquake Engineering*. Prentice-Hall, Inc., second edition edition.

Cizek, V. (1970). “Discrete Hilbert transform.” *IEEE Transactions on Audio and Electroacoustics*, 18(4), 340–343.

Cohen, L. (1995). *Time-frequency analysis*. Prentice Hall PTR New Jersey.

Collins, M.P., Mitchell, D., Adebar, P., and Vecchio, F.J. (1996) "A General Shear Design Method," *ACI Structural Journal,* 93(1), 36-45.

Czaderski, C. and Motavelli, M. (2006) "Determining the Remaining Tendon Force of a Large-Scale, 38-Year-Old Prestressed Concrete Bridge Girder," *PCI Journal,* 51(4), 56-68.

Dang, C. N., Floyd, R. W., Prinz, G. S., and Hale, W. M. (2016). “Determination of the bond stress distribution coefficient by the maximum likelihood method.” ASCE Journal of Structural Engineering, 142(5).

Doebling, S.W., Farrar, C. R., Prime,M. B., and Shevitz, D.W. (1996). “Damage identification and health monitoring of structural and mechanical systems from changes in their vibration characteristics: a literature review.” *Report no.*, Los Alamos National Lab., NM (United States).

Farrar, C. R. and Worden, K. (2007). “An introduction to structural health monitoring.” *Philosophical Transactions of the Royal Society of London A: Mathematical, Physical and Engineering Sciences*, 365(1851), 303–315.

Fédération International de la Précontrainte (FIP) (1982). “Test for the determination of tendon transmission length under static conditions.” Report no., Wexham Springs, U.K.

Feldman,M. (1994a). “Non-linear system vibration analysis using Hilbert transform- I. free vibration analysis method “FREEVIB”.” *Mechanical Systems and Signal Processing*, 8(2), 119–127.

Feldman, M. (1994b). “Non-linear system vibration analysis using Hilbert transform - II. forced vibration analysis method “FORCEVIB”.” *Mechanical Systems and Signal Processing*, 8(3), 309–318.

Feldman, M. (1997). “Non-linear free vibration identification via the Hilbert transform.” *Journal of Sound and Vibration*, 208(3), 475–489.

Feldman, M. (2005). “Time-varying and non-linear dynamical system identification using the hilbert transform.” *ASME 2005 International Design Engineering Technical Conferences and Computers and Information in Engineering Conference*, American Society of Mechanical Engineers, 1309–1317.

Feldman,M. (2006). “Time-varying vibration decomposition and analysis based on the Hilbert transform.” *Journal of Sound and Vibration*, 295(3), 518–530.

Feldman, M. (2011a). *Hilbert Transform Applications in Mechanical Vibration*. John Wiley & Sons.

Feldman, M. (2011b). “Hilbert transform in vibration analysis.” *Mechanical Systems and Signal Processing*, 25, 735–802.

Feldman, M. and Braun, S. (1995). “Identification of non-linear system parameters via the instantaneous frequency: application of the hilbert transform and Wigner-Ville techniques.” *Proc. of the XIII Int. Modal Analysis Conf.*, Nashville, TN, 637–642.

Geßner, S. and Henne, M. (2016). “Bond behavior of indented wired in pretensioning.” 2016 PCI/NBC.

Goyal, D. and Pabla, B. (2015). “The vibration monitoring methods and signal processing techniques for structural health monitoring: A review.” *Archives of Computational Methods in Engineering*, 1–10.

Guyon, Y. (1953). *Prestressed Concrete*. John Wiley.

Hahn, S. L. (1996). *Hilbert transforms in signal processing*, Vol. 2. Artech House Boston.

Halsey, T.J. and Miller, R. (1996) "Destructive Testing of Two Forty-Year-Old Prestressed Concrete Bridge Beams," *PCI Journal,* 41(5), 84-93.

Hamilton III, H. R., Llanos, G., Ross, B. E., (2009) “Shear Performance of Existing Prestressed Concrete Bridge Girders,” BD 545-56, Florida Department of Transportation, Tallahassee, FL.

Hawkins, N.M., Kuchma, D.A., Mast, R.F., and Reineck, K.-H. (2005) "NCHRP 549: Simplified Shear Design of Concrete Members," Transportation Reseach Board, Washington, D.C.

Housner, G. W., Bergman, L. A., Caughey, T. K., Chassiakos, A. G., Claus, R. O., Masri, S. F., Skelton, R. E., Soong, T. T., Spencer, B. F., and Yao, J. T. P. (1997). “Structural control: Past, present, and future.” *ASCE Journal of Engineering Mechanics, special issue*, 123(9), 897–971.

Huang, D., Zhao, J., and Su, J. (2003). “Practical implementation of the Hilbert-Huang transform algorithm.” *Acta Oceanologica Sinica*, 22(1), 1–14.

Jones, J. D. and Pei, J. S. (2009). “Embedded algorithms within an FPGA to classify nonlinear single-degree-of freedom systems.” *IEEE Sensors Journal*, 9(11), 1486–1493 Special Issue on Sensor Systems for Structural Health Monitoring.

Kak, S. (1977). “The discrete finite Hilbert transform.” *Indian Journal Pure and Applied Mathematics*, 8, 1385–1390.

Kaufman, K. and Ramirez, J.A. (1988) “Re-evaluation of the Ultimate Shear Behavior of High-Strength Concrete Prestressed I-Beams,” *ACI Structural Journal*, 85(3), 295–303.

Kerschen, G., Worden, K., Vakakis, A. F., and Golinval, J. C. (2006). “Past, present and future of nonlinear system identification in structural dynamics.” *Mechanical Systems and Signal Processing*, 20(3), 505–592.

Kim, K. and Bazaňt, P. Z. (2014). “Creep design aid: Open-source website program for concrete creep and shrinkage prediction.” *ACI Materials Journal*, 111(1-6).

King, F. W. (2009a). *Hilbert transforms, Volume 1*. Encyclopedia of Mathematics and its Applications.

King, F. W. (2009b). *Hilbert transforms, Volume 2*. Encyclopedia of Mathematics and its Applications.

I. Kovacic and M. Brennan, eds. (2011). *The Duffing Equation: Nonlinear Oscillators and Their Behavior*. Wiley.

LEAP CONSPAN, Bentley, Version 13.00.00.68, 2013.

Liang, Z., Lee, G. C., Dargush, G. F., and Song, J. (2012). *Structural Damping: Applications in Seismic Response Modification*. CRC Press.

Lim, S. N., Choi, Y. C., Oh, B. H., Kim, J. S., Shin, S., and Lee, M. K. “Bond characteristics and transfer length of prestressing strand in pretensioned concrete structures.” *VIII International Conference on Fracture Mechanics of Concrete and Concrete Structures (FraMCoS-8)*, J. Van Mier, G. Ruiz, C. Andrade, R. Yu, and X. Zhang, eds.

Londoño, J., Neild, S., and Cooper, J. (2015). “Identification of backbone curves of nonlinear systems from resonance decay responses.” *Journal of Sound and Vibration*, 348, 224–238.

Loughlin, P. (1998). “Do bounded signals have bounded amplitudes?” *Multidimensional Systems and Signal Processing*, 9, 419–424.

Lundqvist, P. and Riigimaki, J. (2010) "Testing of five 30-year-old prestressed concrete beams," *PCI Journal,* 55(4), 50-58.

Lynch, J. P. and Loh, K. J. (2006). “A summary review of wireless sensors and sensor networks for structural health monitoring.” *The Shock and Vibration Digest*, 38(2), 91–128.

MacGregor, J.G., Sozen, M.A., and Sless, C. (1965) "Strength of prestressed concrete beams with web reinforcement," *ACI Journal Proceedings,* 62(12), 1503-1520.

MacGregor, J.G. and Hanson, J.M. (1969) "Proposed Changes in Shear Provisions for Reinforced and Prestressed Concrete Beams," *ACI Journal,* 66(4), 276-288.

Marple Jr., S. L. (1999). “Computing the discrete-time ‘analytic’ signal via FFT.” *IEEE Transactions on Signal Processing*, 47(9), 2600–2603.

Martin, R. D., Kang, T. H. K., and Pei, J.-S. (2011). “Experimental and code analyses for shear design of AASHTO prestressed concrete girders.” PCI Journal, 56(1), 54–74.

Martí-Vargas, J. R., Arbelaez, C. A., Serna-Ros, P., and Castro-Bugallo, C. (2007). “Reliability of transfer length estimation from strand end slip.” *ACI Structural Journal*, 104(4), 487–494.

Martí-Vargas, J. R., Serna-Ros, P., Fernandez-Prada, M. A., Miguel-Sosa, P. F., and Arbelaez, C. A. (2006). “Test method for determination of the transmission and anchorage lengths in prestressed reinforcement.” *Magazine of Concrete Research*, 58(1), 21–29.

Maruyama, K. and Rizkalla, S.H. (1988) “Shear Design Consideration for Pretensioned Prestressed Beams,” *ACI Structural Journal*, 85(5), 492-498.

Meissner, M. (2012). “Accuracy issues of discrete hilbert transform in identification of instantaneous parameters of vibration signals.” *Acta Physica Polonica - Series A General Physics*, 121(1-A), A–164 – A–167.

Nilson, A.H., Darwin, D., and Dolan, C.W. (2005) Design of Concrete Structures, New York, NY: McGraw-Hill, Inc.

Nordby, G.M. and Venuti, W.J. (1957) “Fatigue and Static Tests of Steel Strand Prestressed Beams of Expanded Shale Concrete and Conventional Concrete,” *ACI Journal Proceedings*, 54(8), 141-160.

Oh, B. H., Kim, E. S., and Choi, Y. C. (2006). “Theoretical analysis of transfer lengths in pretensioned prestressed concrete members.” ASCE Journal of Engineering Mechanics, 132(10), 1057–1066.

Oklahoma Department of Transportation (ODOT) (2009) Standard Specifications Book, Construction Engineering Standards, Specifications, Materials and Testing, http://www.okladot.state.ok.us/c_manuals/specbook/oe_ss_2009.pdf.

Osborn, G. P. (2010) “Ultimate Shear Capacity and Residual Prestress Force of Full-Scale, Forty-One-Year-Old Prestressed-Concrete Girders,” M.S. Thesis, Utah State University, Logan, UT.

Osborn, G.P., Barr, P.J., Petty, D.A., Halling, M.W., and Brackus, T.R. (2010) "Residual prestress forces and shear capacity of salvaged prestressed concrete bridge girders," *Journal of Bridge Engineering,* 17(2), 302-309.

Osborn, G. P., Barr, P., Petty, D., Halling, M., and Brackus, T. (2012) “Residual Prestress Forces and Shear Capacity of Salvaged Prestressed Concrete Bridge Girders,” *Journal of Bridge Engineering*, 17(2), 302–309.

Paz, M. (1994). *International Handbook of Earthquake Engineering: Codes, Programs, and Examples*. Civil engineering. Springer US.

Pei, J. S., Martin, R. D., Sandburg, C. J., and Kang, T. H.-K. (2008). “Rating precast prestressed concrete bridges for shear.” Report No. ODOT SPR ITEM 2186, University of Oklahoma.

Pessiki, S., Kaczinski, M., and Wescott, H. H. (1996) “Evaluation of Effective Prestress Force in 28-Year-Old Prestressed Concrete Bridge Beams,” *PCI Journal*, 41(6), 78–89.

Precast/Prestressed Concrete Institute (PCI) (2010) *PCI Design Handbook*, *Seventh Ed.,* Chicago, IL.

Renson, L., Gonzalez-Buelga, A., Barton, D., and Neild, S. (2016). “Robust identification of backbone curves using control-based continuation.” *Journal of Sound and Vibration*, 367, 145–158.

Ross, B. E., Ansley, M. H., and Hamilton III, H. R. (2011) “Load Testing of 30-Year-Old AASHTO Type III Highway Bridge Girders,” *PCI Journal*, 56(4), 152-163.

Ross, B. E. and Naji, B. (2013). “A model for nominal bond-shear capacity of pretensioned concrete girders.” *Transportation Research Record*, 1(2406), 79–86.

Schlaich, J., Schafer, K. and Jennewein, M. (1987) "Toward a Consistent Design of Structural Concrete," *PCI Journal,* 32(3), 74-150.

Shahawy, M., Robinson, B., Batchelor, B. deV. (1993) “An Investigation of Shear Strength of Prestressed Concrete AASHTO Type II Girders,” Florida Department of Transportation, Tallahassee, FL.

Shenoy, C. V., and Frantz, G. C. (1991) “Structural Tests of 27-Year-Old Prestressed Concrete Bridge Beams,” *PCI Journal*, 36(5), 80-90.

Sohn, H., Farrar, C. R., Hemez, F. M., and Czarnecki, J. J. (2002). “A review of structural health review of structural health monitoring literature 1996-2001.” *Report no.*, Los Alamos National Laboratory.

Tang, P. F. (2015). “Analysis of backbone technique: A Hilbert transform and discrete Hilbert transform-based technique.” Ph.D. thesis, University of Oklahoma, Norman, OK (December).

Testa, R. B. (1998). “Class notes for Columbia University E4113 Advanced Mechanics of Solids.

Vecchio, F.J., and Collins, M.P. (1986) "The Modified Compression-Field Theory for Reinforced Concrete Elements Subjected to Shear," *ACI Journal Proceedings*, 83(2), 219-231.

Watanabe, S. (2007). “Almost all learning machines are singular.” Proceedings of the 2007 IEEE Symposium on Foundations of Computational Intelligence (FOCI 2007), IEEE, 383–388.

Wendling, A. (2014) “Time Dependent Behavior of Self-Consolidating Lightweight Prestressed Members with Top-Strands,” M.S. Thesis, University of Oklahoma, Norman, OK.

Wight, J.K. and MacGregor, J.G. (2012) Reinforced Concrete: Mechanics and Design, Upper Saddle River, NJ: Pearson Education, Inc.

Yu, Q., Bazănt, P. Z., and Wendner, R. (2012). “Improved algorithm for efficient and realis- tic creep analysis of large creep-sensitive concrete structures.” *ACI Structural Journal*, 109(5).

Zia, P., Preston, H. K., Scott, N. L., Workman, E. B. (1979) “Estimating Prestress Losses,” *Concrete International*, 1(6), 32-38.